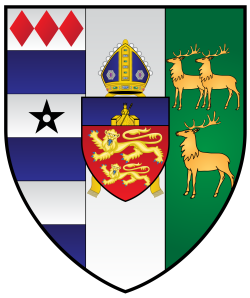
Searches for Scharms and Gluinos with the ATLAS Detector

Charles William Kalderon
Lincoln College, Oxford





Thesis submitted in fulfilment of the requirements
for the degree of Doctor of Philosophy at the University of Oxford

Hilary Term, 2016

Searches for Scharms and Gluinos with the ATLAS Detector

Charles William Kalderon
Lincoln College, Oxford

Thesis submitted in fulfilment of the requirements
for the degree of Doctor of Philosophy at the University of Oxford.

Hilary Term, 2016

Abstract

Following the extremely successful operation of the Large Hadron Collider at CERN during its first years of operation, the ATLAS and CMS collaborations announced the discovery of a new particle compatible with the Higgs boson in July 2012, finishing the complement of particles in the Standard Model. However, no other new particle was even hinted at, confounding predictions of an early discovery of Supersymmetry that would resolve the hierarchy problem and retain low fine-tuning. This thesis presents two searches for new phenomena that would have evaded early efforts. The first, using the full 8 TeV dataset collected in 2012 by ATLAS, targets heavy particles decaying to charm quarks and non-interacting particles through the use of a recently developed charm-jet identification algorithm. No excess is observed over the Standard Model predictions, so results are interpreted in the context of supersymmetric charm production. This is constrained to the highest masses so far, with scharms excluded at the 95% confidence level for masses up to 550 GeV with neutralino masses below 200 GeV. The second search makes use of the 13 TeV dataset collected in 2015, and looks for heavier particles which are produced with far higher cross section at this increased collision energy. It is sensitive to particles decaying via cascades to large numbers (≥ 7 to ≥ 10) of hadronic jets, with sensitivity enhanced through requirements on the number of jets identified as arising from bottom quarks. Again, no excess is observed, and so limits are set on gluino production in two cascade decay scenarios, with a significant increase in reach obtained over 2012 searches for the same final state – gluino masses below 1400 GeV are excluded in the models considered.

Acknowledgements

It is hard to condense into a few paragraphs the many people who have supported and guided me up to this point, and to whom I am hugely indebted. You are more numerous than can be mentioned here, and I am sincerely grateful to each and every one of you.

First of all, I would like to thank my supervisor Claire Gwenlan and Oxford SUSY group leader Alan Barr, both of whom have been incredibly supportive and helpful throughout this time, available to dispense advice at all hours when needed, while at the same time fostering a group I am hugely privileged to have been a part of.

To the generations of students above me I owe many thanks – Chris Young, Alex Dafinca and Mireia Crispín Ortuzar passed on a wealth of knowledge and their infectious enthusiasm, and I would have achieved little without them. Alex responded to any and every query selflessly in my first year, Mireia co-authored the novel spanda search and Chris drew the short straw and has had to work with me until the end. To Will, Jon, Mike and Jesse, I hope I may have been a tenth as helpful. I owe thanks and apologies in equal measure to those with whom I have shared an office – Andrée Robichaud-Véronneau for welcoming me to CERN and introducing me to the SCT, Kathrin Becker for ensuring I didn't break it, Will Fawcett for solidarity during multijet approval marathons, Lydia Beresford for keeping an eye on my screen while I was writing up and Mark Pickering for managing to remaining cheerful after two years – you have all been the source of sage advice and light relief.

I have had the good fortune to work with many colleagues who made it a joy – Dan Guest through enlivening the inevitable Friday evening scharm discussions; Peyton Rose and Chiara Debenedetti through taming the DCS with good humour (aided invaluably by Koichi Nagai, Peter Philips, Tony Weidberg and Dave Robinson) and a wealth of others in the ATLAS SUSY group.

The IT staff at Oxford, in particular Sean Brisbane, have rescued countless deadlines from disaster, setting up numerous emergency batch queues and going far beyond the call of duty, despite my stubborn presence at the top of the Oxford ATLAS disk usage leaderboard. Likewise, organisation was turned from a chore to a pleasure by the immensely helpful and understanding Oxford particle physics administrative staff, in particular Sue Geddes.

Outside ATLAS, Olli Lupton and Faye Cheung have provided excellent company for hundreds of lunches and nearly as many Alpine exploits. From the sailors of Oxford and Cambridge via my compatriots in Lincoln's MCR to the hillwalkers of Geneva and Scotland, there are many others who filled my free time with fun and adventure, none more so than Irene, who has brightened every day.

I would never have arrived at this point without a succession of inspirational teachers. 'Science' Sue under Jane Addis at the Merlin was perhaps the first to ignite my interest in science, and the flame was fanned by Nick Folkard at Colet Court and Ken Zetie, Nigel Hinton and Peter Sammut at St Paul's, among many others. At Cambridge, it was Mark Thomson's excellent tutelage that brought me to particle physics and kept me hooked.

Finally, the most thanks of all goes to my parents, Mark and Sue, for the love, immeasurable support and direction towards inquisitive thought they have given to me and my sisters, Rebecca and Joanna. This thesis is dedicated to all four.

Contents

Preface 1

1 Introduction 3

2 Theoretical background 5
- 2.1 Particle Content of the Standard Model . . . 6
- 2.2 Theoretical description of the Standard Model . . . 9
  - 2.2.1 Quantum Electrodynamics . . . 9
  - 2.2.2 The Standard Model Lagrangian . . . 10
  - 2.2.3 Running couplings and renormalisation . . . 16
- 2.3 QCD Phenomenology and Event Generation . . . 18
  - 2.3.1 Features of QCD . . . 18
  - 2.3.2 Event Generation . . . 19
- 2.4 Supersymmetry . . . 24
  - 2.4.1 SUSY particle content . . . 25
  - 2.4.2 SUSY breaking . . . 27
  - 2.4.3 SUSY at the LHC . . . 29
- 2.5 Conclusions . . . 32

3 The ATLAS experiment 33
- 3.1 The Large Hadron Collider . . . 35
- 3.2 ATLAS . . . 36
  - 3.2.1 Co-ordinate definition . . . 36
  - 3.2.2 Overview . . . 37
  - 3.2.3 Inner Detector . . . 38
  - 3.2.4 Calorimeters . . . 41
  - 3.2.5 Muon System . . . 42
- 3.3 Data Recording . . . 45
  - 3.3.1 Trigger . . . 45
  - 3.3.2 Data Quality . . . 47
- 3.4 Object reconstruction . . . 48
  - 3.4.1 Tracks . . . 48
  - 3.4.2 Electrons . . . 48
  - 3.4.3 Muons . . . 50
  - 3.4.4 Jets . . . 50
  - 3.4.5 Jet flavour tagging . . . 53

3.4.6 Missing transverse momentum . . . 55
3.5 Event Cleaning . . . 55
3.6 Detector simulation . . . 57

4 Search for the scalar partner of the charm quark 60
4.1 Motivation and Sensitivity . . . 61
4.2 Monte Carlo Generation . . . 63
4.2.1 Signal generation . . . 63
4.2.2 Background samples . . . 65
4.3 Charm Tagging . . . 66
4.4 Strategy and Optimisation . . . 68
4.4.1 Baseline selection . . . 69
4.4.2 Optimised selections . . . 70
4.4.3 Charm Tagging . . . 74
4.4.4 Optimisation conclusions . . . 78
4.5 Background estimates . . . 80
4.5.1 Leptonic Control Regions . . . 80
4.5.2 QCD Multijet Estimation . . . 87
4.6 Systematic Uncertainties . . . 88
4.6.1 Experimental Uncertainties . . . 89
4.6.2 Theoretical Uncertainties . . . 92
4.7 Results and Limit Setting . . . 100
4.7.1 Background only fit . . . 100
4.7.2 Exclusion fits . . . 101
4.8 Summary and Outlook . . . 104

5 Search for the partner of the gluon 105
5.1 Motivation . . . 107
5.2 Introductory details . . . 108
5.3 Signal Models . . . 109
5.3.1 2-step Model . . . 109
5.3.2 pMSSM-inspired Model . . . 111
5.4 Event Selection . . . 113
5.4.1 Initial selection . . . 113
5.4.2 Jets selection . . . 113
5.4.3 $E_{\mathrm{T}}^{\mathrm{miss}}$ selection . . . 114
5.4.4 Extra pileup rejection and event cleaning . . . 117
5.5 Leptonic background estimation . . . 122
5.5.1 Leptonic background simulation . . . 122
5.5.2 Control regions . . . 123
5.5.3 Theoretical systematic uncertainties . . . 124
5.5.4 Experimental systematic uncertainties . . . 128
5.6 Multijet background estimation . . . 129
5.6.1 Method . . . 129
5.6.2 $E_{\mathrm{T}}^{\mathrm{miss}}$ definition changes . . . 129

5.6.3 H_T binning . . . 131
5.6.4 Templates with b-jets . . . 132
5.6.5 Multijet closure tests . . . 135
5.6.6 Further systematic uncertainties on the template . . . 136
5.7 Fits and Results . . . 141
5.7.1 Background Only Fit . . . 141
5.7.2 Discovery Fit . . . 148
5.7.3 Exclusion Fit . . . 148
5.8 Summary and Outlook . . . 153

6 Conclusions **154**

A Appendices to the Scharm search (chapter 4) **156**
A.1 Constraint on m_{cc} in $t\bar{t}$ events . . . 156
A.2 Extra post-fit kinematic distributions . . . 157

B Appendices to the Multijet search (chapter 5) **160**
B.1 Branching ratios of pMSSM models . . . 160
B.2 Alternative b-jet templates . . . 162
B.3 Choice of H_T binning for multijet templates . . . 165
B.4 $E_{\mathrm{T}}^{\mathrm{miss}}/\sqrt{H_T}$ distributions in all signal regions . . . 167

Bibliography **171**

Glossary

$\boldsymbol{E}_{\mathbf{T}}^{\mathbf{miss}}$ Missing transverse energy – more correctly the missing transverse momentum. The negative sum of all visible momentum in the plane transverse to the beam.

ATLAS A Toroidal LHC Apparatus – one of the four main LHC experiments, and the subject of this thesis.

blind While a search is being designed and checked, it is customary not to examine data in the signal regions. During this phase, the search is referred to as being 'blind'.

CERN European Organisation for Nuclear Research (formerly Conseil Européen pour la Recherche Nucléaire).

CMS Compact Muon Solenoid – one of the four main LHC experiments, and the partner experiment to ATLAS.

CR Control Region – a set of cuts on the properties of an event in order to enhance a particular background process over the expected signal and other backgrounds, in order to measure it.

CSC Cathode Strip Chambers – part of the MS, precision measurements in the inner end-caps.

CST Calorimeter Soft Term – a term in the $E_{\mathrm{T}}^{\mathrm{miss}}$ calculation, used in Run-1, that consists of the sum of the transverse momenta of calorimeter clusters not associated to any reconstructed objects.

EF Event Filter – the third stage of the Run-1 trigger, performing fast event reconstruction on a full read-out of the detector. Merged with the L2 in Run-2 to form a unified HLT.

EMB Electromagnetic Barrel part of the LAr, $|\eta| < 1.475$.

EMCAL Electromagnetic calorimeter – consisting of LAr detectors in both barrel and endcap regions.

EMEC Electromagnetic Endcap part of the LAr, $1.375 < |\eta| < 3.2$.

EWSB Electroweak Symmetry Breaking – the choice of particular non-zero value of the Higgs potential.

FCAL Forward calorimetry part of the LAr, $3.1 < |\eta| < 4.9$.

HCAL Hadronic calorimeter – consisting of the TileCal in the barrel region and the LAr in the endcap.

HEC Hadronic Endcap part of the LAr, $1.5 < |\eta| < 3.2$.

HLT High Level Trigger – the final stage of the trigger, with an input rate of ~ 100 kHz and an output of ~ 1 kHz.

IBL Insertable B-layer – the innermost layer of the pixel detector, added for Run-2 during LS1.

ID Inner Detector of ATLAS, consisting of the Pixel (and IBL in Run-2), SCT and TRT subsystems.

impact parameter – the closest distance between an extrapolated track and a given point, usually the beamspot or IP. Can be decomposed into *transverse* and *longitudinal* components, d_0 and z_0, referring respectively to the distance in the $x - y$ plane and the z co-ordinate of this point of closest approach.

IP Interaction Point – the point at which the proton beams cross at the centre of ATLAS.

IR Infra-Red – a low-energy, large-scale phenomenon.

ISR Initial State Radiation – a particle radiated from the hard scatter, before the main interaction in the matrix element. This radiation may take the form of a high-energy photon or jet against which the rest of the system will recoil.

JER Jet Energy Resolution – a smearing applied to MC jets so they better describe data.

JES Jet Energy Scale – a set of corrections applied to detector-level jet energies to reproduce the particle-level values.

L1 The first, hardware-based stage of the trigger, taking information from the calorimeters and MS, with an input rate of 20 or 40 MHz (Run-1 vs Run-2) and an output rate of 70 – 100 kHz.

L2 The second, software-based stage of the Run-1 trigger, with access to more detector information within the RoIs identified by L1. Merged with the EF in Run-2 to form a unified HLT.

LAr Liquid Argon calorimeter.

LEP Large Electron Positron collider – operational from 1989 to 2000, in whose tunnel the LHC now resides.

LHC Large Hadron Collider – the principle proton-proton accelerator at CERN.

LO Leading Order – a QCD calculation performed to leading order in α_S.

LS1 Long Shutdown 1 – the extended shutdown of the LHC between February 2013 and April 2015.

LSP Lightest Supersymmetric Particle – the lightest SUSY particle, in many models the lightest neutralino $\tilde{\chi}_1^0$ since this is only weakly interacting and hence a good dark matter candidate. The LSP is, in R-parity conserving SUSY, stable by definition since there are no SUSY particles for it to decay to.

MC Monte Carlo simulation – simulated events are generated using Monte Carlo random number sampling to perform integrations, and the term has become synonymous with the end result of this process, the simulated events themselves.

MDT Monitored Drift Tubes – part of the MS, precision measurement in the barrel and outer endcaps.

MS Muon System / Spectrometer – the outer layers of ATLAS surrounding the HCAL, encompassing the MDT, CSC, RPC and TGC.

MSSM The Minimal Supersymmetric extension of the Standard Model.

NLL Next-to-Leading Logarithm – divergent logarithms in a QCD calculation are regularised to second order.

NLO Next-to-Leading Order – a QCD calculation performed to next-to-leading order in α_S.

NNLL Next-to-next-to-Leading Logarithm – divergent logarithms in a QCD calculation are regularised to third order.

NNLO Next-to-next-to-Leading Order – a QCD calculation performed to next-to-next-to-leading order in α_S.

PDF Parton Distribution Function – a function describing the momentum fraction carried by a particular kind of parton in the proton.

pileup μ, the average number of $p-p$ interactions per bunch crossing, averaged over one revolution of the LHC.

pixel The innermost subsystem of ATLAS, a silicon tracker consisting of modules segmented into small pixels.

pMSSM The phenomenological MSSM – a subset of the MSSM with 19 free parameters ensuring R-parity conservation and no CP violation or flavour-changing neutral currents in the SUSY sector.

PV Primary Vertex – the position of the proton–proton collision of interest in an event.

QCD Quantum Chromodynamics, referring either to the theory of the strong interaction or the resulting jet production in hadron colliders.

QED Quantum Electrodynamics, the theory of the electromagnetic interaction.

RoI Regions of Interest – areas in $\eta - \phi$ space identified by the L1 trigger.

RPC 1. Resistive-plate Chambers – part of the MS, triggering in the barrel
2. R-Parity Conserving SUSY is that which is constrained to forbid SM – SUSY transitions. In RPC SUSY, SUSY particles can only be produced in pairs and the lightest SUSY particle is stable.

Run-1 The initial period of operation of the LHC before LS1, with pp collisions at $\sqrt{s} = 7$ (2010-11) and 8 (2012) TeV.

Run-2 The second phase of operation of the LHC following the end of LS1, with pp collisions at $\sqrt{s} = 13$ TeV in 2015 and 2016 (to commence in April).

SCT Semi-conductor tracker – the second tracking subsystem of ATLAS, consisting of silicon strip modules.

SM Standard Model of particle physics.

SR Signal Region – a set of cuts on the properties of an event in order to enhance a signal process over the expected background.

SUSY Supersymmetry – a theoretically favoured extension of the SM, for which the analyses presented in this thesis were searching.

SV Secondary Vertex – a displaced vertex resulting from the in-flight decay of e.g. a B hadron.

TGC Thin-Gap Chambers – part of the MS, triggering in the endcaps.

TileCal The scintillator tile hadronic calorimeter.

trigger The multi-layer system that determines whether an event is worthy of read-out and storage. Comprising in Run-1 of the hardware-based L1 and software-based L2 and EF, while in Run-2 the latter two were merged into the HLT.

TRT Transition Radiation Tracker, the outer layer of the ID, consisting of Xe- and Ar-filled straw tubes.

TST Track Soft Term – a term in the $E_{\mathrm{T}}^{\mathrm{miss}}$ calculation, used in Run-2, that consists of the sum of the transverse momenta of ID tracks not associated to any reconstructed objects.

TT Trigger Tower – unit of reduced granularity calorimeter signals considered by the L1 trigger.

UV Ultra-Violet – a high-energy, small-scale phenomenon.

VR Validation Region – a set of cuts on the properties of an event lying part way between signal and control regions, in order to test the background estimates obtained from control region fits prior to looking at data in signal regions.

Preface

The work presented within this thesis was performed by me as part of the ATLAS collaboration. There are therefore parts of the analysis described that are crucial to the overall understanding that were not performed by me alone. Where I had little or no input I have been briefer in my description, but have not explicitly stated which parts are solely due to me in the text so as to avoid breaking the flow. Below I list in reverse chronological order the projects I worked on during my DPhil, with a short description of my contributions in each case. In contrast, when a diagram, plot or other figure in this thesis was not produced by me, this is clearly stated in the caption as 'produced by collaborator' or 'from [X]' if from a published work. If these, or figures that I produced, have been published or otherwise made public by the ATLAS collaboration then they are labelled **ATLAS** or **ATLAS Preliminary**.

Pursuit of new phenomena with many jets. For most of 2015, I was lead analyser and 'analysis contact' for the Run-2 'Multijet' search, looking at the 2015 13 TeV dataset, although the search inherited the methodology of the Run-1 7 and 8 TeV searches. As part of this I oversaw and contributed to development of a new analysis framework for the Run-2 Event Data Model and performed a large fraction of the analysis itself – in particular the background estimation and estimation of systematic uncertainties. Some (not-used) optimisation, and the final limit setting, were performed by collaborators. Additionally, I wrote a public note with very early data in the summer for EPS [1] – one of the first public documents from the ATLAS SUSY group in Run-2 – and co-wrote the February 2016 paper [2] and associated preliminary conference note for December 2015 [3], on which chapter 5 is partly based.

Search for the supersymmetric partner of the charm quark. From summer 2013 to early spring 2015, I co-led the 'Scharm' search, the first dedicated SUSY search for a partner of a second-generation fermion, published as [4], forming the basis of chapter 4. As part of this, I worked on the documentation of the charm tagger used in the analysis, JetFitterCharm, in [5]. I prepared the initial signal generation, designed the search strategy, performed the analysis optimisation and studied the flavour composition and its effects in the control regions. The fits, QCD background estimate and limit setting were performed by collaborators.

SCT DCS and operations. Though not described in this thesis, part of my 'service work' to qualify as an ATLAS author was work on the migration of the SCT Detector Control System ('DCS') over the 2013/14 long shutdown of the LHC (LS1). Following this, I was involved in SCT operations through hardware replacement and DAQ/DCS expert on-call shifts, and more general operations through DCS watcher and Run Control shifts.

Monitoring the optical links of the semiconductor tracker. From late 2012 until early 2014, I performed various monitoring of the optical links of the SCT and data transmission errors, also as part of the aforementioned service work. This work, not presented here, showed a 10% annual decrease in optical power received by the on-detector diodes. I verified that this was not correlated with radiation exposure, crate temperature, laser type or installation date, or indeed with any quantity checked. This led to the staged replacement of some of the optoelectronics during LS1, and has prompted ongoing further study during Run-2, which has confirmed the degradation during running but not (at the time of writing) found a cause.

Search for the supersymmetric partner of the bottom quark. During Autumn 2012 and until summer 2013, I performed some simple b-tagging optimisations and evaluated theoretical systematic uncertainties for the 'Sbottom' analysis, published as [6]. As this work performed was similar to that later done for the scharm search, it is not detailed here.

Chapter 1

Introduction

The modern field of particle physics seeks answers to one of the most fundamental questions asked by humanity, "what are we made of?" This quest has been led both by previously unexplained observations and ideas predicting new and at the time unobserved features, from the development of classical mechanics through observations of charge discretisation to the development of quantum theory and cosmic ray observations in the 20^{th} century. Since then, the field has reached increased understanding by progressively probing higher energy scales, corresponding to a finer-grained understanding of the constituents of the universe, through a progression of higher-powered accelerators throughout the latter part of the 20^{th} century. These advances in accelerator and detector technology, coupled with theoretical developments around quantum field theories, as well as increases in computing power allowing the processing of large datasets and the performing of complex calculations, resulted by the 21^{st} century in a well-developed understanding known as the Standard Model (SM) – so accepted it is deserving of capitalisation – which will be outlined in chapter 2.

The final particle of the Standard Model, the Higgs boson, was discovered by the ATLAS (described in chapter 3) and CMS experiments at the Large Hadron Collider (LHC) in data collected during 2011 and 2012. Despite (and to an extent because of) this success however, theoretical problems remain with the SM. Out of the many extensions to the SM proposed to solve some of these problems, Supersymmetry does so in a particularly elegant way and

with the most wide-ranging (positive) consequences (also described in chapter 2). It also predicts that new particles ought to be present at energies around 1 TeV, within the reach of experiment for the first time through the record-breaking collision energies of the LHC.

This thesis concerns the search for Supersymmetry in two different final states, targeting models reflecting the different priorities following the end of the 2012 8 TeV run and at the beginning of the 2015 13 TeV run. The first search (chapter 4) is for a relatively 'niche' model, one where the partners of charm quarks ('scharms') are produced and lead to an excess of events with high missing transverse momentum ($E_{\mathrm{T}}^{\mathrm{miss}}$) and high-$p_{\mathrm{T}}$ charm jets. The second (chapter 5) is for the partners of the gluons, 'gluinos', decaying through various cascades so as to avoid traditional higher-$E_{\mathrm{T}}^{\mathrm{miss}}$ searches and in the process creating large numbers of hadronic jets. Unfortunately the universe did not see fit to smile on the author, and no evidence of either model was found, leading to competitive exclusion limits being set in both SUSY scenarios.

Chapter 2

Theoretical background

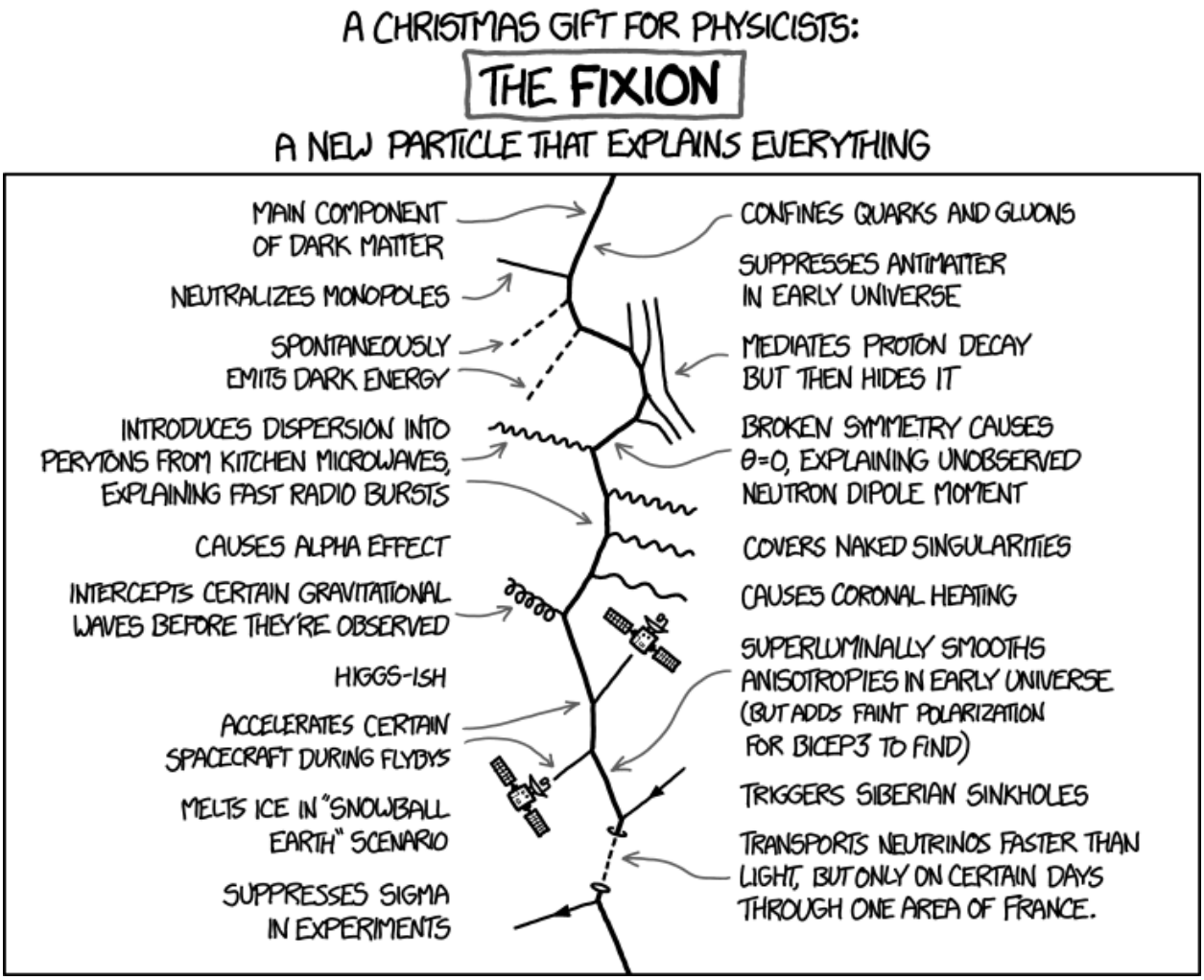


Figure 2.1: The fixion, taken from [7].

Modern particle physics is built upon the 'Standard Model' (SM), the result of over 50 years of prediction and discovery. Behind this model is a theoretical underpinning stemming from that simplest of notions – *symmetry* – which is superbly predictive of the observed make-up of reality.

Coming from an experimental perspective, I first describe the *particle content* of the SM in section 2.1, before expounding the theoretical description in section 2.2. Next, in section 2.3 I describe how this theory, in particular Quantum Chromodynamics, is translated into predictions relevant to hadron collider experiments and hence to this thesis. Finally, in section 2.4 I present Supersymmetry as a solution to some outstanding problems in the SM (as alluded to by figure 2.1), and describe its particle content and relevance to the searches which form the bulk of this thesis.

2.1 Particle Content of the Standard Model

The SM consists of 61 particles that are, to the best of current knowledge, the fundamental 'building blocks' of the universe – i.e. they are point-like. They are classified first according to their internal angular momentum quantum number, called spin, which can be of integer or half-integer magnitude (in units of the reduced Planck constant $\hbar$). Particles with integer spin are called *bosons* and those with half-integer spin are called *fermions*. Within the SM, the fundamental fermions are what might more traditionally be thought of as particles, while the fundamental bosons act as mediators of the interactions between the fermions (and each other) as well as existing as particles in their own right. These boson-mediated interactions account for three of the four known fundamental forces of nature – *strong*, *electromagnetic* and *weak* – but not gravity.

Table 2.1 shows the fundamental fermions of the SM. Each fermion has an antimatter counterpart with equal mass but opposite charge (i.e. $+ \leftrightarrow -$, $0 \rightarrow 0$). Those fermions which interact via all three of the forces of the SM are listed at the top and are known as *quarks* – each one of these has three versions that are identical apart from their differing

Particle		Mass	Charge	Discovery
up	u	2.3 MeV	$+\frac{2}{3}$	1968 [8, 9]
down	d	4.8 MeV	$-\frac{1}{3}$	1968 [8, 9]
charm	c	1.275 GeV	$+\frac{2}{3}$	1974 [10, 11]
strange	s	95 MeV	$-\frac{1}{3}$	1968 [8, 9]
bottom	b	4.18 GeV	$-\frac{1}{3}$	1977 [12]
top	t	173 GeV	$+\frac{2}{3}$	1995 [13, 14]
electron	e	0.511 MeV	-1	1896 [15]
e neutrino	ν_e	$m_{\nu_e}^{(\text{eff})} < 2$ eV	0	1956 [16]
muon	μ	105.7 MeV	-1	1936 [17, 18]
μ neutrino	ν_μ	$m_{\nu_\mu}^{(\text{eff})} < 0.19$ MeV	0	1962 [19]
tau	τ	1.777 GeV	-1	1974-7 [20]
τ neutrino	ν_τ	$m_{\nu_\tau}^{(\text{eff})} < 18.2$ MeV	0	2000 [21]

Table 2.1: The fermions of the SM. The upper 6 are known as quarks and the lower six as leptons. All have spin $\frac{1}{2}$. Masses from the Review of Particle Physics [22].

'colour charge'. The other fermions, which do not interact via the strong force, are called *leptons*, and are further subdivided into neutral and charged subsets. The charged leptons interact via the weak and electromagnetic forces, while the neutral fermions – *neutrinos* – interact only via the weak force. They are massless according to the SM, but have been shown experimentally to have a non-zero (but very small) mass [23–27].

Table 2.2 shows the fundamental bosons of the SM. The photon is the carrier of the electromagnetic force, with zero mass and charge. The charged $W^\pm$ and neutral Z 'vector' bosons carry the weak force. The strong force is carried by eight gluons of different colour combinations. The Higgs does not carry a force analogously to the other bosons, but is instead responsible for giving masses to the vector bosons and the charged fermions.

Together, these make up the 61 fundamental particles of the SM – 6 leptons plus 6 quarks of each of the 3 colours, and their antiparticles; plus 13 bosons. Each of these has been observed experimentally (either individually or in bound states), with the first observations

Particle	Mass	Charge	Spin	Force mediated	Discovery
photon γ	$< 10^{-18}$ eV	0	1	electromagnetic	1923 [28]
$W^{\pm}$	80.4 GeV	± 1	1	weak	1983 [29, 30]
Z	91.2 GeV	0	1	weak	1983 [31, 32]
gluon g	$0^{(*)}$	0	1	strong	1979 [33]
Higgs h	125.1 GeV	0	0	—	2012 [34, 35]

Table 2.2: The bosons of the SM. Masses from the Review of Particle Physics [22]. (*) = Theoretical value.

of each being reported in the above tables.

2.2 Theoretical description of the Standard Model

The *dynamics* of the SM, that is to say the interactions of the particles in section 2.1, are typically described in the Lagrangian formalism, and result from the imposition of various *symmetries* – i.e. that the SM Lagrangian $\mathcal{L}_{\text{SM}}$ is invariant under various transformations.

2.2.1 Quantum Electrodynamics

Quantum Electrodynamics, or QED, can be used as a simple exposition of the relevant principles. Starting from the Dirac Lagrangian applying to a fermion field ψ and mass m:

$$\mathcal{L}_{\text{Dirac}} = i\bar{\psi}\gamma^{\mu}\partial_{\mu}\psi - m\bar{\psi}\psi \tag{2.1}$$

where γ are the four Dirac matrices, we can try applying the U(1) local gauge transformation

$$\psi(x) \to \psi'(x) = e^{i\alpha(x)}\psi(x) \tag{2.2}$$

It can be seen that eq. (2.1) is not invariant under this transformation, but this invariance can be restored through the replacement of the derivative ∂_{μ} by the covariant derivative

$$D_{\mu} = \partial_{\mu} - ieA_{\mu}, \tag{2.3}$$

$$\text{with } A_{\mu} \text{ transforming as } A_{\mu} \to A_{\mu} + \frac{1}{e}(\partial_{\mu}\alpha) \tag{2.4}$$

The resulting A_{μ} gauge field, introduced to restore invariance under the transformation in eq. (2.2), is identified as the four-potential of the electromagnetic field. It has its own contribution to $\mathcal{L}_{\text{QED}} = \mathcal{L}_{\text{Dirac}} + \mathcal{L}_{\text{A}}$ given by

$$\mathcal{L}_{\text{A}} = -\frac{1}{4}F_{\mu\nu}F^{\mu\nu} \tag{2.5}$$

$$\text{where } F_{\mu\nu} = \partial_{\mu}A_{\nu} - \partial_{\nu}A_{\mu} \tag{2.6}$$

yielding the final QED Lagrangian

$$\mathcal{L}_{\text{QED}} = i\bar{\psi}\gamma^{\mu}D_{\mu}\psi - m\bar{\psi}\psi - \frac{1}{4}F_{\mu\nu}F^{\mu\nu} \tag{2.7}$$

As an aside, applying the Euler-Lagrange equation for A_μ to $\mathcal{L}_{\text{QED}}$, one obtains:

$$\partial_\nu\Big(\frac{\partial\mathcal{L}_{\text{QED}}}{\partial(\partial_\nu A_\mu)}\Big) - \frac{\partial\mathcal{L}_{\text{QED}}}{\partial A_\mu} = 0 \tag{2.8}$$

$$\partial_\nu F^{\mu\nu} = e\bar{\psi}\gamma^\mu\psi \tag{2.9}$$

$$\partial_\nu\partial^\nu A^\mu = e\bar{\psi}\gamma^\mu\psi \text{ in the Lorenz gauge, } \partial_\mu A^\mu = 0 \tag{2.10}$$

Equation (2.10) is a wave equation for the electromagnetic field, as one obtains from the classical Maxwell equations, and in fact all the Maxwell equations can be extracted from eq. (2.10).

2.2.2 The Standard Model Lagrangian

The SM Lagrangian can be written in three parts:

$$\mathcal{L}_{\text{SM}} = \mathcal{L}_{\text{QCD}} + \mathcal{L}_{\text{EW}} + \mathcal{L}_{\text{Higgs}} \tag{2.11}$$

where the strong force is described by Quantum Chromodynamics (QCD) in $\mathcal{L}_{\text{QCD}}$, the weak and electromagnetic forces are unified as the 'electroweak' force in $\mathcal{L}_{\text{EW}}$ and the theory is completed by the Higgs contribution $\mathcal{L}_{\text{Higgs}}$.

Quantum Chromodynamics and the Strong force

From section 2.2.1, it can be noted that imposing gauge invariance leads to interacting gauge bosons, which can be identified as the force carriers of the theory. In the case of QCD, the underlying symmetry is a local SU(3) symmetry, describing the interactions between quarks and the appearance of gluons as the gauge bosons. The corresponding Lagrangian is

$$\mathcal{L}_{\text{QCD}} = \bar{\psi}(i\gamma^\mu D_\mu - m)\psi - \frac{1}{4}G^a_{\mu\nu}G^{\mu\nu}_a \tag{2.12}$$

$$\text{where } D_\mu = \partial_\mu + g_s T_a G^a_\mu \tag{2.13}$$

$$\text{and } G^a_{\mu\nu} = \partial_\mu G^a_\nu - \partial_\nu G^a_\mu + g_s f^{abc} G^b_\mu G^c_\mu \tag{2.14}$$

Here, $\psi(x)$ is the fermionic quark field, an $SU(3)_c$ (c for colour, the 'charge' of the strong force, taking values named red, green and blue) triplet with R, G and B components. Each quark carries colour R, G or B and each antiquark carries anti-colour $\bar{R}$, $\bar{G}$ or $\bar{B}$. The relevant gauge transformation is $\psi(x) \rightarrow \exp(iT^a\alpha_a(x))$, where T^a are the eight $(N_c^2 - 1)$ generators of $SU(3)_c$ and can be expressed in terms of the Gell-Mann λ matrices as $T_a = \lambda_a/2$. They have commutation relation $[T_a, T_b] = if_{abc}T_c$ where f_{abc} is the antisymmetric tensor. G_μ^a are the 8 $(N_c^2 - 1)$ gluon vector fields, and unlike in QED these gluon force carriers carry some colour charge themselves – each a combination of some colours and anti-colours as described by the Gell-Mann matrices – meaning that gluons can themselves feel the strong force and self-interact. This, combined with the relatively large g_s and its running (see section 2.2.3) has important ramifications for the phenomenology of the theory.

The Electroweak force

The lepton-gauge boson interaction part of the Electroweak part of the SM Lagrangian, $\mathcal{L}_{\text{EW}}^{\text{int.}}$, is given by

$$\mathcal{L}_{\text{EW}}^{\text{int.}} = \sum_{e,\mu,\tau} \left(\bar{\chi}_L \gamma^\mu D_\mu^L \chi_L + \bar{e}_R \gamma^\mu D_\mu^R e_R \right) \tag{2.15}$$

$$\text{where } D_\mu^L = i\partial_\mu - g\left(\frac{1}{2}\right)\boldsymbol{\tau} \cdot \boldsymbol{W}_\mu - \frac{g'}{2}(-1)B_\mu \tag{2.16}$$

$$\text{and } D_\mu^R = i\partial_\mu - \frac{g'}{2}(-2)B_\mu \tag{2.17}$$

with the sum over the three lepton generations described in section 2.1. The numbers in brackets are the weak isospin charge and weak hypercharge of the fermion fields (see below).

The W_μ^i (i=1,2,3) are the three vector gauge bosons of the SU(2) weak isospin symmetry, resulting from invariance under the gauge transformation

$$\chi_L \rightarrow exp\Big[-ig\frac{\boldsymbol{\tau}}{2} \cdot \boldsymbol{\Delta} + i\frac{g'}{2}\Lambda \Big]\chi_L, \tag{2.18}$$

$$\boldsymbol{W}_\mu \rightarrow \boldsymbol{W}_\mu + g\boldsymbol{\Delta} \times \boldsymbol{W}_\mu + \partial_\mu \boldsymbol{\Delta} \tag{2.19}$$

with $\Lambda(x)$ and $\boldsymbol{\Delta}(x) = \big(\Delta^1(x), \Delta^2(x), \Delta^3(x)\big)$ being the phase factors of the $U(1)_Y$ and

$\mathrm{SU}(2)_L$ transformations respectively (the covariant derivative in eq. (2.16) can be easily identified). The $\mathrm{SU}(2)_L$ symmetry has generators τ_i which are identified with the Pauli matrices. The χ_L fields are weak isospin doublets

$$\chi_L = \begin{pmatrix} \nu_L \\ e_L \end{pmatrix}, \qquad \bar{\chi}_L = \begin{pmatrix} \bar{\nu} & \bar{e}_L \end{pmatrix}$$

with the upper and lower entries having weak isospin $T^3 = \pm\frac{1}{2}$. The fermion fields χ_L couple to the weak isospin gauge bosons with strength g.

B_μ is the gauge vector boson of the $\mathrm{U}(1)_Y$ weak hypercharge symmetry, resulting from invariance under the gauge transformation

$$e_R \to exp\big(ig'\Lambda\big)e_R \tag{2.20}$$

$$B_\mu \to B_\mu + \partial_\mu \Lambda \tag{2.21}$$

e_R is a weak isospin singlet (and there is no ν_R) so only has weak hypercharge. This quantity, Y, relates to electric charge Q and T^3 by $Y = 2(Q - T^3)$ (i.e. an electron, with $Q = -1$ and $T^3 = -\frac{1}{2}$, has $Y = -1$). The coupling strength is $g'/2$.

Expanding the $\boldsymbol{\tau} \cdot \boldsymbol{W}_\mu$ from eq. (2.16), one can obtain

$$\frac{1}{2}\boldsymbol{\tau} \cdot \boldsymbol{W}_\mu = \frac{\tau^1}{2}W_\mu^1 + \frac{\tau^2}{2}W_\mu^2 + \frac{\tau^3}{2}W_\mu^3 \tag{2.22}$$

$$= \frac{1}{\sqrt{2}}\big(\tau^+ W_\mu^+ + \tau^- W_\mu^-\big) + \frac{\tau^3}{2}W_\mu^3 \tag{2.23}$$

where $\tau^\pm = \frac{1}{2}(\tau^1 \pm i\tau^2)$, and $W_\mu^\pm = \frac{1}{\sqrt{2}}(W_\mu^1 \mp iW_\mu^2)$ are the physical W bosons. Expanding the Pauli matrices, one obtains terms like $-\frac{g}{\sqrt{2}}\bar{\nu}_L\gamma_\mu e_L W_\mu^+ +$ h.c. – i.e. the experimentally observed charged currents acting only on left-handed fermions.

Having identified $W^\pm$, there remain the neutral fields W_μ^3 and B_μ which mix to give the physical fields Z_μ and A_μ of the Z boson and photon. This mixing is governed by the weak mixing angle θ_W:

$$\begin{pmatrix} W_\mu^3 \\ B_\mu \end{pmatrix} = \begin{pmatrix} \cos\theta_W & \sin\theta_W \\ -\sin\theta_W & \cos\theta_W \end{pmatrix} \begin{pmatrix} Z_\mu \\ A_\mu \end{pmatrix} \tag{2.24}$$

If θ_W is chosen as $\tan\theta_W = g'/g$, then the relevant part of $\mathcal{L}_{\text{EW}}$ becomes

$$\mathcal{L}_{\text{EW}}^{\text{int. A, Z}} = g\sin\theta_W\left(\bar{e}_L\gamma^\mu e_L + \bar{e}_R\gamma^\mu e_R\right)A_\mu \tag{2.25}$$

$$- \frac{g}{2\cos\theta_W}\left(\bar{\nu}_L\gamma^\mu\nu_L - \bar{e}_L\gamma^\mu e_L + 2\sin^2\theta_W(\bar{e}_L\gamma^\mu e_L + \bar{e}_R\gamma^\mu e_R)\right)Z_\mu \tag{2.26}$$

and identifying $g\sin\theta_W$ as the electric charge e the QED Lagrangian is recovered. Hence both the electromagnetic and weak forces are encompassed in this description.

The kinetic part of the electroweak Lagrangian, describing the boson self-interactions, is given (similarly to that for QED) by

$$\mathcal{L}_{\text{EW}}^{\text{kin.}} = -\frac{1}{4}\boldsymbol{W}_{\mu\nu}\boldsymbol{W}^{\mu\nu} - \frac{1}{4}B_{\mu\nu}B^{\mu\nu} \tag{2.27}$$

$$\text{where } \boldsymbol{W}_{\mu\nu} = \partial_\mu\boldsymbol{W}_\nu - \partial_\nu\boldsymbol{W}_\mu - g\boldsymbol{W}_\mu\times\boldsymbol{W}_\nu \tag{2.28}$$

$$\text{and } B_{\mu\nu} = \partial_\mu B_\nu - \partial_\nu B_\mu \tag{2.29}$$

On substitution of the physical $W^\pm$, Z and A boson fields as above, this yields cubic and quartic terms for $WWWW$, WWZ, WWA, $WWZZ$, $WWAA$ – i.e. the allowed boson self-interactions.

Masses and the Higgs Mechanism

In the above discussion of the electroweak sector of the SM, no mention was made of gauge boson masses, most of which are observed to be non-zero. If generic mass terms of the form $m_V^2V^\mu V_\mu$ are included, then gauge invariance is violated and the description fails. The same is true of putative fermion mass terms, since these link left- and right-handed fields which transform differently under $\text{SU}(2)_L$.

This problem was solved by Brout, Englert, Guralnik, Hagen, Higgs and Kibble in 1964, by introducing a complex scalar SU(2) doublet Θ with weak hypercharge 1 and isospin 1/2. This leads to an addition to the SM Lagrangian

$$\mathcal{L}_{\text{Higgs}} = (D^\mu\Theta)^\dagger(D_\mu\Theta) + y_f(\bar{\chi}_L\Theta e_R + \bar{e}_R\Theta^\dagger\chi_L) + V(\Theta^\dagger\Theta) \tag{2.30}$$

$$\text{with } D_\mu = \partial_\mu + ig\frac{\boldsymbol{\tau}}{2}\cdot\boldsymbol{W}_\mu + ig'(1)\frac{1}{2}B_\mu \tag{2.31}$$

invariant under the $\mathrm{SU}(2)_L$ and $\mathrm{U}(1)_Y$ transformations described above. The first term describes couplings between this new doublet and the EW gauge bosons and the second between it and fermions. It is the final term, the Higgs potential, that is of most interest. It is given by

$$V(\Theta^\dagger\Theta) = \mu^2\Theta^\dagger\Theta + \lambda(\Theta^\dagger\Theta)^2 \tag{2.32}$$

It is clear that for $\mu^2 < 0$, this potential has a set of minima at $|\Theta| = \frac{v}{\sqrt{2}}$, where v is defined as $\sqrt{\frac{-\mu^2}{\lambda}}$. This symmetry can be broken by choosing the vacuum value $\frac{1}{\sqrt{2}}\binom{0}{v}$ and expanding Θ around this point – a process known as *electroweak symmetry breaking* or EWSB. This yields

$$\Theta(x) = \frac{1}{\sqrt{2}}\exp(-i\boldsymbol{\Delta}(x)\cdot\frac{\boldsymbol{\tau}}{2})\begin{pmatrix}0\\ v+h(x)\end{pmatrix} \tag{2.33}$$

with three circular ($\Delta_{1,2,3}$) and one radial (h) degrees of freedom. The three circular degrees of freedom, known as Goldstone bosons, can be absorbed in a gauge choice known as the *Unitary gauge*, and also correspondingly by the EW gauge bosons W^i where they reappear as the longitudinal components of the now massive vector fields. The remaining radial degree of freedom is identified as the physical Higgs boson.

Applying the gauge boson mixing of eq. (2.24) and expanding the covariant derivatives, the $(D^\mu\Theta)^\dagger(D_\mu\Theta)$ term in eq. (2.30) becomes

$$\mathcal{L}^{\mathrm{EW}}_{\mathrm{Higgs}} = \frac{1}{4}g^2(h^2+2vh+v^2)W^+_\mu W^{-\mu} + \frac{1}{8}(g^2+g'^2)(h^2+2vh+v^2)Z_\mu Z^\mu - \mu^2h^2 - \lambda vh^3 - \frac{\lambda}{4}h^4 \tag{2.34}$$

From this, the masses of various particles can be read off from the functional form $\mathcal{L}_m = \frac{1}{2}m_V^2V^2$:

- $m_W = \frac{1}{2}gv$
- $m_Z = \frac{1}{2}\sqrt{(g^2+g'^2)}v = m_W/\cos\theta_W$
- $m_\gamma = 0$

- $m_h = \sqrt{2}|\mu| = v\sqrt{2\lambda}$

The remaining term in eq. (2.30), dealing with fermion-Higgs interactions and known as the *Yukawa* term, simplifies to

$$\mathcal{L}_{\text{Higgs}}^{\text{Yukawa}} = -\frac{y_e}{\sqrt{2}}\big(\bar{e}_L e_R + \bar{e}_R e_L\big)\big(v + h\big) \tag{2.35}$$

The $y_e v\bar{e}e$ terms give the electron mass as $m_e = y_e v/\sqrt{2}$, with y_e being called the Yukawa coupling of the electron, while the $y_e h\bar{e}e$ terms describe the Higgs-fermion coupling with strength proportional to the fermion's mass. It should be noted that the neutrinos, which are solely left-handed, cannot gain a mass in this way without the aid of a $\sim$ non-interacting, "sterile" right-handed neutrino, for which no evidence exists to date.

Quark masses and mixing Quark masses are obtained in a similar manner to lepton ones as described above, with an additional complication. The $\text{SU}(2)_L$ quark doublets can be written $\chi_L^g = \begin{pmatrix} U^g \\ D^g \end{pmatrix}$, with the index g representing the three generations of quarks. U^g and D^g are the weak interaction eigenstates, but it is observed that these do not correspond to the flavour eigenstates, since inter-generational weak interactions such as $s \to u$ are seen to occur. This prompts the rewriting of the doublet as $\chi_L^g = \begin{pmatrix} U^g \\ V^{gg'} D'^g \end{pmatrix}$ with the Cabibbo-Kobayashi-Maskawa (CKM) matrix $V^{gg'}$ mixing the flavour eigenstates into the weak eigenstates. This mixing results in the Higgs Yukawa Lagrangian (with sums over g and g')

$$\mathcal{L}_{\text{Higgs}}^{\text{Yukawa, quarks}} = -\bar{\chi}_L^g Y_D^{gg'} \Theta D_R^{g'} - \bar{\chi}_L^g Y_U^{gg'} \Theta U_R^{g'} + \text{h.c.} \tag{2.36}$$

which, after EWSB, generates quark masses and quark-Higgs interactions in a similar way to the lepton Yukawa terms.

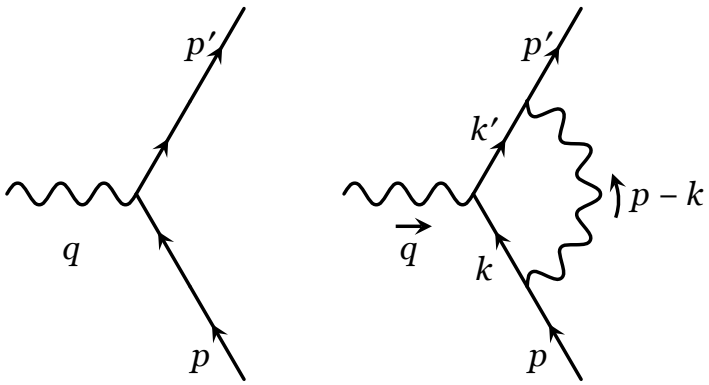


Figure 2.2: A photon – charged fermion interaction, at leading order on the left and at higher order on the right. As long as momentum is conserved at each vertex and $q = p' - p$, the momenta around the loop k and k' are unconstrained. Plot from [36]

2.2.3 Running couplings and renormalisation

Calculations of standard model interactions often make use of perturbation theory in order to approximate the effect of small changes to the non-interacting case. Such calculations are thus only accurate to a given *order* in a relevant small parameter. For example, approximating $(1+\alpha)^3$ as $1+3\alpha$ is accurate to leading order in α, with the second order correction being $3\alpha^2$. Unfortunately, higher order terms in perturbation theory as applied to the processes of the standard model often require solving *loop* integrals, where the momenta of intermediate particles are unconstrained apart from overall conservation. For example, figure 2.2 shows a photon – fermion vertex and a second order term.

This can lead to *divergences* at high or low momenta, known as 'ultra-violet' (UV) and 'infra-red' (IR) respectively. In a *renormalisable quantum field theory* such as QED, these logarithmic divergences can be absorbed by adding scale-dependence to various parameters; in this case the coupling constant $\alpha_{\mathrm{EM}} = g^2/4\pi$ becomes $\alpha_{\mathrm{EM}}(\mu)$ and is said to 'run'. This scale μ is taken as the energy at which a given process is occurring, although the exact choice of value can be a little arbitrary.

For QED, the coupling α_{EM} increases with μ in a phenomenon known as 'screening', while for QCD the coupling α_{S} decreases with μ in what is known as 'asymptotic freedom'. This is shown in figure 2.3 for the couplings of the SM.

While similar procedures can be followed to renormalise most SM parameters and avoid

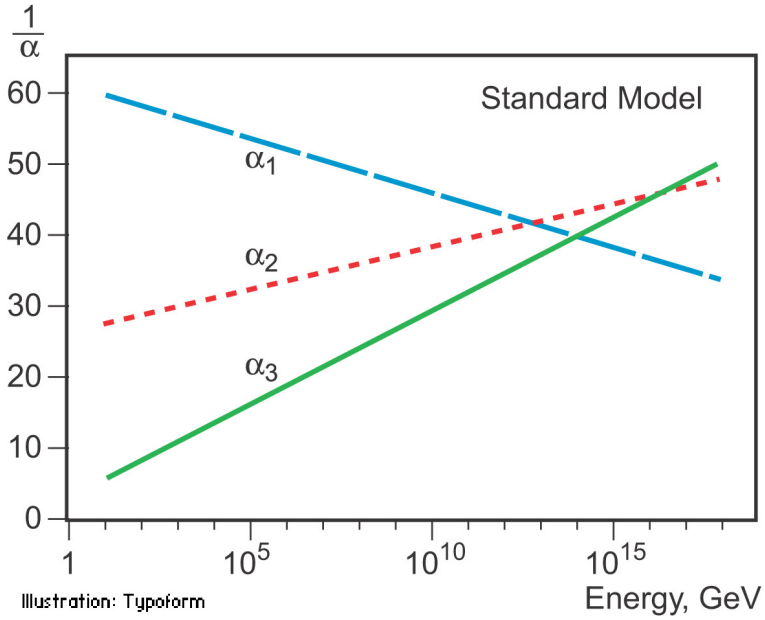


Figure 2.3: The running of the SM couplings – α_1 for $U(1)_Y$, α_2 for $SU(2)_W$ and α_3 for $SU(3)_S$. Plot from [37].

these divergences in most calculations (see section 2.3 for more details), the quadratic divergences arising in Higgs mass calculations yield huge discrepancies between the 'bare' (unrenormalised) and renormalised masses – the former being $\sim M_{\text{Planck}} \sim 10^{19}$ GeV compared with the experimentally observed value of 125 GeV. This requires a large 'fine-tuning' in order to reconcile these values, i.e. a cancellation to 1 part in 10^{17}, an improbably large value. This is known as the *hierarchy problem*, and prompts a search for possible explanations such as Supersymmetry, outlined in section 2.4.

2.3 QCD Phenomenology and Event Generation

Having established the Standard Model, it is only of use to experimentalists if accurate predictions can be made from it. Such predictions use as their basis perturbation theory, i.e. decomposing a complex interaction into a series of terms with increasing orders of a small coupling constant, the idea being that the earlier terms dominate over latter ones, so only a finite number need to be evaluated to well approximate the result of a full calculation (which would often be impractical if not impossible to evaluate). Through performing such calculations, predictions are obtained by simulating large numbers of events of the relevant processes in order to sufficiently sample the relevant phase-space.

However, matters are complicated by QCD, which results in a rich and varied phenomenology. While perturbation theory is easily applicable to QED following coupling renormalisation, various features of QCD make its use problematic. Thus techniques have been developed to decompose simulation into various steps, accounting for different aspects of QCD. Section 2.3.1 details these complications arising from QCD, and section 2.3.2 describes how they are overcome by modern event generators. These generators produce *truth level* events – i.e. where the identity and often progeny of every particle is known – a situation that particle detectors are sadly unable to replicate. The methods by which these truth level events are used to make predictions that are directly comparable to recorded data are described later in chapter 3 (section 3.6).

2.3.1 Features of QCD

Perturbation theory is an excellent method of simplifying difficult calculations of particle interactions, as long as couplings are fairly weak. As described in section 2.2.3, the couplings of the Standard Model are forced to incorporate a scale dependence as a result of renormalisation, meaning that each interaction can only be perturbatively described in a certain energy regime. For QED, the nonperturbative region is above $\sim 10^{90}$ GeV, which is safely out of reach for any calculation of interest. However, for QCD, the coupling α_S *decreases*

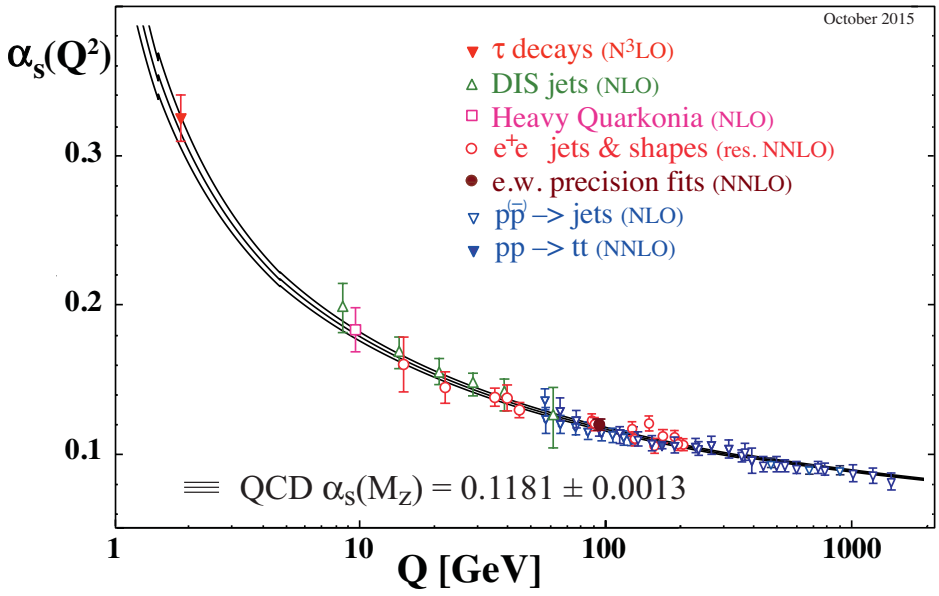


Figure 2.4: Summary of measurements of α_S as a function of the energy scale Q. The respective degree of QCD perturbation theory used in the extraction of α_S is indicated in brackets. Plot and caption from [22].

with scale meaning that it is at low scale, below about 400 MeV, that serious problems arise – and the coupling becomes quite large at GeV scales (figure 2.4).

For perturbative calculations the main implications of this are that logarithmic divergences appear for radiation of partons at low momentum ('soft') or small angle ('collinear'), and that low-scale processes such as hadronisation and intra-proton dynamics are completely nonperturbative so must be evaluated empirically, from data or through other means such as lattice QCD.

2.3.2 Event Generation

The aim of event generation is to provide an accurate prediction for the final states of a particular process – i.e. a set of stable (on detector timescales) particle 4-momenta for each event, whose distributions en masse are true to the underlying theory – within the constraints described in section 2.3.1. These are tackled through splitting event generation into several steps, based on the phenomenology of a proton–proton collision. These steps are itemised below and then explained in more detail.

1. The diagrams or matrix elements to be calculated for the parton-level process are established. These may include higher order diagrams, though there is a factorial growth in the number of diagrams with the order of calculation, as well as increased complication with parton shower matching, so typically this only proceeds to NLO or sometimes NNLO.

2. The relevant integrations and random number samplings are performed, using *Monte Carlo* techniques that give the generation process its name.

3. The probability of extracting the initial state partons from the protons with their given momenta is calculated from the parton distribution functions (PDFs).

4. Any unstable particles (e.g. t, W, τ) are decayed according to their measured branching fractions[1]

5. The momenta of incoming and outgoing partons are modified by a *parton shower*, modelling gluon emission and splitting.

6. The stable quarks are hadronised, and any resulting unstable hadrons decayed[1], to result in a final state of stable hadrons (and leptons).

7. The *underlying event* is simulated.

These steps do not exist in isolation from each other, and the details of their separation result in several of the uncertainties on event generation. For example, steps 1 and 5 overlap where a parton shower takes over from the matrix element generator, and steps 1, 3 and 5 through the scale at which a splitting is regarded as originating from (and absorbed within) the PDF rather than the parton shower or matrix element.

The details of all of these steps can be quite involved, and many are the subject of entire theses in their own right. I will therefore give only a cursory overview of each, focusing on areas where each can be a source of uncertainty relevant to physics analyses.

[1] These steps can occur over a non-infinitesimal length of time, and hence some intermediate particles may travel a measurable distance. This information is retained for detector reconstruction.

Matrix Element Calculation

Matrix element event generators concern steps 1 and 2 above, with the relevant diagrams for a process at a particular order computed and then evaluated. Calculations to higher orders grow rapidly in complexity, since divergences emerge that must be regularised in a way that is consistent with the parton shower. Different approximate methods exist of determining the integrations necessary, and of performing them along with these regularisations, hence there is an inherent uncertainty in their outputs. Additional uncertainty arises from various scale choices in the calculations. Two of these are the *renormalisation scale* at which $\alpha_S(\mu)$ is calculated and the *factorisation scale* at which an emission is assigned to the hard process rather than absorbed into the PDF.

Parton shower

Fixed order calculations from matrix element generators are not capable of simulating the full hadronic activity of an event. Instead matrix element generators must be *interfaced* to parton showers, which treat emission as a probabilistic process based on various splitting functions for a parton of a certain momentum to split into two of given momenta and angular separation. However, these probabilities rely on the emissions being close to the soft or collinear limits (which dominate the emission due to aforementioned divergences), and so are incapable of generating hard[2] emission at large angles, which must be generated by the matrix element.

These emissions are performed in decreasing order of some particular variable, for example p_T (`PYTHIA` 6 [38]) or angle (`HERWIG` [39]). In addition to different ordering schemes, the matching procedure between the parton shower and the matrix element calculation – in order to ensure there is simultaneously no overlap between the two and no missed phase space – and the scales at which this occurs, can be a source of uncertainty. Two different procedures that are used by generator combinations relevant to the forthcoming analyses are `CKKW` [40] and `MLM` [41].

[2]The corollary of soft, i.e. high momentum.

Hadronisation

Dedicated models of hadronisation are used to evolve the final state partons following the shower into observable, stable hadrons. Typically, the same program is responsible for both the parton shower and hadronisation, and there are two principle models of hadronisation: the Lund string model of `PYTHIA` and the cluster model of `HERWIG`.

Lund string Quarks and gluons are assumed to be connected by strings, which stretch and break forming $q\bar{q}$ pairs as they diverge. Thus the string gradually fragments into hadrons.

Cluster Gluons are first split into $q\bar{q}$ pairs, and each quark then paired with an antiquark in a colour singlet. These singlets then form clusters, emulating colour confinement, which decay to hadrons according to the available phase space.

The hadrons created according to these models are then allowed to decay according to standardised branching ratios.

Parton Distribution Functions

Parton distribution functions (PDFs) are probability distributions describing the likelihood of finding a particular parton carrying a given longitudinal momentum fraction x of the proton when probed at a scale Q. They thus provide a mapping between protons at centre-of-mass energies of 8 or 13 TeV and partons at the particular momenta used in the matrix element calculations (and modified by initial state radiation in the parton shower).

PDFs are determined from experimental results from several colliders, with different assumptions and fitting techniques leading to different predictions. There exist several collaborations producing their own PDFs, each with its own set of uncertainty bands resulting from e.g. experimental uncertainties on the data used and parameterisations of the fits.

Underlying event

This refers to all additional activity from the proton–proton collision that does not result from the hard scattering of the two partons, including additional interactions between the two protons ('multi-parton interactions') and the evolution of the proton remnants after the hard parton scattering. This involves both perturbative and nonperturbative calculations, the details of which will not be discussed here, and which are performed by the parton shower generator. The descriptions of the underlying event (and the parton shower) often have several tuneable parameters, leading to the development of 'tunes' to allow these models to better describe collision data.

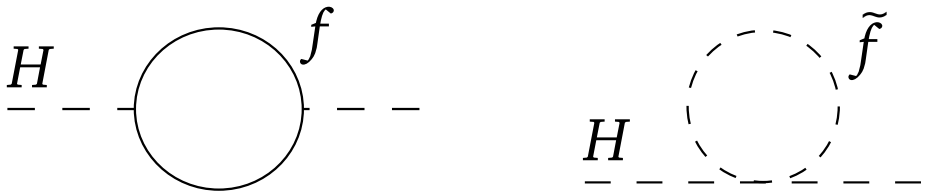


Figure 2.5: The diagrams contributing to corrections to the Higgs mass, left for a fermion and right for its (bosonic) superpartner.

2.4 Supersymmetry

While the SM can accurately predict many processes and explain multiple phenomena, it cannot explain all experimental results and there are some reasons to hope for a deeper underlying theory. For example, it provides no candidate for experimentally observed astrophysical dark matter, makes no attempt to describe gravity and relies on 19 free parameters spanning a large but seemingly arbitrary range.

Multiple extensions to the SM have been suggested, with no single one appearing as the most likely to appear in nature. However, Supersymmetry (SUSY) has garnered the most attention for a number of reasons. Perhaps most importantly, SUSY is an extension of the *symmetries* of the SM, and it is these symmetries which define its dynamics and interactions (as described in section 2.2). This extra symmetry transforms fermions to bosons, meaning that each fermion has a bosonic *superpartner* and vice-versa. A consequence of this is a perfect (in principle) resolution of the hierarchy problem as outlined in section 2.2.3. This arises from loop corrections to the Higgs propagator, such as the one shown in figure 2.5 for the correction from a fermion such as a top quark. This correction is perfectly cancelled by that from boson loops originating from two particles with equal coupling to the Higgs as this fermion, thanks to the spin-statistics theorem. This condition is fulfilled by SUSY, with bosonic and fermionic superpartners having the same Yukawa couplings, hence the hierarchy problem is pleasingly resolved.

Another motivation behind SUSY is that it can naturally provide a dark matter candidate. In the minimal supersymmetric extension to the standard model, or MSSM, which contains the minimal SUSY particle content to resolve the hierarchy problem, a quantity

called 'R-parity' is conserved. This quantity, defined as $P_R = (-1)^{3(B-L)+2s}$, where B and L are baryon and lepton number and s is spin, evaluates to +1 for SM particles and -1 for supersymmetric ones. This conservation is postulated in order to satisfy strong limits on the proton lifetime, which several R-parity violating terms of a more general supersymmetric model would contravene. A consequence is that a SUSY particle cannot decay solely to SM particles (nor be produced alone), meaning that the lightest SUSY particle, known as the LSP, must be stable. This particle, when identified as a mixture of partners of the neutral Higgs and electroweak bosons as is common in the MSSM, only feels the electroweak force (and gravity) and so would satisfy the key criteria for dark matter.

In the following sections I will outline SUSY and its phenomenology, helped by Stephen P. Martin's *A Supersymmetry Primer* [42].

2.4.1 SUSY particle content

In the same way that matter–antimatter symmetry affects only one quantum number – electric charge – unbroken SUSY affects only the quantum number of spin. Thus each SUSY particle shares the same gauge couplings as its SM counterpart. Every fermion, consisting as it does of right- and left-handed components, has separate left- and right-handed bosonic superpartners[3]. Each gauge boson is a massless, spin-1 vector boson with two helicity states before spontaneous symmetry breaking, leading to two fermionic partners – i.e. a massless spin-1/2 fermion. This 1:1 mapping from the SM is contravened only by the Higgs sector, where the single h of the SM becomes two spin-0 chiral multiplets, one coupling to up-type fermions and one to down-type, with h identified as a linear superposition of H_u^0 and H_d^0.

These particles are shown in table 2.3, which also introduces their names – the superpartners of fermions are named by prepending an 's' to the SM partner, and the superpartners of bosons have 'ino' appended. Superpartners are referred to by the same symbol as their SM counterpart, except with a tilde overline.

[3] neutrinos have only a left handed component in the SM, and correspondingly only one superpartner.

Names	spin 0	spin 1/2	spin 1
squarks, quarks	$(\tilde{u}_L \quad \tilde{d}_L)$	$(u_L \quad d_L)$	
(×3 families)	$\tilde{u}_R,\ \tilde{d}_R$	$u_L,\ d_L$	
sleptons, leptons	$(\tilde{\nu}_e \quad \tilde{e}_L)$	$(\nu_e \quad e_L)$	
(×3 families)	$\tilde{e}_R$	e_L	
Higgs, higgsinos	$(H_u^+ \quad H_u^0)$	$(\tilde{H}_u^+ \quad \tilde{H}_u^0)$	
	$(H_d^0 \quad H_d^-)$	$(\tilde{H}_d^0 \quad \tilde{H}_d^-)$	
gluino, gluon		$\tilde{g}$	g
winos, W bosons		$\tilde{W}^{\pm},\ \tilde{W}^0$	$W^{\pm},\ W^0$
bino, B boson		$\tilde{B}^0$	B^0

Table 2.3: The particles of the MSSM prior to electroweak symmetry breaking. SUSY particles are marked with tildes.

Higgs and Gaugino sector

In order to perform electroweak symmetry breaking, the H_u^0 and H_d^0 obtain vacuum expectation values of v_u and v_d respectively, satisfying $v_u^2+v_d^2 = v^2$ for the SM Higgs $v^2 \sim (174\ \text{GeV})^2$. Following this, the $P_R = 1$ MSSM Higgs sector consists of two CP-odd neutral scalars h^0 and H^0 (the former with lower mass, commonly identified as the observed Higgs boson of the SM), one CP-even neutral scalar A^0 and the charged scalars $H^{\pm}$.

EWSB also allows the higgsinos and electroweak gauginos to mix. The four neutral particles ($\tilde{H}_u^0$, $\tilde{H}_d^0$, $\tilde{B}^0$ and $\tilde{W}^0$) combine to form four neutral mass eigenstates known as neutralinos, with symbols χ_i^0 (i=1,2,3,4; mass-ordered from low to high). The charged particles ($\tilde{H}_u^+$, $\tilde{H}_d^-$, $\tilde{W}^+$ and $\tilde{W}^-$) combine to form four charged mass eigenstates known as charginos, denoted $\chi_i^{\pm}$ (i=1,2). Within the MSSM, the lightest neutralino, $\tilde{\chi}_1^0$, is usually assumed to be the LSP, and is thus a good dark matter candidate thanks to its stability and interacting solely through the weak force (and gravity).

2.4.2 SUSY breaking

Despite its theoretical elegance, SUSY is not realised in its pure form in nature. This would imply equal masses between SM and SUSY superpartners, meaning that SUSY would have been trivially discovered decades ago, and hence must be a broken symmetry. Numerous methods to 'break' SUSY by giving higher masses to the sparticles exist, but they must be *soft* breakings, i.e. the cancellation of quadratically divergent terms in the Higgs mass calculation to all orders must still hold[4].

The most general gauge invariant, R-parity conserving addition to the MSSM Lagrangian which breaks the symmetry is:

$$\begin{aligned}\mathcal{L}_{\text{soft}}^{\text{MSSM}} = &-\frac{1}{2}\Big(M_3\ \tilde{g}\tilde{g} + M_2\ \tilde{W}\tilde{W} + M_1\ \tilde{B}\tilde{B} + (\text{c.c.})\Big) \\ &- \Big(\tilde{\bar{u}}\boldsymbol{A_u}\tilde{Q}H_u - \tilde{\bar{d}}\boldsymbol{A_d}\tilde{Q}H_d - \tilde{\bar{e}}^*\boldsymbol{A_e}\tilde{L}H_d + (\text{c.c.})\Big) \\ &- \tilde{Q}^\dagger \boldsymbol{m}_{\boldsymbol{Q}}^2\tilde{Q} - \tilde{L}^\dagger \boldsymbol{m}_{\boldsymbol{L}}^2\tilde{L} - \tilde{u}\boldsymbol{m}_{\boldsymbol{u}}^2\tilde{u}^\dagger - \tilde{\bar{d}}\boldsymbol{m}_{\boldsymbol{d}}^2\tilde{\bar{d}}^\dagger - \tilde{\bar{e}}\boldsymbol{m}_{\boldsymbol{e}}^2\tilde{\bar{e}}^\dagger \\ &- m_{H_u}^2 H_u^* H_u - m_{H_d}^2 H_d^* H_d - (bH_u H_d + (\text{c.c.}))\end{aligned}$$

with quantities in bold being 3×3 matrices across fermion families. Of this large number of extra parameters – there are 105 unique parameters in the MSSM Lagrangian beyond those in the SM – the less obviously named ones are listed in table 2.4. Particular SUSY breaking mechanisms are beyond the scope of this thesis, since with so many free parameters to tune they can yield a large variety of phenomenology and there is little consensus regarding which is most likely to be *the* mechanism.

Naturalness

Closely related to the SUSY breaking mechanism is the concept of *naturalness* – i.e. the degree of fine-tuning required by a particular SUSY breaking model in order to obtain the correct SM masses after radiative corrections. For example, the Higgs mass including the

[4] Of course this is not *necessarily* true, though restoring the hierarchy problem through SUSY breaking would remove one of its main motivations.

Parameter	Description
M_1	Bino mass
M_2	Wino mass
M_3	Gluino mass
μ	Higgsino mass
A_f	Higgs – scalar trilinear coupling for the partner of SM fermion f
$\tan\beta$	Higgs vacuum expectation values ratio, v_u/v_d

Table 2.4: Some of the less intuitively named parameters controlling soft SUSY breaking in the MSSM. The masses are those at the SUSY-breaking scale, and are subject to running in the normal way to obtain low-energy values.

one-loop correction from the $\tilde{t}$ and t is given by:

$$m_H^2 = m_Z^2 \cos^2 2\beta + \frac{3}{2\pi^2}\frac{m_t^4}{v^2}\left(\ln\frac{M_{\text{SUSY}}^2}{m_t^2} + \frac{X_{\text{SUSY}}^2}{M_{\text{SUSY}}^2}\left(1 - \frac{X_{\text{SUSY}}^2}{12M_{\text{SUSY}}^2}\right)\right) + ...$$

where $M_{\text{SUSY}}^2 = m_{\tilde{t}_1} m_{\tilde{t}_2}$ ($\tilde{t}_R$ and $\tilde{t}_L$ mix to form $\tilde{t}_1$ and $\tilde{t}_2$) and $X_{\text{SUSY}} = A_t - \mu\cot\beta$. Thus heavy stops will lead to a large loop correction and some degree of fine tuning (albeit far less than that in the SM). The gluino mass contributes to the stop mass, such that it too cannot be too large without requiring fine-tuning, while the higgsino mass μ affects the Z boson mass. Other sparticle masses do not contribute significantly.

However, the naturalness of a model is somewhat hard to quantify exactly, and opinions differ on what constitutes an acceptably large value. Additionally, the question of 'how likely a universe must we live in?' is highly subjective given we have no knowledge of the size of the sample space. Therefore, while considerations of naturalness may be a useful guide, they should not overly constrain the signatures examined.

Simplified Models

In recent years experimentalists have mostly concerned themselves with *simplified models* which decouple the exact mechanisms of SUSY breaking and instead focus on a particular signature, with some underlying assumptions about mass spectra and branching ratios inspired by but not beholden to a physically viable model. For example, one might consider

light stops in order to satisfy naturalness constraints described above, but be unconcerned about spectra at intermediate scales. Thus a simplified model would be built with only a light $\tilde{t}$ and $\tilde{\chi}_1^0$, with the only other relevant parameters being the branching fractions of the $\tilde{t}$ to $t\tilde{\chi}_1^0$, $bW\tilde{\chi}_1^0$, $c\tilde{\chi}_1^0$ and $bff'\tilde{\chi}_1^0$. These branching fractions are mostly determined by the two sparticle masses and SM parameters – while the $\tilde{\chi}_1^\pm$ mass will impact the latter two, these can equally be tuned to interesting cases like 0, 0.5 or 1.

Of relevance for the analysis described in chapter 4 is that in principle scalars with the same electric charge, R-parity and colour quantum numbers can mix with each other to form mass eigenstates (although many of these potential mixings are constrained by measurements of flavour-changing processes). In general it is assumed that only the third generation squarks undergo substantial mixing, and they are usually considered as the mixed-handedness states $\tilde{t}, \tilde{b}_1, \tilde{t}, \tilde{b}_2$. However, some other mixings are not well constrained by flavour physics, and there exist SUSY-breaking mechanisms where for instance substantial $\tilde{t}-\tilde{c}$ mixing is apparent [43]. The search in chapter 4 is sensitive to such a scenario, despite concentrating on a simplified model with only $\tilde{c}$ and $\tilde{\chi}_1^0$ kinematically accessible without regard to the context in which such a scenario might be realised. For this reason, it is useful for searches to be *model independent* as far as possible, so as to be sensitive to a variety of models outside the direct scope they attempt to probe.

2.4.3 SUSY at the LHC

While SUSY can cause a variety of indirect signals, e.g. through alterations to rare meson decay branching ratios through extra loop contributions, the most striking signature of new particles would of course be their direct detection. The processes with the largest production cross-sections for a given mass are those of squarks and gluinos, due to their direct coupling to the quarks and gluons of the proton via the strong force. The leading order squark and gluino pair-production diagrams are shown in figures 2.6 and 2.7.

In the simplified models considered later in this thesis, there is only ever one light strongly interacting sparticle – a $\tilde{c}$ in chapter 4 and a $\tilde{g}$ in chapter 5 – meaning that t-channel processes

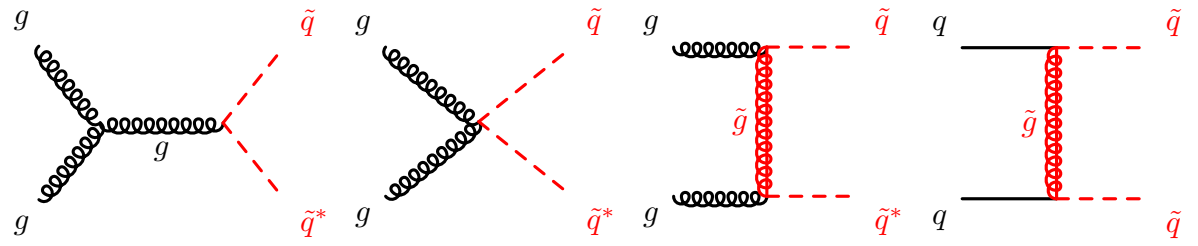


Figure 2.6: Leading order squark production diagrams in proton–proton collisions. The two right hand diagrams (t-channel via a $\tilde{g}$) are suppressed if $m(\tilde{g}) >> m(\tilde{q})$. The rightmost may also proceed with a $q\bar{q}$ initial state, leading to $\tilde{q}\tilde{q}^*$.

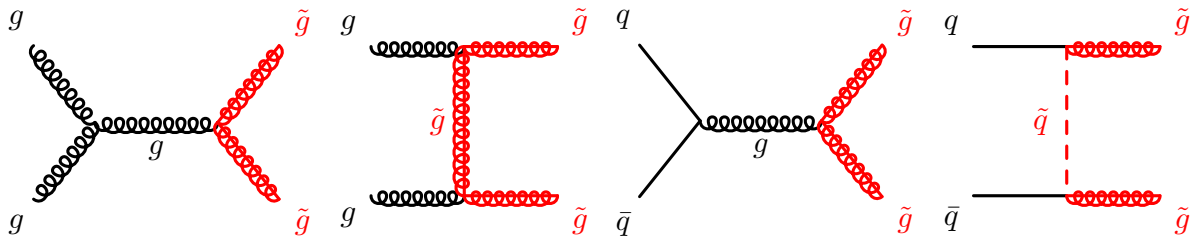


Figure 2.7: Leading order gluino production diagrams in proton–proton collisions. The right hand diagram (t-channel via a $\tilde{q}$) is suppressed if $m(\tilde{q}) >> m(\tilde{g})$.

involving other ones (e.g. $\tilde{q}$ production via $\tilde{g}$ exchange) are suppressed. This has implications for squark production in particular, where a light gluino would enhance $\tilde{c}$ production over $\tilde{t}$ since c quarks in the proton could contribute.

The heavy SUSY particles produced in this way are likely to be produced at rest in the collider frame, since the shape of the PDFs at high x makes it far more likely to extract two partons of similar x than one lower-x parton and another higher-x one (both at higher Q) that would be required for a longitudinally boosted production. This can be seen in figure 2.8, showing the η distributions for a variety of gluino masses, revealing that the bulk of production is within $|\eta| < 1.5$.

Having been (pair-) produced, these SUSY particles tend to decay promptly due to the large mass differences between them and the LSP[5]. In the simplest models, a strongly produced sparticle (e.g. $\tilde{q}$) simply decays to its SM partner and the LSP, leading to the final state of two coloured particles (e.g. q) and two LSPs. The coloured particles hadronise to form jets, and the LSPs escape undetected due to their small interaction cross-sections and

[5] Although the true lifetime is sometimes overlooked by simplified model searches, since long-lived particles result in very different signatures in ATLAS.

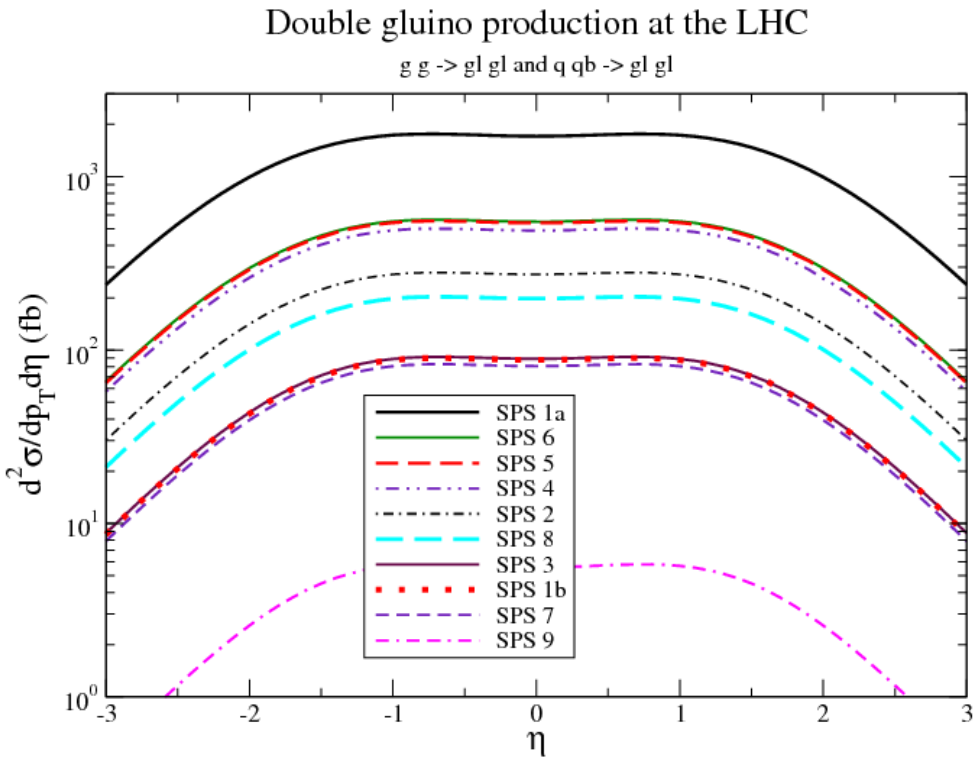


Figure 2.8: Pseudorapidity distributions for gluino production at the LHC for the different SPS points [44, 45], arranged in the legend in increasing order of gluino mass from 600 to 1300 GeV. The hard scale μ^2 is taken as $m_{\tilde{g}}^2 + p_{\mathrm{T},\tilde{g}}^2$. Plot from [46].

thus lead to significant $E_{\mathrm{T}}^{\mathrm{miss}}$. Such signatures can be lessened when there is only a small mass difference between the SUSY particles considered, so that the bulk of the collision energy is transferred to the mass of the LSP, leaving low $E_{\mathrm{T}}^{\mathrm{miss}}$ and low-p_{T} jets. More complex models can have various intermediate-mass SUSY particles, although these are normally weakly interacting such that they are produced less readily than the particle of interest (since production cross-section is strongly dependent on sparticle mass). For example, at $\sqrt{s} = 13$ TeV gluinos with masses around 1200 GeV are pair-produced with a cross-section of 0.1 pb while charginos attain this production cross-section at 400 GeV, at which mass the gluino cross-section is more than 1000 times higher. These intermediate particles can lead to cascades where direct decays to the LSP are disfavoured, resulting in final states with more, but softer, objects.

2.5 Conclusions

This chapter introduced the Standard Model of particle physics – its particle content and the rules governing their interactions. Some important aspects of the strong interaction, in particular the implications of the low-energy non-perturbative regime, were related to the simulation of such events and the problems faced therein. Following this, the idea of Supersymmetry was introduced, motivated by some weaknesses in the SM. Unfortunately SUSY is a broken symmetry, meaning that some of the problems it is invoked to solve (e.g. Higgs fine-tuning) are less satisfactorily resolved than they might be, and this leads many to question its validity.

However, similar arguments can be made about all proposed extensions to the SM, none of which is a silver bullet. As a tool to inspire model building, whereby potentially interesting signatures are identified, SUSY fulfils an inarguably useful role. The analyses presented in chapters 4 and 5 both make use of simplified models inspired by SUSY to guide their optimisation and interpretation, but as with all searches they stand on their own right in constraining the presence of new physics in particular channels.

Chapter 3

The ATLAS experiment

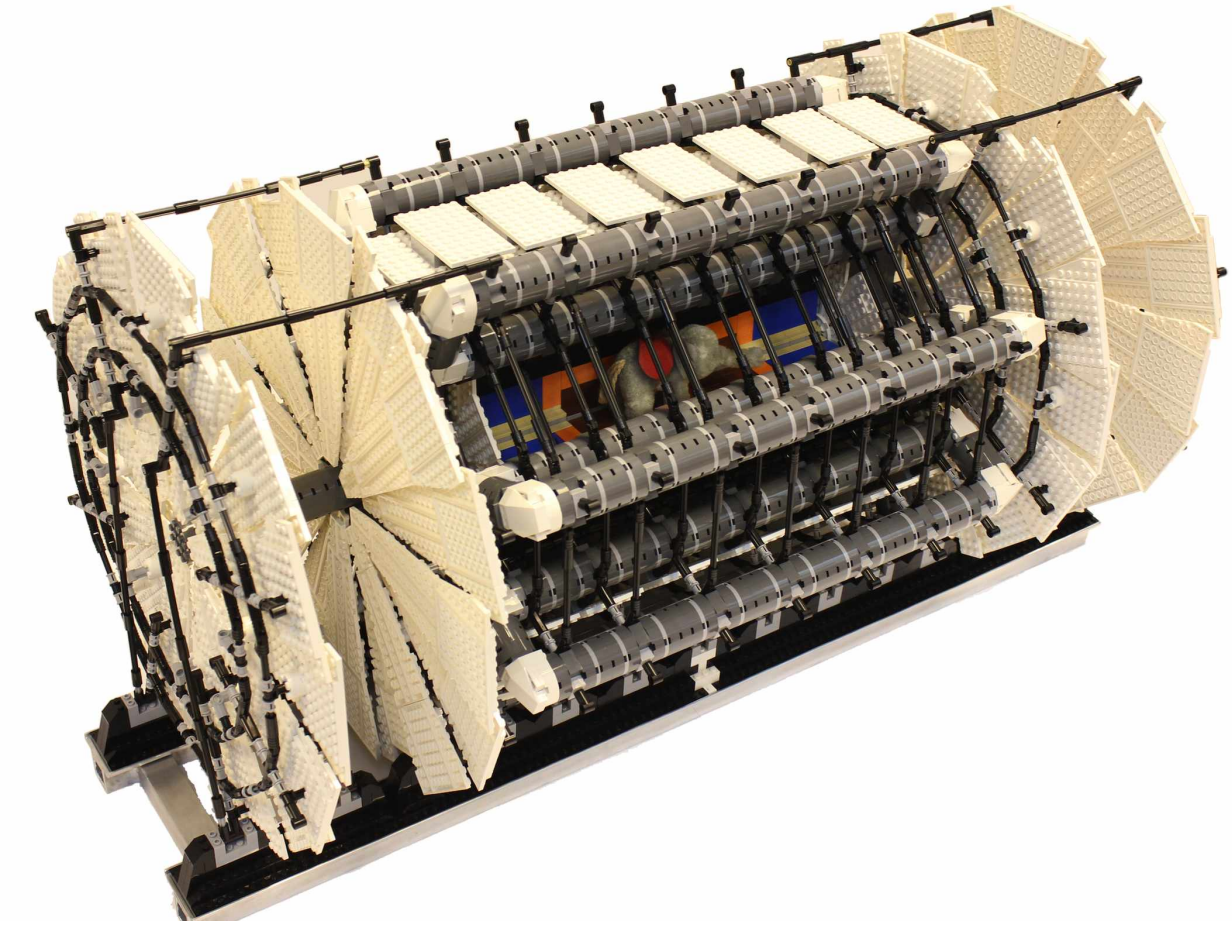


Figure 3.1: A model of the ATLAS experiment, from [47].

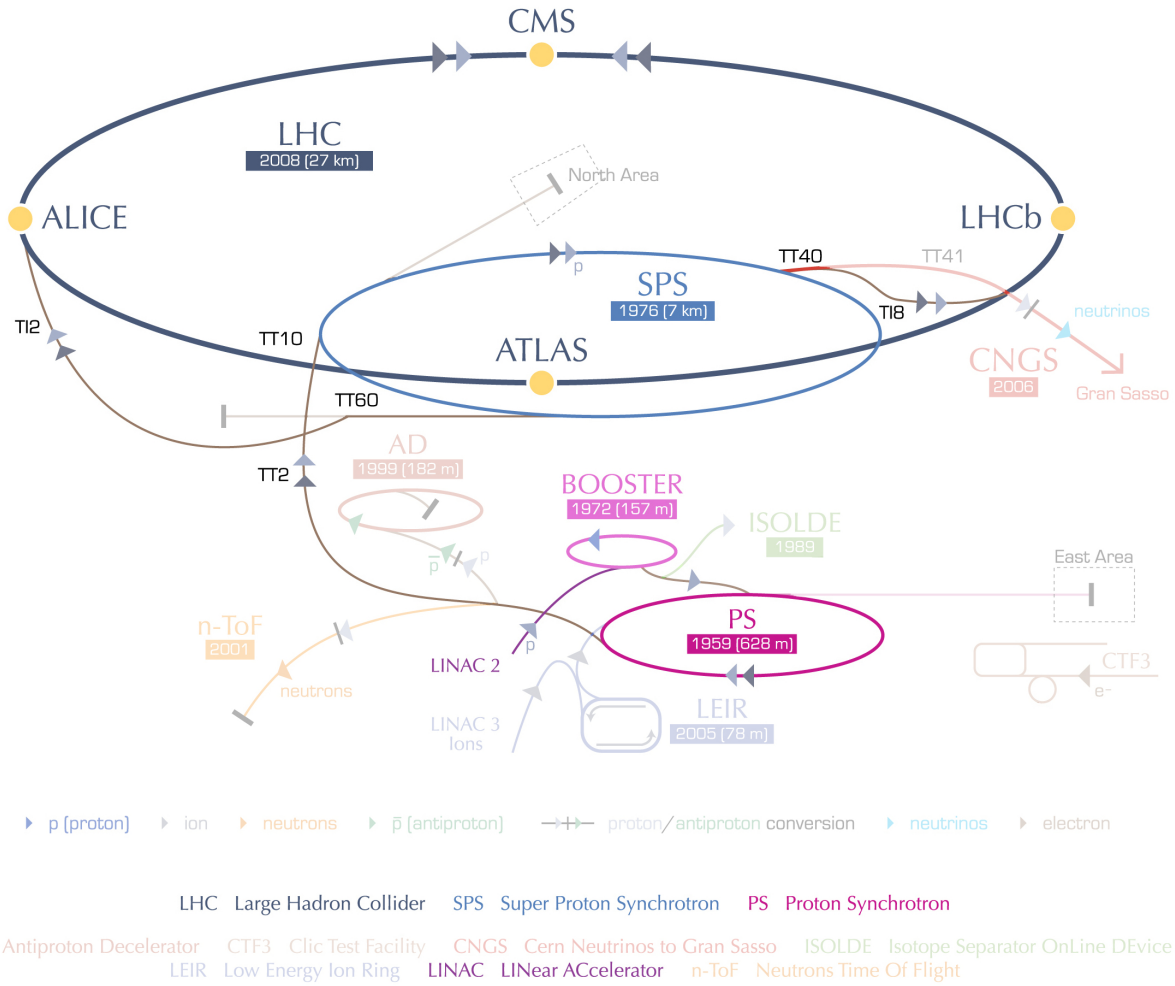
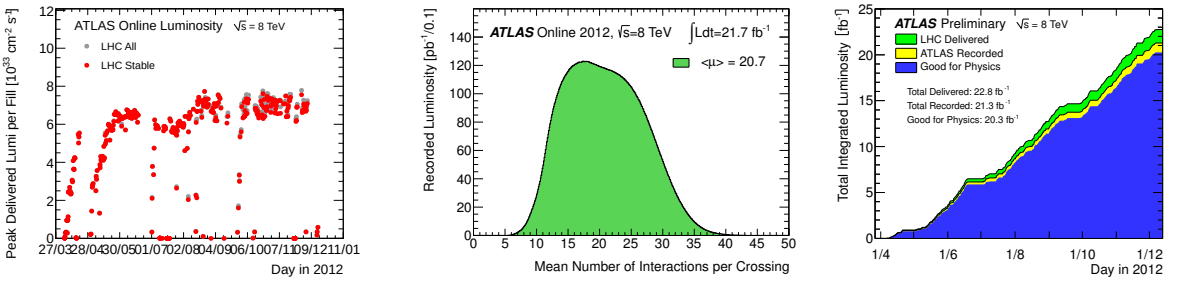


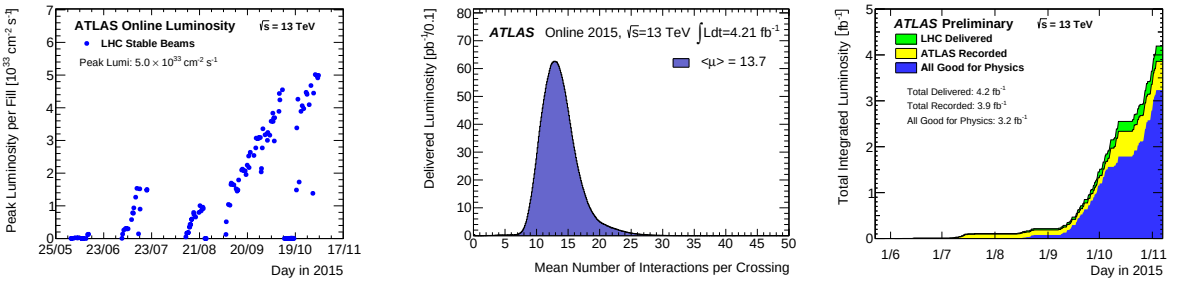
Figure 3.2: The LHC injection chain, modified from [48] to fade components not relevant for LHC proton injection.

ATLAS – "A Toroidal LHC Apparatus", a model of which is shown in figure 3.1 – is one of the four large experiments at the Large Hadron Collider (LHC) at the European particle physics laboratory CERN near Geneva, Switzerland. This chapter will describe the LHC and its performance, ATLAS and its various subsystems, and how it reconstructs the different types of particle to be used in the analyses described in later chapters. Additionally, the steps taken to mitigate the imperfections in the detector, and to accurately simulate them, are also discussed.



(a) Instantaneous luminosity (b) Pileup profile (c) Luminosity recorded

Figure 3.3: LHC Run-1 fill parameters in 2012, from [51].



(a) Instantaneous luminosity (b) Pileup profile (c) Luminosity recorded

Figure 3.4: LHC Run-2 fill parameters in 2015, from [52].

3.1 The Large Hadron Collider

The LHC [49] is a 27 km circumference proton synchrotron inhabiting the tunnel originally built for the Large Electron Positron collider (LEP) in 1988 [50]. It receives protons from the injector chain shown in figure 3.2 – protons are extracted from Hydrogen gas in a strong electric field, before being accelerated to 450 GeV – in two counter-rotating beams. In 2012, the latter part of the LHC's Run-1, each beam was accelerated to 4 TeV giving a pp centre of mass energy of $\sqrt{s} = 8$ TeV. Protons circulated in 5 ns long bunches of $\sim 10^{13}$, with one bunch every 50 ns and with a typical peak luminosity per fill of 7×10^{33} cm^{-2}s^{-1}. In order to reach this collision rate with the given bunch spacing, there had to be multiple $p-p$ interactions per bunch crossing. The average number of interactions per bunch crossing over one LHC revolution is known as pileup, and in 2012 the average pileup was $\langle\mu\rangle = 20.7$, resulting in a total integrated luminosity recorded by ATLAS of 21.3 fb^{-1} – see figure 3.3.

During LS1 various upgrades were undertaken on the LHC dipole magnets, in particular the splice connections between them, allowing the beam energy to be increased to 6.5 TeV

to give $\sqrt{s} = 13$ TeV collisions in Run-2. In addition, the bunch frequency was increased to one every 25 ns, with an accompanying decrease in pileup to $\langle\mu\rangle = 13.7$. Peak instantaneous luminosities approached Run-1 levels – reaching 5×10^{33} cm^{-2}s^{-1} at the end of the run – because the approximate halving in pileup was offset by the LHC being filled with roughly twice as many bunches, and the total recorded integrated luminosity reached 3.9 fb^{-1} – see figure 3.4, and section 3.3.2 for the meaning of 'good for physics' in subfigure (c) thereof.

The first search detailed in this thesis (chapter 4) was performed on Run-1 8 TeV data collected between 5$^{\text{th}}$ April and 6$^{\text{th}}$ December 2012, and the second (chapter 5) on Run-2 13 TeV data collected between 16$^{\text{th}}$ August and 3$^{\text{rd}}$ November 2015.

3.2 ATLAS

3.2.1 Co-ordinate definition

ATLAS [53] uses a right-handed coordinate system with its origin at the nominal interaction point (IP) in the centre of the detector, the z-axis along the beam pipe (south towards Geneva), the x-axis pointing towards the centre of the LHC ring and the y-axis upwards. Cylindrical coordinates (r, ϕ) are used in the transverse plane, ϕ being the azimuthal angle around the beam pipe. The rapidity is $y = \frac{1}{2} \ln \frac{E+p_z}{E-p_z}$, and the pseudorapidity is defined in terms of the polar angle θ as $\eta = -\ln \tan(\theta/2)$; in the massless limit y and η are equivalent. The separation ΔR of objects in $\eta - \phi$ space is defined as $\Delta R = \sqrt{(\Delta\eta)^2 + (\Delta\phi)^2}$.

Given the uncertain initial state in the longitudinal direction (since the momentum fractions of the colliding partons from each proton are unknown), the transverse momentum $\vec{p}_{\text{T}} = (p_x, p_y)$ and other transverse quantities are often preferred since there is (close to) zero initial momentum in the transverse plane. The transverse momentum imbalance – i.e. the negative vector sum of the $\vec{p}_{\text{T}}$ of all visible objects – is known as the 'missing transverse momentum' and has symbol $E_{\text{T}}^{\text{miss}}$.

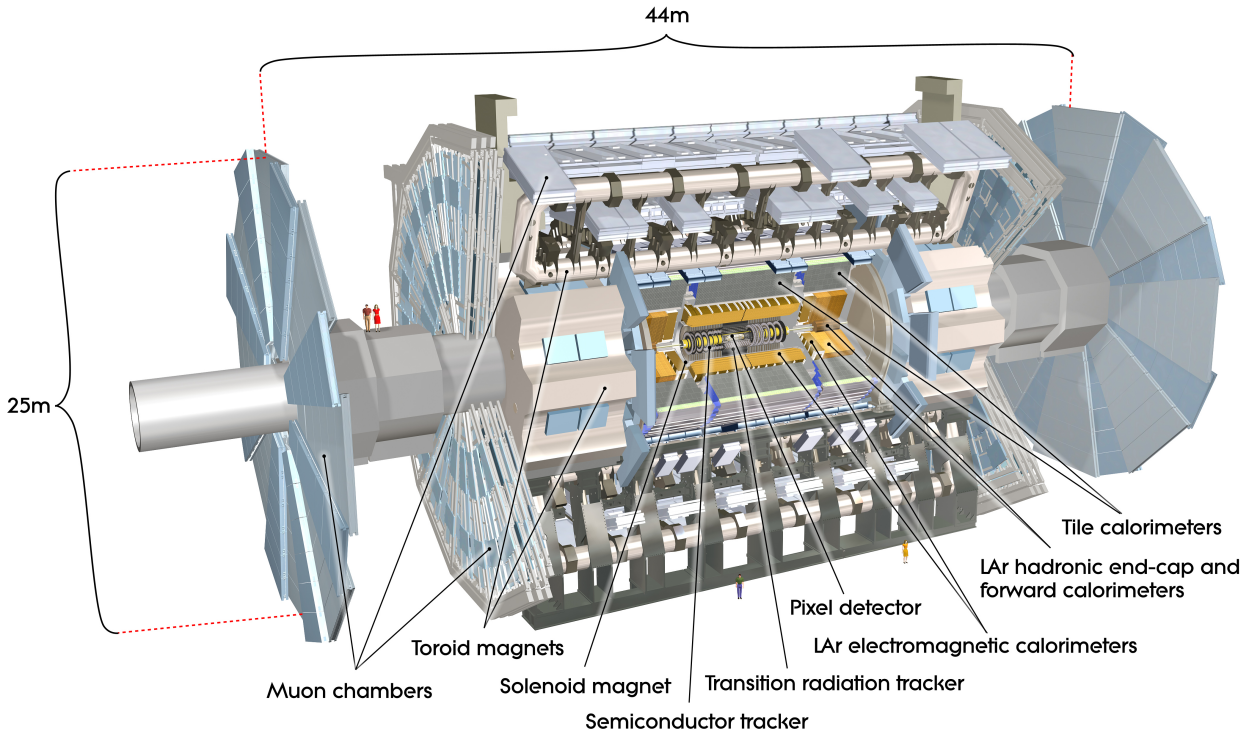


Figure 3.5: The ATLAS detector and subsystems, from [54].

3.2.2 Overview

ATLAS is a classic general purpose particle detector, albeit on an unprecedented scale of 46 m long. It has a near-hermetic cylindrical design, with most subsystems consisting of separate barrel and endcap parts, as can be seen in figure 3.5. At its heart is the inner detector (ID) consisting of silicon pixels, silicon strips (SCT) and a transition radiation tracker (TRT) providing tracking and identification of charged particles within $\eta < 2.5$. Surrounding this volume is a solenoid magnet providing a close-to-uniform axial field of 2 T throughout the ID, allowing momentum measurement from tracking therein. Beyond this lie the electromagnetic and hadronic calorimeters (EMCAL and HCAL), consisting of liquid argon detectors (LAr) in the barrel and endcap regions and plastic scintillator tiles (TileCal) in the barrel only (the LAr subsystem works as both EMCAL and HCAL in the endcap region). Surrounding this there lies a barrel and endcap magnet system providing a ~ 4 T toroidal magnetic field. Amidst and beyond this toroid magnet system is mounted the muon system (MS), consisting of four different technologies for fast triggering and accurate

measurement of the passage of muons.

3.2.3 Inner Detector

Figure 3.6 shows the ATLAS Inner Detector and its subsystems. Its principle purpose is to accurately measure the paths charged particles take through this inner part of the detector – their *tracks*. This track information is used to provide precise momentum measurements through the bending in the solenoid field, to identify the principle 'hard scatter' vertex of an event, and to associate tracks to it or other vertices and hence identify displaced secondary vertices resulting from the in-flight decay of e.g. B-hadrons.

Pixel and IBL

The pixel detector [57] consists of the innermost layers of ATLAS, with three barrel layers and two lots of three endcap disks, spanning radii of 50 to 150 mm from the interaction point. These layers are made from 1744 biased silicon modules finely segmented into a total of ∼80 million pixels, each of size 50×400 μm. The passage of charged particles through these modules liberates electron – hole pairs in the silicon, with the number of carriers related to the energy of the particle. These charge carriers then drift under the influence of the electric field provided by the bias voltage, this charge separation being picked up and amplified to form the recorded signal. The position of charged particles is measured in this way to a precision of ~ 10 μm. Over LS1, the beam pipe through ATLAS was replaced allowing a new innermost layer – the 'Insertable B-layer' [58] (IBL) to be added at 26 mm radius from the IP, with 286 modules containing 13 million pixels with finer segmentation 50×250 μm. The extremely high precision tracking provided by the pixel (and improved by the IBL in Run-2) is especially important for the determination of track impact parameters (particularly for low-momentum tracks), one of the key inputs to the identification of short-lived particles like B- or D- hadrons.

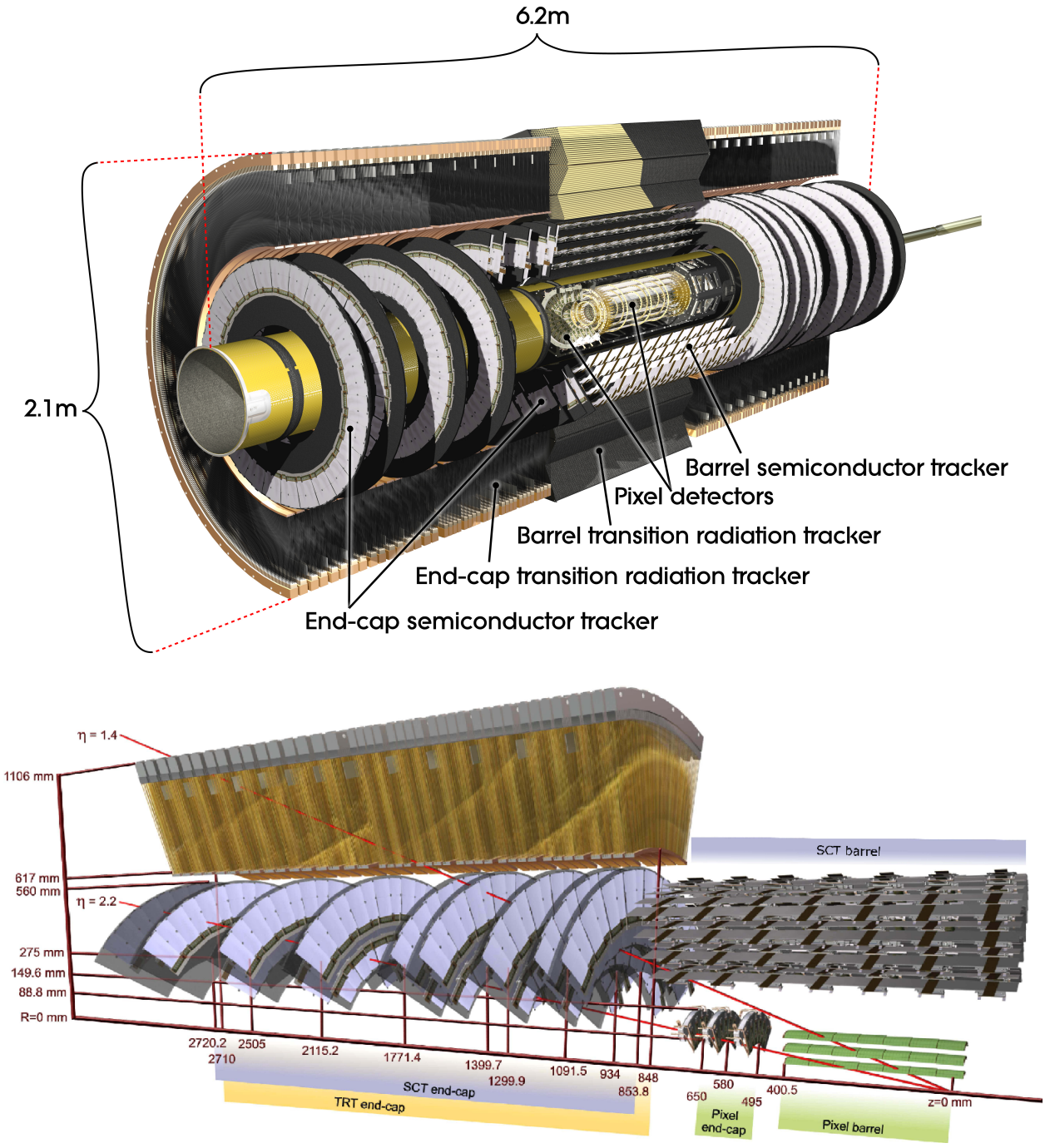


Figure 3.6: The ATLAS Inner Detector. Top: overview, from [55]; bottom: traversed by two 10 GeV tracks with $\eta = 1.4$ and 2.2 (the TRT barrel and IBL detectors are not shown), from [56].

Semi-Conductor Tracker

The semi-conductor tracker [59] (SCT) also makes use of biased silicon as a detector medium, and spans radii of 27.5 to 56 cm from the IP with 4 barrel layers and 9 endcap disks on each side. These are arranged such that tracks originating from the IP within $|\eta| < 2.5$ will traverse four layers. In total there are 4088 double-sided modules, each side segmented into strips 80 μm wide (on average – endcap strips are segmented along radii) and ~13 cm long resulting in 6.2 million channels, providing position measurements in ϕ to a precision of 16 μm. The halves of each module are offset by a small stereo-angle of 40 mrad in order to provide z (in the barrel) and r (in the endcap) measurements to a precision of 580 μm. The fast detector response allows discrimination between bunch crossings 25 ns apart and the removal of hits from interactions occurring in the preceding bunch crossing. Redundancy in both module control and readout optical links allows for a high efficiency, with more than 99% of modules fully operational over Run-1.

Transition Radiation Tracker

The Transition Radiation Tracker [60] (TRT) is built from straw detectors, 4 mm diameter kapton tubes filled with Xenon gas and with a thin (30 μm diameter) anode wire along the centreline. The passage of charged particles liberates electrons from the gas, which are accelerated towards the centre wire and liberate further electrons as they collide with gas atoms along the way. Additionally, materials of varying dielectric constant surrounding the straws emit transition radiation when highly relativistic particles (principally electrons) cross boundaries between them. The Xenon gas is sensitive to this radiation, which results in higher energy electron cascades at the central wire, allowing electron identification. In total, there are 420,000 channels read out, each providing a drift time measurement giving a spatial resolution of 170 μm, and a total gas volume of 3 m^3. Due to ozone production and resulting localised corrosion, some modules developed leaks during Run-1 that were not able to be fixed during LS1. The modules with the highest leak rates were switched to using Argon rather than Xenon in Run-2 to reduce the cost of replenishing leaked gas, reducing

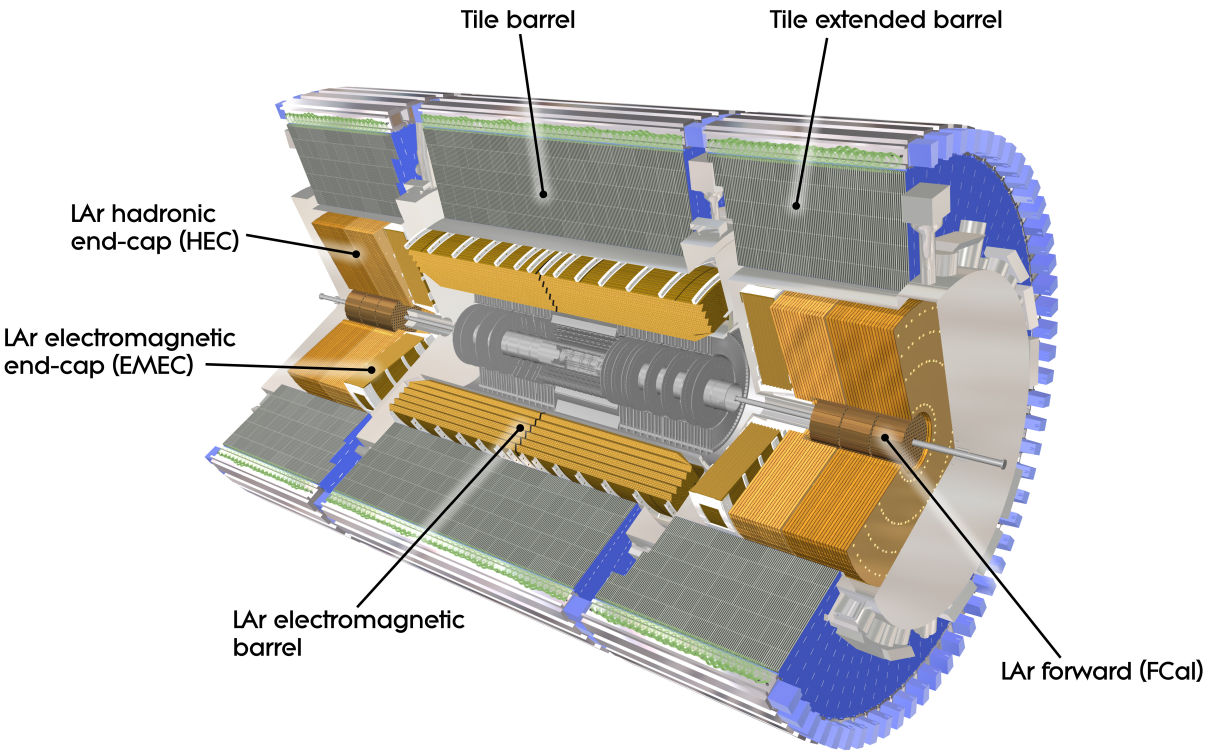


Figure 3.7: The ATLAS Calorimeters, from [61].

the electron identification efficiency but not impacting tracking performance.

Solenoid Magnet

Surrounding the ID is a superconducting solenoid magnet of internal diameter 2.4 m and length 5.3 m. It provides a field of 2 T throughout the ID volume, with a peak field of 2.6 T, allowing momentum measurements of charged particles as their curved paths are tracked though the ID.

3.2.4 Calorimeters

Figure 3.7 shows the ATLAS calorimeters, which surround the solenoid and measure the energies of most incident charged and neutral particles within an acceptance of $|\eta| < 4.9$. Particles interact with *absorber* materials, depositing their energy in showers of subsidiary particles that are then measured.

Liquid Argon Electromagnetic Calorimeter

The Liquid Argon calorimeter [62] (LAr) consists of a barrel (EMB, $|\eta| < 1.475$) and two endcaps each divided into three parts. Closest to the IP lie the electromagnetic endcaps (EMEC, $1.375 < |\eta| < 3.2$), then further out the hadronic endcaps (HEC, $1.5 < |\eta| < 3.2$) and at similar distance but closer to the beam pipe the forward calorimeters (FCAL, $3.1 < |\eta| < 4.9$). The LAr systems use lead plates as absorbers and liquid argon as the active material, and signals are collected by copper-kapton tape electrodes mid-way between lead layers. These layers are arranged in a zig-zag 'accordion' fashion, in order to ensure uniform response in ϕ with no gaps in coverage, and the electrodes are etched so as to predominantly provide read-out in approximately square 'towers' in $\eta - \phi$ space ($\sim 0.025 \times 0.025$). In the EMB, where precision measurements are most useful for e and γ identification, the innermost part is very finely segmented in η, with widths of 4.7 mm corresponding to $\Delta\eta$ of 0.003.

Tile Hadronic Calorimeter

The Tile hadronic Calorimeter [63] (TileCal) is simpler in layout, consisting of a barrel surrounding the EMB and two extended barrels outside the EMECs – i.e. there is no endcap part. It uses iron plates as absorbers and plastic scintillator tiles as the active material, arranged in wedge-shaped modules extending radially for the whole of the barrel thickness. The light produced in the scintillators is transmitted by wavelength shifting fibres (from blue to green) and read out by photomultiplier tubes at the outside edge of the modules. The modules are segmented into three layers of $\sim 1.5 - 4$ nuclear interaction lengths, i.e. about $40 - 120$ cm, and span $\Delta\phi$ of 0.1 throughout and $\Delta\eta$ of 0.1 for the inner two layers and 0.2 for the outer layer.

3.2.5 Muon System

The ATLAS muon system (MS), shown in figure 3.8, comprises several parts in order to meet the requirements on triggering, tracking in high densities in the forward regions and

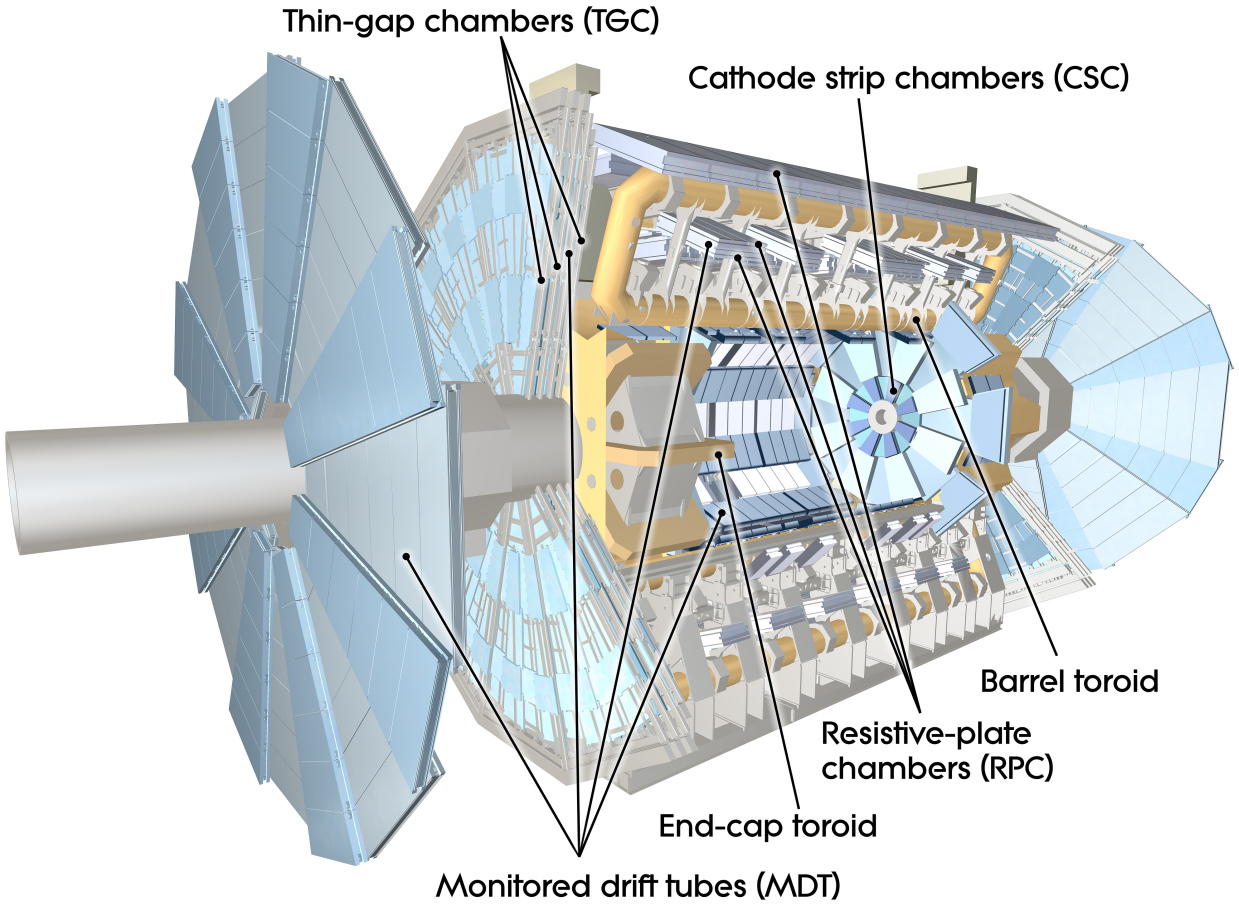


Figure 3.8: The ATLAS Muon systems, from [64].

hermetically covering the large barrel volume, with particles from the IP traversing three sets of muon chambers. In the barrel there is one set within the toroid field, while this is not possible for the smaller endcap toroids as the cryostat envelops them entirely. Here therefore momentum is measured from the change in angle on crossing the magnet, with a large lever arm provided by the 'big muon wheels' displaced from each end. Within $|\eta| < 0.1$ the MS is not fully instrumented to allow access for cabling and services (e.g. cooling) to the calorimeters and ID.

Toroid Magnets

The ATLAS toroid magnet system consists of eight barrel coils and two sets of eight endcap coils, providing peak fields of ~ 4 T with 20.5 kA flowing through superconducting NbSn. The endcap coils are rotated by $\frac{\pi}{8}$ with respect to the barrel ones in order to provide radial overlap and to optimise the field strength in the interface regions.

Monitored Drift Tubes

The bulk of the MS coverage by volume is provided by monitored drift tubes (MDTs), which operate according to similar principles as the TRT straw tubes. They are however somewhat larger, with diameters of 30 mm and lengths between 0.7 and 6.3 m, and are made of aluminium. Each set comprises two sides of 3 or 4 layers each, lying parallel to the toroid field so as to provide the best measurement in the direction of muon bending – about 35 μm.

Cathode Strip Chambers

Closer in than the endcap toroid in the forward region, particle densities are too high for the long MDTs to function usefully, so cathode strip chambers (CSCs) are used instead. These are multiwire proportional chambers with anode wire spacing of 2.5 mm, and perpendicular cathode strips on each side giving a second coordinate. This much finer granularity allows the CSC to function in the high-density environment of the forward region, with radial

precision of 40 μm.

Resistive-plate Chambers

The MDTs have a drift time approaching 500 ns, which is clearly too slow for useful triggering. Thus dedicated resistive-plate chambers (RPCs) are used in the barrel region. These comprise two resistive bakelite plates, separated by a 2 mm gas gap with a uniform electric field, giving a 1 ns time resolution but only a 10 mm positional resolution in the plane of the plates.

Thin-gap Chambers

Similarly to the MDT, the RPCs suffer from poor granularity and so are unsuitable for the dense environment of the endcap regions. They are replaced here by thin-gap chambers (TGCs), comprising a plane of 50 μm anode wires spaced by 2 mm, held between two grounded planes and immersed in a pentane – CO_2 gas mixture. This affords higher granularity while retaining sufficient response speed, and measures the position of a traversing particle to a precision of ∼5 mm.

3.3 Data Recording

3.3.1 Trigger

The collision rate in the LHC of 20 MHz in Run-1 and 40 MHz in Run-2 is far in excess of the read-out and storage capabilities of ATLAS. Thus a trigger system is used to rapidly decide whether each event is worthy of storage and offline analysis. The first stage of the trigger is known as Level 1 (L1), and finds regions of interest (RoIs) in the calorimeters and MS using fast, dedicated hardware, reducing the rate to ∼ 70 kHz (100 kHz in Run-2) with about 2 μs total latency. These events are then passed to the high level trigger (HLT) – comprising two parts known as 'level 2' (L2) and 'event filter' (EF) in Run-1, but merged in Run-2 –

which runs a more complete event reconstruction on a read-out of the whole detector, and results in a trigger acceptance rate of 700 Hz (1 kHz in Run-2). The objects formed in the trigger decisions are necessarily different to the final reconstructed and calibrated 'offline' objects, described in detail in section 3.4, resulting in inefficiencies that typically decrease with object p_{T}.

The Run-1 analysis presented in this thesis made use of $E_{\mathrm{T}}^{\mathrm{miss}}$ and single lepton triggers, and the Run-2 one of multi-jet triggers, so they are briefly outlined here.

$E_{\mathrm{T}}^{\mathrm{miss}}$ trigger (Run-1)

At L1, calorimeter signals are merged into lower-granularity trigger towers (TT) covering $\Delta\eta \times \Delta\phi \sim 0.1 \times 0.1$. These TTs are used to compute the $E_{\mathrm{T}}^{\mathrm{miss}}$ over the full calorimeter acceptance of $|\eta| < 4.9$. The L2 calculation makes use of summary data in the front-end-buffer, and for the EF decision the full calorimeter resolution is used along with cluster-based hadronic calibration and calculation of $E_{\mathrm{T}}^{\mathrm{miss}}$, with the online requirement of 80 GeV reaching 95% efficiency offline for $E_{\mathrm{T}}^{\mathrm{miss}} > 150\,\mathrm{GeV}$.

Electron trigger (Run-1)

At L1, calorimeter TTs are used as for the $E_{\mathrm{T}}^{\mathrm{miss}}$ trigger. The L2 trigger performs a fast calorimeter and ID track reconstruction, and the same reconstruction as offline at EF, with efficiency plateauing at $p_{\mathrm{T}}^{e} = 25\,\mathrm{GeV}$ for an online selection of 24 GeV.

Muon trigger (Run-1)

Muons are triggered at L1 using the RPC and TGC systems as described above. At L2, the precision MDT and RPC systems are included to build muon candidates, along with track information from the ID. The same information is used for the final HLT decision, requiring an online p_{T} above 24 GeV for an offline threshold of $p_{\mathrm{T}}^{\mu} = 25\,\mathrm{GeV}$.

Multi-jet trigger (Run-2)

Jets (see section 3.4.4 for definition) are triggered at L1 with a sliding window algorithm on calorimeter TTs. At the HLT step, topological clusters are constructed from a full scan of the calorimeters, allowing pileup subtraction to be performed and low energy jets to be reliably extracted in a selection that is close to that used offline. The resulting 6-jet trigger, requiring jets above 45 GeV, is 90% efficient for a 6^{th} jet of $p_{\text{T}} = 50$ GeV.

3.3.2 Data Quality

Due to the size and complexity of ATLAS, and the harsh radiation environment in which it operates, invariably there are occasional problems in operation. These fall into several categories: transient issues that cause data recording to be paused, problems leading to the recorded data being unsuitable for use in analysis and smaller issues leading mostly to acceptably small drops in performance. Examples of the first include periods of time when subsystems are changing operational state (e.g. high voltage ramping in silicon detectors) at the start of a run, and when data taking is temporarily paused due to reconfiguration of a subsystem to e.g. reset or suppress a set of noisy channels. The second include periods when detectors were misconfigured, when certain subsystems were not fully operational and when a certain fraction of channels became unacceptably noisy. After removing such data, there were 20.3 fb^{-1} of useable data in Run-1 out of the 21.3 fb^{-1} recorded and 22.8 fb^{-1} delivered, and 3.2 fb^{-1} in Run-2 from 3.9 fb^{-1} recorded and 4.2 fb^{-1} delivered – see figures 3.3 and 3.4 in section 3.1.

The third class of defects – i.e. ones that are mostly tolerable – include the fact that the silicon detectors of the ID have a small fraction of channels permanently disabled for various reasons. In general, however, the impact of these smaller defects is mitigated by the quality requirements placed on reconstructed objects, as described in the following sections.

3.4 Object reconstruction

As alluded to in section 3.3.1, the process by which signals provided by detector subsystems are identified as physical objects is a crucial one. Signals must be grouped, particles reconstructed and identified, and their properties calibrated. Finally, care is taken to guard against double-counting – i.e. the same detector signal contributing to multiple objects – in a process known as overlap removal.

3.4.1 Tracks

ID tracks are not used as standalone objects in physics analysis, but they are important inputs to most of the objects that follow. They are formed by taking pixel, SCT and TRT information to extract space points, and using these to seed tracks in the innermost layers and extend them outwards. Fitting, fake removal and cleaning algorithms are then applied, followed by a re-fitting across all inputs on the remaining candidate tracks. ID tracks are used to find the primary vertex (PV) – the vertex with the largest value of Σp_T^2 for all tracks associated with it – to reject pileup contributions. Additionally, they are used as inputs to secondary vertex (SV) finding algorithms used to select e.g. b-jets, as well as providing lepton p_{T} measurements.

3.4.2 Electrons

Electron candidates are reconstructed from energy clusters in the EMCAL which match a track in the ID. Clusters are formed using a fixed-size sliding-window algorithm [65], operating on 200×256 towers in $\eta - \phi$ space with the granularity of the central layer of the LAr. Within the tracking acceptance of $|\eta| < 2.47$, tracks from the ID are then matched to these clusters, and clusters with no matching tracks are classified as photons. Outside this η range it is not possible to identify electrons.

Once electron candidates have been formed, the cluster η and ϕ are updated according to

Baseline Electron	
Acceptance	$E_T > 7$ GeV, $\lvert\eta^{\text{calorimeter cluster}}\rvert < 2.47$
Quality	*Medium++* working point
Cleaning	cut on quality flag el_OQ
Overlap	$\Delta R(e, \text{jet}) < 0.2$ or > 0.4
Signal Electron	
Quality	*Tight++* working point
Track Isolation	$\sum p_{\text{T}}(\text{tracks}, \Delta R < 0.3)/p_{\text{T}}(e) < 0.15$
Calorimeter Isolation	$\sum E_{\text{T}}(\text{pileup-corrected topoclusters}, \Delta R < 0.3)/p_{\text{T}}(e) < 0.18$
Longitudinal IP	$z_0 \sin\theta < 0.4$mm
Transverse IP significance	$d_0/\sigma_{d_0} < 5$

Table 3.1: Summary of the electron definition cuts applied in the Run-1 scharm analysis. Similar variables are used for the Run-2 multijets analysis.

the ID information, and the energy is adjusted by reclustering in different calorimeter regions and correcting for energy deposits outside the EMCAL (measured in benchmark processes such as $W \to e\nu$ and $Z \to ee$).

These calibrated electron candidates are then subject to identification criteria, based on combining various calorimeter and tracking information such as calorimeter shower shapes, track – cluster matching quality, and association to the primary vertex (PV). The details varied between Run-1 [66] and Run-2 [67], but in both cases multiple 'working points' were available, trading purity for efficiency. Electrons are initially classified according to loose criteria and with low p_{T} thresholds, and are known as *baseline* electrons. These are used to veto events if a region has an upper limit on the number of electrons. When an electron is required to be present, it is subject to more stringent criteria and is known as a *signal* electron. An outline of these two sets of criteria are shown in table 3.1.

3.4.3 Muons

Muon candidates are identified according to information from all sub-detectors, and classified into four types [68, 69]:

Combined (CB) MS track and ID track – these make up the majority of muon candidates and have the best performance in terms of sample purity and momentum resolution.

Segment-Tagged (ST) ID track and at least one track segment in the MDT or CSC

Stand-Alone (SA) Track only in MS

Calorimeter-Tagged (CT) ID tracks matched to calorimeter energy deposit compatible with a minimally ionising particle.

CT and ST muons are only used within $|\eta| < 0.1$ (where the MS is non-hermetic), and SA muons between $2.5 < |\eta| < 2.7$ to extend beyond the ID acceptance.

Similarly to electrons, following the identification of muon candidates their 4-vectors are then calibrated to correct for e.g. energy loss in the calorimeters, again measured in processes such as $Z \to \mu\mu$. They are then subject to various quality requirements designed to reject fakes and provide good momentum measurements, again with various working points, and may also be classified as *signal* and/or *baseline*. These criteria are outlined in table 3.2.

3.4.4 Jets

The ATLAS calorimeters do not have sufficient segmentation or resolution to identify and measure each individual hadron emerging from a collision. Thus, unlike previously mentioned objects, hadronic activity is defined not in terms of physical particles but rather in terms of artificial constructs known as jets that attempt to coherently cluster the outgoing hadrons.

In order to be stable against the divergences mentioned in section 2.2.3, and hence be theoretically calculable at the particle level, jets must be infrared and collinear 'safe'. This means that the clustering of constituents should not change in the event of soft or collinear

Baseline Muon	
Algorithm	STACO, combined or segment-tagged muon
Acceptance	$p_{\mathrm{T}} > 6$ GeV, $\lvert\eta\rvert < 2.4$
Quality	*Loose* working point
ID track quality	$\geqslant 1$ b-layer hit when it can be expected
	$\geqslant 1$ pixel hit or crossed dead pixel sensor
	$\geqslant 5$ SCT hits or crossed dead SCT sensor
	pixel holes + SCT holes < 3
	η-dependent TRT hit requirements
Overlap	$\Delta R(\mu, jet) > 0.4$
Signal Muon	
Quality	*Loose* working point
Cosmic rejection	$\lvert z_\mu - z_{PV}\rvert < 1$ mm, $d_0 < 0.2$ mm
Track Isolation	$\sum p_{\mathrm{T}}(\text{ID tracks}, \Delta R < 0.3)/p_{\mathrm{T}}(\mu) < 0.12$
Calorimeter Isolation	$\sum E_{\mathrm{T}}(\text{pileup-corrected topoclusters}, \Delta R < 0.3)/p_{\mathrm{T}}(\mu) < 0.12$
Longitudinal IP	$z_0 \sin\theta < 0.4$ mm
Transverse IP significance	$d_0/\sigma_{d_0} < 3$

Table 3.2: Summary of the muon definition cuts applied in the Run-1 scharm analysis. Similar variables are used for the Run-2 multijets analysis, except the cosmic muon cuts are not applied.

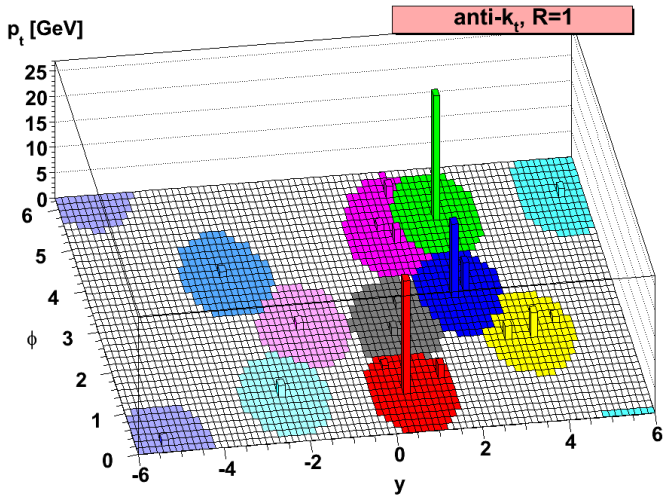


Figure 3.9: The outcome of anti-k_t clustering with radius parameter $R = 1$, from [71].

parton emission. The most intuitive clustering of collimated particles, a fixed-radius cone, is unfortunately not infra-red or collinear safe so cone algorithms are generally not used[1]. However, the algorithm predominantly used in ATLAS, anti-k_t [71, 72], does fulfil these criteria and results mostly in conically shaped jets. It proceeds by defining a distance measure between every pair of particles i and j in terms of a radius parameter R:

$$d_{ij} = \min\left(\frac{1}{p_{\mathrm{T},i}^2}, \frac{1}{p_{\mathrm{T},j}^2}\right)\frac{\Delta R_{ij}^2}{R^2}$$

For each particle, a 'beam distance' $d_{iB} = 1/p_{\mathrm{T},i}^2$ is additionally defined. Then, starting from the smallest of these distances, if it is between two particles then they are merged, through adding their 4-momenta, and the distances are recomputed. If however the smallest is a beam distance then that constituent is labelled a jet and removed from the process. This results in clusterings starting from hard particles, which will 'gather up' soft particles within a radius R to form a conical jet provided there is no other hard particle within $2R$. If there is one with $R < \Delta R < 2R$ then the cones will be clipped in the overlap region depending on the relative p_{T} of each, and if hard particles are within R of one another they will be merged. This behaviour can be seen in figure 3.9.

The smallest possible calorimeter jet constituent in ATLAS is a calorimeter cell. However,

[1]The cone-based algorithm SIScone [70] is stable against these emissions, at the cost of resulting in irregularly-shaped jets.

the initial stage of jet reconstruction is to form topological clusters [65] of calorimeter cells with a signal to noise ratio above a certain threshold. These clusters are calibrated assuming energy deposition by electromagnetic showers alone, then corrected for hadronic effects – the calorimeter response to hadrons is typically about 75% of that for electrons – according to e.g. the energy densities and shower depths in the EMCAL and HCAL. Only then are jets formed from these clusters, using the anti-k_t clustering algorithm with jet radius parameter $R = 0.4$.

Following this, jets are calibrated in a multi-stage process. First, the effect of pileup on jet energies – i.e. energy deposited in calorimeter cells within a jet but from a different pp collision – is suppressed using a jet area based correction and further corrected for using a parameterisation in terms of the pileup and number of pp collisions reconstructed for that event [73]. Second, the jet direction is changed to point back to the PV instead of the detector co-ordinate origin, and third a p_{T} and η dependent correction (derived from simulation) is applied to the reconstructed energy [74]. Fourth, a residual correction derived from measurements of benchmark processes – i.e. jets balancing against well-measured objects – is applied. Finally, the energy resolution of the jets is improved by using a set of sequential calibrations based on properties such as hits in the MS behind the jet [75].

To further reduce the effect of pileup, a jet having 20 GeV $< p_{\mathrm{T}} <$ 50 GeV and $|\eta| < 2.4$ is disregarded when the p_{T}-weighted sum of its tracks indicates that it originated from a pileup collision and not the PV, based on a simple ratio in Run-1 (JVF, $\sum p_{\mathrm{T}}$(tracks associated with PV) / $\sum p_{\mathrm{T}}$(tracks associated with any vertex)) and a multivariate jet vertex tagger in Run-2 (JVT, described in [73]).

3.4.5 Jet flavour tagging

Jets can originate from many different objects, e.g. gluons, τ leptons and hadrons formed from any of the five u, d, s, c, b quarks. Of particular interest to the analyses described here is the ability to distinguish 'light flavour' jets (those originating from gluons and hadrons only containing u, d and s quarks) from 'heavy flavour' jets (those originating from B- or

D- hadrons, i.e. those containing b or c quarks). This ability to distinguish light-jets, c-jets and b-jets is useful both to enhance particular signals of interest and to purify particular background selections.

These different flavours of jet are distinguishable thanks to the difference in lifetime of the different progenitors. Gluons split and hadronise rapidly and light hadrons are either stable or decay rapidly via electromagnetic interactions, hence the final state particles are formed almost immediately. B and D hadrons, by contrast, have small but finite lifetimes[2], of around 1.6 (1.5) $\times 10^{-12}$ s, $c\tau = 490$ (450) μm for $B^{\pm}$ (B^0) mesons and 1.0 (0.4) $\times 10^{-12}$ s, $c\tau = 300$ (120) μm for $D^{\pm}$ (D^0) mesons. At energies of 100 GeV, giving Lorentz γ factors of around 20 and 50 for typical B and D meson masses of 5.3 GeV and 1.9 GeV respectively [22], these correspond to flight distances in mm of $D^{\pm}$: 16, D^0: 6, $B^{\pm}$: 9, B^0: 8 at this typical jet energy scale (assuming $\eta = 0$ for simplicity).

These flight distances can be observed in two main ways. First, the presence of a secondary vertex (SV) can be inferred from tracks inside the resulting jet that do not point to the PV but that instead intersect at the heavy hadron decay point. Second, the decay of a heavy hadron imparts a certain lateral (with respect to the flight direction) boost to its individual decay products. If some of these are neutral, then the charged particles will on average be displaced from the original direction of travel, leading to a finite impact parameter with respect to the PV. B-hadrons are distinguished from D-hadrons by the fact that B-hadrons decay almost exclusively to D-hadrons, leading to the presence of tertiary vertices for B-hadrons. Additionally, they provide a larger transverse boost to their daughters, resulting in larger impact parameters.

This impact parameter and SV information is used to train multivariate algorithms dedicated to selecting a particular flavour of jet – *MV2c20* [76, 77] for b-jets in Run-2 and *JetFitterCharm* [5] for c-jets in Run-1. Further details of each algorithm is found in the relevant chapters – 5 for *MV2c20* and 4 for *JetFitterCharm*.

[2]Clearly flavourless mesons such as bottomonium, Υ, decay more rapidly through strong and electromagnetic interactions.

3.4.6 Missing transverse momentum

The missing transverse momentum, $\vec{E}_{\mathrm{T}}^{\mathrm{miss}}$, is the negative two-vector sum of the calibrated $\vec{p}_{\mathrm{T}}$ of reconstructed objects, with magnitude $E_{\mathrm{T}}^{\mathrm{miss}}$ – this notation is hereafter used to describe both the scalar and vector quantities. The objects considered are jets with $p_{\mathrm{T}} > 20\,\mathrm{GeV}$ and electrons, muons and photons with $p_{\mathrm{T}} > 10\,\mathrm{GeV}$ (within the η acceptances described above). To reduce the effect of pileup, jets do not contribute to the calculation when they are disregarded as described above. Additionally, there is a final 'soft' term included, which differed between Run-1 and Run-2. In Run-1, this comprised all jets with $p_{\mathrm{T}} < 20\,\mathrm{GeV}$ and all unmatched calorimeter clusters (calibrated as described above) [78], and was particularly sensitive to pileup. In Run-2, the soft term was instead constructed from ID tracks associated to the PV but not any of the reconstructed objects in the calculation [79], and as a result was far less dependent on pileup. Some implications of this change, and details of the $E_{\mathrm{T}}^{\mathrm{miss}}$ calculation more generally, will be discussed in chapter 5.

3.5 Event Cleaning

Various event-by-event criteria are imposed in order to mitigate the effect of stochastic detector and environmental effects such as noise bursts and stray beam particles. The latter broadly consist of 'cosmic' events, where high energy particles (predominantly muons) created in the upper atmosphere reach ATLAS and are coincident (within detector timing) with a beam crossing, and 'beam induced backgrounds', where stray beam particles traverse regions of the detector. The cuts to reject these backgrounds are mostly common between the two analyses discussed in this thesis, and are summarised, along with data quality cuts applied at the analysis level, in table 3.3.

Vertex Selection Events with ≤ 4 tracks (2012) or ≤ 2 tracks (2015) associated to the primary vertex are rejected, in order to reduce the effect of pileup through incorrect identification of the PV.

Bad muons Fake muons can be reconstructed from high hit multiplicities in the muon spectrometer due to very energetic 'punch-through' jets, or from badly measured inner detector tracks in jets wrongly matched to muon spectrometer segments. Such fake muons are a potential source of fake $E_{\mathrm{T}}^{\mathrm{miss}}$. Events containing such bad muons are rejected by vetoing any events satisfying $\frac{\sigma(q/p)}{|q/p|} > 0.2$, in which q/p is the fraction of track charge to track momentum. In 2012, events where a muon was consistent with a cosmic ray, based on transverse and longitudinal impact parameters ($|z_\mu - z_{\mathrm{PV}}| < 1$ mm, $d_0 < 0.2$ mm), were also rejected. This requirement was not applied in 2015 since other selections were found to sufficiently reject events with cosmic muons.

Jet Cleaning Fake jets can arise from non-collision backgrounds, cosmic muons with large energy deposition in the calorimeters or fake signals in the calorimeter arising either from noise bursts or the presence of coherent noise [80].

Such jets can be identified through the timing of the calorimeter signal with respect to that of the bunch crossing. Events are required to have an energy-weighted jet timing, calculated using the measured energy of the leading two jets after overlap removal, $|\langle t \rangle|$ smaller than 5 ns in order to reject out-of-time pileup (from slow response of LAr cells, for instance).

Additionally, at least 2% of a jet's p_{T} must be attributable to its ID tracks if it falls within $|\eta| < 2$, or 5% if its electromagnetic fraction is above 9%. This cut is very effective at rejecting cosmic muons, beam background or detector noise where no track is expected and only accidental overlap of tracks from a pileup vertex can contribute.

Other criteria such as the quality of the fit of the calorimeter pulse shapes and the fraction of jet energy belonging to specific calorimeter regions are also applied. Events are then rejected if any of the jets with $p_{\mathrm{T}} > 20$ GeV (after removing overlapping objects) meet any of these criteria.

Hot tile cells In some periods of 2012 data taking, there was a hot TileCal cell that had not been masked in the reconstruction. This was mitigated by removing events where a jet pointed to the (η,ϕ) region close to that TileCal module ($\eta = -0.15$, $\phi = 2.7$), if this jet had its largest energy fraction in the second TileCal layer and this fraction was large ($E_{\text{layer}}/E_{\text{jet}} > 0.6$).

Dead Tile cells A non-negligible fraction (1-3%) of TileCal modules were non-operational during data taking, mostly due to low voltage power supply problems. This caused gaps in acceptance in particular layers, of size $\Delta\eta \times \Delta\phi \sim 1.0 \times 0.1$, resulting in jet mismeasurement and fake $E_{\text{T}}^{\text{miss}}$.

In 2012, MC-based methods were used to predict the energy expected from these dead Tile cells. The fraction of a jet's energy arising from this correction was known as BCH_{jet}^{corr}, and events overly affected by dead Tile cells were rejected by vetoing events with any jet satisfying p_{T} >40 GeV, $BCH_{jet}^{corr} > 0.05$ and $\Delta\phi(j, E_{\text{T}}^{\text{miss}}) < 0.3$. In 2015 this was not repeated, and so an analysis-specific rejection was developed as described in section 5.4.4.

LAr and Tile cleaning Events affected by LAr noise bursts and data corruption in either the LAr or TileCal are flagged and rejected. In 2012, events where a trip in the Tile high voltage power supply occurred are also rejected, as are events in 2015 with data corruption in the SCT.

Incomplete events In 2012, events that were not completely written to the buffer due to a TTC problem were removed. This problem was resolved for 2015 data taking.

3.6 Detector simulation

An important part of the understanding of the ATLAS detector is being able to accurately simulate its response. Event generation programs as described in section 2.3.2 create sets

Name	Description
Data quality GRL	Events must be in time periods included in the final 2012 (2015) good runs list
Good primary vertex	At least 4 (2) tracks pointing to primary vertex
Bad muons	No pre-selected muons before overlap removal with $\sigma(q/p)/\lvert q/p\rvert > 0.2$
Bad jets	Veto events with bad jets with $p_T > 20$ GeV after jet-electron overlap removal
– Timing	Average timing of two leading jets within 5 ns of bunch crossing
– Jet charged fraction	Both two leading jets must, if within $\lvert\eta\rvert < 2$, have $\Sigma p_{\mathrm{T}}^{\mathrm{tracks}}/p_{\mathrm{T}}^{\mathrm{jet}} > 0.02$, or > 0.05 if the electromagnetic energy fraction of the jet is above 9%
Bad Tile Cells	Reject events most affected by not-operational TileCal drawers
LAr and Tile errors	Events with known errors in the LAr or Tile calorimeter are vetoed
TTC reset	Events that have not been completely written to the buffer due to a TTC (timing, trigger and control) problem are removed
Pile-up jets	Jets with $p_{\mathrm{T}} < 50$ GeV, $\lvert\eta\rvert < 2.4$ and $\lvert\mathrm{JVF}\rvert < 0.5$ ($JVT < 0.64$) are removed from the list of jets

Table 3.3: Summary of the event cleaning and data quality cuts. Where a selection has a bracketed and non-bracketed value, these apply to 2012 (2015) data.

of events consisting of lists of particle 4-momenta. In order to compare these 'truth level' predictions to real ATLAS data, the responses they elicit in the detector must be simulated and reconstruction of the simulated signals performed in the same way as for data.

The first stage of this process is the construction of a detailed model of the detector *geometry*, that is to say a reproduction of all the material in the various subsystems, supporting structures and services (power, cooling, etc). This is then exported to GEANT4 [81], which models the interactions between the particles provided by the event generators and the material of ATLAS. This results in a detailed map of particle 'hits' in the various subdetectors. These hits are then subject to digitisation – i.e. transformation into the expected signals recorded – through consideration of the spatial and timing resolutions of the various detector components, including any known malfunctioning parts, and limitations of the detector read-out system (a more detailed description may be found in [82].) At this stage, multiple QCD events are overlaid to emulate the effect of pileup, according to a predetermined distribution intended to match that in data. The end result is a data format identical to that of recorded data, which is run through the same reconstruction.

This procedure results in a good overall simulation of collision events in ATLAS. Residual discrepancies are corrected for object-by-object, with efficiency corrections derived for e.g. lepton identification and jet flavour tagging algorithms. The cost of this accurate simulation is that it is of high complexity, and hence can be very time consuming. Thus parameterisations have been developed for the slowest stages of the simulation, tracking in the ID and interactions with the calorimeters [83]. These significantly increase the speed of simulation with only mild impacts on its fidelity, and so are used for the simulation of the signal samples used in later sections, for which tail effects, most strongly impacted by the fast simulation, are less important.

Chapter 4

Search for the scalar partner of the charm quark

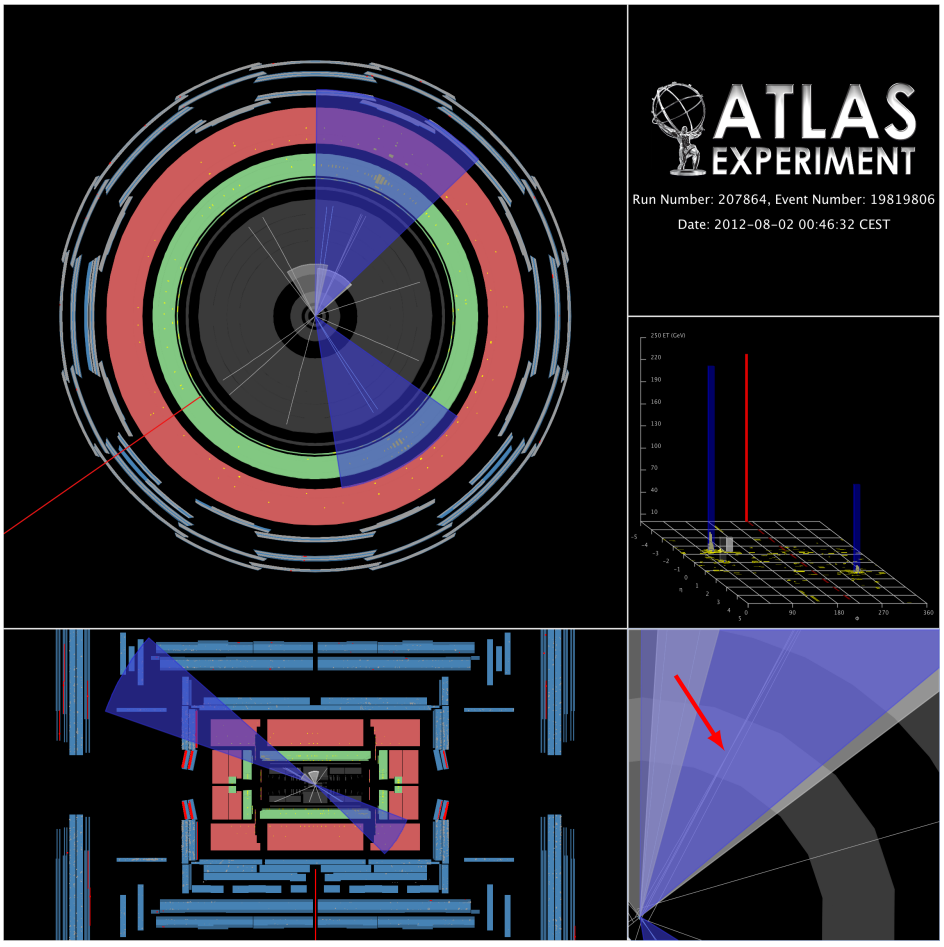


Figure 4.1: Event display of a signal candidate in the scharm analysis [4], featuring 2 charm-tagged jets (in blue) and high $E_{\mathrm{T}}^{\mathrm{miss}}$ (red line). The lower right inset shows a displaced vertex (tracks converging at the point marked by an arrow) inside one of the charm-tagged jets.

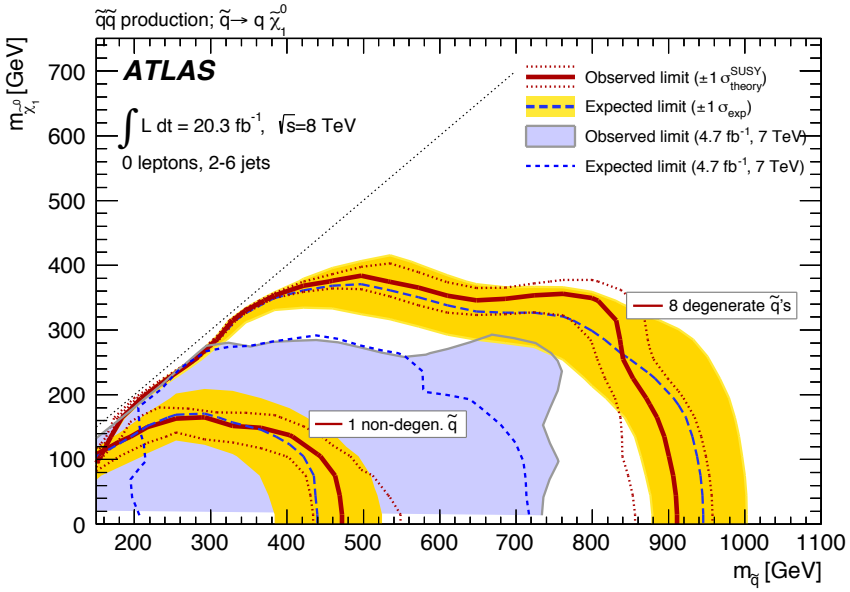


Figure 4.2: Exclusion limits for light squarks with decoupled gluinos from the inclusive zero-lepton 2-6 jets search [84], showing both the eight-fold degenerate case and that for a single light squark. Modified from [84].

4.1 Motivation and Sensitivity

Searches for the scalar partners of light quarks – i.e. $\tilde{u}$, $\tilde{d}$, $\tilde{s}$, $\tilde{c}$ – generally assume that they are *degenerate*, i.e. have the same mass. In the case that only one light squark exists these limits are substantially weakened, especially if only one of the left- and right-handed partners[1] is kinematically accessible. This can be seen in figure 4.2, where limits for a generic squark search are rendered far weaker when the eight-fold degeneracy is broken.

The $\tilde{t}$ and $\tilde{b}$ squarks are generally not considered to be mass-degenerate with the others, for two reasons. First, naturalness arguments are often used to motivate light third-generation squarks (see section 2.4); but more pragmatically it is feasible to look for $\tilde{t}$ and $\tilde{b}$ squarks in isolation since they lead to final states with b-jets and hence are more easily identifiable than final states with solely light-quark jets. With the Run-1 dataset, single $\tilde{b}$ were excluded up to ~ 650 GeV [85]. If a similar procedure can be followed with a $\tilde{c}$ search, then limits should be improved over the inclusive search case. The sbottom search is in fact sensitive to some degree to scharm production, since the b-tagging algorithm used has

[1] While the partners of squarks are bosons and hence do not have a handedness, each fermion has a left- and right-handed state, and these states each have a bosonic superpartner. Thus a 'left-handed squark' is more correctly the partner of a left-handed quark.

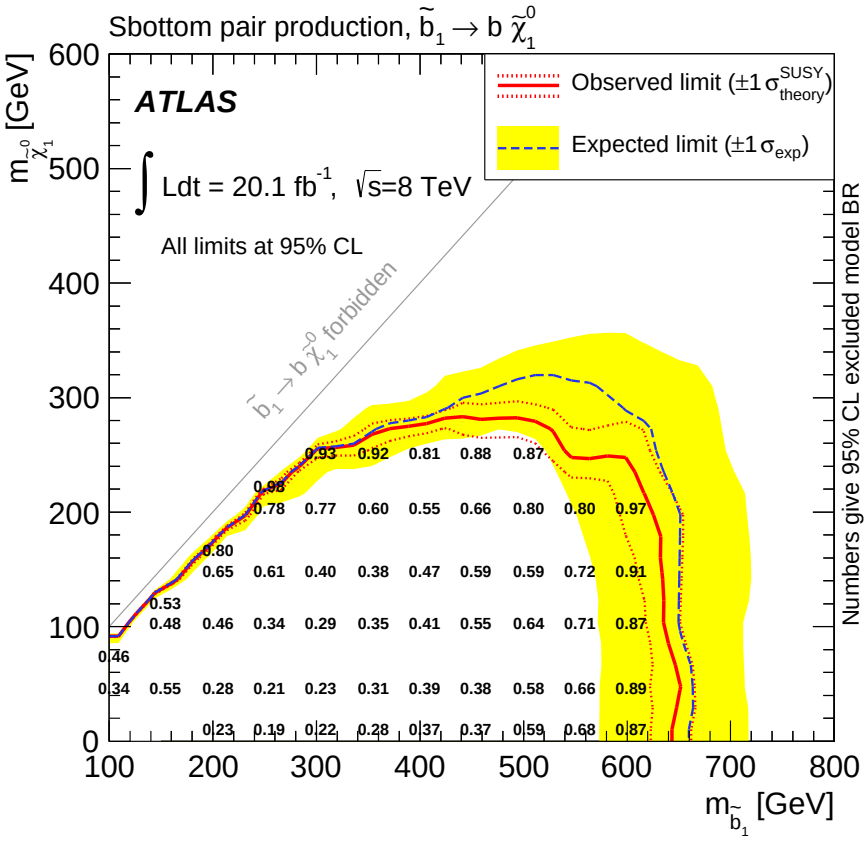


Figure 4.3: Exclusion limits from [85] for $\tilde{b}$ squarks, showing the minimum branching fraction $\tilde{b} \rightarrow b\tilde{\chi}_1^0$ excluded at each point.

a charm rejection factor of 8, meaning that 1 in 8 c-jets are incorrectly identified as b-jets. Hence the observed yield from $\tilde{c}$ production is identical to that from $\tilde{b}$ production with a reduced branching ratio to visible final states (i.e. those that would fall in the relevant signal regions). This effective branching ratio is given simply by $\epsilon_c/\epsilon_b = 0.125/0.6 \sim 0.2$, where $\epsilon_{c,b}$ are the b-tagging efficiencies for true b- and c-jets respectively. Examining figure 4.3, which shows the minimum excluded branching fraction for each model point considered by the sbottom analysis, the sensitivity to $\tilde{c}$ is thus limited to a small island around 250 GeV at low $\tilde{\chi}_1^0$ mass – much less than the inclusive search above.

A $\tilde{c}$ search would, in contrast, make use of dedicated c-tagging with better b-jet rejection – with charm efficiencies of about twice that of the b-tagging algorithm. Such an algorithm, which will be discussed in more detail in section 4.3, became available mid-way through Run-1, improving c-jet selection efficiency and opening new prospects for searches. This was used in the 'stop-to-charm' search, which was designed to be sensitive to compressed regions of $\tilde{t}$-$\tilde{\chi}_1^0$

space where the $\tilde{t}$ may only be able to decay to $c\tilde{\chi}_1^0$ (i.e. $m(\tilde{t}) - m(\tilde{\chi}_1^0) < m(W) + m(b)$). This search was, therefore, optimised for small mass differences and required ISR, and so is only sensitive to $\tilde{c}$ production at low masses (at higher masses the reduced cross-sections, coupled with the requirement of ISR, makes the process unobservably rare). For $\Delta m(\tilde{c}, \tilde{\chi}_1^0) < 85$ GeV, this search excludes $\tilde{c}$ masses below ~ 250 GeV.

Hence a dedicated search, making use of the new charm tagging algorithm but focused on the high $\tilde{c}$ mass, low $\tilde{\chi}_1^0$ mass region, will be sensitive to previously unexplored models. While such models, with a light $\tilde{c}$ and heavy $\tilde{q}$, $\tilde{b}$ and $\tilde{t}$, seem unlikely, they are worth pursuing since $\tilde{t}$–$\tilde{c}$ mixing is fairly unconstrained by precision flavour measurements, meaning that $\tilde{t}$ limits can be evaded through its decaying to c-quarks even in the 'bulk' kinematic region. Additionally, this search serves as a rare direct probe of new physics in the second fermion generation regardless of its SUSY justification.

4.2 Monte Carlo Generation

In order to design a search distinguishing a scharm signal from SM backgrounds, the expected signatures of each must be determined. Both signal and background events are generated as described in section 2.3, with the specific details given below.

4.2.1 Signal generation

In order to isolate the process of interest, a *simplified model* is considered. No attempt is made to satisfy the various indirect constraints that would apply to a viable physical model, such as dark matter relic density, and all SUSY particles other than the directly relevant ones are assigned an arbitrarily large mass. This results in the signal model shown in figure 4.4, with pair production of scharms which each decay to a charm quark and a neutralino LSP. Only one handedness of scharm is considered, since mechanisms to split the degeneracy of the light flavour squarks are often dependent on this, and it results in more

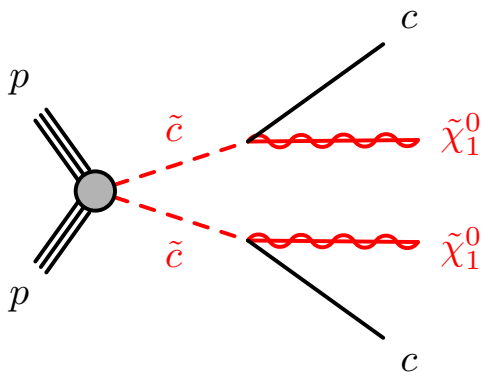


Figure 4.4: Feynman diagram for scharm pair production and decay to $c\tilde{\chi}_1^0$.

conservative estimates of sensitivity. The designation of the one light handedness as left or right is arbitrary, since it has no impact on the scharm decays or production cross-sections – a consequence of this being a simplified model. This gives the search signature of two high-p_{T} c-jets, large $E_{\mathrm{T}}^{\mathrm{miss}}$ from the non-interacting neutralinos and no leptons.

Owing to difficulties in calculating dedicated scharm production cross sections in the limit that all other squarks and gluinos are decoupled, cross-sections for sbottom production are used instead. Since the gluino is decoupled in both simplified models, there is very little t- and u-channel production from heavy flavour quarks in the proton, so production is dominated by the s-channel via a gluon and will be close-to-identical for $\tilde{c}$ and $\tilde{b}$. The cross-sections are calculated to next-to-leading order in the strong coupling constant α_{S}, adding the resummation of soft gluon emission at next-to-leading-logarithm accuracy (NLO+NLL) [86–88]. The uncertainty on each nominal cross section is defined by an envelope of predictions using different PDF sets and factorisation and renormalisation scales, as described in Ref. [89].

Signal points were generated across a sparse grid in the $\tilde{c}$ and $\tilde{\chi}_1^0$ mass plane, using `MadGraph`-5.1.5.11 [90] interfaced to `PYTHIA`-6.427 [38] for the parton shower, fragmentation, and hadronisation. Events were generated with a $E_{\mathrm{T}}^{\mathrm{miss}}$ filter at the particle level in order to increase the number of events in the signal regions while reducing the overall number required. This filter had a lower limit at 80 GeV for samples across the plane, while for points with $m(\tilde{c}) - m(\tilde{\chi}_1^0) \leq 200\,\mathrm{GeV}$, with low signal acceptances expected, three separate

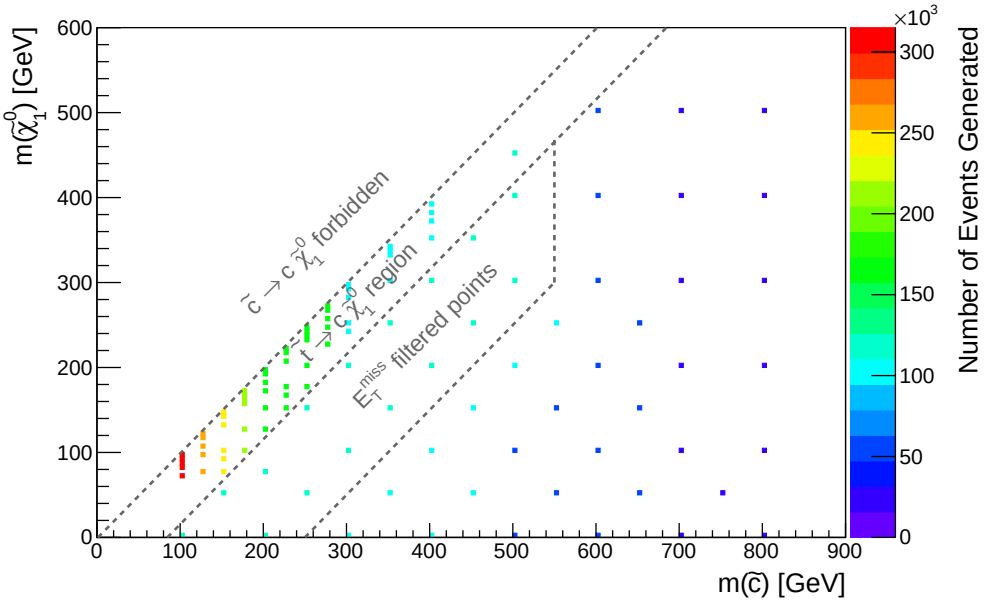


Figure 4.5: Number of events generated for each point in the $\tilde{c}$- $\tilde{\chi}_1^0$ mass plane. Those within the $\tilde{t} \to c\tilde{\chi}_1^0$ region were generated for the stop-to-charm analysis, and those marked "$E_{\mathrm{T}}^{\mathrm{miss}}$ filtered" have the three $E_{\mathrm{T}}^{\mathrm{miss}}$-filtered slices described in the text.

slices were generated with $80 < E_{\mathrm{T}}^{\mathrm{miss}} < 180$, $180 < E_{\mathrm{T}}^{\mathrm{miss}} < 300$ and $E_{\mathrm{T}}^{\mathrm{miss}} > 300$. Figure 4.5 shows the number of events generated at each point across this grid. The number of events per point was chosen as the minimum that would give at least 100 MC events in each SR – determined from scaling the sbottom acceptance and efficiency and cross-checking with some privately generated points on a dummy selection at truth level.

4.2.2 Background samples

The samples used for SM background processes are summarised in table 4.1. Top quark pair and single top production in the s and Wt channels are simulated with `Powheg-Box`-1.0 (r2092) [91] with the Perugia 2011C tune, while the t channel single top production is simulated using `AcerMC` 3.8 [92]. A top quark mass of 172.5 GeV is used, and the $t\bar{t}$ simulation is normalised to the cross-section calculated to next-to-next-to-leading order (NNLO) in perturbative QCD, including soft-gluon resummation to next-to-next-to-leading-log (NNLL) accuracy.

The parton shower, fragmentation, and hadronisation are performed with `PYTHIA`-6.426 [38].

Samples of W+jets, Z+jets, and dibosons (WW, WZ, ZZ) with light and heavy flavour jets are generated with SHERPA 1.4 [93], with up to 4 additional partons (3 for diboson) in the matrix element plus parton shower, assuming massive b/c quarks. The W+jets and Z+jets events are normalised to NNLO cross-sections [94]. Samples of $Zt\bar{t}$ and $Wt\bar{t}$ are generated with MadGraph-5.1.3.33 [90] interfaced to PYTHIA-6.426, with up to two extra partons in the matrix element.

Background process	Generator	Comments
$t\bar{t}$	Powheg-Box + PYTHIA 6	Lepton filtered
Single Top	AcerMC + PYTHIA 6	t-channel
	Powheg-Box + PYTHIA 6	s- and Wt-channels
$t\bar{t}+W/Z$	MadGraph + PYTHIA 6	$0, 1, \geq 2$ extra partons
W+jets	SHERPA 1.4	Massive b- and c-quarks, filtered by W p_{T} and parton flavour
Z+jets	SHERPA 1.4	Massive b- and c-quarks, filtered by Z p_{T} and parton flavour
diboson	SHERPA 1.4	Massive b- and c-quarks

Table 4.1: Summary of background MC used.

4.3 Charm Tagging

An integral part of this search is the charm tagging, which is done using the *JetFitterCharm* algorithm [5]. This algorithm, developed by a collaborator, uses IP and SV information together with a 'flight line' that attempts to reconstruct the primary - b - c decay chain from single- and multi-track vertices. Each of these distinct algorithms has several useful outputs, giving a total of 19 inputs to the two-hidden-layer neural network.

The outputs of this neural network are the three probabilities P_c, P_b and P_{light}, summing to 1, that denote the probabilities of a given jet resulting from a c-quark, b-quark or light-quark or gluon respectively. These are combined into two discriminants, the 'anti-b'

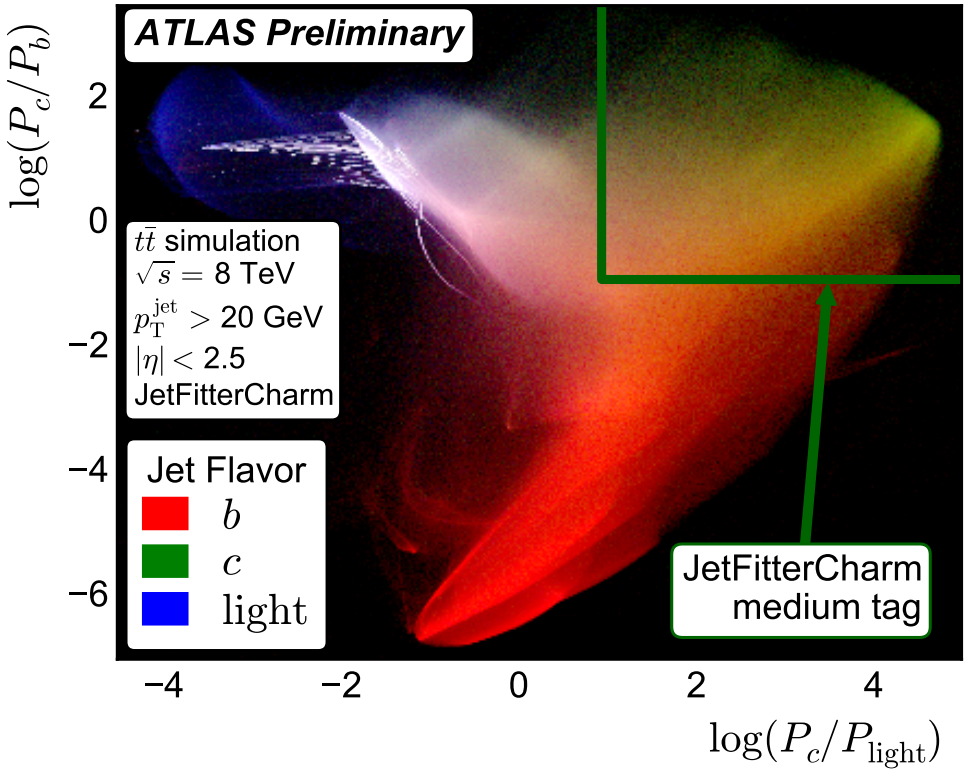


Figure 4.6: Two-dimensional distribution of the JetFitterCharm anti-b ($\log(P_c/P_b)$) and anti-light ($\log(P_c/P_{\mathrm{light}})$) discriminants in $t\bar{t}$ simulation. The density of red, green, and blue reflect the density of b, c, and light jets, and the 'medium' operating point used in this analysis is marked. The complex structures result from the use of discretised p_{T} and η inputs and the substitution of default values when an input is not physically meaningful, e.g. when no secondary vertex is found. Plot taken from [5].

$\log(P_c/P_b)$ and the 'anti-light' $\log(P_c/P_{\mathrm{light}})$, the distributions of which in $t\bar{t}$ simulation are shown in figure 4.6.

The expected performance of the operating point used in this analysis – originally designed and calibrated for the stop-to-charm analysis – is shown in figure 4.7, with a c-tagging efficiency of around 20% and a b-jet mistag rate of around 13%. The c-tagging efficiency is quite strongly dependent on the jet p_{T}, a reflection of the balancing act performed to distinguish c-like jets from in between b-like and light-like ones. The actual performance is determined for b-jets from measurements of dileptonic $t\bar{t}$ events [95] and for c-jets from events containing D^* mesons [96]. It is shown in figure 4.8, where it can be seen that the observed c-tagging efficiency drops to a peak of about 17% while the b-jet mistag rate remains mostly unchanged at around 13% in the p_{T} range of interest (100 - 200 GeV). The impact of the

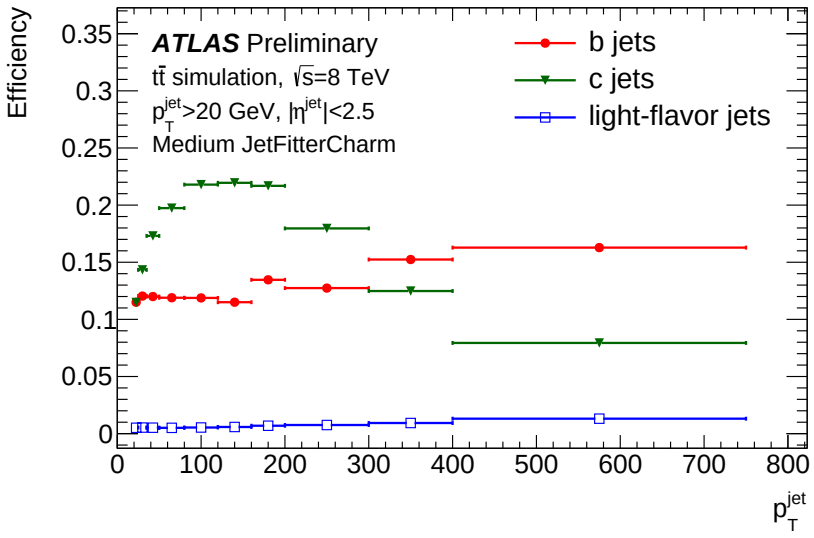
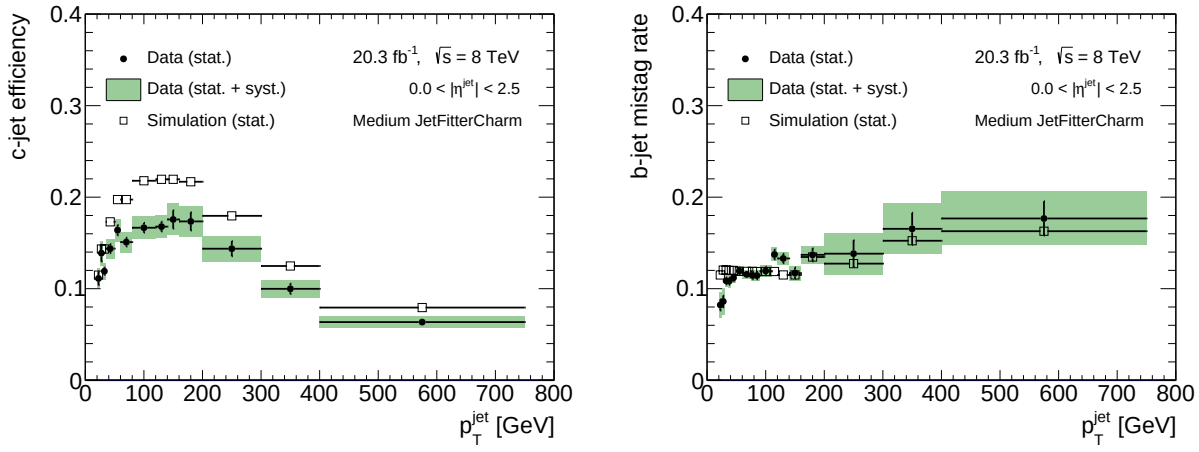


Figure 4.7: Uncalibrated (from $t\bar{t}$ MC only) c-tagging efficiency and b- and light-jet mistagging rates, taken from [5].

fairly large uncertainties on these calibrations will be discussed in section 4.6.1.

4.4 Strategy and Optimisation

The signal of interest for this search, having a final state of two charm quarks and two neutralinos, is identical to that of the sbottom search with the b-quarks exchanged for c-quarks. Thus the starting point for this search is to reproduce the sbottom selection and exchange b-tagging for the c-tagging described above. There are however three important differences between the searches. First, there is no need for a signal region targeting compressed $\tilde{c}$-$\tilde{\chi}_1^0$, since the stop-to-charm analysis is sensitive there. Second, the c-tagging efficiency of about 17% here compares to a b-tagging efficiency of about 60% in the sbottom search. This is compounded in the case that both jets are tagged, with a relative efficiency difference of $(17/60)^2 \sim 0.1$, meaning that some analysis features need to be revisited. Finally, the selection of c-rich events over b-rich ones has a marked impact on the background composition, particularly on $t\bar{t}$, with ramifications for the various rejection cuts and control regions.



(a) c-jet efficiency (b) b-jet mistag rate

Figure 4.8: Calibrated c-tagging efficiency and b-jet mistagging rate, calculated from the same information used to make figures in [5]. Error bars are indicative only, and in some cases underestimates, since some bins have been split without changing the absolute error. The calibration results in a lower c-tagging efficiency than expected.

4.4.1 Baseline selection

Despite these differences, there are various aspects of the sbottom search that were left untouched or only slightly modified. Data is selected with an $E_{\mathrm{T}}^{\mathrm{miss}}$ trigger as for the sbottom analysis, but using a different version with tighter online requirements which maintained full responsiveness[2] throughout the 2012 data-taking period while still being fully efficient at the cut value of 150 GeV. Event cleaning is performed as described in section 3.5.

This search is, like the sbottom one, a zero-lepton search, and so if any baseline lepton (see sections 3.4.2 and 3.4.3) survives overlap removal then the event is vetoed; with the p_{T} and $|\eta|$ thresholds of > 7 (6) GeV and < 2.47 (2.4) for electrons (muons) being retained. Also retained are the QCD rejection cuts, which target QCD multijet events where significant $E_{\mathrm{T}}^{\mathrm{miss}}$ is generated through jet mismeasurement. This is achieved through first rejecting events where the azimuthal angle between the $\vec{E}_{\mathrm{T}}^{\mathrm{miss}}$ and any of the three leading jets, $\Delta\phi_{\mathrm{min}}(3\text{ jets}, \vec{E}_{\mathrm{T}}^{\mathrm{miss}})$, is less than 0.4, since $E_{\mathrm{T}}^{\mathrm{miss}}$ resulting from jet mismeasurement should lie along the axis of the mismeasured jet. Additionally, since the $E_{\mathrm{T}}^{\mathrm{miss}}$ in such events originates from 'missed' hadronic energy, rather than real momentum from invisible parti-

[2]The trigger used for the sbottom analysis dropped the first three bunch crossings in a train.

Quantity	Requirement
Trigger	$E_{\mathrm{T}}^{\mathrm{miss}}$ trigger $> 99\%$ efficient for $E_{\mathrm{T}}^{\mathrm{miss}} > 150$ GeV
Event cleaning	As described above
Lepton veto	No e/μ after overlap removal with $p_{\mathrm{T}} > 7(6)$ GeV for $e(\mu)$.
$\Delta\phi_{\mathrm{min}}(\mathbf{E}_{\mathrm{T}}^{\mathrm{miss}}, 3 \text{ jets})$	> 0.4
$E_{\mathrm{T}}^{\mathrm{miss}}/(p_{\mathrm{T}}^{j_1} + p_{\mathrm{T}}^{j_2})$	$> 1/3$
$E_{\mathrm{T}}^{\mathrm{miss}}$	> 150 GeV
Leading jet $p_{\mathrm{T}}(j_1)$	> 130 GeV, $\lvert\eta\rvert < 2.8$
Second jet $p_{\mathrm{T}}(j_2)$	> 50 GeV, $\lvert\eta\rvert < 2.8$
Third jet $p_{\mathrm{T}}(j_3)$	veto if > 50 GeV, $\lvert\eta\rvert < 2.8$
b-jet multiplicity	leading 2 jets ($p_{\mathrm{T}} > 50$ GeV, $\lvert\eta\rvert < 2.5$)
m_{CT}	$> 150, 200, 250, 300, 350$ GeV
m_{bb}	> 200 GeV

Table 4.2: Summary of the event selection in the signal regions of the sbottom analysis. Cuts in the bottom part are considered in this section.

cles, the ratio of $E_{\mathrm{T}}^{\mathrm{miss}}$ to the scalar sum of the two leading jets' p_{T} is required to be above one-third[3].

4.4.2 Optimised selections

Following the event cleaning, lepton veto and event selection described above, the sbottom analysis imposed $E_{\mathrm{T}}^{\mathrm{miss}}$ criteria in accordance with the trigger and p_{T} and b-tagging selections on all jets. The main selection was then performed by the variables m_{bb}, the mass of the two leading (and b-tagged) jets, and the *contransverse mass* m_{CT} to select high mass signals and suppress $t\bar{t}$. Each of these signal region (SR) selections, shown in table 4.2, was re-evaluated for the scharm analysis.

[3]This is alternatively formulated in terms of the *effective mass* $\mathrm{m_{eff}}$, given by the scalar sum of the $E_{\mathrm{T}}^{\mathrm{miss}}$ and jets' p_{T} (in this case, the two leading jets), as $E_{\mathrm{T}}^{\mathrm{miss}}/\ \mathrm{m_{eff}} > 0.25$.

As the aim of this optimisation procedure was to find the signal region selections that provided exclusion limits covering the largest area in the $\tilde{c} - \tilde{\chi}_1^0$ plane, without regard to the exact location of the boundaries of this exclusion, a simplified procedure was considered sufficient. This used a figure of merit approximating the significance of a signal yield S over a background expectation B, $\frac{S}{\sqrt{S+B+(\Delta B)^2}}$, encompassing the impact of low signal yields through the inclusion of S in $\sqrt{S+B}$ and systematic uncertainties through the additional $(\Delta B)^2$ term. A signal point was considered excluded at 95% confidence level if this significance measure exceeded 1.64. The uncertainty ΔB was taken as a systematic uncertainty added in quadrature to the Monte Carlo statistical uncertainty. To avoid a full and costly calculation of the systematic uncertainty for each possible selection, while avoiding some pitfalls of assuming a uniform uncertainty, separate values were used for each m_{CT} region. Since the overall systematic uncertainty was observed to rise $\sim$ linearly with m_{CT} in the sbottom analysis, an approximation for this search was obtained by fitting this uncertainty as a function of m_{CT}. The fitted uncertainty is given by:

$$\frac{\Delta B}{B} = 0.05\% \cdot m_{\mathrm{CT}}[\mathrm{GeV}] + 5.5\%. \tag{4.1}$$

$E_{\mathrm{T}}^{\mathrm{miss}}$

In order to remain on the trigger plateau, there must be an offline $E_{\mathrm{T}}^{\mathrm{miss}}$ cut at 150 GeV. Tighter cuts are considered in figure 4.9, but any small gain in scharm mass reach is offset by a reduction in neutralino mass reach, and higher cut values would also reduce control region statistics and increase uncertainties, so the cut is left at 150 GeV.

Jet p_{T}

Scans of the two leading jets' p_{T} are shown in figure 4.10, from which it was decided to keep the leading jet p_{T} cut at 130 GeV and to raise the second leading jet cut to 100 GeV from 50 GeV to exploit a moderate increase in sensitivity at large neutralino masses.

The sbottom analysis vetoes events containing a third jet with $p_{\mathrm{T}} > 50$ GeV, in order to

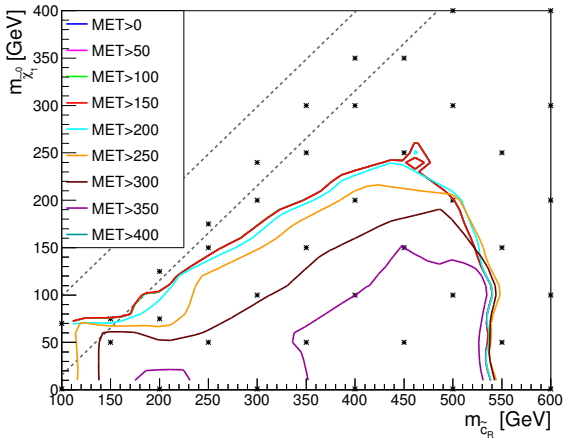


Figure 4.9: Exclusion limits in the $\tilde{c} - \tilde{\chi}_1^0$ mass plane, obtained by varying the requirement on $E_{\mathrm{T}}^{\mathrm{miss}}$, with all other cuts applied.

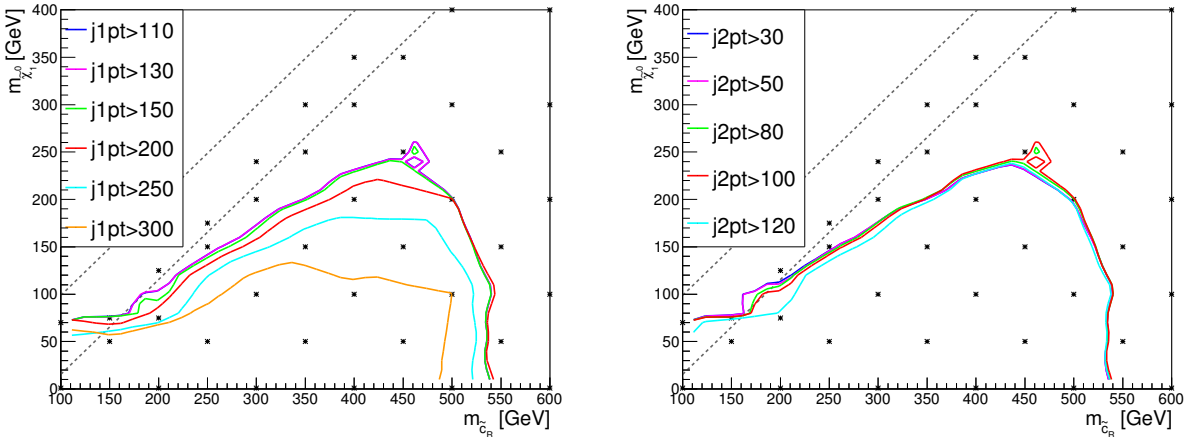


Figure 4.10: Exclusion limits in the $\tilde{c} - \tilde{\chi}_1^0$ mass plane, obtained by varying the requirements on the p_{T} of the leading two jets (left: leading jets p_{T}; right: sub-leading jet p_{T}), with all other SR cuts applied. The optimal value for the leading jet p_{T} requirement found in the sbottom analysis of 130 GeV is optimal in the current analysis as well. The second leading jet p_{T} requirement is found to be optimal at 100 GeV, which marginally increases the neutralino mass reach without affecting the scharm mass reach.

suppress $t\bar{t}$. As $t\bar{t}$ is a less important background for this analysis, due to the requirement of c-jets rather than b-jets, the removal of this veto is beneficial since it increases signal statistics for high scharm mass points, as can be seen in figure 4.11. Having allowed this third jet a b-veto was considered for it to reject additional $t\bar{t}$, but this was also found to be detrimental to the expected exclusion.

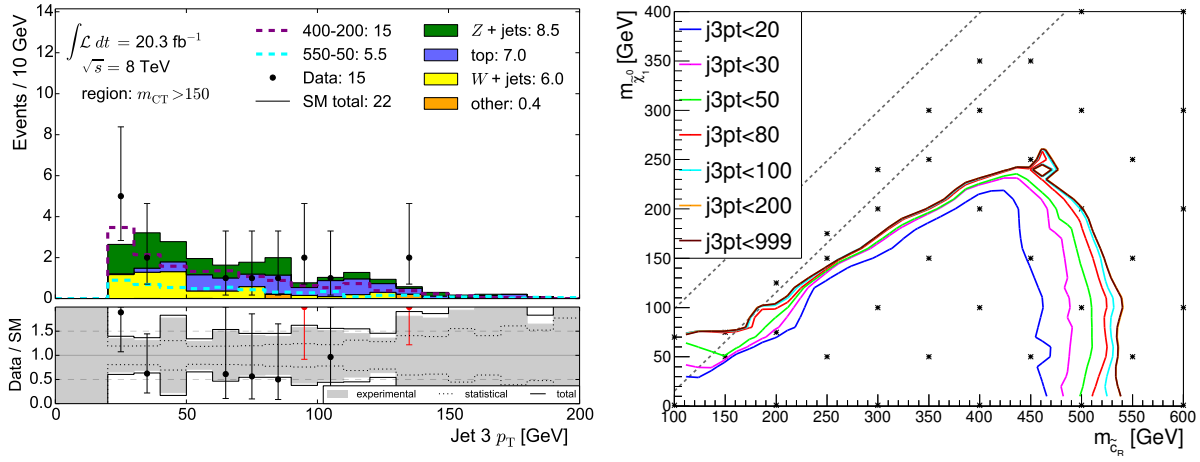


Figure 4.11: Left: Plot made by collaborator, showing the third jet p_T distribution in SR150. The dashed lines show distributions for signal models with $m_{\tilde{c}} = 400$ GeV, $m_{\tilde{\chi}_1^0} = 200$ GeV (purple line) and $m_{\tilde{c}} = 550$ GeV, $m_{\tilde{\chi}_1^0} = 50$ GeV (cyan line). Right: Expected exclusion limits in the $\tilde{c} - \tilde{\chi}_1^0$ mass plane for various third jet p_T veto levels, with all other SR cuts applied – an event is vetoed if it has a third jet above this p_T. The scharm mass reach is fairly significantly improved by raising this arbitrarily high, i.e. removing the veto.

m_{CT} vs m_{T2}

The 'stransverse' mass, m_{T2} [97–99], is a kinematic variable similar to m_{CT} (section 4.4.3) that may provide better signal – background separation. It is given by:

$$m_{T2}(\mathbf{p}_T^1, \mathbf{p}_T^2, \mathbf{q}_T, m_\chi) = \min\{\max[m_T(\mathbf{p}_T^1, \mathbf{q}_T^1, m_\chi), m_T(\mathbf{p}_T^2, \mathbf{q}_T^2, m_\chi)]\} \tag{4.2}$$

where $\mathbf{p}_T^j$ is the $\mathbf{p}_T$ of the j^{th} jet and $\mathbf{q}_T$ is the missing transverse momentum decomposed into $\mathbf{q}_T = \mathbf{q}_T^1 + \mathbf{q}_T^2$. This attempts to assign each invisible LSP (of mass m_χ, here set to zero) a transverse momentum $\mathbf{q}_T^i$, and the minimisation is performed over all possible decompositions. The transverse mass m_T is given in terms of the transverse energy, $E_T = \sqrt{\mathbf{p}_T^2 - m^2}$, by $m_T(\mathbf{p}_T^a, \mathbf{p}_T^b) = m_a^2 + m_b^2 + 2(E_T^a E_T^b - \mathbf{p}_T^a \cdot \mathbf{p}_T^b)$

As can be seen in figure 4.12, m_{CT} and m_{T2} are highly correlated for the main backgrounds – in fact the two are analytically identical for massless c and $\tilde{\chi}_1^0$ with no transverse ISR [100]. When scanning over a variety of m_{CT} and m_{T2} cut values, the combination of the best m_{CT} selections gave a significantly better expected exclusion limit at high $\tilde{c}$ masses.

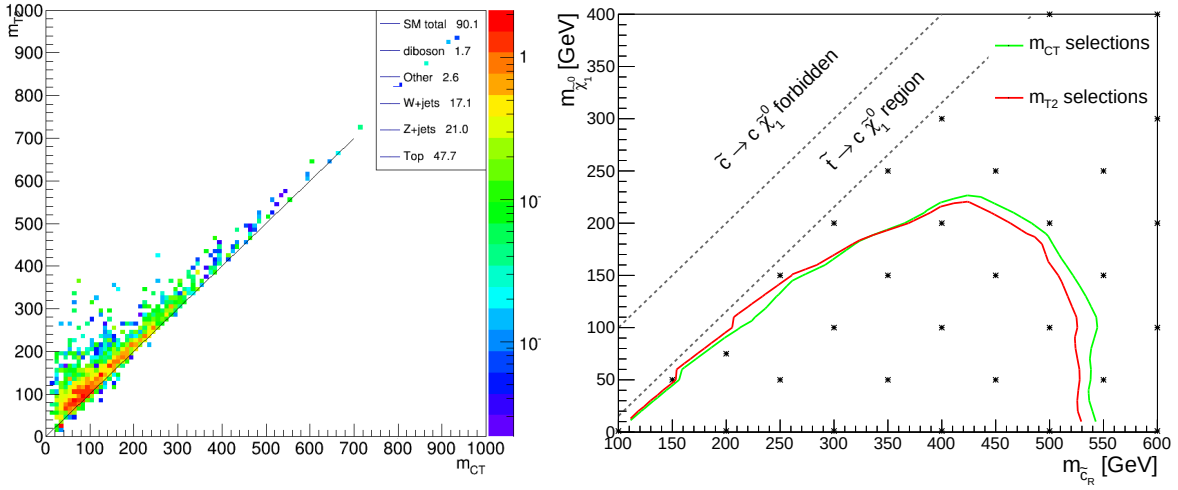


Figure 4.12: Left: plot showing the high degree of correlation between m_{CT} and m_{T2}, as expected, with all SR cuts apart from m_{CT} applied. The line $m_{\mathrm{CT}} = m_{\mathrm{T2}}$ is overlaid. Right: Exclusion contours obtained from the best m_{CT} and m_{T2} selections for each point. m_{CT} outperforms m_{T2} at high $\tilde{c}$ mass.

4.4.3 Charm Tagging

Given that charm tagging is the major new component of this analysis over the sbottom one, it would have been desirable to optimise this important feature. However, due to difficulties with calibration and the timescales involved (various analyses performed by collaborators with many other critical tasks), the only options available were pre-existing operating points used in the stop-to-charm analysis. *JetFitterCharm* provides anti-b and anti-light selections, which can either be used in isolation or both together for a c-tag. Since the detailed tracking of the inner detector extends only to $|\eta| = 2.5$, jets can only be tagged within this range, and so if the leading jet falls outside this it will fail any selection.

Figure 4.13 shows the effect of varying the jet tagging requirements for the leading two jets, with the conclusion that requiring two c-tags is the best available option. The relatively small difference between the two c-tag option and that requiring only two anti-light jets shows that the dominant gain comes from the light-jet rejection. This is further emphasised in figure 4.14, showing the truth-level flavours of the three leading jets in the signal regions. The leading two jets in signal are predominantly charm, while the third jet is usually of light flavour, and for the main backgrounds following charm tagging the two leading jets are a

reasonably even split between b, c and light flavour, suggesting that a reasonable balance between b and light rejection has been struck.

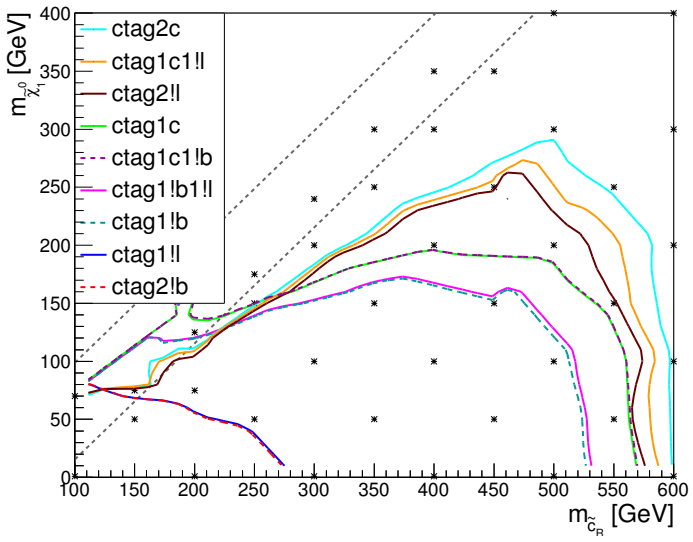


Figure 4.13: Estimated exclusion contours in the $\tilde{c} - \tilde{\chi}_1^0$ mass plane for different c-tagging configurations applied to the two leading jets, with all other SR cuts applied and the best m_{CT} region taken for each point. To denote the tagging requirements, $1c1!b$ indicates that one jet is required to be c-tagged and a further jet is required to pass the anti-b cut. The pale blue line, corresponding to requiring both leading jets to be c-tagged, provides significantly better exclusion compared to the second-best option (orange) of requiring one jet to be c-tagged and the other only to be anti-light. The purple contour, corresponding to one c-tag and one anti-b – i.e. the 'loose' *JetFitterCharm* cut used in the stop-to-charm analysis, is preferable in the compressed region where that analysis focuses.

m_{CT} and m_{cc}

The contransverse mass, m_{CT} [101], is a kinematic variable that can be used to measure the masses of pair-produced semi-invisibly decaying heavy particles. For two identical decays of heavy particles into two visible particles v_1 and v_2, and into invisible particles, the m_{CT} in the centre-of-mass frame, m'_{CT}, is defined as:

$$m'_{\mathrm{CT}}(v_1, v_2)^2 = \left[E'_{\mathrm{T}}(v_1) + E'_{\mathrm{T}}(v_2)\right]^2 - \left[\mathbf{p}'_{\mathrm{T}}(v_1) - \mathbf{p}'_{\mathrm{T}}(v_2)\right]^2 \tag{4.3}$$

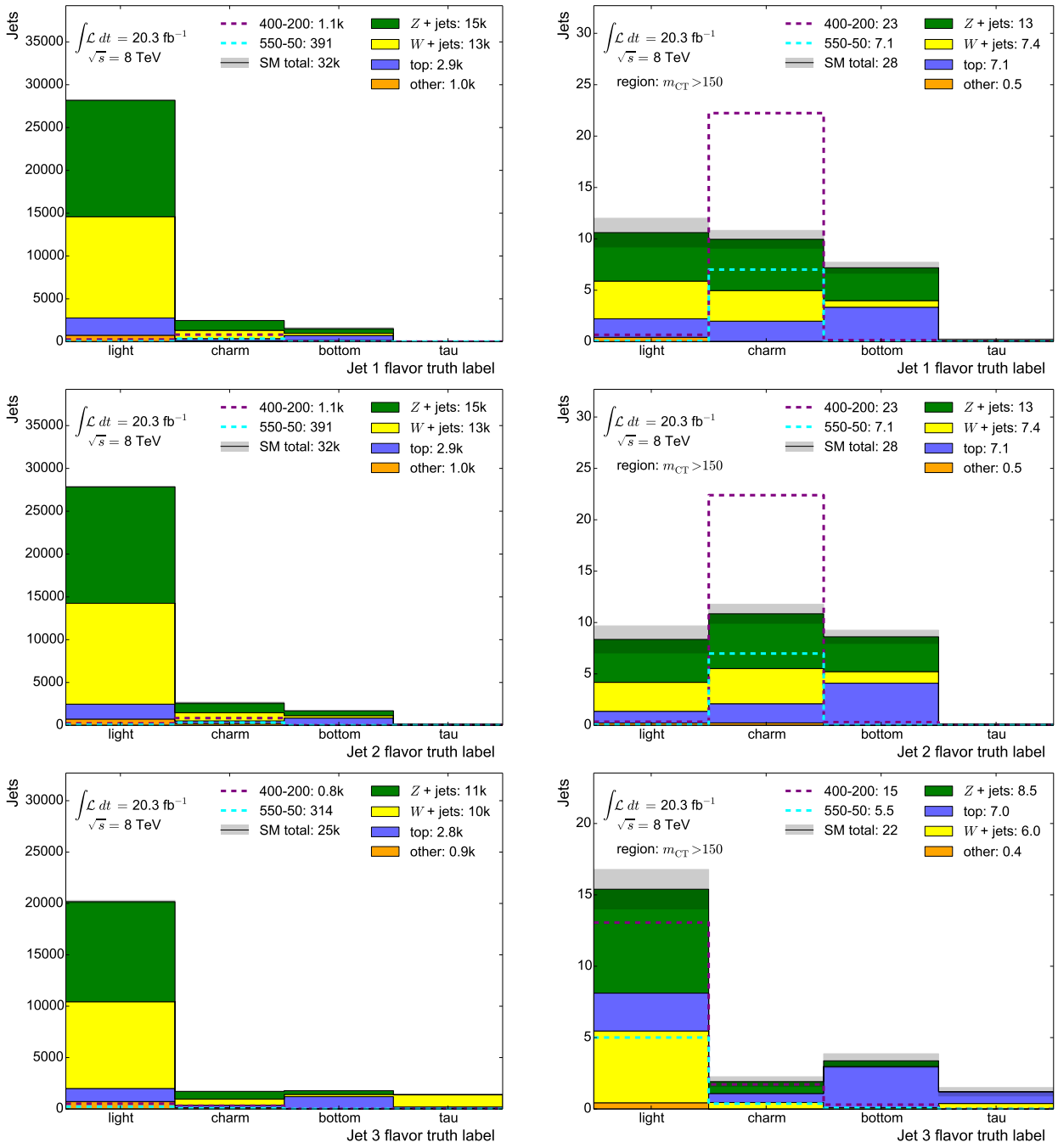


Figure 4.14: Plots made by collaborator showing truth flavours of the three leading jets, top to bottom. The left hand plots show the SR150 signal region without tagging applied, while the right hand plots show the region after tagging.

where $E_{\mathrm{T}} = \sqrt{\mathbf{p}_{\mathrm{T}}^2 + m^2}$ and all primed variables are in the centre-of-mass frame[4]. When the parent particles have no net transverse boost, allowing m'_{CT} to be calculated from laboratory frame four-momenta, it is bounded from above by an analytical combination of particle masses (eq. (4.4)). However when the parents are subject to a transverse boost, due to e.g. initial state radiation, the values of the visible particles' four-momenta in the centre-of-mass frame are not equal to those in the laboratory frame and the value of m'_{CT} calculated with laboratory frame four-momenta can exceed this endpoint. A boost correction [102], using the $E_{\mathrm{T}}^{\mathrm{miss}}$ to estimate the transverse boost, can be applied to m'_{CT} to generate the analysis variable m_{CT}. This is calculated only from laboratory-frame quantities, and always lies below m'_{CT} such that initial state radiation does not cause the kinematic bound to be violated. This bound is reached when the two visible objects are collinear, and for a parent p decaying to the visible daughter v and invisible daughter i is given by

$$m_{\mathrm{CT}}^{\mathrm{max}} = \frac{m(p)^2 + m(v)^2 - m(i)^2}{m(p)} \tag{4.4}$$

This limit evaluates to $\frac{m(t)^2+m(b)^2-m(W)^2}{m(t)} = 135$ GeV for $t\bar{t}$ when the b-jets are used to construct m_{CT}, and so a cut above this is a powerful discriminant.

However, once c-tagging has been applied, the prevalence of c-jets in the leading two jets of $t\bar{t}$ events is quite high, with bb and bc being roughly equally prevalent. When m_{CT} is constructed from a c-jet and a b-jet, the endpoint no longer necessarily applies, and so m_{CT} alone is not a good discriminant against $t\bar{t}$, as seen in figure 4.15. Events with the leading jets having truth flavour bb do indeed satisfy the expected m_{CT} endpoint, but the situation is more complicated for the bc. Here, there are two distinct populations, one at low m_{CT} and high m_{cc}, and one at high m_{CT} and low m_{cc}. This likely occurs because the c-jet can originate either from the same top quark as the leading b-jet, in which case m_{CT} is often large since $\mathbf{p}_{\mathrm{T}}(j_1)$ and $\mathbf{p}_{\mathrm{T}}(j_2)$ are similar (see eq. (4.3)). However, such events are constrained to have $m_{cc} < m_{\mathrm{top}}$, as shown in appendix A.1, explaining the population at high m_{CT} and low m_{cc}. If, on the other hand, the c-jet originates from the other top quark to the b-jet, it will

[4]Strictly speaking, m'_{CT} is invariant under longitudinal boosts, so the frame requires only that the parents have zero net transverse momentum.

have fairly similar kinematics to the b-jet on its side of the decay. Thus it will result in an m_{CT} value not dissimilar to that which would have been obtained from that b-jet, and so these events lead to a distribution similar to that seen in the bb plot, explaining the second population in bc.

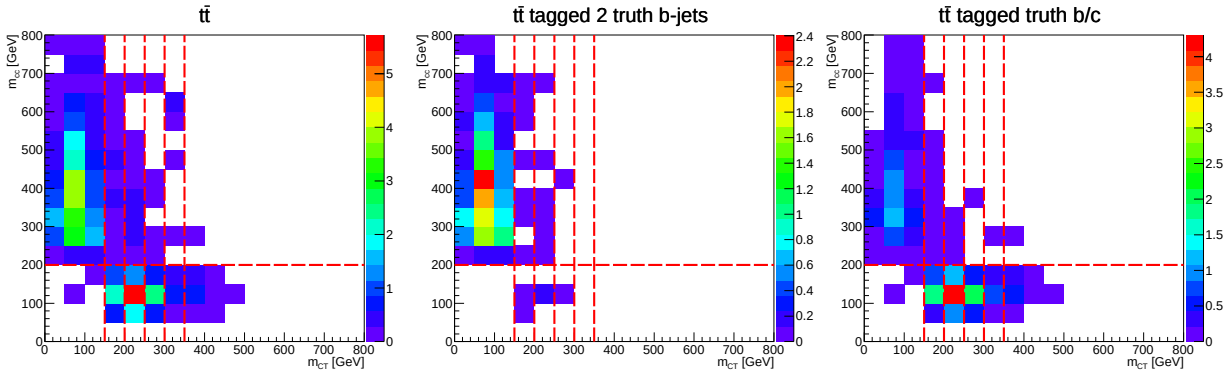


Figure 4.15: Plots, made by a collaborator, showing m_{CT} vs. m_{cc} in $t\bar{t}$ simulation. Left: inclusive in flavor; middle: leading jets bb (at truth level), right: leading jets bc or cb. The dotted red lines indicate the requirements on the m_{cc} and m_{CT}.

The same method as employed above was used to find the optimal m_{CT} and m_{cc} cuts. For m_{cc}, a cut value of 200 GeV is optimal – as might be expected, lying as it does slightly above the top quark mass. For m_{CT}, tighter cuts provide sensitivity to higher $\tilde{c}$ masses, until low cross-sections render tight cuts ineffective. With the lower tagging efficiency of c-jets compared to b-jets, this point is reached at about 250 GeV, although a cut at the bb $t\bar{t}$ threshold of 135 GeV performs worse than one at 150 GeV. Thus three signal regions are defined, with m_{CT} cuts at 150, 200 and 250 GeV.

4.4.4 Optimisation conclusions

After all these considerations, the selection giving the best expected sensitivity is shown in table 4.3. In order to refer to the different m_{CT} thresholds, the notation `SR150`, `SR200` and `SR250` is used. This final selection was checked by collaborators and found to be insensitive to pileup, with the only (small) dependence originating from the $E_{\mathrm{T}}^{\mathrm{miss}}$ trigger. This is shown in figure 4.17, where the dependence of $E_{\mathrm{T}}^{\mathrm{miss}}$ and c-tagging efficiencies on the number of reconstructed vertices is shown. The only observable meaningful deviation is for the $E_{\mathrm{T}}^{\mathrm{miss}}$

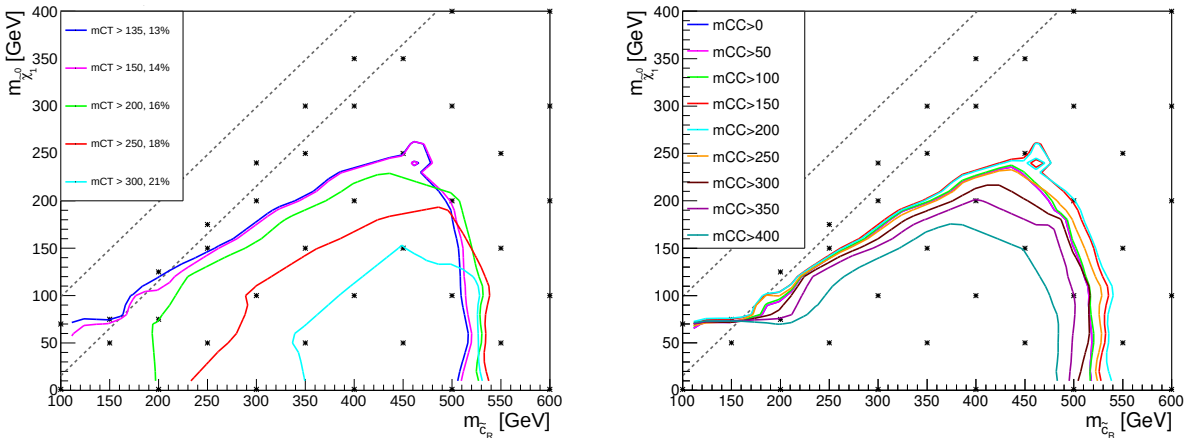


Figure 4.16: Exclusion limits in the $\tilde{c} - \tilde{\chi}_1^0$ mass plane, obtained by varying the m_{CT} (left) and m_{cc} (right) cuts, after all other SR cuts. The systematic uncertainties used for each m_{CT} cut, obtained as explained in eq. (4.1), are indicated in the legend.

selection in data events, which tend to have lower efficiencies at high and low numbers of vertices. This was partly attributed to differing noise thresholds in the $E_{\mathrm{T}}^{\mathrm{miss}}$ trigger in early runs, and was at most a 10% effect for the bulk of the N_{vertex} spectrum.

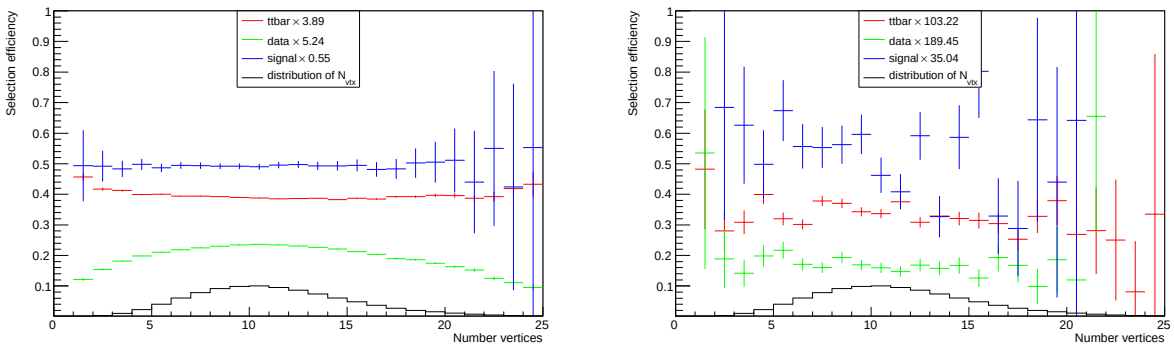


Figure 4.17: Selection efficiencies (scaled according to the legends) in data (green), $t\bar{t}$ MC (red) and signal MC ($m_{\tilde{c}} = 550$ GeV, $m_{\tilde{\chi}_1^0} = 50$ GeV, blue). Shown also is the distribution of number of vertices with at least 5 tracks in data events. Left: selection efficiency of the offline $E_{\mathrm{T}}^{\mathrm{miss}}$ requirement for events passing the $E_{\mathrm{T}}^{\mathrm{miss}}$ trigger and in the GRL. Right: selection efficiency of two c-tagged jets for events passing the offline $E_{\mathrm{T}}^{\mathrm{miss}}$ requirement, $E_{\mathrm{T}}^{\mathrm{miss}}$ trigger and in the GRL.

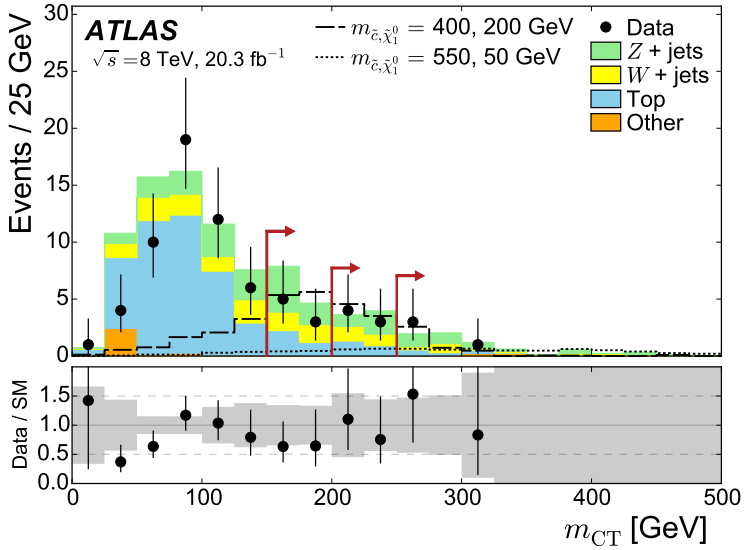


Figure 4.18: m_{CT} distribution in the signal regions, with all selections other than the m_{CT} cuts – marked by the red arrows – applied. Plot made by a collaborator, using MC predictions only for the backgrounds.

4.5 Background estimates

Following the definition of signal regions, the backgrounds to any signal present in these regions must be determined. As can be seen in figure 4.18, the dominant backgrounds are Z+jets, W+jets and 'top' – consisting mostly (60-70%) of $t\bar{t}$, with the single-top component dominated by Wt-channel production. Each of these backgrounds is determined with a semi-data-driven method, whereby their normalisations are determined in fits to control regions enhanced in each background, as described in section 4.5.1. The subdominant QCD background is determined from a separate data-driven method, based on inverting the QCD rejection cuts described above, outlined in section 4.5.2. Other small backgrounds are determined purely from their MC predictions.

4.5.1 Leptonic Control Regions

The MC predictions of the three main backgrounds are measured against data in *control regions* (CRs), where signal contamination is low, data yields are high enough to provide reasonable statistical precision and there are minimal kinematic differences between CR and

SR. These control regions all make use of selections with at least one lepton, in contrast to the zero-lepton signal, and data is collected with single-lepton triggers requiring an offline cut of $p_{\mathrm{T}} > 25$ GeV. The normalisations of the MC are then allowed to float in a combined fit to the data, which has the effect of allowing cancellation of systematic uncertainties between signal and control regions if they are similar in each. Since c-tagging is a dominant source of uncertainty, and the key feature of this analysis, all control regions have the same c-tagging criteria as the signal regions, i.e. the leading two jets must be c-tagged. This has the consequence of low data yields in the CRs thanks to low c-tagging efficiencies and low cross sections and branching ratios to final states with two c-jets, and so various cuts have to be relaxed or removed in order to obtain control regions with meaningful statistical power. For example, requiring a lepton greatly reduces the prevalence of QCD multijet events, so the QCD rejection cuts are not applied.

The chosen CRs are shown in table 4.3 and explained below. In order to ensure this procedure results in a reasonable background estimate, and to obtain a maximum cancellation of systematic uncertainties, the flavour composition of each background in its control regions should be as similar as possible to that in the signal regions. The flavour composition of the $m_{\mathrm{CT}} > 150$ and $m_{\mathrm{CT}} > 250$ signal regions is shown in figure 4.19, and will be compared to the control region compositions for each background in turn.

Z + jets – CRZ

The dominant Z+jets background enters the SRs when the Z decays to two neutrinos, giving appreciable $E_{\mathrm{T}}^{\mathrm{miss}}$, and is produced in association with at two high p_{T} jets. A suitable control region, therefore, is one where the Z decays to e^+e^- or $\mu^+\mu^-$, allowing it to be identified and selected through an invariant mass cut $m_{\ell\ell} - m_Z < 15\,\mathrm{GeV}$. These leptons are then treated as neutrinos by adding their p_{T} to the $E_{\mathrm{T}}^{\mathrm{miss}}$. In order to ensure high purity of Z+jets over $t\bar{t}$ while rejecting a minimum of Z+jets events, a moderate cut is placed on the leading lepton p_{T}, shown in figure 4.20. The m_{CT} and m_{cc} cuts are not applied, and the $E_{\mathrm{T}}^{\mathrm{miss,lep}}$ and jet p_{T} cuts are loosened, in order to increase event yields. Even so, the total expected

	SR	CRZ	CRT	CRW
Trigger	$E_{\mathrm{T}}^{\mathrm{miss}}$	single lepton (dilepton)	single lepton	single lepton
Event cleaning	Common to all SRs and CRs			
Lepton selection	—	2 SF OS	2 DF OS	1
	No further e/μ after overlap removal with $p_{\mathrm{T}} > 7(6)$ for $e(\mu)$.			
$\Delta\phi_{\mathrm{min}}(\mathbf{E}_{\mathrm{T}}^{\mathrm{miss}}, 3\text{ jets})$	> 0.4	—	—	—
$E_{\mathrm{T}}^{\mathrm{miss}}/(p_{\mathrm{T}}^{j1} + p_{\mathrm{T}}^{j2})$	$> 1/3$	—	—	—
$E_{\mathrm{T}}^{\mathrm{miss}}$	> 150	—	> 50 (> 100)	> 100
$E_{\mathrm{T}}^{\mathrm{miss,lep}}$	—	> 100	—	—
Leading jet $p_{\mathrm{T}}(j_1)$	> 130	> 50	> 50 (> 130)	> 130
Second jet $p_{\mathrm{T}}(j_2)$	> 100 (> 50)	> 50	> 50	> 50
Third jet $p_{\mathrm{T}}(j_3)$	— (veto > 50)	—	—	—
c-tagging	leading 2 jets ($p_{\mathrm{T}} > 50$, $\lvert\eta\rvert < 2.5$), 'medium' *JetFitterCharm*			
Leading lepton p_{T}	—	> 70 (> 90)	> 25	> 50 (> 25)
m_{ll}	—	90 ± 15	> 50	—
m_T	—	—	—	$40 - 100$
m_{cc}	> 200	— (> 200)	—	—
m_{CT}	$> 150, 200, 250$ (also $> 300, 350$)	—	— (> 75)	> 150

Table 4.3: Summary of the event selection in the signal and control regions. SF (DF) indicates same-flavour (opposite-flavour) lepton pairs, and OS indicates opposite-sign lepton pairs. All energies, momenta and masses are quoted in GeV. Where differences exist between the scharm and the sbottom selection, the sbottom requirements are indicated in brackets, and the scharm requirements coloured according to tightness of the scharm cut versus the sbottom one, as follows: tighter, looser, more complex difference.

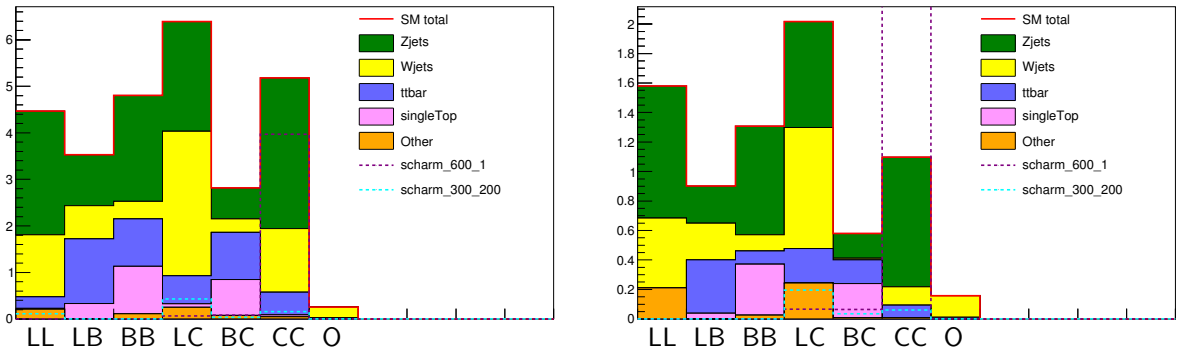


Figure 4.19: Flavour composition of the $m_{\mathrm{CT}} > 150$ and $m_{\mathrm{CT}} > 250$ signal regions. The bin labels have the format XX, indicating the flavours of the two leading jets (with no ordering), with shorthands: L - light jet, B - b-jet, C - c-jet. The bin labelled 'O' is for other combinations, i.e. those with τ-jets. The dashed lines show distributions for signal models, with the legend indicating the $\tilde{c}$ and $\tilde{\chi}_1^0$ masses as "scharm_{$\tilde{c}$ mass}_{$\tilde{\chi}_1^0$ mass}". There is a slight increase in LL at the expense of CC for the high m_{CT} region, and $t\bar{t}$ sees a marked drop in BB as expected, but otherwise the compositions are similar.

yield is only around 50 events. In the SRs, there is a clear preference for same-flavour pairs of jets (along with some LC), suggesting that these c-tagged jets are originating from gluon splittings (albeit with unusually high masses). This pattern is repeated in figure 4.21, which shows the flavour composition in `CRZ`, although LL is under-represented, probably since the removal of the m_{cc} cut allows $g \to cc/bb$ to dominate over gluon jets with their low c-tagging probability but higher invariant mass.

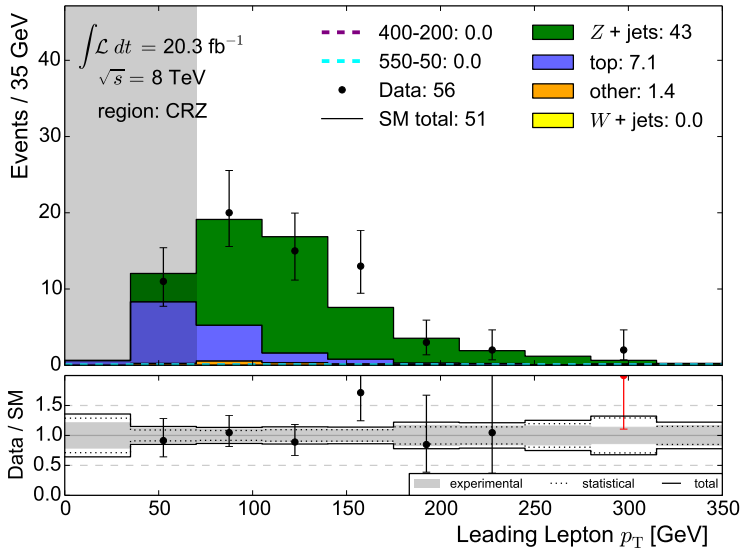


Figure 4.20: Plot made by a collaborator, showing the p_{T} of the leading lepton in `CRZ`.

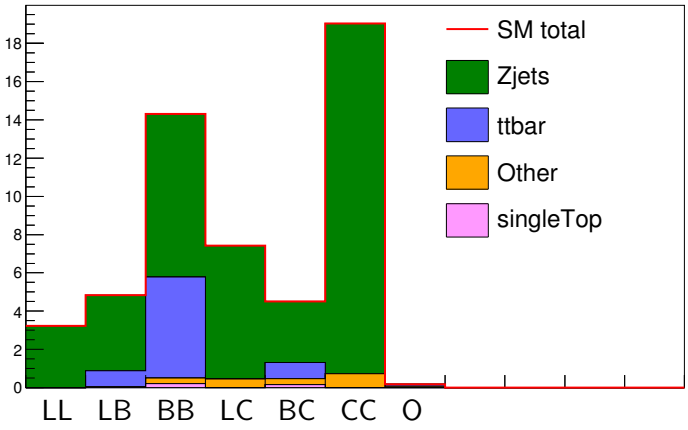


Figure 4.21: Flavour composition of CRZ.

$t\bar{t}$ – CRT

$t\bar{t}$ events entering the signal region are predominantly semileptonic decays, with one W boson decaying to a hadronic τ or a light lepton out of acceptance and the other to jets. The associated control region has two leptons of opposite sign, but with opposite flavours so as to select $t\bar{t}$ over Z. Again, kinematic selections are loosened in order to reduce statistical uncertainty, resulting in 124 expected events – it can be seen from figure 4.22 that even a modest cut on m_{CT} would severely reduce the number of events. As discussed previously, the m_{CT} and m_{cc} cuts result in a complex flavour structure, with most combinations being important in the SRs. However, since in CRT both W bosons from the top quarks are forced to decay leptonically in order to give the $e\mu$ signature, the only jets available for possible c-tagging are the two b-jets, and this is reflected in figure 4.23.

W + jets – CRW

W+jets events enter the SRs in a similar way to $t\bar{t}$, with W decays to a hadronic τ or an out-of-acceptance e/μ. They are controlled in a one-lepton region, with the kinematic cuts closer to the SRs since this is a less restrictive lepton selection. The m_{CT} cut in particular is retained in order to reduce $t\bar{t}$ contamination, and a cut is introduced on the *transverse mass*, m_{T}, between the $E_{\mathrm{T}}^{\mathrm{miss}}$ and the lepton, with a lower bound to reject fake leptons and

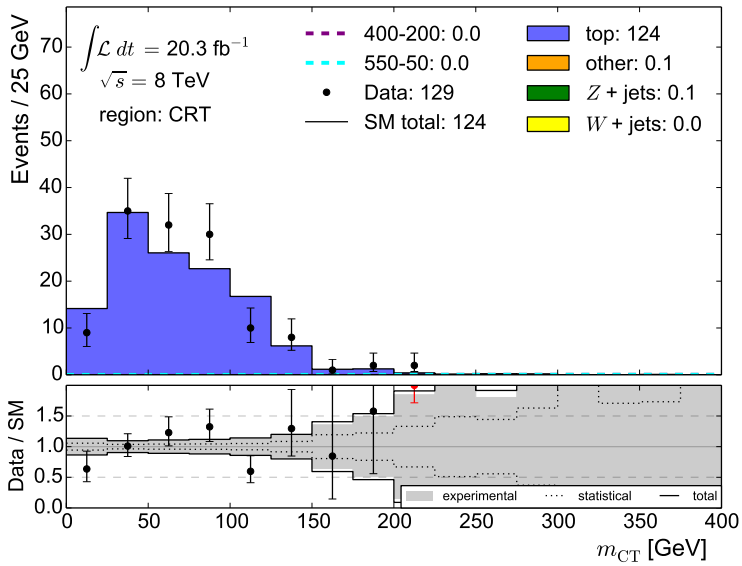


Figure 4.22: Plot made by a collaborator, showing the m_{CT} distribution in CRT.

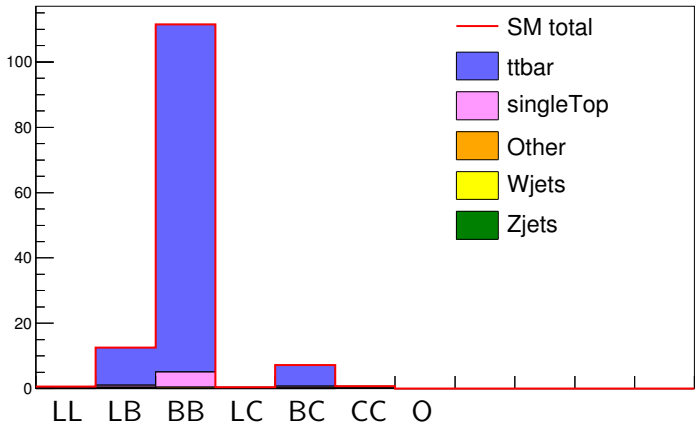


Figure 4.23: Flavour composition of CRT.

an upper bound to reduce possible signal contamination in the event of a signal decaying partially to leptons. The lepton p_{T} cut is raised to 50 GeV from the threshold of 25 in order to reduce the effect of poor modelling at low p_{T}, shown in figure 4.24 and seen in both e and μ channels, since this was thoroughly investigated (ruling out QCD fakes contributions and flavour mismodelling) but not understood.

This selection results in an expected yield of 60 events, of which only 16 are W+jets. However, examining figure 4.25 it is apparent that the $t\bar{t}$ contamination is predominantly from bc and lc events, in contrast to the bb of CRT. In addition, there is a reasonably sizeable

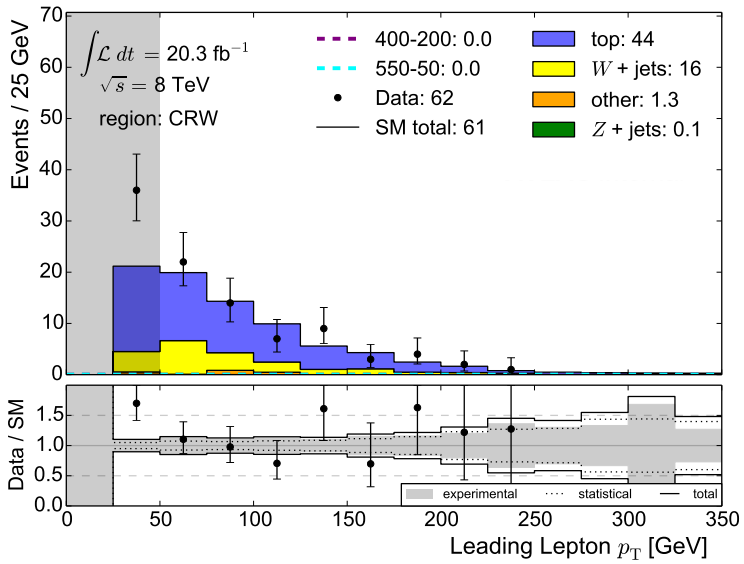


Figure 4.24: Plot made by a collaborator, showing the p_{T} of the leading lepton in CRW.

single top contribution, partly offsetting its lack in CRT. Thus, while only loosely constraining W+jets, this region is useful to constrain the top background and ensure an even flavour representation (this is reasonably well reproduced for W+jets, although lc dominates more in the SRs).

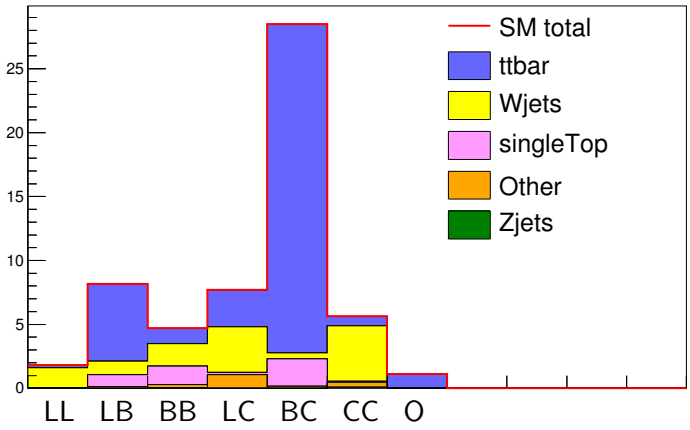


Figure 4.25: Flavour composition of CRW. The $t\bar{t}$ here is predominantly one true charm - in fact there is less true $b\bar{b}$ from $t\bar{t}$ than in the SR - making this a complimentary top control region to CRT. The flavour composition of W+jets is reasonably close to that in the SR.

Further plots of relevant distributions in the signal and control regions are reproduced in appendix A.2.

4.5.2 QCD Multijet Estimation

QCD multijet events enter the signal regions when jets are mismeasured, principally due to random fluctuations in detector response, giving rise to significant reconstructed $E_{\mathrm{T}}^{\mathrm{miss}}$. As mentioned in section 4.4.1, these events are rejected through cuts on $\Delta\phi_{\mathrm{min}}(\mathbf{E}_{\mathrm{T}}^{\mathrm{miss}}, 3\text{ jets})$ and $E_{\mathrm{T}}^{\mathrm{miss}}/(p_{\mathrm{T}}^{j1} + p_{\mathrm{T}}^{j2})$ and as a result, in combination with the high $E_{\mathrm{T}}^{\mathrm{miss}}$ cut, are very rare. This rarity makes this background difficult to estimate, especially from MC since very large samples of events with full calorimeter simulation would be required. Hence a data-driven estimate is performed. The process, performed by a collaborator and described in detail in [103], is outlined below.

1. Smearing functions, i.e. distributions of reconstructed jet momenta in given bins of truth level momentum, are derived from simulated dijet events. Different smearing functions are defined for jets that are b-tagged versus those that are not, to account for the additional tail at low jet response $R = \frac{p_T^{\mathrm{reco}}}{p_T^{\mathrm{truth}}}$ due to missing neutrinos and muons in b-jets.

2. Low $E_{\mathrm{T}}^{\mathrm{miss}}$ significance seed events with at least 2 c-tagged jets are selected in data.

3. The momenta of these jets are smeared (jet-by-jet) by the functions defined in (1), 20000 times per seed event in order to generate a large sample of pseudo-data.

4. These pseudo-data events are passed through the same analysis cuts as the data and the non-multijet MC to give the expected multijet distributions. Normalisation is performed in a multijet enriched control region, constructed by inverting the $\Delta\phi(E_{\mathrm{T}}^{\mathrm{miss}}, \text{jets 1-3})$ cut and subtracting the non-multijet component (from MC expectation).

Following this procedure, the QCD background is estimated to contribute less than one event in any of the signal regions, and a conservative uncertainty of 100% is applied. Figure 4.26 shows the normalisation of the m_{CT} distribution and the resulting expectation in the loosest signal region.

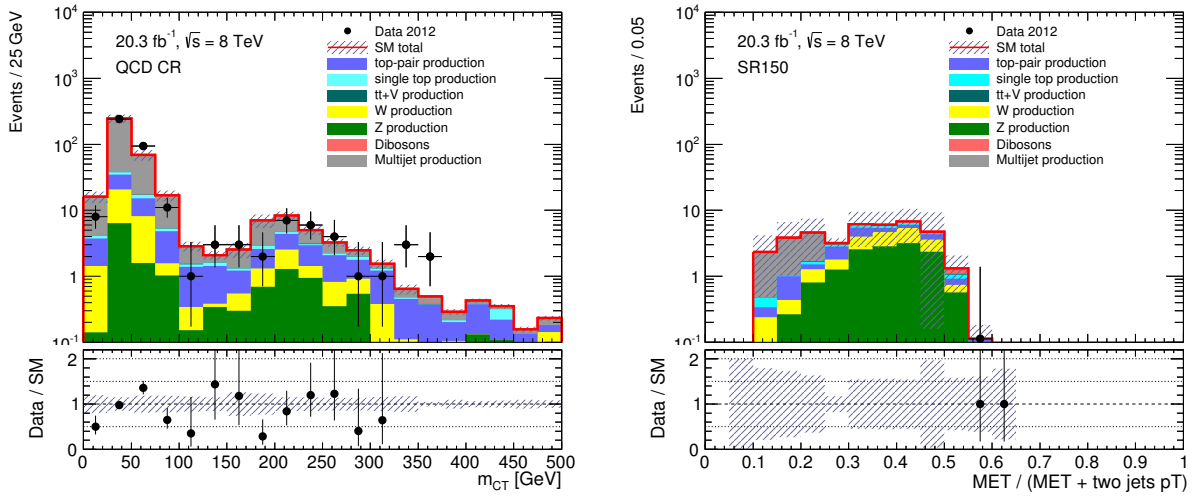


Figure 4.26: Plots made by collaborator, showing QCD distributions determined from the jet smearing method. Left: m_{CT} distribution in the QCD control region. Right: $E_{\mathrm{T}}^{\mathrm{miss}}/(E_{\mathrm{T}}^{\mathrm{miss}} + p_{\mathrm{T}}^{j1} + p_{\mathrm{T}}^{j2})$ in SR150. This variable is equal to 0.25 when $E_{\mathrm{T}}^{\mathrm{miss}}/(p_{\mathrm{T}}^{j1} + p_{\mathrm{T}}^{j2}) = 1/3$, and data is not displayed.

4.6 Systematic Uncertainties

In order to be able to gauge the significance of any excess or deficit that may be observed in the signal regions, a thorough evaluation of the uncertainties involved in the predictions is needed. These uncertainties are split into two main categories – experimental, originating from detector effects and associated uncertainty in event measurement and reconstruction, described in section 4.6.1; and theoretical, originating from uncertainties in the MC modelling, discussed in section 4.6.2. Often, comparisons are made between the nominal yield and the yield as a result of some change that represents a particular uncertainty. If there is a single variation, or if the up and down variations are considered in isolation from the nominal, the uncertainty can be *symmetrised* by halving the difference between the variation and nominal (or the up and down variation as appropriate) and taking that to apply in both the up and down directions.

4.6.1 Experimental Uncertainties

Experimental uncertainties are evaluated for both signals and backgrounds, and partitioned according to the objects they relate to. Their determination was mostly performed by collaborators, and so only a brief outline is given here. In general, signal and control region yields are evaluated when using altered reconstruction parameters (usually up and down by the uncertainty on said parameters) and then compared to the nominal yields in order to determine the impact of a given uncertainty and allow for cancellation between signal and control regions, and background and signal processes, in the fits.

Jet Related Uncertainties

Jet Energy Scale and Resolution The jet energy is scaled up and down by the 1σ uncertainty resulting from the calibrations described in section 3.4.4, referred to as the jet energy scale (JES). Additionally, an extra p_{T} smearing is added to the jets based on their p_{T} and η to account for possible underestimates of the jet energy resolution (JER) in MC simulation. This single uncertainty is then symmetrised.

Jet Vertex Fraction In order to reduce the impact of pileup, signal jets are required to have a JVF > 0.5 if they are within $|\eta| < 2.4$ and have $p_{\mathrm{T}} < 50$ GeV. Up and down systematic uncertainties are derived by requiring instead JVF cuts of 0.53 and 0.47.

***c*-Tagging Efficiency** The c-tagging uncertainty is evaluated by varying the η-, p_{T}- and flavour-dependent scale factors applied to each jet in the simulation within a range that reflects the systematic uncertainty on the measured tagging efficiency and mistag rates. These variations are applied separately to b-jets, c-jets, τ-jets and light-jets, leading to four uncorrelated systematic uncertainties.

Lepton Related Uncertainties

A set of lepton related uncertainties enter the analysis due to the veto on leptonic activity in the event and the requirement of one or two leptons in the control regions. However these uncertainties themselves are small, with the lepton energy scale and resolution being known to within a few percent, and they have little impact on the analysis compared to the jet related uncertainties.

Uncertainties Related to $\boldsymbol{E}_{\mathbf{T}}^{\mathbf{miss}}$

The impact of the uncertainty on the energy scale of the calorimeter clusters not associated to any other objects, which enter the $E_{\mathrm{T}}^{\mathrm{miss}}$ calculation in the 'soft' term, is estimated by varying these scales up and down. The resolution uncertainty on this term is included as another parameter, with the single uncertainty symmetrised.

Pileup Uncertainties

When reweighting MC to match the pileup distribution of data, the average number of interactions per bunch crossing in simulation is scaled by 1.09 (the default value) $\pm$ 0.04. Since the analysis selection is relatively insensitive to pileup, this results in a small uncertainty.

Luminosity Uncertainties

The uncertainty on the integrated luminosity for the 2012 dataset was estimated to be 2.8% using techniques described in [104].

Trigger Uncertainties

Uncertainties on the lepton trigger efficiency and scale factors are not considered since the CPU and human time required to do so was not justified for these small uncertainties affecting

only the control regions, while a 2% uncertainty on the $E_{\mathrm{T}}^{\mathrm{miss}}$ trigger efficiency is applied to the signal regions.

Flat Uncertainty on "Other" Backgrounds

Backgrounds not controlled as described above, i.e. $t\bar{t} + W/Z$ and diboson, have near negligible yields in the signal regions and so are assigned a conservative 50% overall uncertainty rather than evaluating the uncertainties fully.

QCD Multijet Background

A conservative uncertainty of 100% is assumed on the multijet background yield obtained from the data-driven method described in section 4.5.2.

Summary of experimental uncertainties

The dominant experimental uncertainties on the backgrounds in the control regions and `SR150` are shown in figure 4.27, of which the tagging and jet energy scale uncertainties are largest. The largest of these is light jet mistagging which reaches 20% in `SR150`, but they otherwise remain below 10%. This emphasises the importance of reasonably similar flavour compositions in signal and control regions described in section 4.5.1 in order to maximise cancellation of these large uncertainties.

The dominant uncertainties on the signal are the c-tagging uncertainty (up to 31%) and the jet energy scale (up to 32%), followed by the uncertainty related to the mistagging of light jets as c-jets (up to 15%) and the jet energy resolution (up to 15%). The b-mistag uncertainty is negligible for signal since there are no true b-jets.

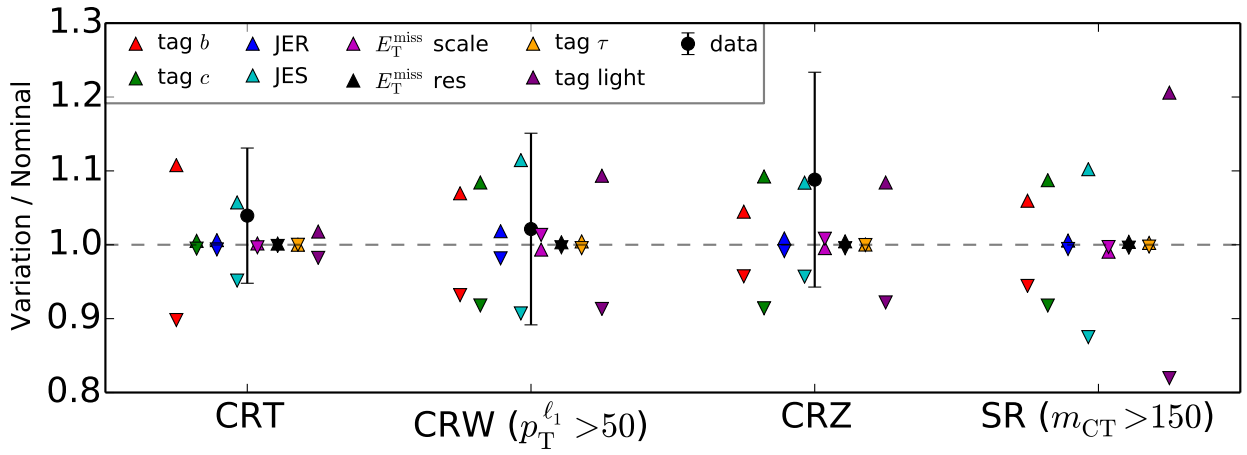


Figure 4.27: The leading 8 experimental systematic uncertainties in the three control regions and SR150. Plot made by collaborator.

4.6.2 Theoretical Uncertainties

Theoretical uncertainties, i.e. uncertainties on the MC modelling of the various backgrounds, whose origins are described in section 2.3.2, are determined through comparing samples produced with different generators and / or different parameter settings.

These uncertainties were evaluated following the recommended approach for the ATLAS SUSY group[5], for the $t\bar{t}$, single top, W+jets and Z+jets backgrounds, with the minor $t\bar{t}+V$ and diboson backgrounds having simply a global 50% uncertainty applied.

For each MC sample, event yields are evaluated for each signal, control and validation region. Since several of the specialised MC samples for these studies have not been processed at reconstructed level, these yields are evaluated at truth level. As it is not possible to implement the c-tagging algorithm at truth level, but differences in treatment of heavy and light quarks are an important contribution, c-tagging is emulated by applying c-tagging weights for the leading two jets according to efficiency maps provided by the flavour tagging group as a function of p_{T} and η for each truth jet flavour. In addition, a different lepton-jet overlap removal is used at truth level, to avoid soft leptons in b-jets and c-jets causing their parent jets to be removed. Cleaning cuts and trigger selections are not required, but in all other respects the truth level selection is the same as for reconstructed level. The differences

[5] https://twiki.cern.ch/twiki/bin/viewauth/AtlasProtected/SUSYSystematicUncertainties2012

expected between truth-level and detector-smeared jet kinematics, and the tagging scale factors between data and reconstructed level simulation, are assumed to be of secondary importance and decoupled from the theoretical uncertainties on MC generation.

The treatment of theoretical uncertainties in the various fits performed (see section 4.7) is different to that of the experimental systematics. The cancellation between signal and control regions is directly evaluated by comparing ratios $R_{SR1,CR1} = \frac{Y_{SR1}}{Y_{CR1}}$. These quantities R, for different MC samples, are then manipulated as described below to give the uncertainties for e.g. the $CR1 \rightarrow SR1$ transfer factor, and it is these uncertainties that are propagated to the fit.

PDF uncertainties

Uncertainties resulting from the PDFs were evaluated through reweighting events, based on the momentum fractions and types of the initial state partons, to mimic both the intra-PDF uncertainty given by the CT10 PDF error set (all MC apart from single top uses this PDF) and the inter-PDF uncertainty given by the comparison of the central CT10 value and the central MSTW08 value. The symmetric uncertainty on the yield X in each region is then taken as the envelope

$$\sigma_{\text{PDF}} = \frac{1}{2}\left[\max\left(X_{\text{CT10}} + \Delta X_{\text{CT10}}, X_{\text{MSTW08}}\right) - \min\left(X_{\text{CT10}} - \Delta X_{\text{CT10}}, X_{\text{MSTW08}}\right)\right] / X_{\text{CT10}}$$

These uncertainties are generally below 10%, and correlated between signal and control regions, such that their overall impacts, quoted in the following tables for each background process, is small.

Top Quark Single and Pair Production

As the $t\bar{t}$ and single top backgrounds are considered together in the fit and associated transfer factors, an overall uncertainty for the two backgrounds combined must be computed. In some cases, the required variations samples exist only for $t\bar{t}$ (or $t\bar{t}$ plus Wt-channel single top), but

the uncertainty is relevant to all top production channels. Here, the event yields are taken only including these variations samples, and the resulting uncertainty is taken to apply to the other channels equally (for example, $t\bar{t}$ scale variations). The impact of wrongly assigning an uncertainty in this way is small, since $t\bar{t}$ and single top Wt-channel production are by far dominant over single top t-channel and s-channel production, for example $t\bar{t}$: single top Wt-channel : single top t- and s-channel yields are $4.77 : 1.56 : 0.68$ in `SR150`.

In other cases, where the variation applies to only a specific single top production channel (e.g. s-channel), the event yields compared include the full $t\bar{t}$ + single top sample set, with only the relevant channel varied, in order to properly obtain the effect of this variation on the total $t\bar{t}$ + single top background.

Where statistical uncertainties on the MC yields obtained are relevant, the MC uncertainty on each of the *varied* sample yields is computed, and is then scaled by the relative contribution of that variation sample to the relevant overall yield. (i.e. if a variation sample makes up only 50% of the total $t\bar{t}$ + single top yield, then the MC statistical uncertainty carried forward will be 50% of that on the variation sample itself.) Then, the larger of these two quantities (one for each variation sample) is taken, and added in quadrature to the systematic uncertainty computed for that variation.

The final $t\bar{t}$ + single top uncertainties propagated to the fit are then the quadrature sum of the quantities obtained by the procedures described below.

Generator Comparison

$t\bar{t}$ and single top Wt-channel samples generated with `Powheg-Box` are compared to samples generated with `MC@NLO`. These are both next-to-leading-order (NLO) event generators, with `Powheg-Box` generating the highest p_{T} emission at NLO accuracy and the parton shower reacting accordingly, while `MC@NLO` removes the NLO terms from its calculation that would be duplicated by the parton shower [105]. Both sets of samples are interfaced to `HERWIG` for parton showering and hadronisation, since it is not possible to interface `MC@NLO` to `PYTHIA` 6 and the two effects should be decoupled. The full difference between the two generators is

taken as a symmetric uncertainty after adding also the larger statistical uncertainty of the two sample sets. Included in the ratios are the varied $t\bar{t}$ and single top Wt-channel samples, and the unvaried s-channel sample, but not any t-channel contribution. This is because the uncertainty derived here is taken to apply to the t-channel production also, since no suitable variation samples exist for it.

Parton Shower

$t\bar{t}$ and single top Wt-channel samples generated with `Powheg-Box` are interfaced either to `PYTHIA` 6 or `HERWIG` to compare the parton shower modelling. `PYTHIA` 6 uses a p_{T}-ordered parton shower[6] followed by the Lund string model for hadronisation, while `HERWIG` uses an angular-ordered shower and a cluster model of hadronisation. Since the samples are generated from the same `Powheg-Box` output events, no statistical uncertainty is added and the difference between the samples is symmetrised as the full uncertainty. The same processes are considered as for the generator comparison above, i.e. the varied $t\bar{t}$ and single top Wt-channel samples, unvaried s-channel and no t-channel contribution.

Generator and Parton Shower for single top s-channel

For this smaller background, the Generator and Parton Shower systematics are evaluated together, by comparing a sample generated with `Powheg-Box` and showered by `PYTHIA` 6 to one generated with `MC@NLO` and showered by `HERWIG`. For this uncertainty, the full $t\bar{t}$ + single top yields are included in the ratios, as uncertainties on both Wt-channel and t-channel single top production are included above.

Interference between Single Top and Pair Production

At NLO, single top production receives contributions from LO $t\bar{t}$ production that dwarf the LO Wt-channel cross-section. This interference can be accounted for by subtracting the $t\bar{t}$-like contributions, at either the amplitude level ("Diagram Removal", DR, the baseline procedure) or the cross-section level ("Diagram subtraction", DS). The difference between

[6] This is the default in ATLAS, although `PYTHIA` 6 can also use virtuality.

these two schemes is taken as a systematic uncertainty on Wt-channel single top production. `Powheg-Box` + `PYTHIA` 6 samples for single top Wt-channel production in both schemes exist, and these are combined with $t\bar{t}$ and other single top channels as the systematic only applies to Wt. The full difference is taken as a symmetric uncertainty.

An alternative prescription for the evaluation of this uncertainty is to make a comparison with an inclusive `AcerMC` + `PYTHIA` 6 $WWbb$ sample that accounts for both processes simultaneously. However, this comparison convolutes multiple effects (e.g. `AcerMC` is a leading order generator, versus `Powheg-Box` at next-to-leading-order) and so is included only for reference (in general it leads to a smaller uncertainty in comparisons with `CRT`).

Initial and Final State Radiation

Samples for $t\bar{t}$ and Wt-channel single top production, with more and less parton shower activity, are generated with `AcerMC` + `PYTHIA` 6. The uncertainty is taken as half the difference between the two extremes, and applied also to the t-channel and s-channel samples (i.e. in the ratios, only $t\bar{t}$ and Wt-channel single top are included).

Scale Variations

Considered in $t\bar{t}$ events here are the renormalisation scale and the factorisation scale. Events are generated with `Powheg-Box`, for $t\bar{t}$ only, changing each scale up and down by a factor of two in turn[7]. The conservative (i.e. assuming no correlation) asymmetric uncertainty is taken as the quadrature sum of all variations up, and separately the sum of all variations down, of the scaled samples relative to the nominal $t\bar{t}$ sample. This uncertainty is taken to apply also to single top production, so only the $t\bar{t}$ yields are included in the ratios.

Results

Results for the combination of $t\bar{t}$ and single top are shown in table 4.4. The dominant uncertainty in each region is that on the parton shower modelling, at around 22 - 26%, leading

[7]The scales are chosen event-by-event, so it is the scale choice for each event which is altered rather than a global scale.

Variation	$\frac{\text{mCT 150}}{\text{CRT}}$	$\frac{\text{mCT 200}}{\text{CRT}}$	$\frac{\text{mCT 250}}{\text{CRT}}$
$t\bar{t}$ scales up	11.4	12.9	19.1
$t\bar{t}$ scales down	0.0	0.0	0.0
$t\bar{t}$ + t Gen	11.9	16.5	17.0
$t\bar{t}$ + t Gen stat	12.2	17.0	18.0
$t\bar{t}$ + t PS	21.6	25.5	25.5
$t\bar{t}$ + t ISR/FSR	10.8	10.3	8.7
$t\bar{t}$ + t DR vs WWbb	4.6	12.0	13.1
$t\bar{t}$ + t DR vs WWbb stat	5.3	12.6	14.4
$t\bar{t}$ + t DR vs DS	14.6	17.0	19.5
$t\bar{t}$ + t DR vs DS stat	14.6	17.0	19.5
$t\bar{t}$ + t schan	0.2	0.1	0.2
$t\bar{t}$ + t schan stat	0.2	0.2	0.2
$t\bar{t}$ + t PDF	0.4	1.7	7.4
$t\bar{t}$ + t overall up	29.3	34.6	37.9
$t\bar{t}$ + t overall up stat	29.4	34.9	38.4
$t\bar{t}$ + t overall down	26.9	32.2	32.7
$t\bar{t}$ + t overall down stat	27.1	32.4	33.3

Table 4.4: $t\bar{t}$ and single top theoretical systematic uncertainties, in %. Where a row heading is duplicated with 'stat' added, this indicates a variation for which the statistical uncertainty is included in the calculation, and the row without 'stat' is lacking this contribution, in order to gauge its effect. The final numbers input to the fit are '$t\bar{t}+t$ overall up / down stat', with only comparisons between SRs and `CRT` shown.

to overall uncertainties between SR and CR of between 27 and 38%. When performing the background only fit (see section 4.7) this yields an overall uncertainty on SR yields of around 7%, about 30-40% of the total background systematic.

W+Jets Production

Scale Variations

In addition to the factorisation and renormalisation scales considered above, the CKKW matching scale is also considered. $W \rightarrow e\nu$ + jets samples generated with `SHERPA` and variations of these three scales are compared to the relevant nominal W+jets samples to

Variation	$\frac{\text{mCT 150}}{\text{CRW}}$	$\frac{\text{mCT 200}}{\text{CRW}}$	$\frac{\text{mCT 250}}{\text{CRW}}$
W+jets scales up	16.6	26.2	31.4
W+jets scales down	4.3	4.2	0.0
W+jets num. partons	3.1	5.0	2.8
W+jets num. partons stat	3.6	5.6	4.5
W+jets PDF	1.0	1.4	2.7
W+jets overall up	16.9	26.7	31.7
W+jets overall up stat	17.0	26.8	31.9
W+jets overall down	5.4	6.7	3.9
W+jets overall down stat	5.7	7.1	5.3

Table 4.5: W+jets theoretical systematic uncertainties, in %. The final numbers input to the fit are 'W+jets overall up / down stat'

derive the resulting uncertainty. The combination of the different variations is as for $t\bar{t}$, i.e. separate sums of all positive and negative variations.

Finite Number of Partons

To estimate the impact of the number of partons included in the matrix element step of the event generation, samples with up to 4 additional partons required are compared to samples with up five additional partons. The full difference, added to the statistical uncertainty, is taken as a symmetric uncertainty.

Results

Results for the W+jets theoretical systematics are shown in table 4.5. The uncertainty is dominated by the scale uncertainty, leading to an (asymmetric) uncertainty of $\sim$ 20-30% and a final impact about half that of the theory uncertainties on the top background, at around 3-4% on the overall signal region background expectation.

Variation	$\frac{\text{mCT 150}}{\text{CRZ}}$	$\frac{\text{mCT 200}}{\text{CRZ}}$	$\frac{\text{mCT 250}}{\text{CRZ}}$
Z+jets scales up	1.4	2.1	2.7
Z+jets scales down	1.4	2.2	2.8
Z+jets num. partons	5.0	8.7	3.6
Z+jets num. partons stat	5.2	8.9	4.4
Z+jets PDF	1.5	1.6	2.2
Z+jets overall up	5.5	9.1	5.0
Z+jets overall up stat	5.6	9.3	5.6
Z+jets overall down	5.5	9.1	5.1
Z+jets overall down stat	5.6	9.3	5.7

Table 4.6: Z+jets theoretical systematic uncertainties, in %. The final numbers input to the fit are 'Z+jets overall up / down stat'

Z+Jets Production

Scale Variations

Since SHERPA samples with scale variations were not available for Z+jets, they are emulated by applying weights, determined from ALPGEN samples, that parametrise the effects of the scale variations as a function of the number of jets with $p_{\mathrm{T}} > 30$ GeV. These account for factorisation and renormalisation scales, and the matching MLM scale (since ALPGEN uses this rather than CKKW).

Finite Number of Partons

An identical procedure is followed as for W+jets.

Results

Results for the Z+jets theoretical systematics are shown in table 4.6. The reweighting procedure results in a much smaller scale uncertainty than for W+jets, leading to overall uncertainties below 10%. Since Z+jets is a larger background than W+jets, however, the overall impact on the overall background estimate is very similar.

4.7 Results and Limit Setting

The limit setting procedure is described in more detail in section 5.7, and so only the aspects particular to this analysis are described here. A background only fit is used to obtain the normalisations of the $t\bar{t}$, Z+jets and W+jets backgrounds through the three control regions, and constrain their uncertainties, in a signal-agnostic manner. A discovery fit is performed on the outputs of this, providing model-independent limits on the cross-section of new processes falling in the signal regions. Following this, in the absence of a visible signal, exclusion limits are set within the context of the simplified model described in section 4.2.1.

4.7.1 Background only fit

The results of the background only fit, taking as inputs the background yields and uncertainties described in previous sections, are shown in table 4.7 and figure 4.28, which shows distributions of m_{cc} and m_{CT} in the signal regions. The Z+jets and $t\bar{t}$ backgrounds are both scaled up slightly by the fit, by 9% and 4%, while W+jets is scaled down by 3%. There is a slight deficit observed in the signal regions, of about 1.5σ when accounting for statistical and systematic uncertainties. Since the signal regions overlap, the deficit of 4 events in `SR250` would reduce this to 0.3σ and 0.9σ in `SR200` and `SR250` respectively, i.e. it can to a large extent be explained by this single fluctuation. Several possible sources of the deficit were checked, notably constructing validation regions with less extrapolation in kinematics than between control and signal regions, and in all cases no significant discrepancies were observed. Thus the small deficit is assigned to a statistical fluctuation.

The systematic uncertainties following the fit are given in table 4.8, with the total background systematic uncertainties constrained to below 25% in all signal regions, roughly equalling the statistical uncertainty in the loosest region and greatly surpassing it in the tightest. Systematic uncertainties are dominated by c-tagging and jet energy calibration, with limited statistics in both signal and control regions also being important.

	Control Regions			Signal Regions, m_{CT} [GeV]		
	CRT	CRZ	CRW	>150	>200	>250
Top	129 ± 11	7.3 ± 0.8	45 ± 7	7.4 ± 2.7	3.9 ± 1.6	1.6 ± 0.7
	(124)	(7.1)	(44)	(7.1)	(3.7)	(1.5)
Z+jets	0.1 ± 0.0	47 ± 7	0.1 ± 0.1	14 ± 3	7.7 ± 1.7	4.3 ± 1.2
	(0.1)	(43)	(0.1)	(13)	(7.0)	(3.9)
W+jets	< 0.1	< 0.1	15 ± 9	7.2 ± 4.5	4.1 ± 2.6	1.9 ± 1.2
	(< 0.1)	(< 0.1)	(16)	(7.4)	(4.2)	(1.9)
Multijets	–	–	–	0.3 ± 0.3	0.2 ± 0.2	0.05 ± 0.05
Others	0.1 ± 0.1	1.4 ± 0.8	1.3 ± 0.8	0.5 ± 0.3	0.4 ± 0.3	0.4 ± 0.3
Total	129 ± 11	56 ± 7	62 ± 7	$\mathbf{30 \pm 6}$	$\mathbf{16 \pm 3}$	$\mathbf{8.2 \pm 1.9}$
Data	129	56	62	**19**	**11**	**4**

Table 4.7: Expected and observed number of events for an integrated luminosity of 20.3 fb^{-1}, following the background only fit (the fitted CR values are equal to the corresponding observed values by construction.) For comparison, the numbers obtained using MC simulations only are shown in parentheses. The column labelled as 'Others' is the combination of subdominant electroweak backgrounds estimated from MC only.

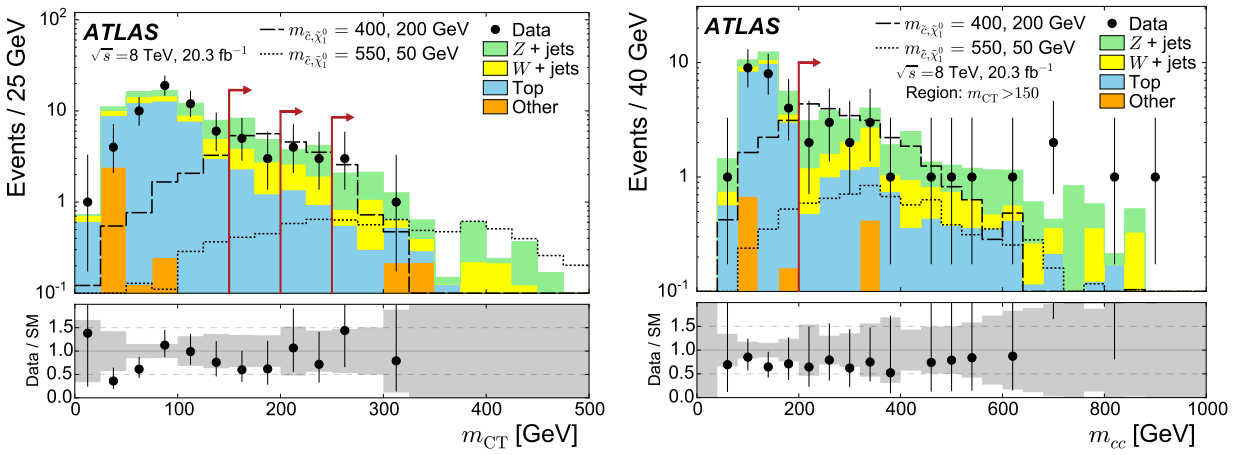


Figure 4.28: Distributions of m_{CT} (left) and m_{cc} (right) following the background only fit. Signal region selections ($m_{CT} > 150$ GeV for the m_{cc} distribution) are applied, other than for the variable plotted. Arrows indicate the SR requirements on m_{CT} and m_{cc}. In the ratio plots, the grey bands correspond to the combined MC statistical and experimental systematic uncertainty. Plot from [4].

4.7.2 Exclusion fits

Fits similar to the background only one, but taking into account a specific signal model, are performed for each signal point independently. For a given background estimate, signal expectation and observed event count, and in the absence of a visible signal, a significance test

Uncertainty of channel	$m_{CT} > 150$	$m_{CT} > 200$	$m_{CT} > 250$
Total background expectation	29.60	16.30	8.21
Total statistical ($\sqrt{N_{exp}}$)	±5.44	±4.04	±2.87
Total background systematic	±5.57 [18.82%]	±3.46 [21.22%]	±1.94 [23.61%]
ϵ_{tag} for light-jets	±5.59	±3.38	±1.95
W + jets normalization	±5.31	±3.03	±1.39
jet energy scale	±3.26	±1.84	±1.12
Z + jets normalization	±3.21	±1.73	±0.97
ϵ_{tag} for c-jets	±2.46	±1.33	±0.67
combined top theory	±2.13	±1.32	±0.57
$m_{CT} > 150$ stat error	±1.86	±0.00	±0.00
ϵ_{tag} for b-jets	±1.69	±0.98	±0.51
top normalization	±1.12	±0.58	±0.24
E_T^{miss} resolution	±0.96	±0.52	±0.27
Lumi	±0.82	±0.45	±0.23
combined W theory	±0.82	±0.69	±0.35
combined Z theory	±0.80	±0.69	±0.26
E_T^{miss} trigger SF	±0.59	±0.33	±0.16
flat "other" systematic	±0.22	±0.22	±0.22
jet energy resolution	±0.22	±0.03	±0.14
E_T^{miss} scale	±0.11	±0.10	±0.19
ϵ_{tag} for τ-jets	±0.06	±0.06	±0.04
pileup	±0.05	±0.14	±0.02
e resolution from $Z \to ee$	±0.01	±0.00	±0.00
jet vertex fraction	±0.00	±0.00	±0.00
e ID SF	±0.00	±0.00	±0.00
μ energy scale	±0.00	±0.00	±0.00
e low p_T	±0.00	±0.00	±0.00
$m_{CT} > 250$ stat error	±0.00	±0.00	±0.85
$m_{CT} > 200$ stat error	±0.00	±1.38	±0.00
μ ID SF	±0.00	±0.00	±0.00

Table 4.8: Results of the background-only fit uncertainties, extrapolated to the signal regions. Those below the horizontal line are $\lesssim 10\%$ of the total background systematic uncertainty.

is performed to obtain a measure of exclusion power for each point, CL_s. Expected yields are varied within systematic uncertainties, and signal yields within cross-section uncertainties, in order to produce a CL_s value for each of these conditions in turn. The results of this search are then combined with those of the stop-to-charm search, in order to show an overall sensitivity to $\tilde{c}$ production at both high and low mass differences between it and the $\tilde{\chi}_1^0$. This yields 5 signal regions under consideration – the three m_{CT} choices here, and two from the stop-to-charm analysis. The region with the best expected exclusion power (i.e. without considering data in the signal regions) is used to form the observed exclusions, which are shown in figure 4.29. The analysis described here is sensitive in the high mass region it was targeted at, and limits are significantly extended beyond the reach of the other analyses sensitive to this final state.

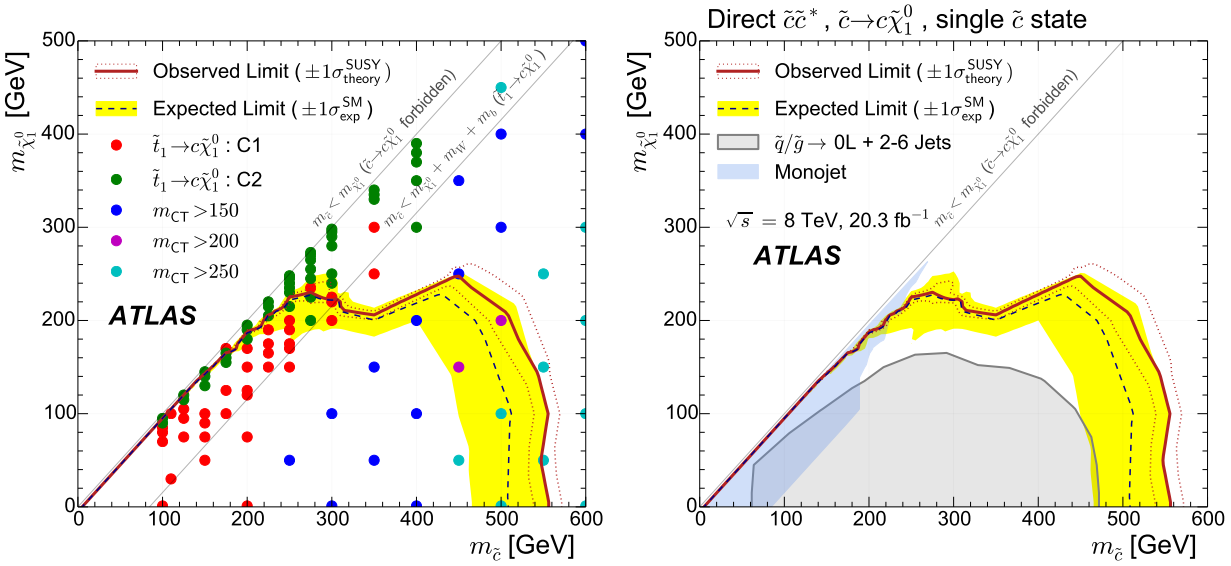


Figure 4.29: Exclusion limits at 95% C.L. in the $\tilde{c}$–$\tilde{\chi}_1^0$ mass plane, for a combination of this analysis and stop-to-charm c-tagged regions. The observed (solid red line) and expected (dashed blue line) limits include all uncertainties except for the theoretical signal cross-section uncertainty (PDF and scale). The band around the expected limits show $\pm1\sigma$ uncertainties. The dotted lines around the observed limits represent the results obtained when moving the nominal signal cross section up or down by the $\pm1\sigma$ theoretical uncertainty. Left: the best expected region for each point in the $\tilde{c}$-$\tilde{\chi}_1^0$ mass plane. Right: Final contours in comparison to the stop-to-charm monojet and inclusive 2-6 jets searches. Plots from [4], made by collaborator.

4.8 Summary and Outlook

This chapter described a search for a previously unexplored final state, that of two high-p_{T} charm jets and $E_{\mathrm{T}}^{\mathrm{miss}}$, resulting from the pair-production of the scalar partner of the charm quark, using 20.3fb^{-1} of 8 TeV pp collision data collected with the ATLAS detector at the LHC during 2012. It made use of a new charm tagging algorithm, developed for another SUSY search but used most extensively here, with unprecedented charm tagging efficiency for its light- and b-rejection power. This new tagging was merged with an earlier search for two b-jets, with most of the analysis selections re-optimised, in order to obtain leading sensitivity to scharms, which were excluded below a mass of 550 GeV in the case of the $\tilde{\chi}_1^0$ mass lying below 200 GeV.

This search is recognised as being useful to constrain charm production in a variety of scenarios, in particular those with enhanced $\tilde{t}$-$\tilde{c}$ mixing [43,106]. Additionally, the techniques demonstrated here are relevant beyond this to e.g. possibly constraining the charm Yukawa coupling [107,108]. Improvements to c-tagging are certainly possible with the introduction of the IBL over LS1, and through an analysis-specific optimisation of the new algorithm. Additionally, the large increase in integrated luminosity of Run-2 over Run-1 should allow for a significant increase in precision, so a future version of this analysis should yield strong and important results.

Chapter 5

Search for the partner of the gluon

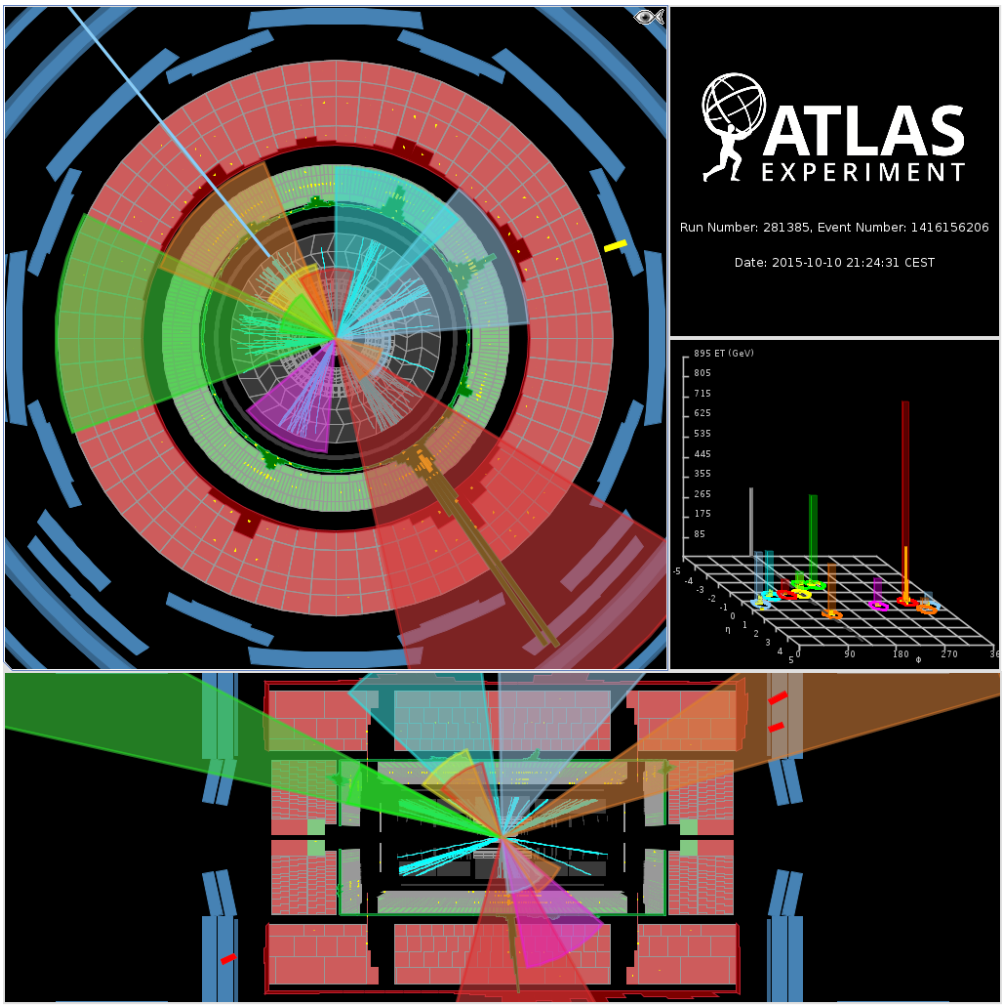


Figure 5.1: Event display in a signal region of the multijet analysis, featuring 11 jets with $p_{\mathrm{T}} > 50$ GeV. From [2].

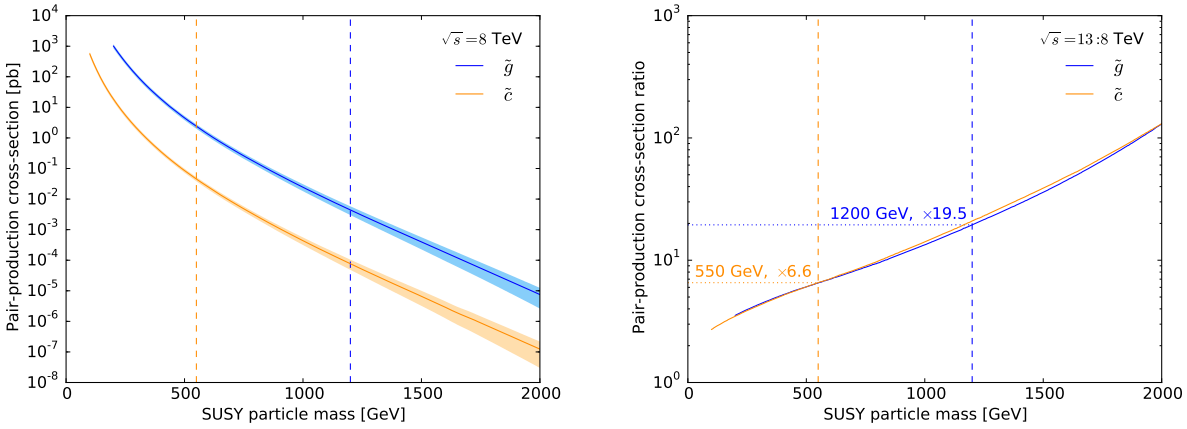


Figure 5.2: Left: $\tilde{c}$ and $\tilde{g}$ cross-sections at $\sqrt{s} = 8$ TeV as a function of SUSY particle mass. Right: ratios of pair-production cross-sections between $\sqrt{s} = 8$ and 13 TeV for $\tilde{c}$ and $\tilde{g}$, as a function of SUSY particle mass. The vertical dashed lines are the observed Run-1 exclusion limits from [4] (described in chapter 4) and [109] (to be described in this chapter, with the limit from the 'two-step' simplified model interpretation). Cross-sections taken from the LHC SUSY cross-section working group [110], calculated from [111].

With the LHC upgraded to allow running at $\sqrt{s} = 13$ TeV, analysing the first data for hints of new physics was a priority having completed the scharm analysis in early 2015. As can be seen in figure 5.2, the cross-section for $\tilde{c}$ production just heavier than excluded in Run-1 was expected to grow by a factor of 6.6 with the increase in $\sqrt{s}$. However, the lower end of integrated luminosity predictions (which reality favoured unfortunately) were for only a few fb^{-1} of $\sqrt{s} = 13$ TeV data, meaning the expected number of at-threshold scharms was similar to that in 20.3 fb^{-1} of $\sqrt{s} = 8$ TeV data. Thus the likelihood of being sensitive to $\tilde{c}$ squarks beyond Run-1 limits was slim for this statistically-limited analysis, and this search is better left until later in Run-2.

In contrast, gluinos are excluded by Run-1 searches up to the much higher mass of around 1200 GeV, meaning that their cross-sections increase by a factor of about 20. This is a sufficiently large increase that previously unexcluded gluino masses were predicted to be discoverable with the projected LHC luminosity in 2015.

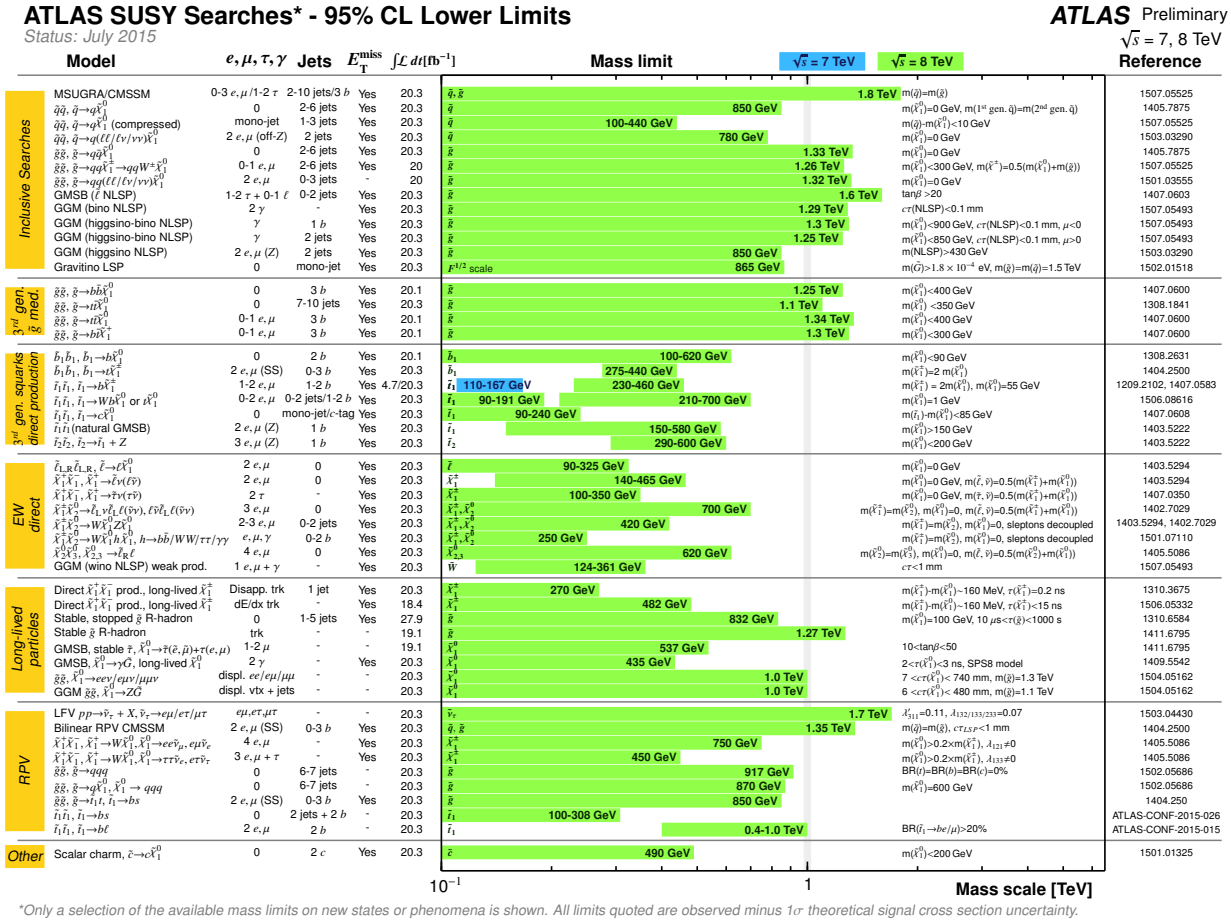


Figure 5.3: Representative summary of the mass reach of ATLAS searches for Supersymmetry. Reproduced from [112].

5.1 Motivation

Chapter 4 detailed a search for a specific final state sensitive to a relatively narrow class of models – coming after the 'first round' of LHC Run-1 analyses the more 'obvious' searches had already been performed, and gains were best made through new techniques targeting less 'obvious' final states. The situation at the beginning of Run-2, with the opening of a new energy frontier and associated large increase in heavy particle cross-sections described above, was the opposite of this. Searches focusing on high-mass particle production decaying to well-studied final states and using established techniques were prioritised. For RPC SUSY searches, the highest mass limits in Run-1 were for gluinos, as can be seen in figure 5.3, so these searches were expected to be the most sensitive to potential discoveries early in Run-2.

The particular $\tilde{g}$ search performed here is motivated by trying to increase sensitivity

to new phenomena that result in high jet multiplicities but relatively little $E_{\mathrm{T}}^{\mathrm{miss}}$. Most 'traditional' searches require high $E_{\mathrm{T}}^{\mathrm{miss}}$ either to trigger on or to reject SM backgrounds, in particular the QCD background for those analyses which veto leptons, and so would be insensitive to these final states despite their striking characteristics. This is exemplified by a scan of the pMSSM parameter space [113], which revealed a certain set of models (see section 5.3.2) which were excluded by this search but by no others in Run-1.

5.2 Introductory details

The analysis described here is an update of a series of previously reported searches for new particles [109, 114–116] in multijet+$E_{\mathrm{T}}^{\mathrm{miss}}$ final states. The most recent of those analyses prior to this one was detailed in a summer 2013 paper [109] based on data from the whole of the $\sqrt{s} = 8$ TeV 2012 proton-proton run, corresponding to an integrated luminosity of $20.3\,\mathrm{fb}^{-1}$. The analysis selected events with no leptons and 7, 8, 9 or greater than 10 jets. Following this, each jet multiplicity was split into three by its b-jet multiplicity – zero, one or at least two – and finally a cut was placed on a proxy for the $E_{\mathrm{T}}^{\mathrm{miss}}$ significance, allowing a non-standard method of estimating the QCD background and permitting the analysis to remain sensitive to new physics scenarios with relatively low $E_{\mathrm{T}}^{\mathrm{miss}}$ – the $E_{\mathrm{T}}^{\mathrm{miss}}$ significance cut translates to $E_{\mathrm{T}}^{\mathrm{miss}} > 80$ GeV for the lowest jet multiplicity region.

The goal was to repeat this search with an expected dataset of between 2 and 5 fb^{-1} of $\sqrt{s} = 13$ TeV data, to be collected with the upgraded ATLAS detector as described in chapter 3. Key changes, which will be described below, included a re-evaluation of signal interpretations, optimisation for discovery rather than exclusion and changes to background estimation as a result of low expected integrated luminosity and a redefinition of $E_{\mathrm{T}}^{\mathrm{miss}}$ as mentioned in section 3.4.6. The results of this update were submitted and accepted for publication in early 2016 [2].

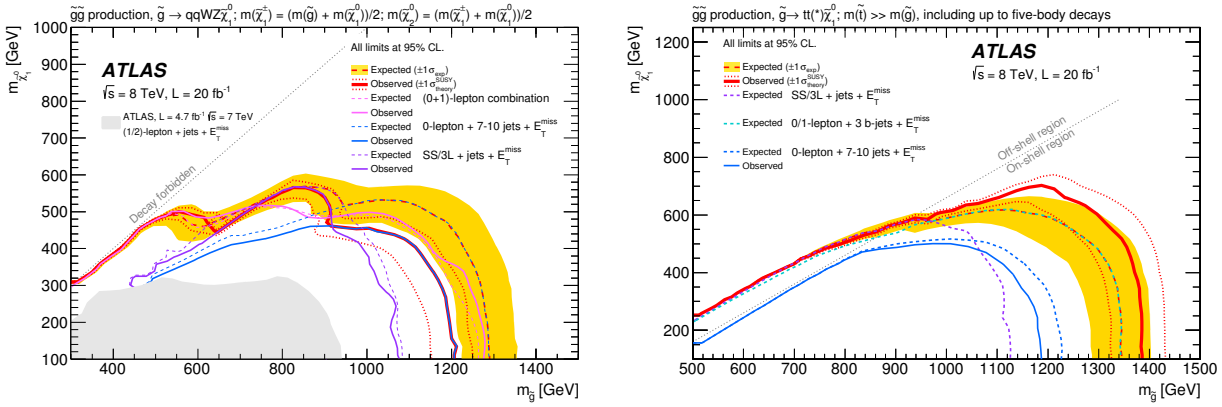


Figure 5.4: Run-1 exclusions, reproduced from [117], showing impact of the multijet ("0-lepton + 7-10 jets + $E_{\mathrm{T}}^{\mathrm{miss}}$ ") search in blue. Left: in the '2-step' grid, where the multijet search has the best sensitivity at high $\tilde{g}$ masses. Right: in the 'gtt' grid, with the multijet limit from [109] overlaid, where this search is uncompetitive at high $\tilde{g}$ masses.

5.3 Signal Models

In Run-1, results were interpreted in many models, setting exclusion limits in various planes of parameter space. Two of these are shown in figure 5.4, which compares these limits with those of other ATLAS searches. These both have pair-produced gluinos, each decaying in the case of gtt directly to $t\bar{t}^{(*)}\tilde{\chi}_1^0$ and in the case of 2-step via a cascade to $qqW^{\pm}Z\tilde{\chi}_1^0$ (see below for details). In the 2-step model, the multijet analysis is the most sensitive one at high $\tilde{g}$ mass, while for the gtt model other (newer) searches were more sensitive. Thus it was decided not to interpret in this model for the early search, but to just set limits in models where the multijet analysis was expected to be the most sensitive. Within this criterion, two SUSY models were selected, as described below.

5.3.1 2-step Model

In addition to being a model where this analysis was the most sensitive in Run-1, the inclusion of the 2-step model also allows direct comparison to Run-1 sensitivity. Pair-produced gluinos decay via the cascade

$\tilde{g} \to qq\ (q = u, d, s, c)\ \tilde{\chi}_1^{\pm},\ \tilde{\chi}_1^{\pm} \to W^{\pm}\tilde{\chi}_2^0,\ \tilde{\chi}_2^0 \to Z\tilde{\chi}_1^0$

leading to the final state $qqqqW^+W^-ZZ\tilde{\chi}_1^0\tilde{\chi}_1^0$. It is defined by mass parameters $m_{\tilde{g}}$ and

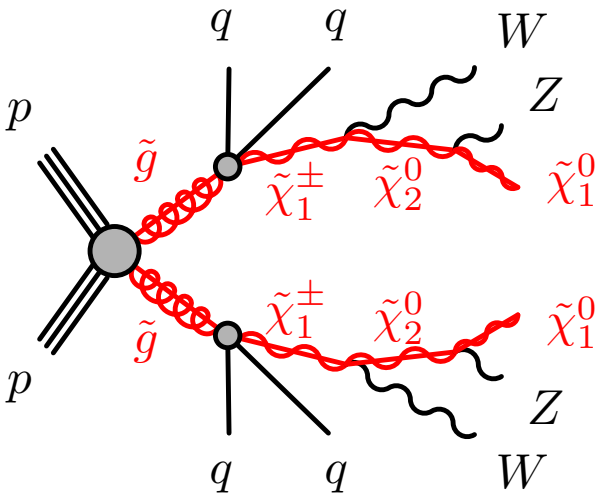


Figure 5.5: The Feynman diagram for the 2-step simplified model.

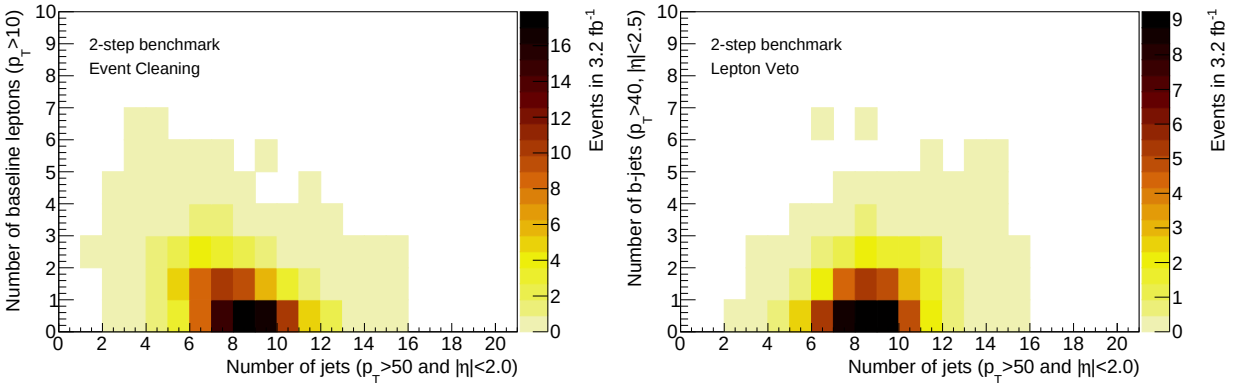


Figure 5.6: The number of jets against: left, the number of baseline leptons following event cleaning and right, the number of b-tagged jets following event cleaning and a lepton veto, for the 2-step benchmark point.

$m_{\tilde{\chi}_1^0}$, with $m_{\tilde{\chi}_1^{\pm}} = \frac{1}{2}(m_{\tilde{g}} + m_{\tilde{\chi}_1^0})$ and $m_{\tilde{\chi}_2^0} = \frac{1}{2}(m_{\tilde{\chi}_1^{\pm}} + m_{\tilde{\chi}_1^0})$. The Feynman diagram for this simplified model is shown in figure 5.5.

The model is characterised by very high jet multiplicity (usually more than 7 jets with $p_{\mathrm{T}} > 50$ GeV, $|\eta| < 2$) and low lepton multiplicity, as can be seen in figure 5.6. There are additionally very few b-tagged jets, as expected since their only source is $Z \to b\bar{b}$, and in fact about a third of b-tagged jets originate from c-jets since these can additionally be produced from $W \to cs$ and then mis-tagged as b-jets with $\sim 22\%$ probability.

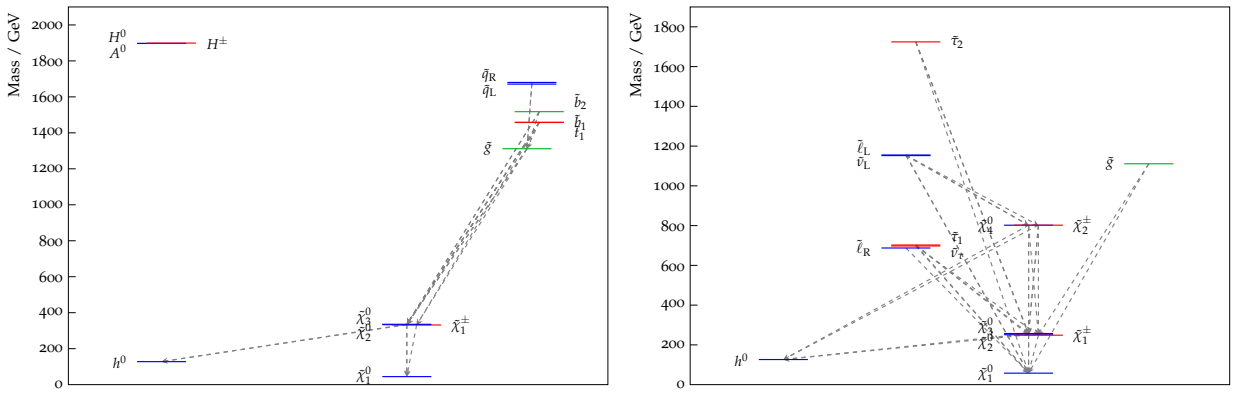


Figure 5.7: The particle spectra for two models which are excluded by the multi-jet search and not by any other ATLAS search in Run-1. Gluino production cross-sections are much higher than those for individual squarks, sleptons and gauginos, such that gluino production dominates both of these models. Produced using *PySLHA* [119] from spectrum files provided by [113], with masses above 2 TeV and decays with branching fraction < 0.1 not shown.

5.3.2 pMSSM-inspired Model

Taking the results of the large scan of SUSY models that was performed for the pMSSM paper [118], a class of models were identified that the Run-1 version of this analysis excluded but that were not excluded by any other analysis. These points tended to have a bino LSP on either the Higgs or Z pole, light higgsinos and a gluino around 1.2 TeV, as can be seen in figure 5.7 which shows the spectra of two representative points.

The relevant parameters thus identified, a slice of this parameter space was formed, varying the higgsino and gluino masses (through μ and M_3 respectively) and fixing the LSP mass by setting M_1 to 60 GeV. The rest of the spectrum was set to $M_A = M_2 = 3$ TeV, $A_\tau = 0$, $\tan\beta = 10$, $A_t = A_b = m_{\tilde{L}_{(1,2,3)}} = m_{(\tilde{e},\tilde{\mu},\tilde{\tau})} = m_{\tilde{Q}_{(1,2,3)}} = m_{(\tilde{u},\tilde{c},\tilde{t})} = m_{(\tilde{d},\tilde{s},\tilde{b})} = 5$ TeV such that the Higgs mass is around 125 GeV.

The typical decay chain of the gluino in these models is exemplified by a 'benchmark' point (just above expected Run-1 exclusion limits), whose spectrum can be seen in figure 5.8, with $(m(\tilde{g}), m(\tilde{\chi}_1^\pm)) = (1300, 200)$ GeV:

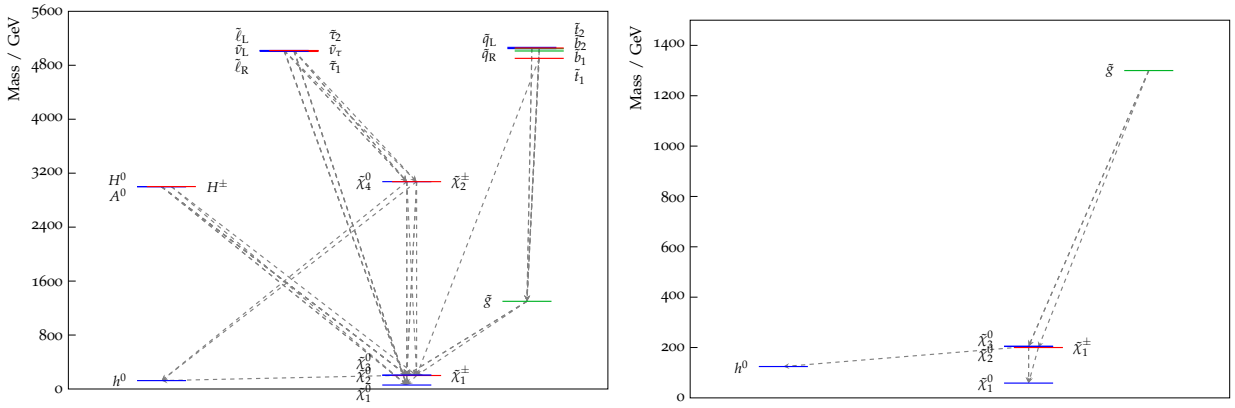


Figure 5.8: The particle spectra for the benchmark simplified model for the Run-2 multijet search. Left: the full spectrum, right: only masses below 2 TeV. Comparing to figure 5.7, it can be see that the key particle content is isolated at low mass. Produced using *PySLHA* [119], with decays with branching fraction < 0.1 not shown.

$$\tilde{g} \rightarrow t + b + \tilde{\chi}_1^{\pm} \quad (44\%) \qquad \tilde{\chi}_1^{\pm} \rightarrow W^{\pm} + \tilde{\chi}_1^0 \quad (100\%)$$

$$\tilde{g} \rightarrow t\bar{t} + \tilde{\chi}_{2,3}^0 \quad (37\%)$$

$$\tilde{g} \rightarrow q\bar{q} + \tilde{\chi}_1^0 \quad (10\%) \qquad \tilde{\chi}_2^0 \rightarrow Z + \tilde{\chi}_1^0 \quad (58\%)$$

$$\tilde{g} \rightarrow t\bar{t} + \tilde{\chi}_1^0 \quad (3\%) \qquad \tilde{\chi}_2^0 \rightarrow h + \tilde{\chi}_1^0 \quad (42\%)$$

$$\tilde{g} \rightarrow g + \tilde{\chi}_{2,3}^0 \quad (3\%)$$

$$\tilde{g} \rightarrow b\bar{b} + \tilde{\chi}_1^0 \quad (1\%) \qquad \tilde{\chi}_3^0 \rightarrow Z + \tilde{\chi}_1^0 \quad (90\%)$$

$$\tilde{g} \rightarrow b\bar{b} + \tilde{\chi}_{2,3}^0 \quad (1\%) \qquad \tilde{\chi}_3^0 \rightarrow h + \tilde{\chi}_1^0 \quad (10\%)$$

These branching fractions are similar for points with chargino masses below 500 GeV and gluino masses over 1200 GeV, and result in large numbers of jets being produced in gluino cascade decays, many of which are b-jets – on average each point has 4 b-jets and 2 c-jets at truth level with $p_{\mathrm{T}} > 40$ GeV and $|\eta| < 2.5$. Further details can be found in appendix B.1.

As shown in figure 5.9, the model is characterised by high jet multiplicity and low numbers of leptons, especially at the highest jet multiplicities where hadronic W and Z decays are preferentially selected. There are additionally large numbers of b-tagged jets as expected, usually 2 or 3 for events with high jet multiplicity.

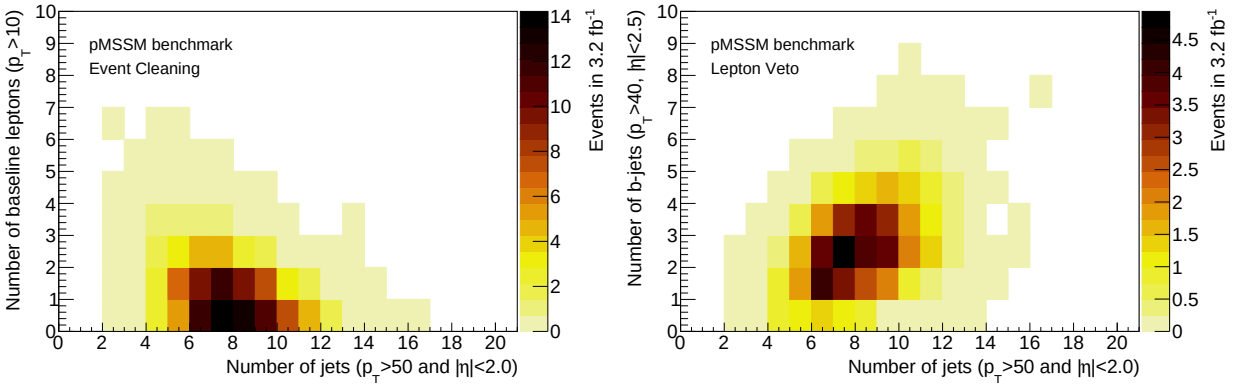


Figure 5.9: The number of jets against: left, the number of baseline leptons following event cleaning and right, the number of b-tagged jets following event cleaning and a lepton veto, for the pMSSM benchmark point.

5.4 Event Selection

The features described above – the lack of leptons, large numbers of jets and different b-jet multiplicities – form the basis of the event selection, with these being three of the four main criteria in defining signal regions (SRs).

5.4.1 Initial selection

Events are recorded based on the decision of two multijet triggers, one requiring five jets with $p_{\mathrm{T}} > 70$ GeV (`5j70`) and the other six jets with $p_{\mathrm{T}} > 45$ GeV and $|\eta| < 2.4$ (`6j45_0eta240`). Following this, events are subject to various cleaning cuts as described in section 3.5. Then, events with any 'baseline' electrons or muons – i.e. those passing relatively loose selection criteria and with $p_{\mathrm{T}} > 10$ GeV – are removed.

5.4.2 Jets selection

A remaining event is then categorised according to one of three criteria. The first two are jet multiplicity counts, n_{50} and n_{80}, which are the number of jets with $|\eta| < 2.0$ having $p_{\mathrm{T}} > 50$ or 80 GeV respectively, corresponding to the efficiency plateaus of the triggers mentioned above. The narrow η range is to exploit the fact that the massive gluinos are likely to be

produced at rest, and hence decay to fairly central jets, while the main backgrounds result from much lower mass progenitors which are more likely to be boosted longitudinally, and hence give rise to jets in the forward or backward directions.

The next criterion is $n_{b\text{-jet}}$, the number of b-tagged jets (using the *MV2c20* algorithm, at the 70% efficiency *operating point*) that have $p_{\mathrm{T}} > 40$ GeV and lie within $|\eta| < 2.5$ (the extent of the inner detector, beyond which accurate tracking cannot be performed). This b-tagging point, with a c-jet rejection factor of 8 and a light-jet rejection factor of 400 in $t\bar{t}$ MC, was found to give the better expected discovery reach in the pMSSM grid compared to both looser and tighter b-tagging requirements, balancing signal acceptance and background rejection. These b-tagged jets are henceforth referred to as b-jets.

Regions are named based on these jet selection criteria, e.g. `8ij50-1ib` for a region with at least 8 jets of 50 GeV p_{T} and at least one b-jet, and `6ej80-0eb`, for a region with exactly 6 jets of 80 GeV p_{T} and no b-jets ("i" for inclusive, i.e. $\geq N$, and "e" for exclusive, i.e. $= N$ jets or b-jets). The inclusive / exclusive marker may be omitted, in which case the region should be assumed to be inclusive, and likewise the '0ib' may not be stated (such that `8j50` and `8ij50-0ib` are equivalent). The signal regions are shown in table 5.1, and consist of the multiplicity requirements $n_{50} \geq 8$, ≥ 9 or ≥ 10 and $n_{80} \geq 7$ or ≥ 8, each for the three b-jet requirements $n_{b\text{-jet}} \geq 0$, ≥ 1 or ≥ 2, making 15 SRs in total. This choice of overlapping and inclusive signal regions was made in order to maximise discovery potential for an unknown signal and in the face of uncertain integrated luminosity projections.

5.4.3 $E_{\mathrm{T}}^{\mathrm{miss}}$ selection

The cross-section of QCD multijet production, hereafter referred to simply as the 'multijet' background, is so large that even at such high multiplicities it is hugely dominant. The signal models considered clearly both have a certain amount of $E_{\mathrm{T}}^{\mathrm{miss}}$, both from the non-interacting $\tilde{\chi}_1^0$ and from $Z \to \nu\nu$. This is plotted in figure 5.10, which shows how this separates signal and backgrounds, particularly multijet. However, in order to maintain a reasonable signal efficiency for these cascade decays, with the presence of many intermediate

	8j50	8j50-1b	8j50-2b	9j50	9j50-1b	9j50-2b	10j50	10j50-1b	10j50-2b
n_{50}	≥ 8			≥ 9			≥ 10		
$n_{b\text{-jet}}$	—	≥ 1	≥ 2	—	≥ 1	≥ 2	—	≥ 1	≥ 2
$E_{\mathrm{T}}^{\mathrm{miss}}/\sqrt{H_T}$	$> 4\,\mathrm{GeV}^{1/2}$								

(a) Signal regions using n_{50}

	7j80	7j80-1b	7j80-2b	8j80	8j80-1b	8j80-2b
n_{80}	≥ 7			≥ 8		
$n_{b\text{-jet}}$	—	≥ 1	≥ 2	—	≥ 1	≥ 2
$E_{\mathrm{T}}^{\mathrm{miss}}/\sqrt{H_T}$	$> 4\,\mathrm{GeV}^{1/2}$					

(b) Signal regions using n_{80}

Table 5.1: Definition of the signal regions. A long dash '—' indicates that no requirement is made. Events with leptons are vetoed.

particles 'diluting' the $E_{\mathrm{T}}^{\mathrm{miss}}$, a reasonable selection value of ~ 200 GeV leaves a background composed of at least 50% multijet. Multijet production is poorly modelled at such high jet multiplicities, and data-driven methods such as that used in the scharm analysis typically rely on applying and then inverting a cut on geometric variables such as $\Delta\phi(\text{jet}, E_{\mathrm{T}}^{\mathrm{miss}})$. This is problematic in this case, since because of the high jet multiplicity there is a fairly high chance that real $E_{\mathrm{T}}^{\mathrm{miss}}$ will fall close to a jet, reducing signal acceptance by around 60% for the 2-step benchmark model when requiring $\Delta\phi(\text{jet}, E_{\mathrm{T}}^{\mathrm{miss}}) > 0.4$. This can be seen in figure 5.11, where both the poor multijet modelling and propensity of signal to lie at low values are evident.

An alternative variable that can be used as a discriminant is $E_{\mathrm{T}}^{\mathrm{miss}}/\sqrt{H_T}$, with H_T being the sum of the jets' transverse momenta. This variable is a proxy for the $E_{\mathrm{T}}^{\mathrm{miss}}$ significance (i.e. $E_{\mathrm{T}}^{\mathrm{miss}}/\sigma(E_{\mathrm{T}}^{\mathrm{miss}})$, where $\sigma(E_{\mathrm{T}}^{\mathrm{miss}})$ is the uncertainty on the measured value of $E_{\mathrm{T}}^{\mathrm{miss}}$) when its error is dominated by jet mismeasurement, which is the case in high multiplicity QCD events. Its distribution is shown in figure 5.12.

Figure 5.13 shows that $E_{\mathrm{T}}^{\mathrm{miss}}/\sqrt{H_T}$ and $E_{\mathrm{T}}^{\mathrm{miss}}$ are, as one would expect, highly correlated. The slightly steeper slope for the signal point means that $E_{\mathrm{T}}^{\mathrm{miss}}$ has a better background rejection for a given signal efficiency, however this is rendered obsolete by the fact that the

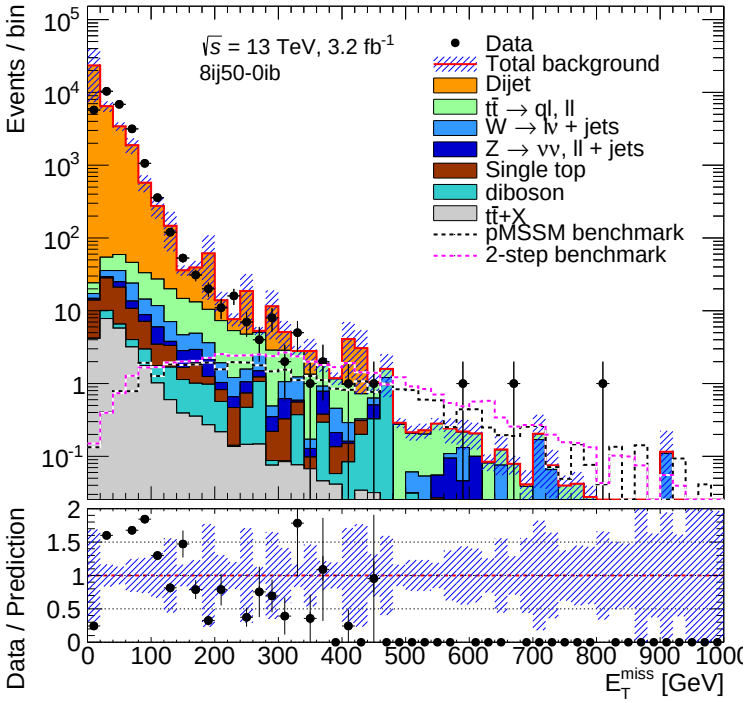


Figure 5.10: $E_{\mathrm{T}}^{\mathrm{miss}}$ distribution in `8ij50` for expected backgrounds from simulation, including the multijet contribution in orange, the benchmark signal models in the dashed lines and data in black. For all values below 400 GeV, the multijet component comprises at least half of the total.

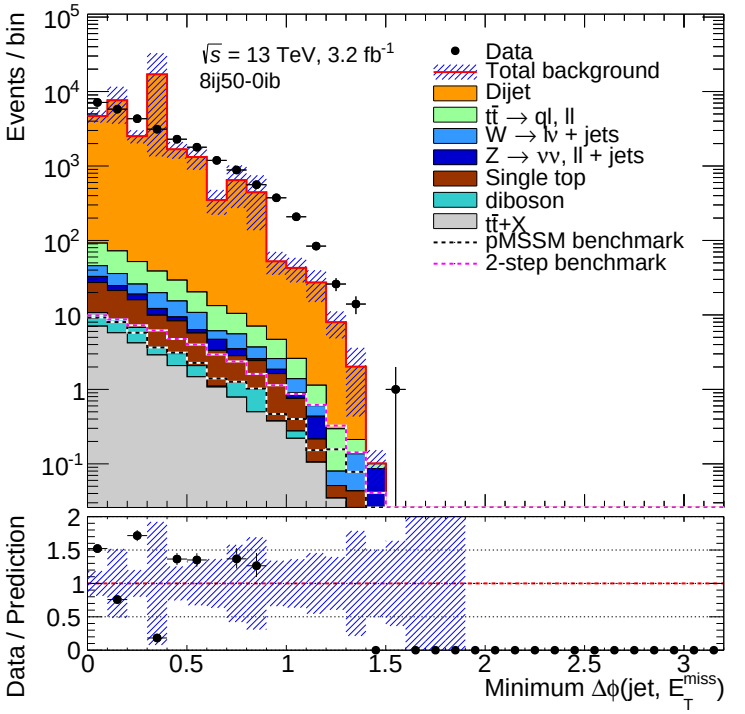


Figure 5.11: Minimum $\Delta\phi$ between a jet and the $E_{\mathrm{T}}^{\mathrm{miss}}$ in `8ij50`. The signal shape is very similar to the dominant multijet background, meaning that no appreciable improvement in multijet rejection is expected as a result of the imposition of a selection on this variable.

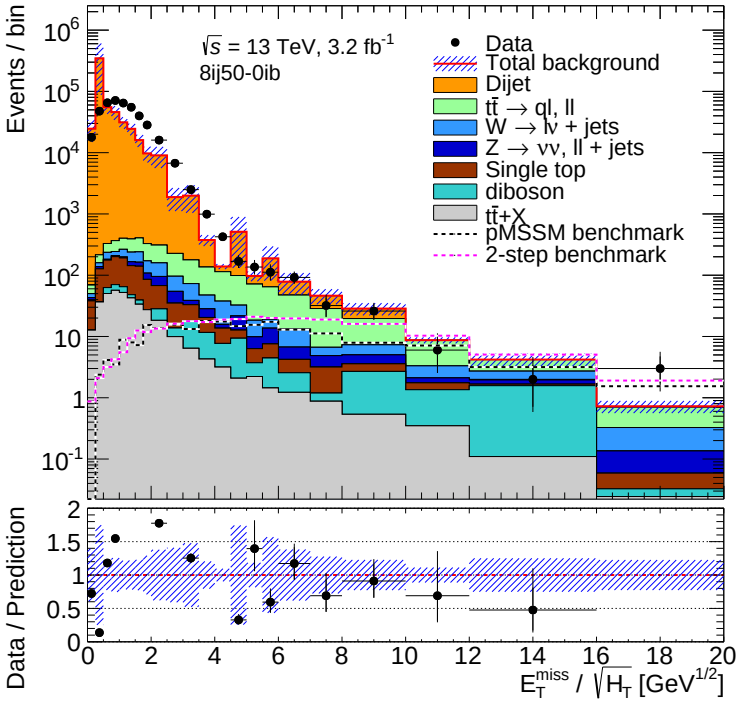


Figure 5.12: $E_{\mathrm{T}}^{\mathrm{miss}}/\sqrt{H_T}$ distribution in `8ij50`.

$E_{\mathrm{T}}^{\mathrm{miss}}/\sqrt{H_T}$ distribution can, in contrast to $E_{\mathrm{T}}^{\mathrm{miss}}$, be estimated well from data for the multijet background, as will be described in section 5.6. For signal regions, a value of $E_{\mathrm{T}}^{\mathrm{miss}}/\sqrt{H_T} > 4$ GeV$^{1/2}$ is required – a balance between background rejection and signal efficiency.

5.4.4 Extra pileup rejection and event cleaning

In order to ensure the $E_{\mathrm{T}}^{\mathrm{miss}}$ is in fact dominated by jet mismeasurement, extra care is taken to remove other sources of $E_{\mathrm{T}}^{\mathrm{miss}}$ by applying more stringent requirements than the standard event cleaning and pileup suppression described in section 3.5.

Since this search selects jets above 50 GeV, the upper cut-off of standard pileup suppression, it is overly sensitive to pileup jets slightly above this which, although rare, are not nonexistent. If a pileup event leads to jets either side of the 50 GeV threshold, the softer one is likely to be identified as such and removed from the calculation. The same is true if the 'recoil' from the harder jet is not itself clustered into a jet, since the $E_{\mathrm{T}}^{\mathrm{miss}}$ 'soft term' – i.e. the residual contribution once all reconstructed objects (jets, electrons, muons and photons) are considered – is built from tracks and so has little sensitivity to hadronic

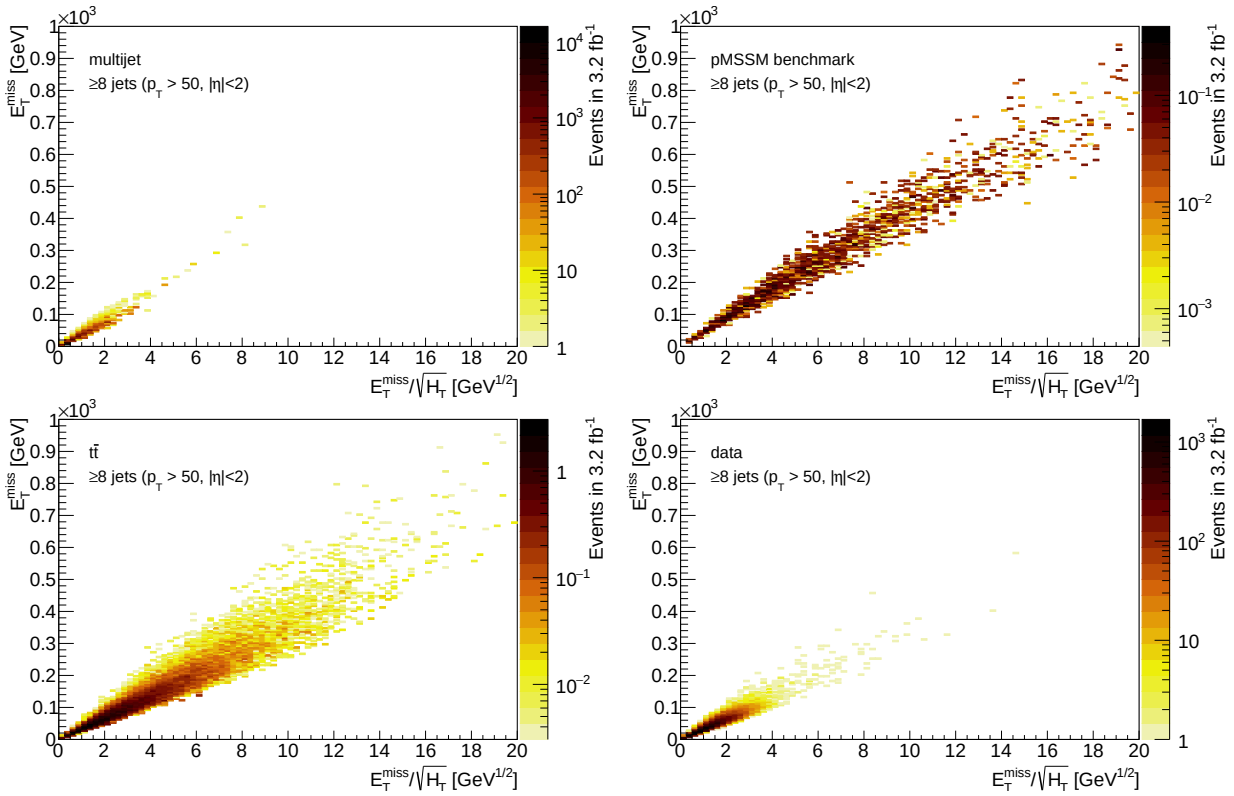


Figure 5.13: $E_{\mathrm{T}}^{\mathrm{miss}}/\sqrt{H_T}$ vs $E_{\mathrm{T}}^{\mathrm{miss}}$ following a lepton veto and requiring at least 8 jets, for top left: the multijet background, top right: the pMSSM signal benchmark model, bottom left: the dominant $t\bar{t}$ background and bottom right: data.

activity not from the primary vertex. However, the harder jet will contribute to the $E_{\mathrm{T}}^{\mathrm{miss}}$ calculation, and will have no balancing jet or soft component, and so will lead to $E_{\mathrm{T}}^{\mathrm{miss}}$ in the direction opposite to itself. The acceptance of such events is reduced by applying the standard pileup rejection to jets with p_{T} between 50 and 70 GeV that are back-to-back with the $E_{\mathrm{T}}^{\mathrm{miss}}$, i.e. $\Delta\phi(\mathrm{jet}, E_{\mathrm{T}}^{\mathrm{miss}}) > 2.2$. Among events with pileup jets above the 50 GeV threshold (5% and 17% of those with $E_{\mathrm{T}}^{\mathrm{miss}}/\sqrt{H_T} < 2$ and > 3 GeV$^{1/2}$ respectively), the prevalence of high $E_{\mathrm{T}}^{\mathrm{miss}}/\sqrt{H_T}$ events with this jet opposite the $E_{\mathrm{T}}^{\mathrm{miss}}$ is shown is figure 5.14. Rejecting these events reduces signal acceptance by less than 1% in the region of the expected discovery / exclusion limit, and increases the sensitivity boundary by about 50 GeV in gluino mass.

As mentioned in section 3.3.2, there were some malfunctioning regions of the TileCal during 2015 data taking, meaning that jets overlapping these regions are likely to have their energies undermeasured. This is demonstrated in figure 5.15, where the dead region in the tile barrel is clearly visible from the excess of high $E_{\mathrm{T}}^{\mathrm{miss}}/\sqrt{H_T}$ events with the jet closest to

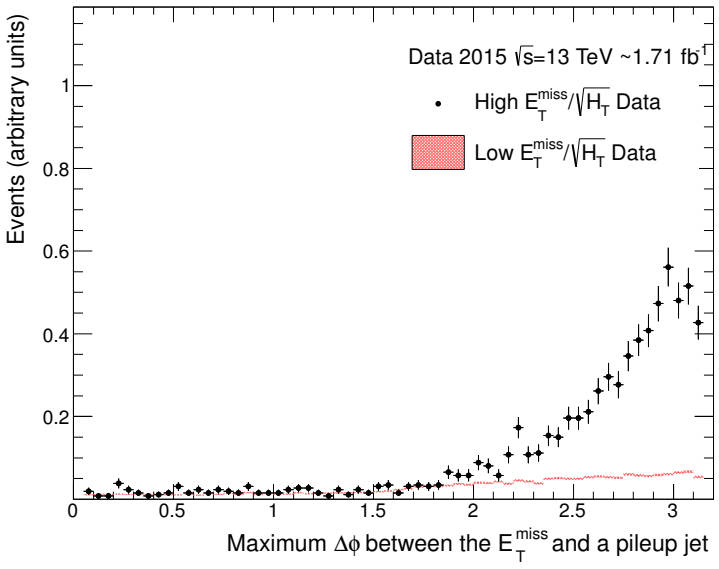


Figure 5.14: Maximum $\Delta\phi$ between a jet failing the pileup rejection requirements and the $E_{\mathrm{T}}^{\mathrm{miss}}$ in 6-jet data for high (> 3) and low (< 2) $E_{\mathrm{T}}^{\mathrm{miss}}/\sqrt{H_T}$ separately. Plot made by collaborator.

the $E_{\mathrm{T}}^{\mathrm{miss}}$ falling in it. Thus events where the jet closest to the $E_{\mathrm{T}}^{\mathrm{miss}}$ lies within $0.8 < \phi < 1.1$. and $-0.1 < \eta < 1.0$ are removed. This again has a sub-1% effect on signal acceptance while significantly reducing the QCD background.

Following the final selection, the signal region compositions are shown in figure 5.16. Both multijet and other backgrounds, collectively known as 'leptonic' backgrounds, are seen to be important, each comprising roughly half the total. The next section describes how each type of background is estimated.

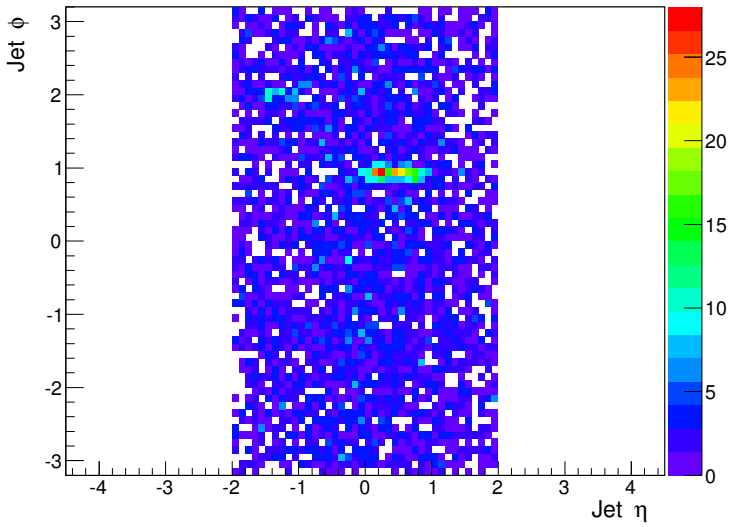
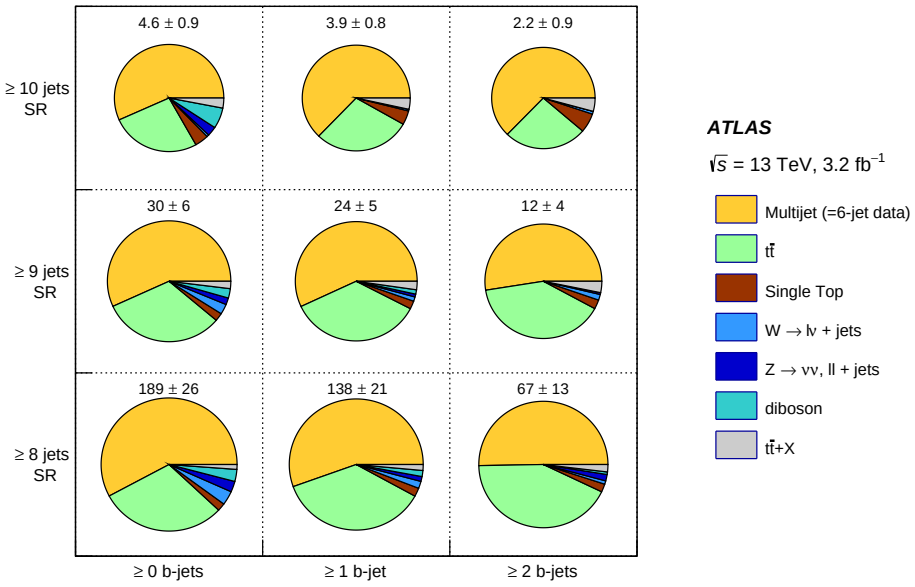
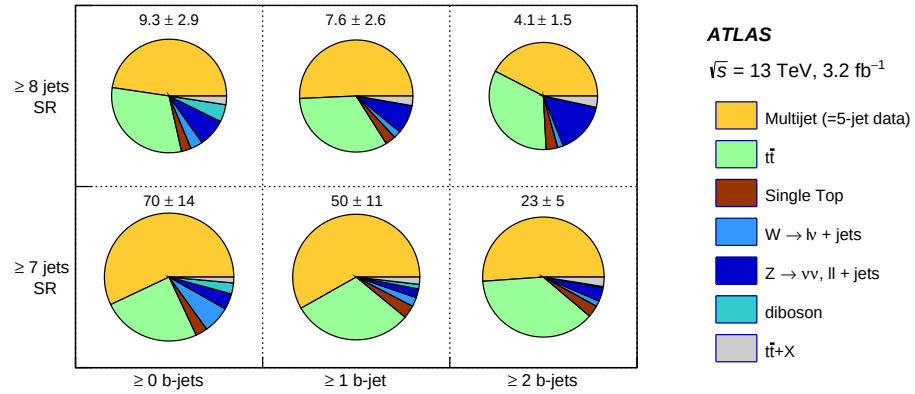


Figure 5.15: η–ϕ map for the jet closest to the $E_{\mathrm{T}}^{\mathrm{miss}}$ in ϕ, in data events in `6j50` with $E_{\mathrm{T}}^{\mathrm{miss}}/\sqrt{H_T} > 4$ GeV$^{1/2}$. Plot made by collaborator.



(a) n_{50}



(b) n_{80}

Figure 5.16: Final signal region compositions, after the background estimation described in sections 5.5 and 5.6. The area of each pie chart is scaled to $\log_{10}$ of the total expected yield (which is printed above each one).

5.5 Leptonic background estimation

The two classes of background, multijet and leptonic, are estimated in different ways. As stated above, the multijet background cannot be reliably estimated from simulation, and so its estimate is entirely data-driven, and will be described in section 5.6. Since the estimation of this background, and the uncertainties thereon, rely on first having estimated the leptonic backgrounds, the process by which this is performed is described first.

Simulation of leptonic backgrounds is simpler than of the multijet one, since lower orders of QCD calculation and resummation are required to reach high accuracy for a given jet multiplicity. Thus the smaller backgrounds are determined entirely from simulation, and the larger ones rely on simulation normalised to data in dedicated control regions. The principle behind the leptonic background estimate is identical to that employed in the scharm analysis, as described in section 4.5.1, so will not be described in detail here.

5.5.1 Leptonic background simulation

$t\bar{t}$ and single top quarks in the Wt and s-channels [120] are generated using `Powheg-Box` v2 [121] with the CT10 PDF set [122] in the matrix element calculations. Electroweak t-channel single-top-quark events are generated using `Powheg-Box` v1. For this process, the top quarks are decayed using `MadSpin` [123] preserving all spin correlations, while for all processes the parton shower, fragmentation, and the underlying event are simulated using `PYTHIA` v6.428 [124] with the CTEQ6L1 PDF set [125] and the corresponding Perugia 2012 tune [126]. The top quark mass is set to 172.5 GeV. The `EvtGen` v1.2.0 program [127] models the bottom and charm hadron decays, as it does for all non-`SHERPA`-simulated processes mentioned below. Prior to the fit, the $t\bar{t}$ simulation is normalised to the cross-section calculated to next-to-next-to-leading order (NNLO) in perturbative QCD, including soft-gluon resummation to next-to-next-to-leading-log (NNLL) accuracy [128].

Events containing $t\bar{t}$ and additional heavy particles – comprising three-top, four-top, $t\bar{t}+W$, $t\bar{t}+Z$ and $t\bar{t}+WW$ production [129] – are simulated at NLO (LO for three-

top) using MadGraph v2.2.2 [130] with up to two additional partons in the matrix element, interfaced to PYTHIA 8.186 [124,131], with the A14 tune of the PYTHIA parameters [132] and the NNPDF2.3LO PDF set [133].

Events containing W or Z bosons with associated jets [134] are likewise simulated using MadGraph interfaced to PYTHIA 8 with the same tunes and particle decay programs, but with up to four additional final-state partons in the matrix element. The W+jets and Z+jets events are normalised to NNLO cross-sections [94]. Diboson processes with at least one boson decaying leptonically [135] are simulated using the SHERPA v2.1.1 generator [93]. The matrix element calculations contain all diagrams with four electroweak vertices. They are calculated at NLO for up to one (for 4ℓ, $2\ell{+}2\nu$, semileptonic ZZ) or no additional partons (for $3\ell{+}1\nu$, other semileptonic processes), and at LO for up to three additional partons. This is performed by the Comix [136] and OpenLoops [137] matrix element generators interfaced with the SHERPA parton shower [138] using the ME+PS@NLO prescription [139]. The CT10 PDF set is used in conjunction with dedicated parton shower tuning developed by the SHERPA authors.

5.5.2 Control regions

For each of the five jet multiplicities considered (and inclusive of b-jet multiplicity), two control regions are defined as shown in table 5.2 – one requiring no b-jets and one with at least one, in order to select W+jets and $t\bar{t}$ events respectively. These both require the presence of exactly one baseline lepton, which must additionally pass the signal requirements described in section 3.4 and have $p_{\mathrm{T}} > 20$ GeV to avoid contamination from fakes. This lepton is treated as a jet for the purposes of the H_T, $E_{\mathrm{T}}^{\mathrm{miss}}/\sqrt{H_T}$ and n_{jet} calculations – so long as it satisfies the relevant p_{T} and η requirements – although given the much lower selection threshold it often does not.

As can be seen in figure 5.17, which shows m_{T} distributions in the 7j50-1b and 9j50-0b control regions, there is significant signal contamination at high m_{T} for higher multiplicity regions (dominated by 2-step points in 0eb regions and pMSSM in 1ib ones). Thus an upper

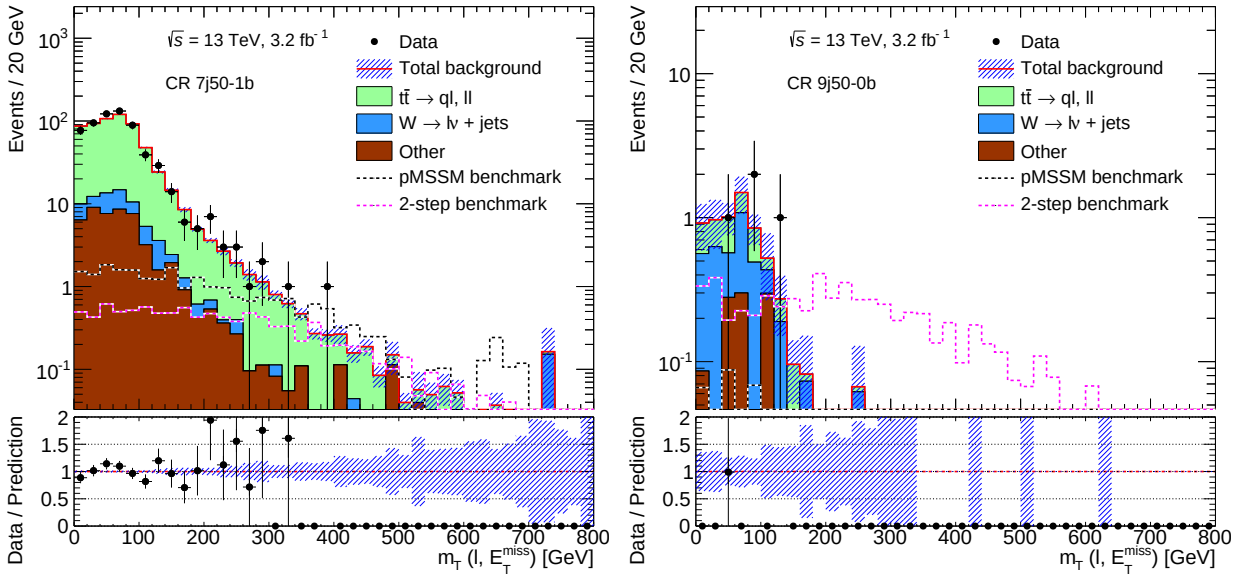


Figure 5.17: Transverse mass distribution in the `7j50-1b` (left) and `9j50-0b` (right) control regions before applying the upper bound on this variable at 120 GeV.

bound of 120 GeV is placed on the transverse mass m_{T} in order to suppress this without reducing the $t\bar{t}$ and W+jets contributions too much.

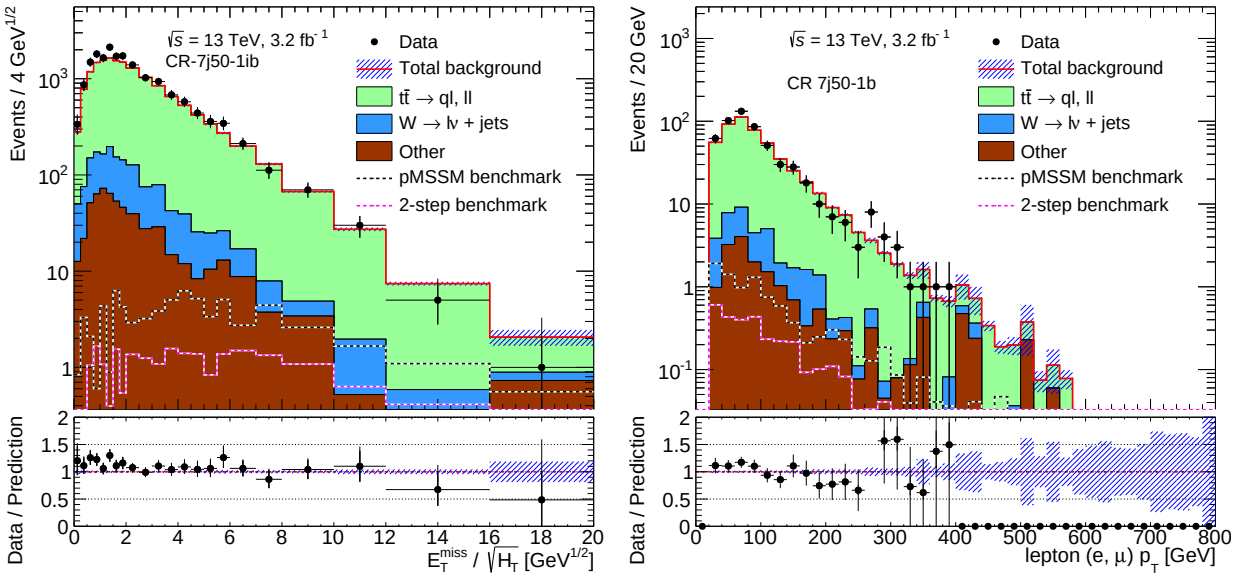
In order to obtain reasonable event counts and hence reasonable constraining power in these control regions, the n_{jet} and $E_{\mathrm{T}}^{\mathrm{miss}}/\sqrt{H_T}$ selections are both loosened slightly with respect to the signal regions – n_{jet} to one fewer than the corresponding signal region, and $E_{\mathrm{T}}^{\mathrm{miss}}/\sqrt{H_T}$ to $> 3\,\mathrm{GeV}^{1/2}$. Since both are well-modelled, as shown in figures 5.18 and 5.19, the resulting extrapolation between SR and CR is not problematic, although it does lead to some systematic uncertainties being larger than they otherwise would be (see later sections). Crucially, however, the control regions are all of sufficiently high jet multiplicity that the signal region triggers can be used. This means that a lower lepton p_{T} threshold is possible (it would have to be 25 GeV if single electron and muon triggers were used) which gives a larger data sample in these control regions.

5.5.3 Theoretical systematic uncertainties

Theoretical systematic uncertainties were introduced in section 4.6.2. They are treated similarly here, except that the relevant sample comparisons are performed on samples at

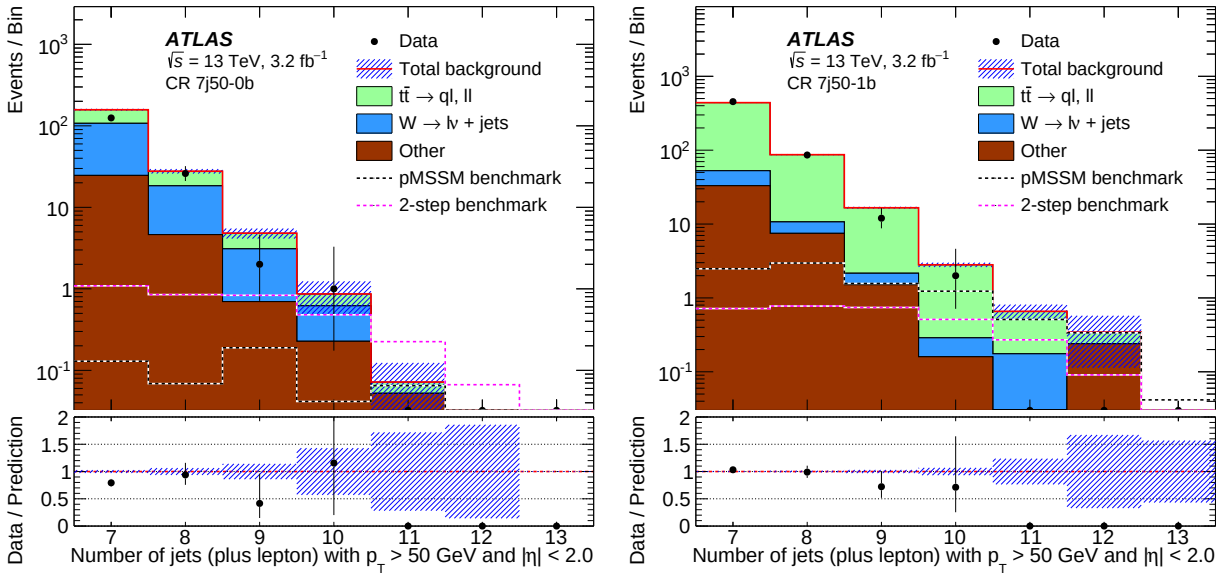
SR name	***n*j50 or *n*j50-1b or *n*j50-2b**		***n*j80 or *n*j80-1b or *n*j80-2b**	
CR name	**(*n* − 1)j50-0b**	**(*n* − 1)j50-1b**	**(*n* − 1)j80-0b**	**(*n* − 1)j80-1b**
p_{T}^{ℓ} ($\ell \in \{e\,\mu\}$)	> 20 GeV			
m_{T}	< 120 GeV			
$E_{\mathrm{T}}^{\mathrm{miss}}/\sqrt{H_T}$	$> 3\,\mathrm{GeV}^{1/2}$			
n_{50}	$\geq n_{50} - 1$		—	
n_{80}	—		$\geq n_{80} - 1$	
$n_{b\text{-jet}}$	0	≥ 1	0	≥ 1

Table 5.2: Leptonic control region definitions for each of the signal regions. In the names, the symbols n and $n-1$ refer to the corresponding jet multiplicity requirements. For example the three signal regions `9j50`, `9j50-1b` and `9j50-2b` are each independently controlled by both the `8j50-0b` and `8j50-1b` control regions.



(a) $E_{\mathrm{T}}^{\mathrm{miss}}/\sqrt{H_T}$ (b) Lepton p_{T}

Figure 5.18: $E_{\mathrm{T}}^{\mathrm{miss}}/\sqrt{H_T}$ and lepton p_{T} distributions in the `7j50-1b` control region, showing good agreement between $t\bar{t}$ MC and data.



(a) $n_{b\text{-jet}} = 0$ (b) $n_{b\text{-jet}} \geq 1$

Figure 5.19: Jet multiplicity distributions for the `7j50` control regions (and by extension all n_{50} ones). The lepton is permitted to contribute to the jet multiplicity count and to H_T. All backgrounds are normalised according to their theoretical (pre-fit) cross-sections, and the blue hatched band is the statistical uncertainty on MC predictions (no systematic uncertainties shown). Plot also in [2].

reconstructed level rather than truth, since the relevant samples were available to make this improved comparison (albeit with fast calorimeter simulation for $t\bar{t}$). They are considered for all simulated samples, although only evaluated in detail for $t\bar{t}$ and W+jets.

For $t\bar{t}$, by far the most important process, several samples are compared. Samples are produced with the factorisation and renormalisation scales varied coherently, along with variations of the resummation damping parameter and with more/less radiation tunes of the parton shower [140]. Additionally the nominal sample is compared to one with `Powheg-Box` interfaced with `Herwig++` [39] and to a `SHERPA` v2.1.1 sample with up to one additional jet at next-to-leading order using `OpenLoops` and up to four additional jets at leading order, to account for uncertainties in the parton shower and the generator respectively. The comparison with the `SHERPA` sample dominates the uncertainty in the signal region prediction.

For W+jets the uncertainty resulting from the generator choice is given by a comparison of the nominal (`MadGraph` interfaced with `PYTHIA` 8) to `SHERPA`. There were no variations samples available for the nominal generator, so they are emulated by reweighting the nom-

inal sample according to the number of truth jets in an event, as determined from SHERPA variations, in a similar fashion to Z+jets in the scharm analysis.

In contrast to the procedure followed in the scharm search (chapter 4), the $t\bar{t}$ and W+jets theoretical uncertainties are calculated for each region in turn and input to the fit in the same way as experimental uncertainties. Table 5.3 shows these uncertainties in the 8j50 signal regions and their 7j50 control regions, demonstrating the reasonable degree of cancellation of these uncertainties between signal and control regions. For higher jet multiplicities, statistical uncertainties become large such that the systematic uncertainties are often dominated by them; and $t\bar{t}$ theory uncertainties are among the largest sources of uncertainty on the final background estimate (see section 5.7).

Systematic	8ij50-0ib	8ij50-1ib	8ij50-2ib	7ij50-1ib	7ij50-0eb
$t\bar{t}$ Radiation	30.72 ± 4.66	29.50 ± 4.90	29.77 ± 6.64	18.57 ± 1.51	30.43 ± 4.26
$t\bar{t}$ Parton Shower	-26.05 ± 5.09	-25.21 ± 5.44	-7.30 ± 7.25	-9.10 ± 1.77	-29.11 ± 4.84
$t\bar{t}$ Generator	-60.51 ± 6.67	-57.40 ± 7.18	-63.46 ± 9.73	-20.73 ± 2.85	-32.64 ± 7.68
W+jets Generator	-1.11 ± 7.69	23.69 ± 13.26	49.09 ± 23.78	12.13 ± 5.10	15.22 ± 3.41
W+jets Ren. scale	-10	—	—	—	-30
W+jets Fac. scale	46	—	—	—	10

Table 5.3: Theoretical systematic uncertainties, in percent, for the 8j50 signal regions and their 7j50 control regions. For each uncertainty (apart from W+jets scales), the first number is the systematic variation and the second is statistical uncertainty (from limited MC statistics) associated with it.

For other backgrounds, for which variations are either not available or severely statistically limited, a global uncertainty is taken – drawn from the $t\bar{t}$ and W+jets values established above, and including the cross-section uncertainties for each process – as follows:

- di-boson: 50%
- Z+jets: 40%
- $t\bar{t} + X$: 30%
- Single top: 30%

5.5.4 Experimental systematic uncertainties

Various aspects of event reconstruction and recording in ATLAS are subject to a certain amount of uncertainty. These are accounted for by re-running object calibration event-by-event with altered parameters that reflect the window of uncertainty on each. For this analysis, and for the scharm one, the dominant experimental systematic uncertainties arise from jet energy determination and flavour tagging. They were evaluated only for $t\bar{t}$, W+jets and signal in order to save computation time, with the values for other MC-determined processes being taken as the $t\bar{t}$-derived ones. Since these other backgrounds are a very small fraction of the total, and since their uncertainties are mostly dominated by MC statistics, any falsities inherent in this approximation will have a negligible impact on the final result.

Calibration of the b-tagging algorithms was performed with 2012 data, and only updated to 2015 conditions through simulation studies, so the description in section 4.3 for c-tagging with *JetFitterCharm* applies equally to b-tagging with *MV2c20* here. The resulting uncertainties led to a variation in expected yields of around 10 % for the `2b` signal regions.

ATLAS's jet calibration is described in section 3.4.4. It relies both on MC simulation and data, being performed by studying the momentum balance between well-measured reference objects and recoiling jet(s) to calibrate the reconstruction of jet energies, known as the Jet Energy Scale or JES. There are over 30 resulting variations extracted, which can be combined into sets of four 'reduced' variations in four different ways. The set of combinations found to give the largest value for the uncertainty is the one used, with one of the four variations dominating and leading to changes in yield of up to 20%. A closely related uncertainty is that on the Jet Energy Resolution (JER), which accounts for the difference between the true event-by-event jet energy and the post-JES calibration value, which is a set of calibrations on average properties. This yields an extra resolution of about 10%, and the uncertainty on this leads to differences of at most 5% for the multijet analysis.

5.6 Multijet background estimation

The key to this data-driven method is the observation (first made in Run-1) that the shape of the $E_{\mathrm{T}}^{\mathrm{miss}}/\sqrt{H_T}$ distribution is close to invariant under changes in jet multiplicity. The same is shown to be approximately true for Run-2 data in figure 5.20. Taking advantage of this shape invariance, the multijet background in the high multiplicity signal regions can be estimated from lower multiplicity control regions.

5.6.1 Method

First, since the non-QCD backgrounds are not expected to necessarily display the same $E_{\mathrm{T}}^{\mathrm{miss}}/\sqrt{H_T}$ invariance with jet multiplicity, their expected contribution is subtracted from the data distribution[1]. The resulting $E_{\mathrm{T}}^{\mathrm{miss}}/\sqrt{H_T}$ template is then applied to the signal region multiplicities, normalised to the SR data in the region $E_{\mathrm{T}}^{\mathrm{miss}}/\sqrt{H_T} < 1.5\,\mathrm{GeV}^{1/2}$ where signal contributions are negligible compared to the multijet background. For the n_{50} SRs, the $E_{\mathrm{T}}^{\mathrm{miss}}/\sqrt{H_T}$ shape is taken from regions with 6 jets, and for the n_{80} ones from 5-jet regions. This is two lower than the lowest SR multiplicity in order to be able to validate the method on the first extrapolation, as will be detailed below.

5.6.2 $\boldsymbol{E}_{\mathbf{T}}^{\mathbf{miss}}$ definition changes

As mentioned in chapter 3, the $E_{\mathrm{T}}^{\mathrm{miss}}$ calculation changed between Run-1 and Run-2. In Run-1 the soft term was constructed from calorimeter clusters not associated to any hard objects and was known as the 'calorimeter soft term' or CST. This was sensitive to pileup since an individual calorimeter cluster cannot be associated definitively to the PV, so in anticipation of higher pileup running the default $E_{\mathrm{T}}^{\mathrm{miss}}$ definition was changed to one using inner-detector tracks to evaluate the soft term, called the 'track soft term' or TST. Figure 5.21 shows the difference between these two definitions, with the new TST definition having a narrower $E_{\mathrm{T}}^{\mathrm{miss}}/\sqrt{H_T}$ distribution.

[1] This is done prior to the fit discussed in section 5.7.

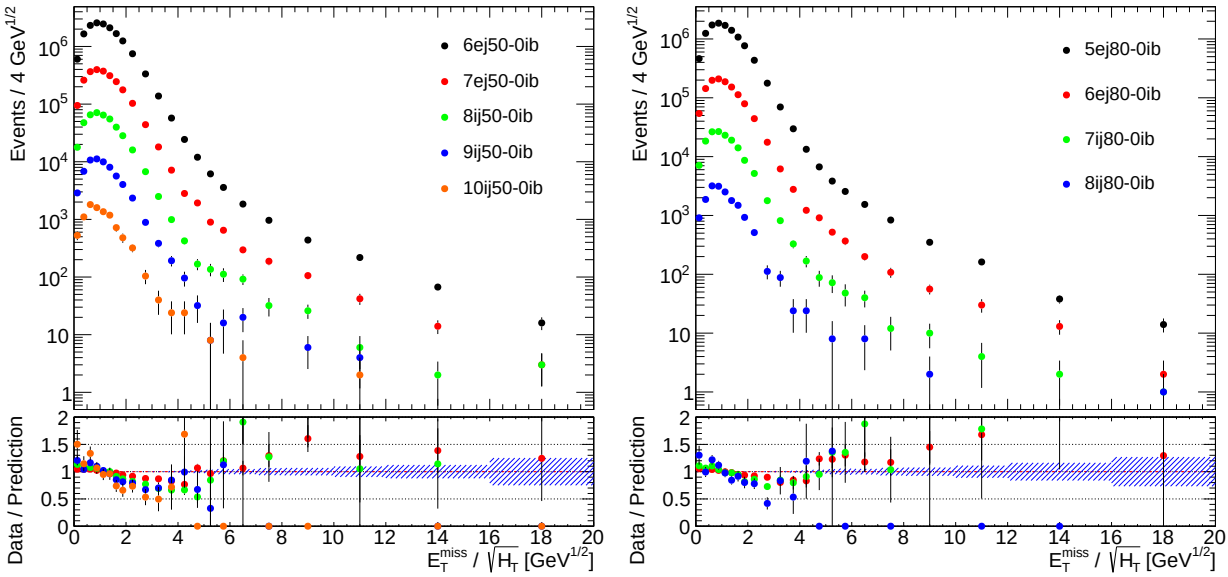


Figure 5.20: Data for varying jet multiplicities and no b-jet selection, left for jets with $p_{\mathrm{T}} > 50$ GeV and right for those with $p_{\mathrm{T}} > 80$ GeV. The ratio plots compare data to the 'prediction' provided by the shape of the lowest multiplicity data. These ratios are fairly flat, especially for lower multiplicities, meaning that the shape at high multiplicity can be reasonably obtained from that at low multiplicity.

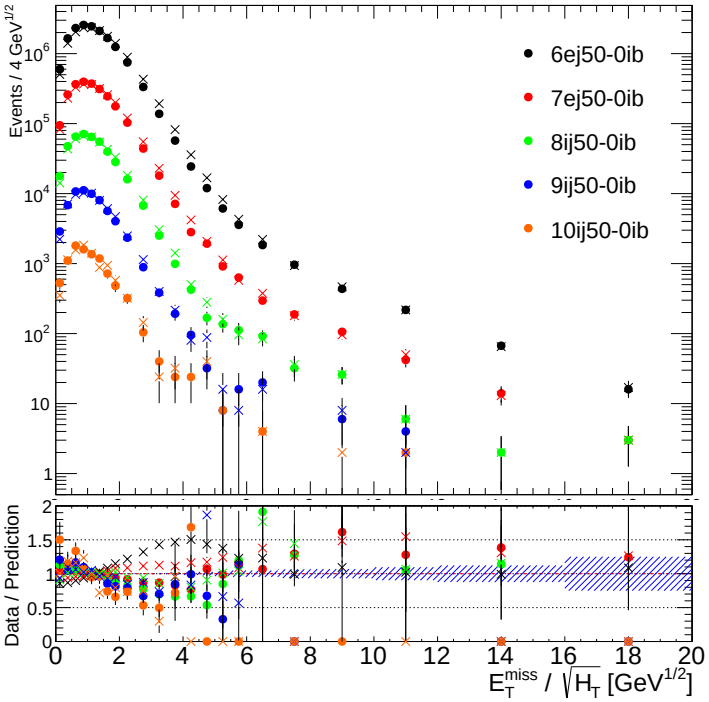


Figure 5.21: Data for varying jet multiplicities and no b-jet selection, as in figure 5.20, for jets with $p_{\mathrm{T}} > 50$ GeV. The crosses mark the distributions for CST $E_{\mathrm{T}}^{\mathrm{miss}}$, and the solid circles for TST $E_{\mathrm{T}}^{\mathrm{miss}}$. The ratio is to the 'prediction' of `6ej50-0ib` with TST $E_{\mathrm{T}}^{\mathrm{miss}}$.

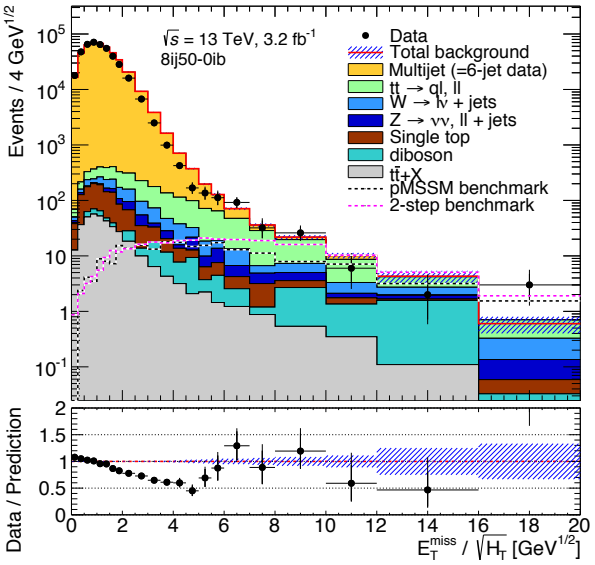


Figure 5.22: $E_{\mathrm{T}}^{\mathrm{miss}}/\sqrt{H_T}$ template from $n_{50} = 6$ extrapolated to $n_{50} \geq 8$. The template does not describe the data particularly well.

However, the change in the $E_{\mathrm{T}}^{\mathrm{miss}}$ soft term is not exclusively beneficial – since it is taken from tracks, there is intrinsic $E_{\mathrm{T}}^{\mathrm{miss}}$ in all events from soft forward particles outside the ID acceptance and from central neutral particles, neither of which give rise to tracks. This increased contribution to the $E_{\mathrm{T}}^{\mathrm{miss}}$ from soft particles contributes to the non-perfect agreement in figure 5.21, which is made more obvious in figure 5.22. It can be seen that the 6-jet template has a wider $E_{\mathrm{T}}^{\mathrm{miss}}/\sqrt{H_T}$ distribution than the 8-jet data, and so the template is clearly not suitable for an accurate estimate of the multijet background.

5.6.3 H_T binning

The reason for the discrepancy is further explained by figure 5.23. This shows that while $E_{\mathrm{T}}^{\mathrm{miss}}/\sqrt{H_T}$ is broadly independent of H_T in the regime with high H_T, and hence jet mismeasurement is dominating the $E_{\mathrm{T}}^{\mathrm{miss}}$, this independence breaks down at lower values ($\lesssim$ 1TeV)

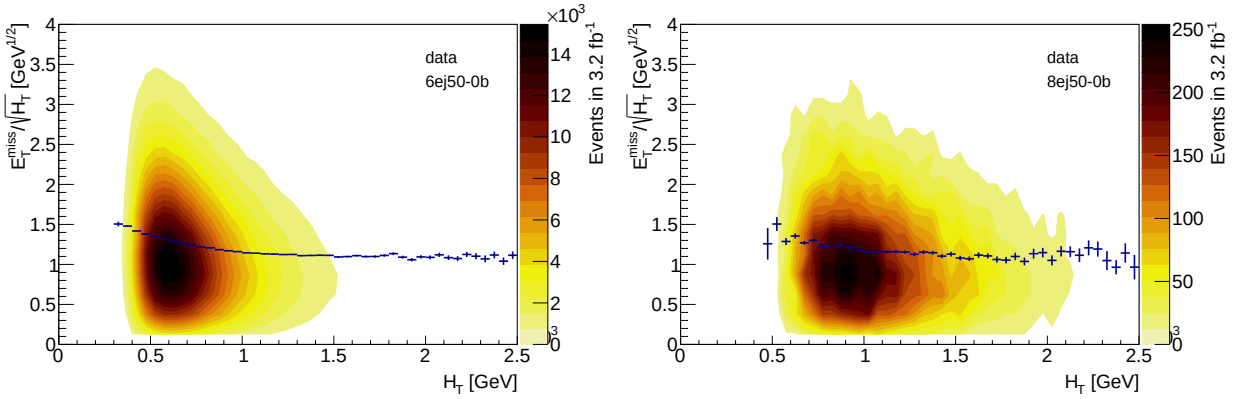


Figure 5.23: H_T versus $E_{\mathrm{T}}^{\mathrm{miss}}/\sqrt{H_T}$ for $n_{50} = 6$ (left) and $n_{50} = 8$ (right). The long tails of the $E_{\mathrm{T}}^{\mathrm{miss}}/\sqrt{H_T}$ distributions cause the profile values to lie above the peak in each H_T bin.

where other contributions to the $E_{\mathrm{T}}^{\mathrm{miss}}$ become important. Since regions with lower jet multiplicity necessarily have lower H_T on average, a template built from N jets will oversample this region compared to the SRs with at least N+2 jets, and hence will have a broader $E_{\mathrm{T}}^{\mathrm{miss}}/\sqrt{H_T}$ distribution than the data.

Since this behaviour seems broadly independent of jet multiplicity (i.e. the H_T – $E_{\mathrm{T}}^{\mathrm{miss}}/\sqrt{H_T}$ shape is similar across multiplicities) the accuracy of the template can be restored through constructing it separately in bins of H_T. The choice of H_T bins is made such that there are reasonable statistics in each bin across jet multiplicities while maintaining approximate H_T independence within each, resulting in bins spanning $H_T = 0 - 600 - 800 - 1000 - \infty$ GeV. Figure 5.24 shows how this H_T binning modifies the shape of the multijet predictions in all SRs, while figure 5.25 shows the result of the H_T-binned template in `8j50-0b`, with much better agreement than before its implementation.

5.6.4 Templates with *b*-jets

Figure 5.26 shows the comparison in shape between different b-jet multiplicities. There is a larger $E_{\mathrm{T}}^{\mathrm{miss}}/\sqrt{H_T}$ tail for larger b-jet multiplicities, since real $E_{\mathrm{T}}^{\mathrm{miss}}$ from B-hadron decays is increasingly important, although this effect is slightly less pronounced for the higher multiplicity regions since 2 b-jets make up a lower fraction of the total number of jets. A comparison of the templates and data for all `2ib` regions is shown in figure 5.27,

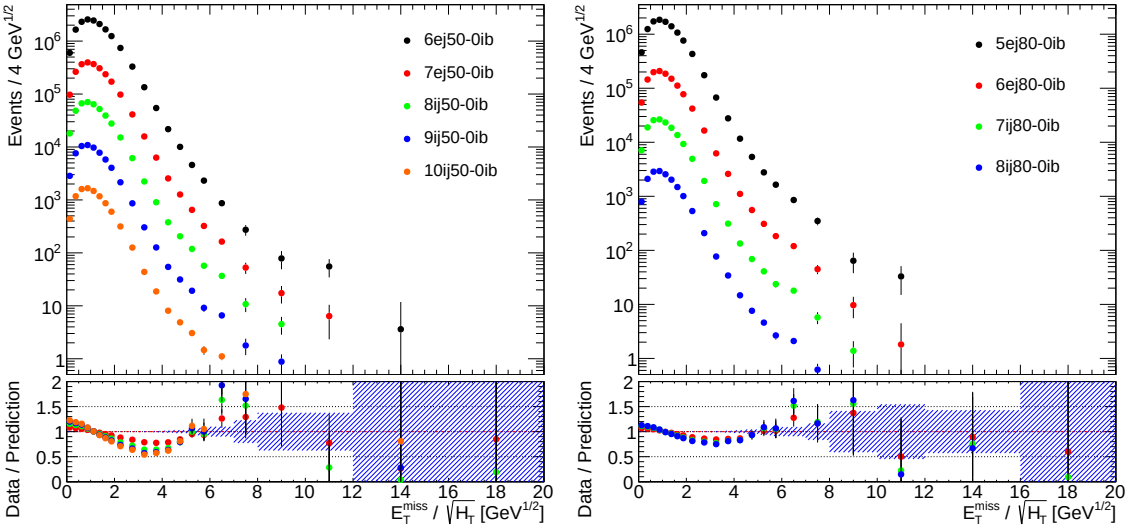


Figure 5.24: Data (lowest multiplicities) and templates for varying jet multiplicities (both with no *b*-jet selection), left for jets with $p_{\mathrm{T}} > 50$ GeV and right for those with $p_{\mathrm{T}} > 80$ GeV. The ratio plots show templates formed from binning in H_T compared to the lowest multiplicity data, and replicate the shapes seen in Figure 5.20, showing how the H_T binning restores agreement.

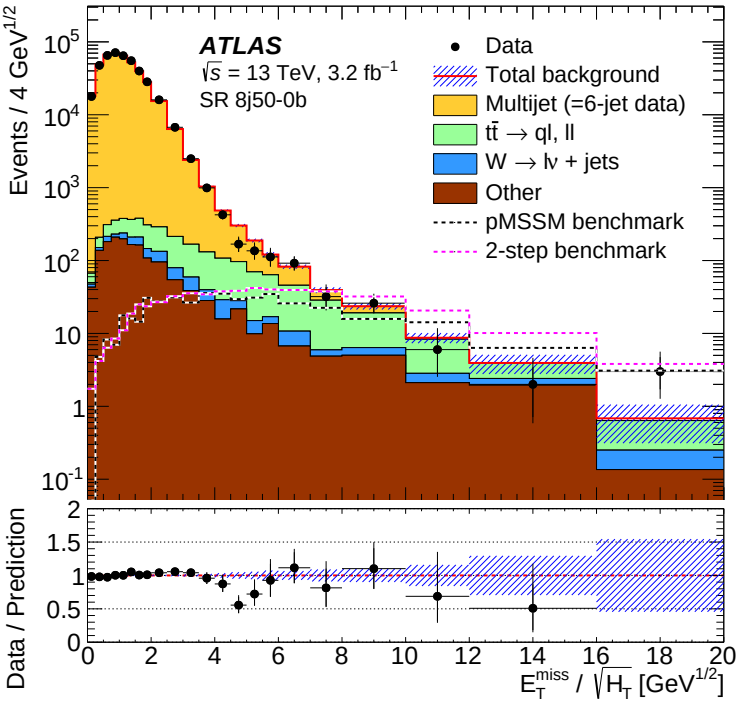


Figure 5.25: $E_{\mathrm{T}}^{\mathrm{miss}}/\sqrt{H_T}$ template constructed in bins of H_T, with much better agreement than figure 5.22. This figure also appears in [2].

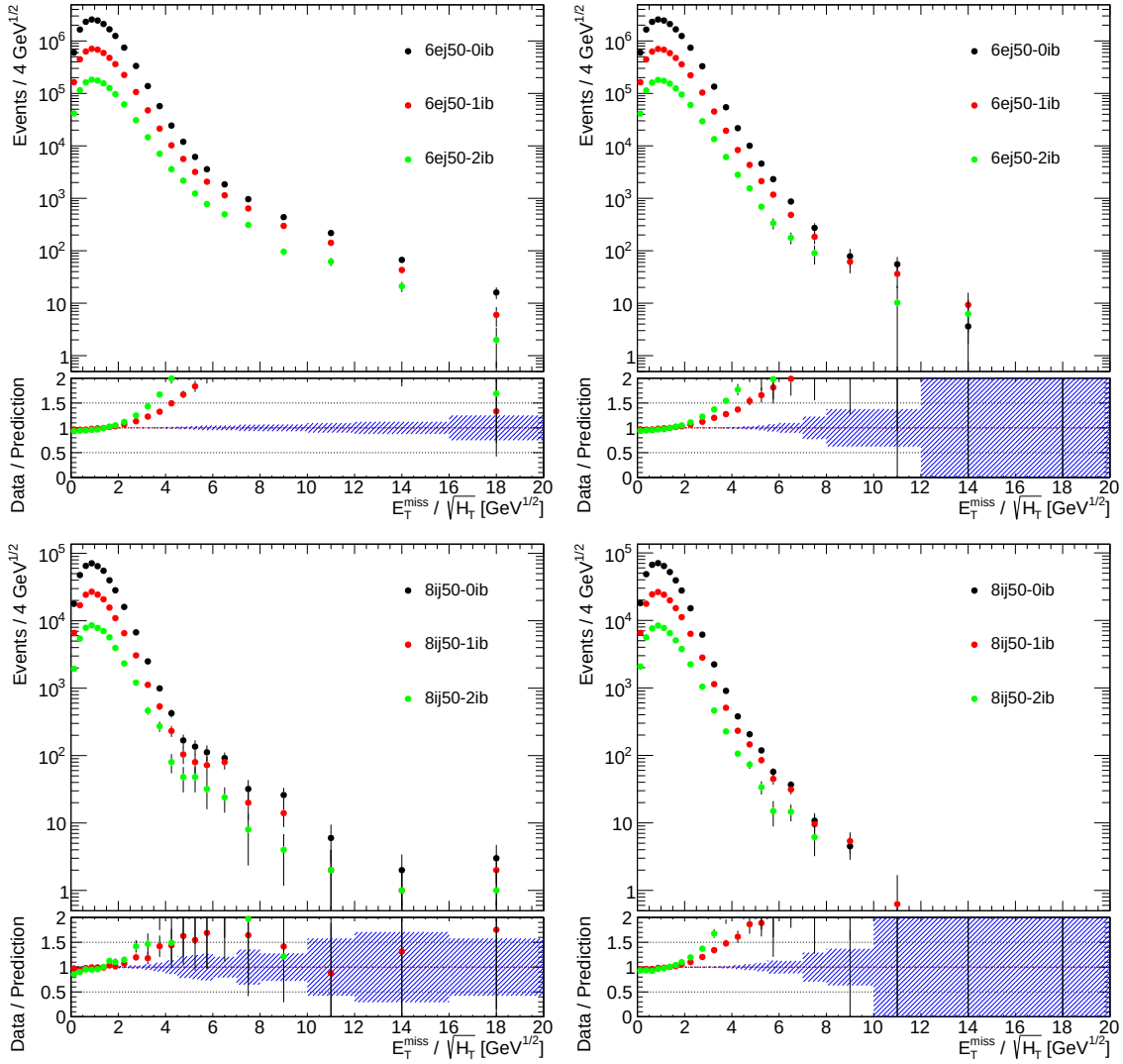


Figure 5.26: Data (left) and templates (right) for `6ej50` (top) and `8ij50` (bottom) with the three *b*-jet requirements. The ratio plots are of `1ib` and `2ib` to `0ib`.

showing reasonable replication of the data distribution within statistical uncertainties. This demonstrates the validity of the method but underscores the need for separate templates for each *b* multiplicity.

There are thus 6 'combined' (i.e. having summed the bins of H_T) templates formed – one for each *b*-jet multiplicity considered (no requirement, ≥ 1, ≥ 2) for each jet p_{T} (6 jets $>$ 50 GeV, 5 jets $>$ 80 GeV). These templates are applied to validation regions (VRs) one higher in jet multiplicity – exclusive so as to remain blind – i.e. `7ej50` and `6ej80`. The agreement between templates and data is measured in these VRs in order to obtain an uncertainty on the multijet prediction, as described in section 5.6.5.

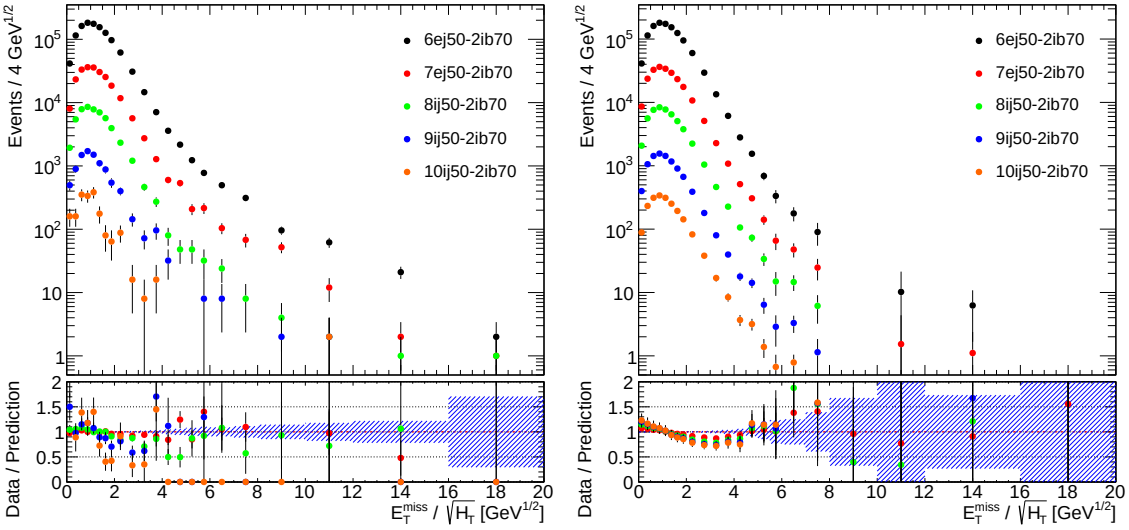


Figure 5.27: Data (left) and templates (right) in the SRs with ≥ 2 b-jets, with the ratio plots relative to `6ej50-2ib`.

5.6.5 Multijet closure tests

The dominant systematic uncertainty on the template method as described above is quantified from the degree to which the method is observed to work in regions where little signal is expected. This so-called 'closure' of the prediction against the number of observed events is tested in regions with $E_{\mathrm{T}}^{\mathrm{miss}}/\sqrt{H_T}$ lying in the ranges $1.5-2.0$, $2.0-2.5$ and $2.5-3.5$ GeV$^{1/2}$ for jet multiplicities `8ij50`, `9ij50`, `10ij50`, `7ij80` and `8ij80`, separately for `0ib`, `1ib` and `2ib`. Furthermore, the closure is checked in the VR of $E_{\mathrm{T}}^{\mathrm{miss}}/\sqrt{H_T} > 4\,\mathrm{GeV}^{1/2}$ for `7ej50` and `6ej80`. Closure is therefore checked both at signal region multiplicities and also for cuts at lower multiplicity, while remaining blind during this check of the background estimation.

The (symmetrical) systematic uncertainty on any signal region is given by the maximal deviation in any of the closure validation regions of the same jet multiplicity or lower, for the same b-tagging requirements. For example, the systematic on the signal region `9j50-1b` is given by considering all of `7ej50-1ib`, `8ij50-1ib` and `9ij50-1ib` but not any `0ib`, `2ib`, `10ij50` or `j80` regions.

Tables 5.4 and 5.5 show the values obtained from this procedure, also shown graphically in figures 5.28 to 5.30. There appears to be a slight deficit of data in several of these validation regions which at first sight is verging on significant. However, inspecting figures

n_{50} (0ib)	[1.5, 2]	[2, 2.5]	[2.5, 3.5]	[4, ∞]	total
=7	2.8%	4.5%	5.9%	-1.0%	—
≥8	0.7%	3.9%	4.9%	-17.8%	4.9%
≥9	-3.0%	6.1%	3.0%	-4.9%	6.1%
≥10	-19.4%	-2.1%	-21.0%	13.3%	21.0%

n_{50} (1ib)	[1.5, 2]	[2, 2.5]	[2.5, 3.5]	[4, ∞]	total
=7	3.7%	2.4%	3.9%	-5.7%	—
≥8	-1.0%	-0.2%	-1.2%	-29.7%	1.2%
≥9	-1.0%	1.4%	-14.0%	-14.1%	14.0%
≥10	-24.8%	0.6%	-25.2%	-33.1%	25.2%

n_{50} (2ib)	[1.5, 2]	[2, 2.5]	[2.5, 3.5]	[4, ∞]	total
=7	4.9%	5.4%	5.1%	0.4%	—
≥8	5.7%	-0.9%	0.7%	-41.4%	5.7%
≥9	-12.6%	-2.9%	-25.3%	-28.1%	25.3%
≥10	-58.4%	-0.4%	-61.7%	-61.4%	61.7%

Table 5.4: The degree of closure observed in the various multi-jet control regions for the j50 SRs. The bracketed ranges indicate the $E_{\mathrm{T}}^{\mathrm{miss}}/\sqrt{H_T}$ interval considered, in $\mathrm{GeV}^{1/2}$. Blue highlighted cells mark VRs, red cells SRs and green cells the closure systematic taken for each SR.

5.31, 5.32 and 5.33, which show the non-overlapping bins that make up the various VRs, it can be seen that the discrepancies arise from a small number of bins primarily with ≥ 2 b-jets, consistent with statistical fluctuations. A change to the templates in regions requiring b-jets, performed after this analysis was completed, is described in appendix B.2 and results in slightly improved agreement between predictions and data.

5.6.6 Further systematic uncertainties on the template

In addition the the closure uncertainty described above, there are two other, generally sub-dominant uncertainties considered.

As described more fully in appendix B.3, the uncertainty resulting from the choice of H_T bins used to form the templates is evaluated simply by picking another set and taking the

n_{80} (0ib)	[1.5, 2]	[2, 2.5]	[2.5, 3.5]	[4, ∞]	total
=6	0.6%	3.6%	0.5%	0.3%	—
≥7	-1.9%	2.0%	-7.6%	-7.4%	7.6%
≥8	-4.7%	-7.7%	-37.4%	-19.2%	37.4%

n_{80} (1ib)	[1.5, 2]	[2, 2.5]	[2.5, 3.5]	[4, ∞]	total
=6	1.7%	0.4%	0.3%	-5.6%	—
≥7	2.2%	-6.3%	-0.9%	-22.2%	6.3%
≥8	-13.5%	-14.2%	-34.6%	-50.4%	34.6%

n_{80} (2ib)	[1.5, 2]	[2, 2.5]	[2.5, 3.5]	[4, ∞]	total
=6	8.0%	1.8%	-3.5%	-8.8%	—
≥7	4.7%	-8.8%	11.1%	-23.1%	11.1%
≥8	0.4%	-15.2%	-49.3%	-53.2%	49.3%

Table 5.5: The degree of closure observed in the various multi-jet control regions for the j80 SRs. The bracketed ranges indicate the $E_{\mathrm{T}}^{\mathrm{miss}}/\sqrt{H_T}$ interval considered, in $\mathrm{GeV}^{1/2}$. Blue highlighted cells mark VRs, red cells SRs and green cells the closure systematic taken for each SR.

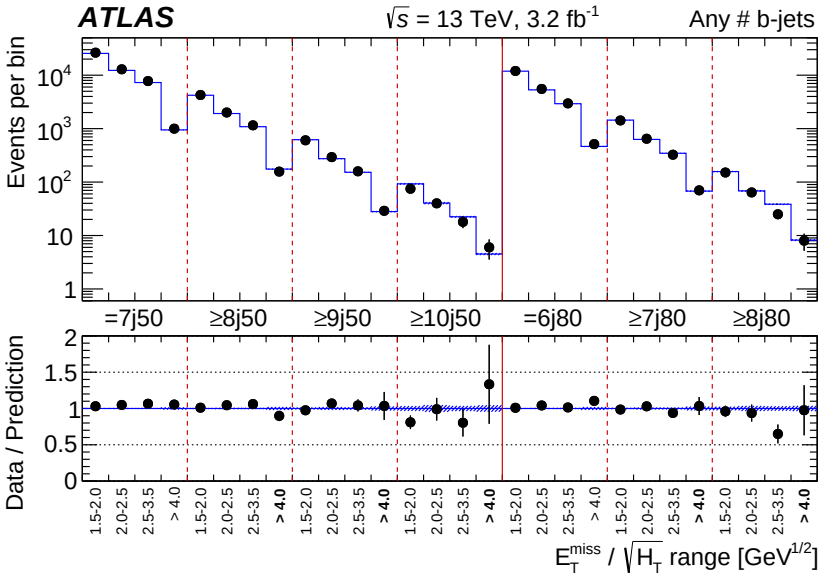


Figure 5.28: The degree of closure observed in the various multi-jet control regions for the regions with ≥ 0 b-tagged jets. The solid lines are the predicted numbers of events and the points are the observed numbers. Plot also in [2].

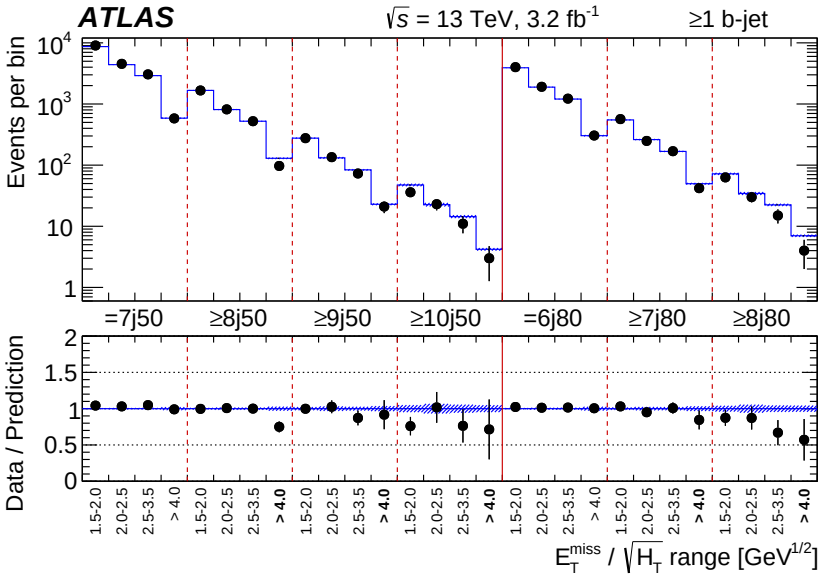


Figure 5.29: The degree of closure observed in the various multi-jet control regions for the regions with ≥ 1 b-tagged jets. The solid lines are the predicted numbers of events and the points are the observed numbers. Plot also in [2].

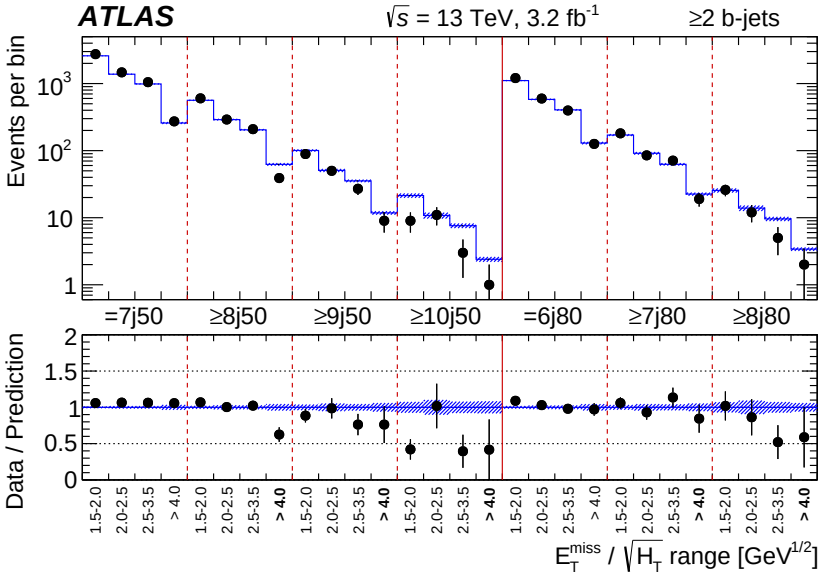


Figure 5.30: The degree of closure observed in the various multi-jet control regions for the regions with ≥ 2 b-tagged jets. The solid lines are the predicted numbers of events and the points are the observed numbers. Plot also in [2].

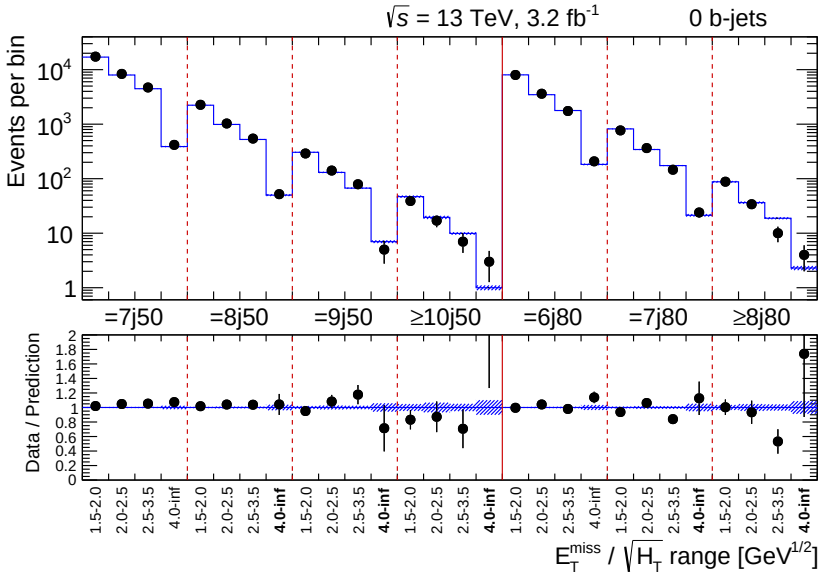


Figure 5.31: The degree of closure observed in various exclusive bins making up the multi-jet control regions, with = 0 b-tagged jets. The solid lines are the predicted numbers of events and the points are the observed numbers.

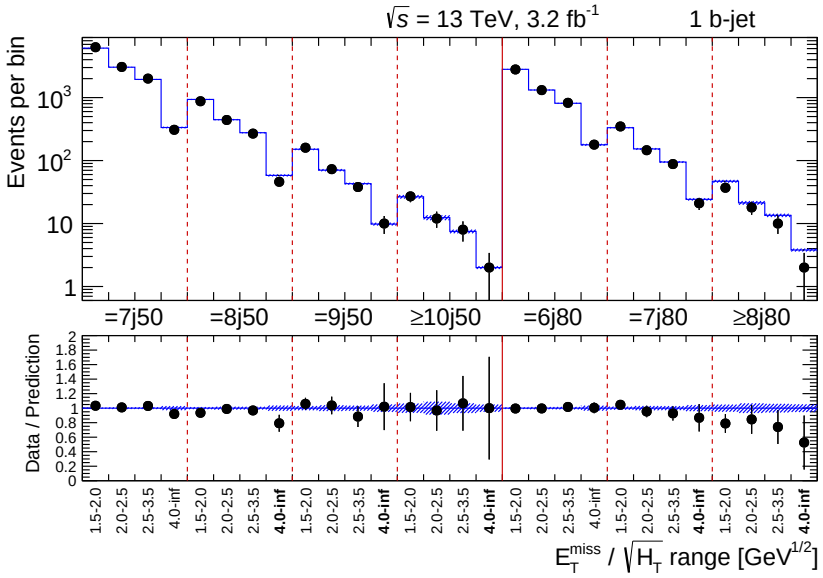


Figure 5.32: The degree of closure observed in various exclusive bins making up the multi-jet control regions, with = 1 b-tagged jet. The solid lines are the predicted numbers of events and the points are the observed numbers.

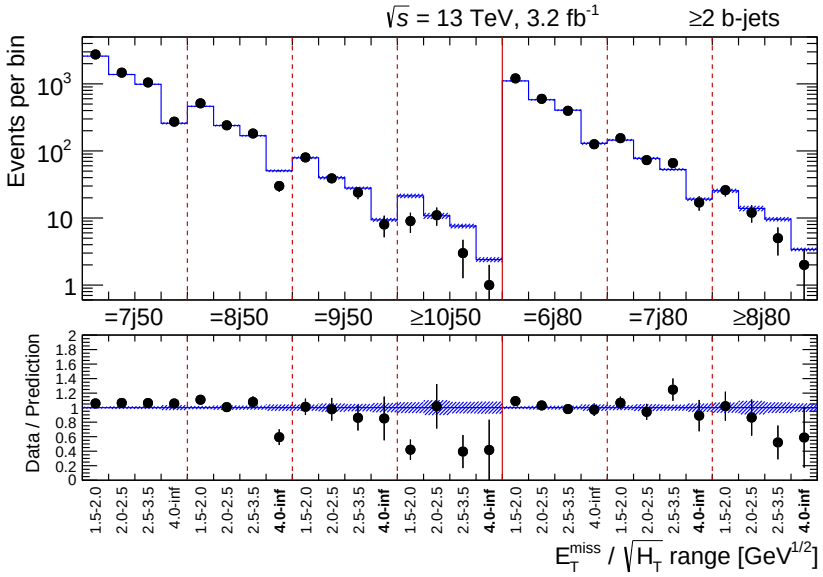


Figure 5.33: The degree of closure observed in various exclusive bins making up the multi-jet control regions, with ≥ 2 b-tagged jets. The solid lines are the predicted numbers of events and the points are the observed numbers.

difference. No bias is observed, and the resulting systematic uncertainty lies below 6% in all regions.

Additionally, there is an uncertainty arising from the subtraction of leptonic backgrounds in the construction of the template. Since these backgrounds are scaled by the fits described in section 5.7, which have a particular uncertainty associated with them, there is an inherent uncertainty in their normalisations. This does not have a noticeable impact on the normalisation of templates at SR multiplicities, since the leptonic contribution makes up ∼1% of the total in the normalisation region $E_{\mathrm{T}}^{\mathrm{miss}}/\sqrt{H_T} < 1.5\,\mathrm{GeV}^{1/2}$, but it can affect the formation of the template in lower jet multiplicity and high $E_{\mathrm{T}}^{\mathrm{miss}}/\sqrt{H_T}$ regions where leptonic backgrounds are more important.

Since no fits are performed to estimate the leptonic backgrounds at the template formation multiplicities of `6j50` and `5j80`, there is no direct estimate of their normalisation uncertainties. However, as the uncertainties on the normalisations are observed to grow with jet multiplicity, values are taken from the lowest SR multiplicity. Given that the μ values mostly lie below 1, and that the leptonic background is dominated by $t\bar{t}$, the variations considered are just $\mu_{t\bar{t}} - 1\sigma$, equalling 0.7 for n_{50} regions and 0.5 for n_{80} ones. These

scalings are applied to the total leptonic prediction when constructing the templates, and these modified templates are compared to the nominal ones. Again, the impact is found to be small compared to the closure uncertainty, being always less than 10% in n_{80} regions and less than 4% in n_{50} regions.

5.7 Fits and Results

Three types of fit are employed in order to estimate the backgrounds in the signal regions, constrain the systematic uncertainties and, since no excess is observed, set limits on new processes. A likelihood function is built as the product of Poisson probability functions describing the observed and expected number of events in the control and signal regions, and systematic uncertainties are treated as nuisance parameters in the fits, i.e. Gaussian functions with standard deviation equal to the size of the corresponding uncertainty. I calculated most of the inputs to the fits but the fits themselves were predominantly run by a collaborator (with the exception of the discovery fits, see section 5.7.2) using the *HistFitter* package [141].

5.7.1 Background Only Fit

The background only fit is used to normalise the MC expectations for the $t\bar{t}$ and W+jets backgrounds in the corresponding control regions, allowing their normalisations to float within the uncertainties described above. *HistFitter* does this by first setting up a probability distribution function:

$$\mathcal{P}(n_c, a_p|\mu_s, \alpha_p) = \prod_c \text{Pois}(n_c|v_c) \cdot G(L_0|\lambda, \Delta_L) \cdot \prod_p P_p(a_p|\alpha_p) \tag{5.1}$$

the three terms in which are explained below.

If v_c events are expected in channel c, then the observed distribution of n_c is expected to

be Poissonian,

$$\text{Pois}(n_c|v_c) = \frac{v_c^{n_c}}{n_c!}e^{-v_c} \tag{5.2}$$

The expected number of events v_c is determined from multiple backgrounds b (e.g. $t\bar{t}$ and W+jets), and is given by

$$v_c = \sum_b \lambda_c \; \mu_b \; \eta_{b,c}(\alpha) \; y_{b,c} \tag{5.3}$$

Here, λ_c is the true luminosity available, constrained by a Gaussian probability distribution $G(L_0|\lambda, \Delta_L)$ centred at the measured value L_0. L_0 and its uncertainty Δ_L are determined from beam-separation scans similar to those described in [104] – 3.2 ± 0.2 fb^{-1} in this case – accounting for the second term in eq. (5.1).

μ_b are per-sample normalisations, the same across all channels c, the determination of which is the object of the background-only fit. For samples not to be constrained by these fits, i.e. QCD multijet and minor leptonic backgrounds, μ_b is exactly 1.

$\eta_{b,c}(\alpha)$ are the relative values of the event yields v_c when a parameter of a systematic uncertainty is changed by a fraction α of its standard deviation. $\eta(0) = 1$ by definition, and the values of $\eta(1)$ and $\eta(-1)$ are determined as described in sections 5.5.3 and 5.5.4. Intermediate values are interpolated using methods from the *HistFactory* package [142] that guarantee $\eta > 0$.

Finally, $y_{b,c}$ is the raw (unscaled) estimate of the expected number of events in channel c from background b per unit integrated luminosity. This can also be expressed as $\sigma \times \mathcal{A} \times \epsilon$ – i.e. the process's total cross-section multiplied by its acceptance into the channel c multiplied by the efficiency with which the detector reconstructs events that should, given their truth-level properties, fall into channel c.

Since the values of α are allowed to float, the fit can result in 'profiling' of the systematic uncertainties, whereby they are shifted to values with large $|\alpha|$ to better fit the data in the particular channel. This behaviour is only tolerated within a certain degree, since the calibrations provided by the relevant performance group are inherently more trustworthy than

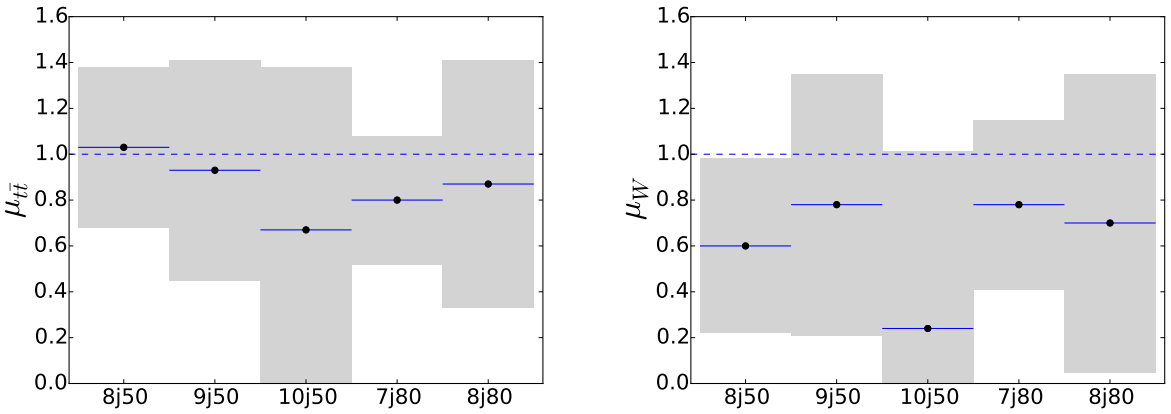


Figure 5.34: The values of $\mu_{t\bar{t}}$ (left) and μ_W (right) obtained from the background only fit. The central values are marked by the black points and blue lines, and the uncertainties on them by the grey bands.

the single, often statistically limited measurements being performed here. Thus Gaussian constraints on α, $P_p(a_p|\alpha_p)$, are introduced for each systematic variation p, with a_p such that P has width 1 and is centred on 0.

Equation (5.1) can be reinterpreted as a likelihood function, and it is the maximisation of this likelihood function that constitutes the background only fit, resulting in $\mu_{t\bar{t}}$ and μ_W for each fit performed. One fit is run for each jet multiplicity – i.e. it considers the two control regions `(n-1)jXX-0eb` and `(n-1)jXX-1ib` and the three signal regions `njXX-0ib`, `njXX-1ib` and `njXX-2ib`. When a systematic uncertainty is correlated between regions (signal and control) or processes it factorises into an overall normalisation factor and a residual uncertainty that can be substantially less than the original.

The μ-values determined from these fits are shown in figure 5.34. In general the central values for $t\bar{t}$ are close to one, but the statistically limited W+jets normalisations deviate more, as do both in `10j50`. These are applied to the expected signal region yields, resulting in the overall SM expectations shown in table 5.6 and figure 5.35. Final $E_{\mathrm{T}}^{\mathrm{miss}}/\sqrt{H_T}$ distributions in each signal region can be found in appendix B.4.

The dominant systematic uncertainties in each of the signal regions following the fits are shown in tables 5.7 to 5.11. As discussed earlier, they are dominated by theoretical uncertainties on $t\bar{t}$ modelling, the jet energy scale and the multijet template closure.

Signal region	Fitted background			Obs events
	Multijet	Leptonic	Total	
8j50	109.3 ± 6.9	80 ± 25	189 ± 26	157
8j50-1b	76.7 ± 2.7	62 ± 21	138 ± 21	97
8j50-2b	33.8 ± 2.1	33 ± 13	67 ± 13	39
9j50	16.8 ± 1.3	12.8 ± 5.4	29.6 ± 5.6	29
9j50-1b	13.5 ± 2.0	10.2 ± 4.9	23.8 ± 5.3	21
9j50-2b	6.4 ± 1.6	5.8 ± 3.3	12.1 ± 3.6	9
10j50	2.61 ± 0.61	1.99 ± 0.62	4.60 ± 0.87	6
10j50-1b	2.42 ± 0.62	1.44 ± 0.49	3.86 ± 0.79	3
10j50-2b	1.40 ± 0.87	0.83 ± 0.37	2.23 ± 0.94	1
7j80	40.0 ± 5.3	30 ± 13	70 ± 14	70
7j80-1b	29.1 ± 3.4	20.8 ± 10	50 ± 11	42
7j80-2b	11.5 ± 1.6	11.0 ± 5.0	22.5 ± 5.2	19
8j80	4.5 ± 1.9	4.9 ± 2.2	9.3 ± 2.9	8
8j80-1b	3.9 ± 1.5	3.8 ± 2.1	7.6 ± 2.6	4
8j80-2b	1.72 ± 0.93	2.3 ± 1.1	4.1 ± 1.5	2

Table 5.6: For each signal region, the expected SM background (and separately the multijet and leptonic contributions) and the observed number of data events. The SM background normalisations are obtained from the background only fit.

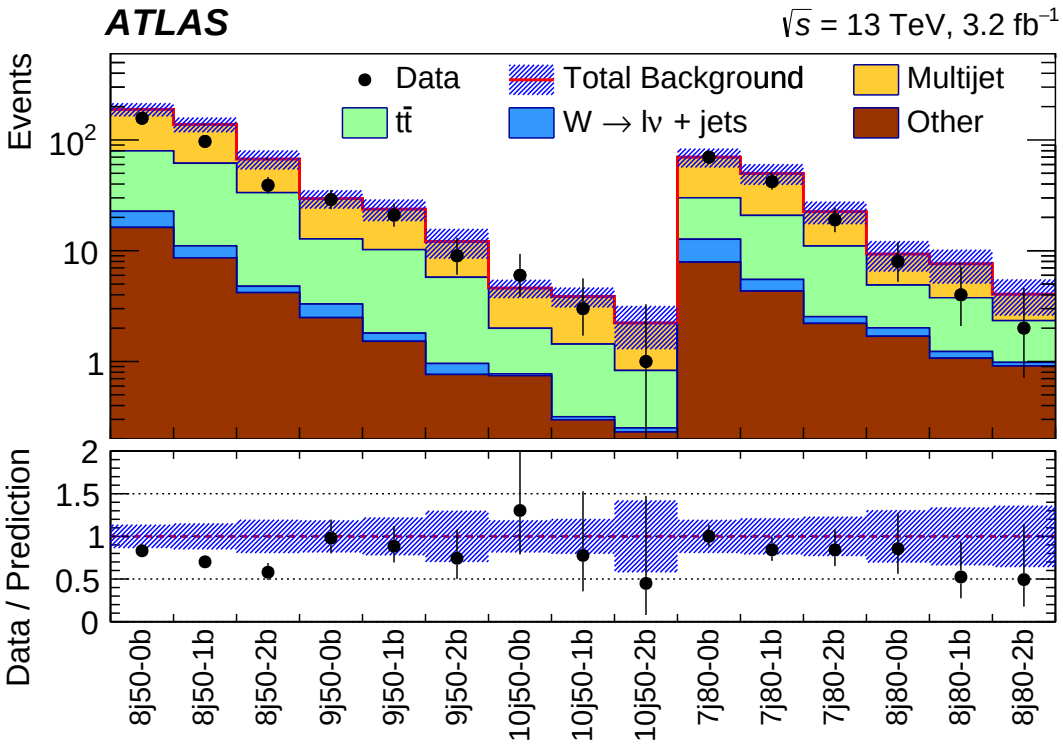


Figure 5.35: The fitted backgrounds from the background only fit, and observed data, in each SR. No excess is observed over the SM prediction.

Uncertainty of channel	SR 7j80	SR 7j80-1b	SR 7j80-2b
Total background expectation	70	50	23
Total statistical ($\sqrt{N_{\text{exp}}}$)	12%	14%	21%
Total background systematic	19%	21%	23%
$t\bar{t}$ theory - generator choice	23%	26%	30%
$t\bar{t}$ fit scaling	8%	11%	13%
$t\bar{t}$ theory - radiation parameters	7%	7%	8%
Jet Energy Scale variation #1	5%	5%	6%
Multijet Template Closure	4%	4%	6%
b-tagging- b ID	0.0%	0.9%	5%
Multijet Template MC subtraction	6%	5%	4%

Table 5.7: Dominant (> 5% in any region) post-fit systematic uncertainties for the `7j80` signal regions. Uncertainties are correlated so may add to more than the totals quoted.

Uncertainty of channel	SR 8j80	SR 8j80-1b	SR 8j80-2b
Total background expectation	9.3	7.6	4.0
Total statistical ($\sqrt{N_{\text{exp}}}$)	33%	36%	50%
Total background systematic	31%	34%	36%
$t\bar{t}$ theory - generator choice	25%	28%	33%
Multijet Template Closure	18%	18%	21%
$t\bar{t}$ fit scaling	19%	21%	21%
Limited SR 8j80-2b statistics	0.0%	0.0%	15%
$t\bar{t}$ theory - parton shower choice	18%	23%	14%
Jet Energy Scale variation #1	6%	7%	9%
$t\bar{t}$ theory - radiation parameters	10%	11%	8%
Multijet Template MC subtraction	8%	7%	6%
Z+jets theory	3%	3%	6%
b-tagging- b ID	0.0%	1%	5%
Limited SR 8j80 statistics	8%	0.0%	0.0%
Limited SR 8j80-1b statistics	0.0%	8%	0.0%

Table 5.8: Dominant (> 5% in any region) post-fit systematic uncertainties for the `8j80` signal regions. Uncertainties are correlated so may add to more than the totals quoted.

Uncertainty of channel	SR 8j50	SR 8j50-1b	SR 8j50-2b
Total background expectation	189	138	67
Total statistical ($\sqrt{N_{\text{exp}}}$)	7%	8%	12%
Total background systematic	14%	15%	20%
$t\bar{t}$ theory - generator choice	18%	21%	27%
$t\bar{t}$ fit scaling	10%	12%	14%
$t\bar{t}$ theory - radiation parameters	9%	11%	13%
Jet Energy Scale variation #1	7%	7%	9%
b-tagging- b ID	0.0%	0.9%	5%
$t\bar{t}$ theory - parton shower choice	8%	9%	3%

Table 5.9: Dominant (> 5% in any region) post-fit systematic uncertainties for the `8j50` signal regions. Uncertainties are correlated so may add to more than the totals quoted.

Uncertainty of channel	SR 9j50	SR 9j50-1b	SR 9j50-2b
Total background expectation	30	24	12
Total statistical ($\sqrt{N_{\text{exp}}}$)	18%	21%	29%
Total background systematic	19%	22%	30%
$t\bar{t}$ theory - generator choice	28%	32%	39%
$t\bar{t}$ fit scaling	16%	18%	20%
$t\bar{t}$ theory - radiation parameters	12%	13%	15%
Multijet Template Closure	3%	8%	13%
Jet Energy Scale variation #1	8%	7%	9%
$t\bar{t}$ theory - parton shower choice	6%	8%	3%

Table 5.10: Dominant (> 5% in any region) post-fit systematic uncertainties for the `9j50` signal regions. Uncertainties are correlated so may add to more than the totals quoted.

Uncertainty of channel	SR 10j50	SR 10j50-1b	SR 10j50-2b
Total background expectation	4.6	3.9	2.2
Total statistical ($\sqrt{N_{\text{exp}}}$)	47%	51%	67%
Total background systematic	19%	20%	42%
Multijet Template Closure	12%	16%	39%
$t\bar{t}$ theory - generator choice	20%	24%	32%
$t\bar{t}$ fit scaling	27%	30%	26%
$t\bar{t}$ theory - radiation parameters	12%	16%	14%
$t\bar{t}$ theory - parton shower choice	4%	5%	9%
Jet Energy Scale variation #1	9%	8%	7%
Limited SR 10j50-2b statistics	0.0%	0.0%	5%
Limited SR 10j50 statistics	7%	0.0%	0.0%

Table 5.11: Dominant ($> 5\%$ in any region) post-fit systematic uncertainties for the `10j50` signal regions. Uncertainties are correlated so may add to more than the totals quoted.

5.7.2 Discovery Fit

Having performed the background only fit, it is obvious that there is no excess above the standard model prediction. A quantitative statement as to what generic new physics can be ruled out is given by a discovery fit, more appropriately termed a model-independent exclusion fit in this case. The fit is performed separately for each signal region, using the background predictions and uncertainties from the background only fit, and assuming zero signal contamination in control regions. It performs a scan of signal strengths to determine the upper limit on new physics cross-section that could be compatible with the observed results.

The fits were run by throwing 100,000 toys (sets of pseudo-data varying according to the uncertainties) for each region. All values were checked to have converged within their quoted precisions with this number of toys, shown for example in figure 5.36 for S^{95}_{obs} in `9j50-1b`.

The results are given in table 5.12. Some CL_B values – i.e. the confidence level observed for the background-only hypothesis – are quite low, especially for `8j50-1b` and `8j50-2b`, but this appears to be the result of statistical fluctuations as described above.

5.7.3 Exclusion Fit

The final fit performed is the exclusion fit. This is in some sense a combination of the previous two fits while taking into account the presence of a particular signal model throughout, through the inclusion of each signal point in turn as an addition to v_c in eq. (5.3) with signal strength $\mu = 1$, and asking whether or not that model can be excluded. To avoid biasing by fluctuations in the data, the signal region used in this evaluation is chosen to be that for which the expected exclusion is best – i.e. assuming that the data exactly match the MC predictions in the SRs. The measure used to judge exclusion power is CL_s, which reduces the exclusion power for the signal plus background hypothesis if the data is inconsistent with the background, by normalising the signal plus background p-value by the p-value of the background-only hypothesis [143]. The signal regions with the best-expected CL_s value

Signal region	$\langle\epsilon\sigma\rangle^{95}_{\text{obs}}$[fb]	S^{95}_{obs}	S^{95}_{exp}	CL_B	$p(s=0)$
8j50	11	36	49^{+19}_{-13}	0.14	0.50
8j50-1b	6.8	22	37^{+13}_{-10}	0.04	0.50
8j50-2b	3.8	12	22^{+8}_{-6}	0.03	0.50
9j50	5.8	19	19^{+4}_{-5}	0.490	0.50
9j50-1b	5	16	17^{+2}_{-6}	0.38	0.50
9j50-2b	2.6	8	10^{+3}_{-2}	0.31	0.50
10j50	2.5	8	6^{+3}_{-1}	0.74	0.26
10j50-1b	1.6	5	6^{+2}_{-1}	0.37	0.50
10j50-2b	1.1	4	4^{+2}_{-1}	0.27	0.50
7j80	10	32	32^{+11}_{-9}	0.51	0.50
7j80-1b	6.2	20	24^{+6}_{-5}	0.29	0.50
7j80-2b	4.2	14	14^{+6}_{-2}	0.33	0.50
8j80	3.2	10	11^{+2}_{-4}	0.41	0.50
8j80-1b	1.7	5	7^{+3}_{-2}	0.20	0.50
8j80-2b	1.4	4	5^{+2}_{-1}	0.24	0.50

Table 5.12: The results of the 'discovery' fits. Left to right: 95% CL upper limits on the visible cross-section ($\langle\epsilon\sigma\rangle^{95}_{\text{obs}}$) and on the number of signal events (S^{95}_{obs}). Convergence and stability tests of the fits suggest uncertainties of order 5% on S^{95}_{obs} resulting from these effects. The third column (S^{95}_{exp}) shows the 95% CL upper limit on the number of signal events, given the expected number (and $\pm 1\sigma$ excursions on the expectation) of background events. The last two columns indicate the CL_B value, i.e. the confidence level observed for the background-only hypothesis, and the discovery p-value ($p(s=0)$). The test is one-sided, so the p-value is 0.50 when the observed number of events is smaller than the prediction. Yields are not statistically independent, since there are correlated systematic uncertainties and since signal regions overlap.

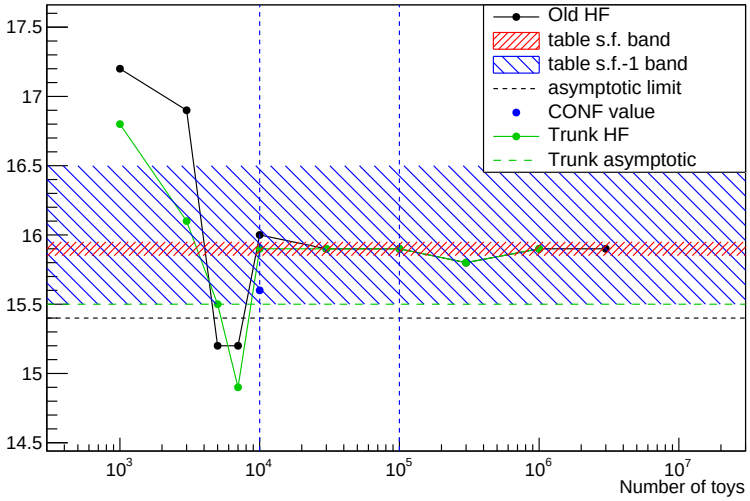
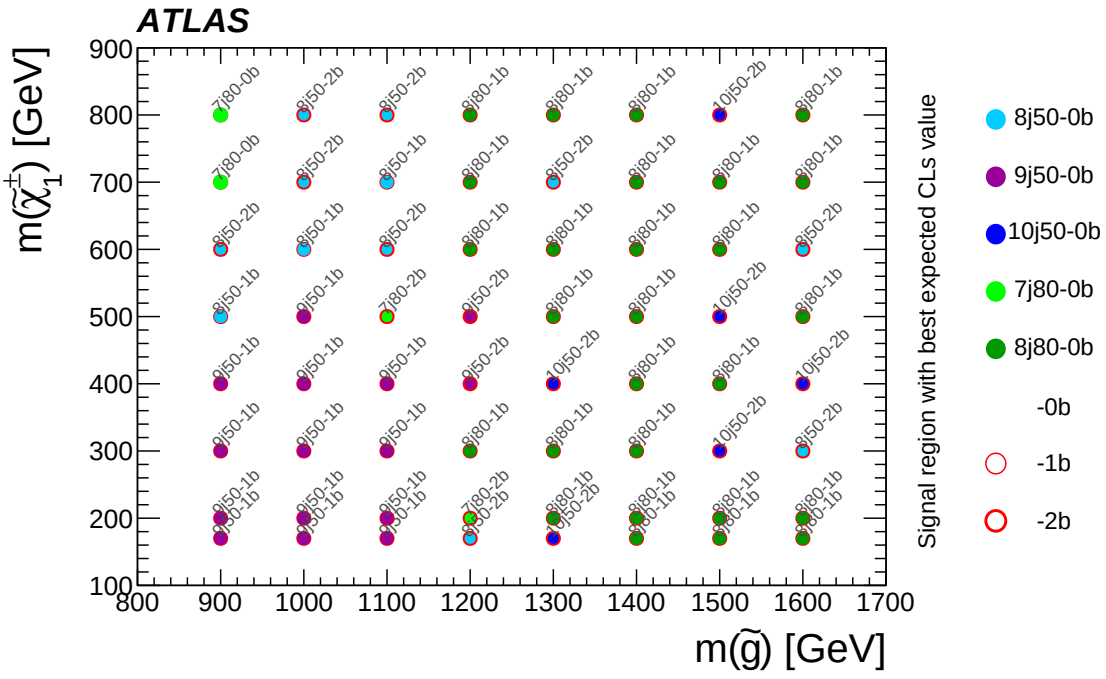


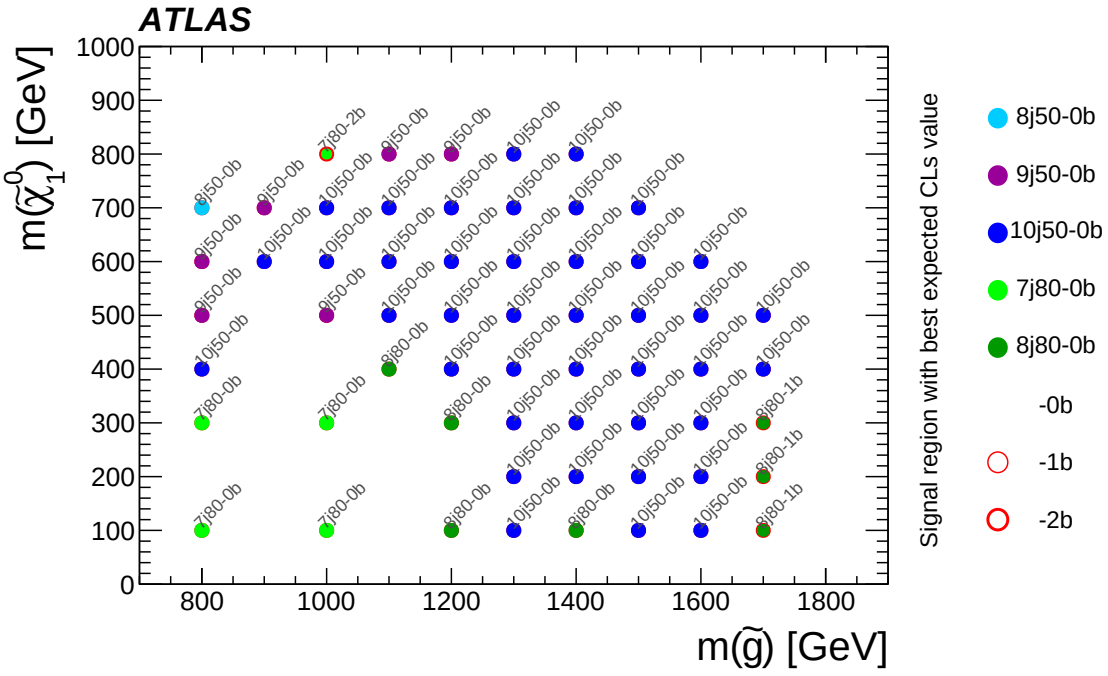
Figure 5.36: Convergence of S^{95}_{obs} in `9j50-1b`. The black and green lines correspond to different *HistFitter* versions, with the solid lines showing the value as a function of the number of toys and the dashed lines showing the asymptotic limits. The blue hatched area corresponds to the precision quoted here and in the final paper [2] and the red hatched area to that of the intermediate result [3], whose value is shown by the blue marker.

for each point in each grid are shown in figure 5.37. Multiple signal regions are close in sensitivity for the pMSSM grid, with `8j80` and `9j50` multiplicities tending to dominate, in conjunction with one or two b-jets as expected. For the 2-step grid, `10j50-0b` is the most powerful over most of the relevant parameter space, reflecting the low heavy flavour content of this model.

Having established the region with the best expected CL_s, the fits are performed with the actual observed data counts. Systematic uncertainties can be further reduced by these over the background only fits, since they are in many cases correlated between signals and backgrounds. The results are presented in figure 5.38, which additionally compare the resulting exclusion to that obtained by a combination of 2012 analyses – this limit is significantly extended by these results, and in both models gluinos of up to 1400 GeV are excluded at 95% confidence level for non-compressed scenarios. The observed fluctuations in the yellow band of the pMSSM exclusion limit arise from the varying signal regions used in this region (figure 5.37), and the smoother limits for the 2-step grid reflect the correspondingly more uniform SR choice.

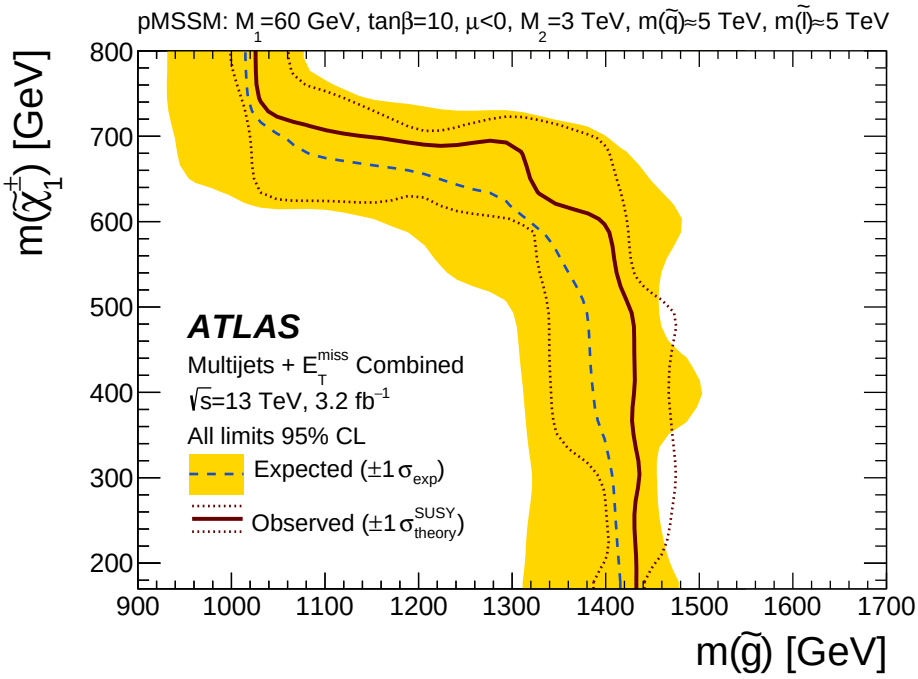


(a) pMSSM

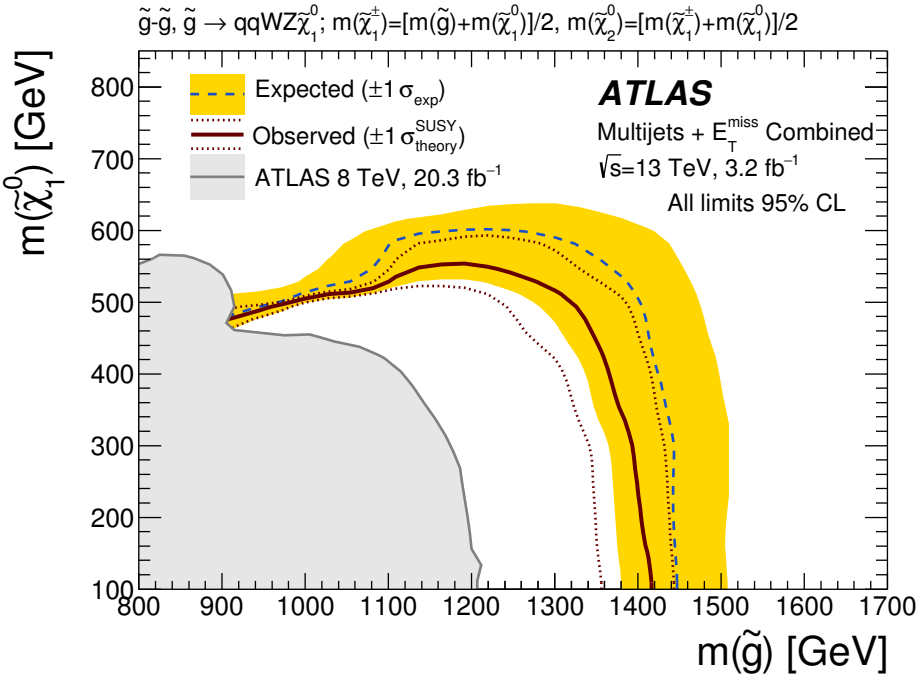


(b) 2-step

Figure 5.37: The signal region yielding the best expected CL_s value for each signal point considered. Plots also in auxiliary material of [2].



(a) pMSSM



(b) 2-step

Figure 5.38: 95% CL exclusion curves for the two supersymmetric models described. The solid red and dashed blue curves show the 95% CL observed and expected limits, respectively, including all uncertainties except the theoretical signal cross-section uncertainty (PDF and scale). The dotted red lines bracketing the observed limit represent the result produced when moving the signal cross-section by $\pm 1\sigma$ (as defined by the cross-section uncertainties). The shaded yellow band around the expected limit shows the $\pm 1\sigma$ variation of the expected limit. The shaded grey area shows the observed exclusion from the combination of ATLAS $\sqrt{s} = 8$ TeV analyses performed in [117] (figure 25 therein). Excluded regions are below and to the left of the relevant lines. Plots made by a collaborator, and shown in [2].

5.8 Summary and Outlook

This chapter presented the latest iteration of the pursuit of new phenomena in final states with large jet multiplicities (from 7 to $\geq$ 10) and missing transverse momentum, using 3.2 fb^{-1} of 13 TeV pp collision data collected with the ATLAS detector at the LHC. Key to the search, and allowing for relatively low $E_{\mathrm{T}}^{\mathrm{miss}}$ thresholds, is the data-driven estimate of the dominant QCD multijet background, described in section 5.6. Other backgrounds are determined from simulation and controlled using semi-data-driven methods, described in section 5.5, with sensitivity to a new class of signal model derived from the pMSSM being evaluated for the first time. Results are found to be consistent with the Standard Model predictions, allowing limits to be set on gluino production, as shown in section 5.7. For both models considered, gluinos below 1400 GeV are excluded – for neutralino masses below 500 GeV in the simplified model and for chargino masses below 600 GeV in the pMSSM-inspired model. This is an increase of around 200 GeV in gluino mass from the analysis performed with the 2012 dataset, showing the power of increased collision energy on high-mass searches such as this.

The LHC will resume proton–proton collisions in late spring 2016, with an expected integrated luminosity of about 25 fb^{-1} foreseen by the end of the year. This large increase in data volume will allow for numerous improvements to the analysis. Tighter selections in signal regions will be possible, such as improved lepton vetoes or higher jet multiplicities, to further enhance potential signals over the backgrounds. Additionally, the template method at high jet and b-jet multiplicities will be more easily studied, and control of leptonic backgrounds will improve through selections closer to that of signal regions.

Chapter 6

Conclusions

During the first run of the LHC, protons were collided at the highest energies ever achieved up to that point and with record luminosity for a hadron collider. This excellent performance, combined with superb operation of the ATLAS and CMS detectors, enabled the discovery of the Higgs boson in 2012. This was simultaneously the last piece to slot into the puzzle of the Standard Model and one of its biggest curiosities pointing to more discoveries beyond, although none were forthcoming in early searches.

This thesis presented in chapter 4 a search for new physics that would have eluded these early searches, that of pair-produced scharms each decaying to a charm quark and a neutralino, making use of developments allowing the identification of charm quarks with unprecedented efficiency. Despite these improvements, the selection efficiency for two charm quarks was still less than 4%, prompting an optimisation of the analysis strategy to remain sensitive to signals with low cross-sections at high mass. Since no excess was observed over the Standard Model prediction, scharm masses below 550 GeV were excluded for neutralino masses below 200 GeV, a significant increase over previous limits for such models.

In 2015, the LHC began its second phase of operation, Run-2, after two years of consolidation to allow operation at increased centre-of-mass energy, 13 TeV compared to 8 TeV in Run-1. Such a jump in collision energy results in a huge increase in production cross-section for particles at the TeV scale, greatly increasing sensitivity to them over Run-1 despite the

smaller dataset obtained in a startup year. Chapter 5 presented a search for gluinos that would evade most $E_{\mathrm{T}}^{\mathrm{miss}}$-based SUSY searches by decaying via cascades to large numbers of hadronic jets. It made use of a data-driven background estimation technique pioneered in Run-1, but updated to account for new reconstruction and object definitions in Run-2. Again, however, no excess of high-multiplicity events was observed and gluinos were constrained to lie above 1400 GeV for the models considered, a ∼200 GeV increase over Run-1.

The second run of the LHC resumes in a matter of weeks at the time of writing, and will hopefully be well under way by the time this work is examined. There is still much scope to explore areas of SUSY parameter space with the coming years' data, which will provide sensitivity to many viable models that would not have been seen yet, particularly those with low production cross-sections that need large quantities of data for the small signals to emerge from statistical noise. It is of course possible that nature has provided no new particles accessible to the LHC – perhaps we do just live in a fine-tuned universe, or the new physics that solves the hierarchy problem is impossible to find with the current experiments. However, LHC physicists have at their disposal an incredible machine and experiments capable of probing the universe in more detail than ever before, and it is not an opportunity to be missed.

Appendix A

Appendices to the Scharm search (chapter 4)

A.1 Constraint on m_{cc} in $t\bar{t}$ events

In section 4.4.3, it is asserted that the mass of the combination of a b-jet and a c-jet from a top decay (there called m_{cc} since the b-jet is tagged incorrectly as a c-jet) is less than that of the top itself.

The relevant process is that of a top quark, t, decaying into a b-quark, a c-quark and an s-quark (the intermediate W is irrelevant to the argument). Considering the bc pair as a single object, it has 4-momentum:

$$(E_{bc}, \vec{p}_{bc}) = (E_t - E_s, \vec{p}_t - \vec{p}_s)$$

Thus its mass, m_{bc}, is given by

$$\begin{aligned} m_{bc}^2 =& E_{bc}^2 - \vec{p}_{bc}^{\,2} \\ =& (E_t - E_s)^2 - (\vec{p}_t - \vec{p}_s)^2 \\ =& E_t^2 - 2E_tE_s + E_s^2 - \vec{p}_t^{\,2} + 2\vec{p}_t \cdot \vec{p}_s - \vec{p}_s^{\,2} \\ =& m_t^2 + m_s^2 - 2E_tE_s + 2\vec{p}_t \cdot \vec{p}_s \end{aligned}$$

Since these are all Lorentz invariant quantities, we can boost into the top's centre-of-mass frame where $\vec{p}_t = \vec{0}$ and hence $E_t = m_t$, giving

$$m_{bc}^2 = m_t^2 + m_s^2 - 2m_t E_s$$

Since $m_t > m_s$ by observation and $E_s \geq m_s$ by definition, $2m_t E_s > m_s^2$ and we obtain

$$m_{bc} < m_t$$

as asserted.

A.2 Extra post-fit kinematic distributions

Shown here are some kinematic distributions in the signal and control regions of the scharm search, in all cases after the fitting of the backgrounds in the control regions. They are taken from the auxiliary material to [4], and were made by a collaborator (who performed the fit they depend on). In all plots, the red arrows indicate the SR and CR requirements on the variables plotted, and the grey bands correspond to the combined MC statistical and experimental systematic uncertainties. No mismodelling is evident in any of these distributions.

Signal Region SR150

Distributions of m_{CT} and m_{cc} are shown in section 4.7.1, and those of $E_{\mathrm{T}}^{\mathrm{miss}}$ and leading jet p_{T} in figure A.1.

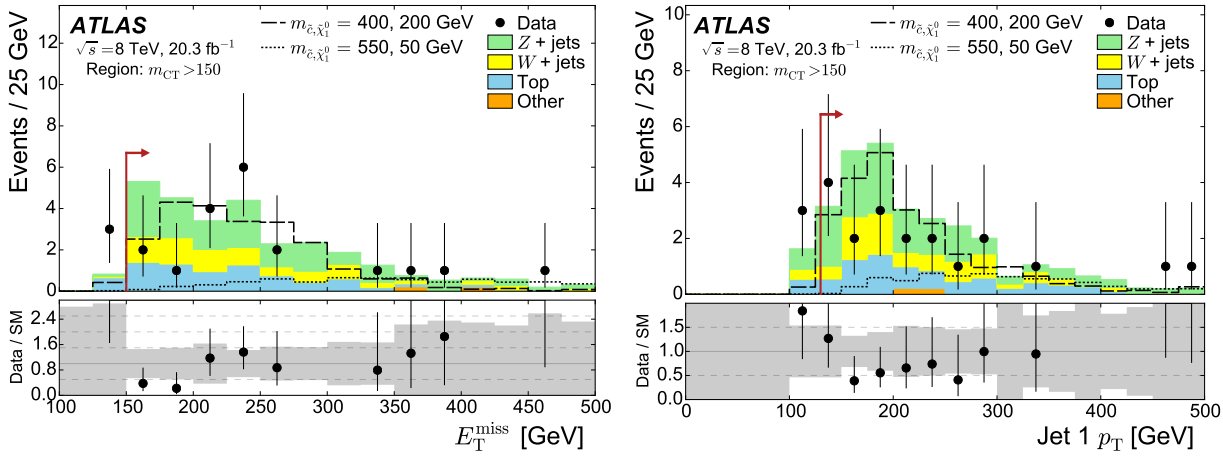


Figure A.1: Distributions of $E_{\mathrm{T}}^{\mathrm{miss}}$ (left) and leading jet p_{T} (right) in the signal region with $m_{\mathrm{CT}} > 150$ GeV following the background only fit. Plots from [4].

Control Region CRZ

The leading lepton p_{T} distribution is shown in section 4.5.1, and those of m_{CT} and $\mathrm{m}_{\ell\ell}$ in figure A.2.

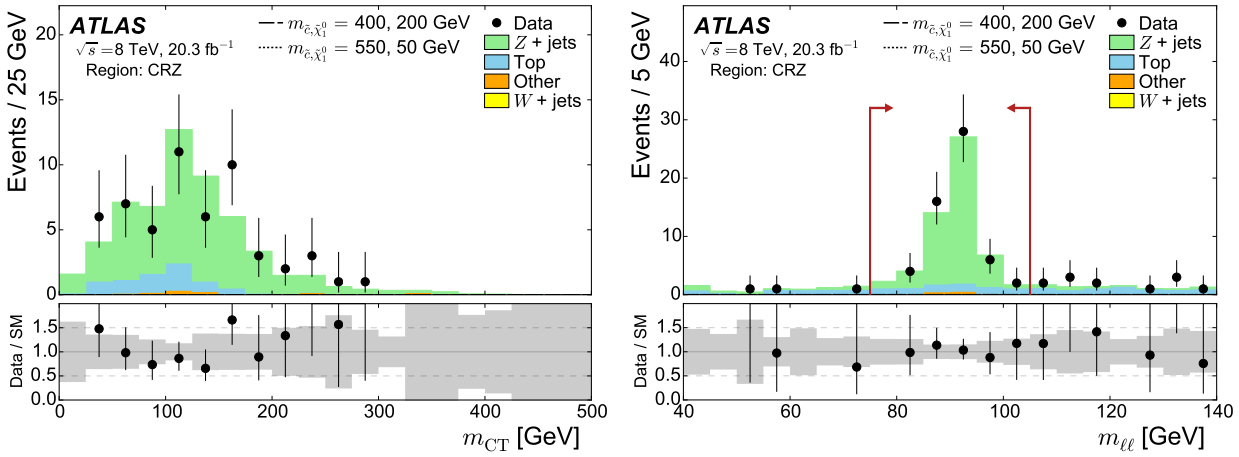


Figure A.2: Distributions of m_{CT} (left) and invariant mass of the ee or $\mu\mu$ pair (right) in control region CRZ. Plots from [4].

Control Region CRT

The m_{CT} distribution is shown in section 4.5.1, and those of $E_{\mathrm{T}}^{\mathrm{miss}}$ and $m_{\ell\ell}$ in figure A.3.

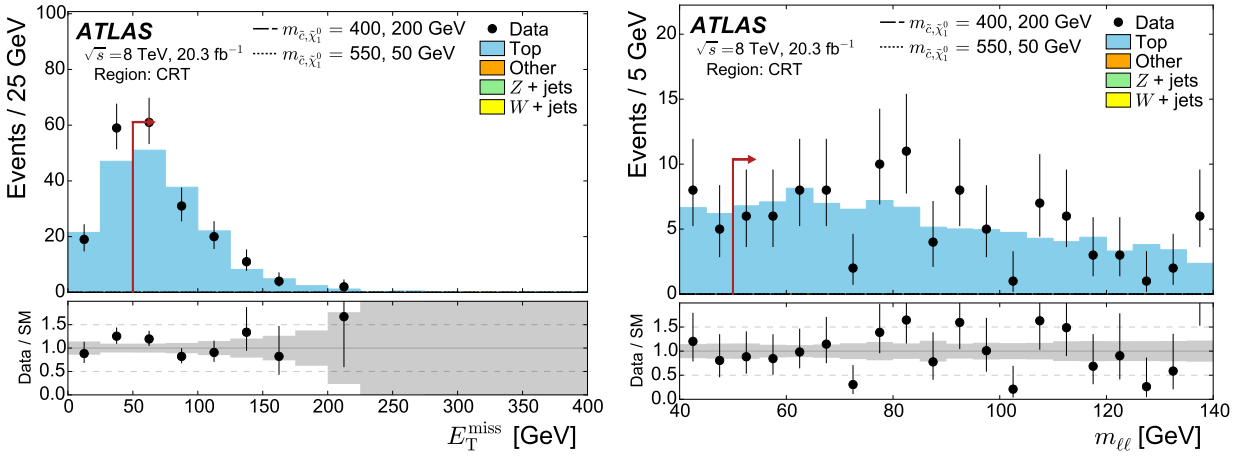


Figure A.3: Distributions of $E_{\mathrm{T}}^{\mathrm{miss}}$ (left) and invariant mass of the ee or $\mu\mu$ pair (right) in control region CRT. Plots from [4].

Control Region CRW

The leading lepton p_{T} distribution is shown in section 4.5.1, and those of m_{CT} and $E_{\mathrm{T}}^{\mathrm{miss}}$ in figure A.4.

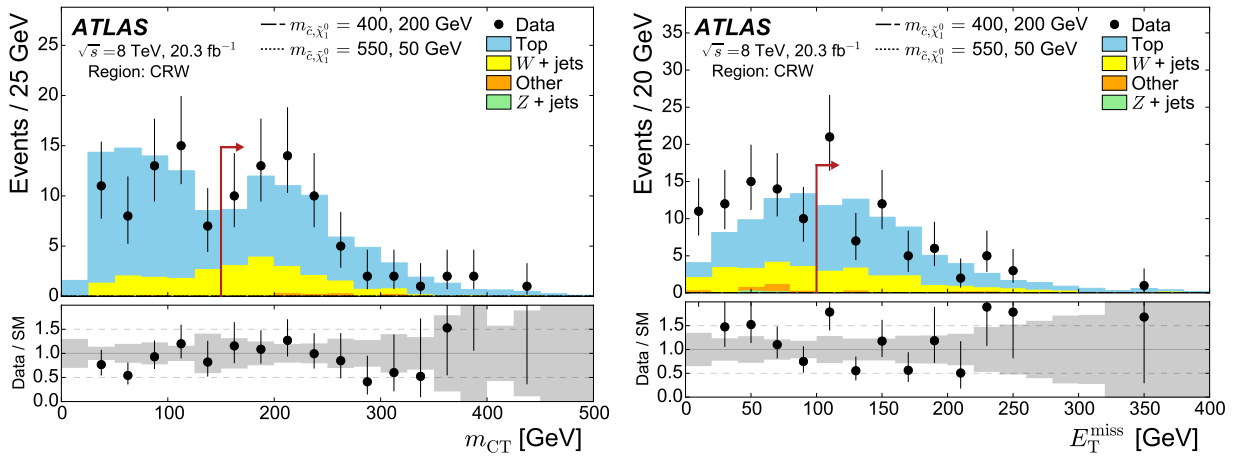


Figure A.4: Distributions of m_{CT} (left) and $E_{\mathrm{T}}^{\mathrm{miss}}$ (right) in control region CRW. Plots from [4].

Appendix B

Appendices to the Multijet search (chapter 5)

B.1 Branching ratios of pMSSM models

The search described in chapter 5 made use of a model based on the pMSSM, with gluinos pair produced and decaying via cascades with variable branching ratios. Figure B.1 shows the branching fractions of the $\tilde{g}$, with the high-multiplicity states of $t\bar{b}\tilde{\chi}_1^{\pm}$ and $t\bar{t}\tilde{\chi}_2^0$ accounting for about 80% of $\tilde{g}$ decays when $m(\tilde{\chi}_1^{\pm}) \lesssim 300$ GeV. At higher $\tilde{\chi}_1^{\pm}$ masses, especially at low $\tilde{g}$ masses, direct decays to the $\tilde{\chi}_1^0$ and a quark-antiquark pair become more prevalent. Unless this quark pair consists of top quarks, the resulting signature will only have 4 jets from these hard quarks and so this search is rendered insensitive. The search is sensitive when $\tilde{g} \to t\bar{t}\tilde{\chi}_1^0$, but the low branching fraction of around 10–15% restricts this to lower $\tilde{g}$ masses with higher production cross-sections.

The $\tilde{\chi}_2^0$ and $\tilde{\chi}_3^0$ have branching fractions of $\sim 50\%$ to each of $Z/h + \tilde{\chi}_1^0$ for $m(\tilde{\chi}_1^{\pm}) \gtrsim 300$ GeV, but decays to $Z\tilde{\chi}_1^0$ predominate below this since decays to the Higgs become kinematically inaccessible sooner (the $\tilde{\chi}_1^0$ mass is fixed at 60 GeV).

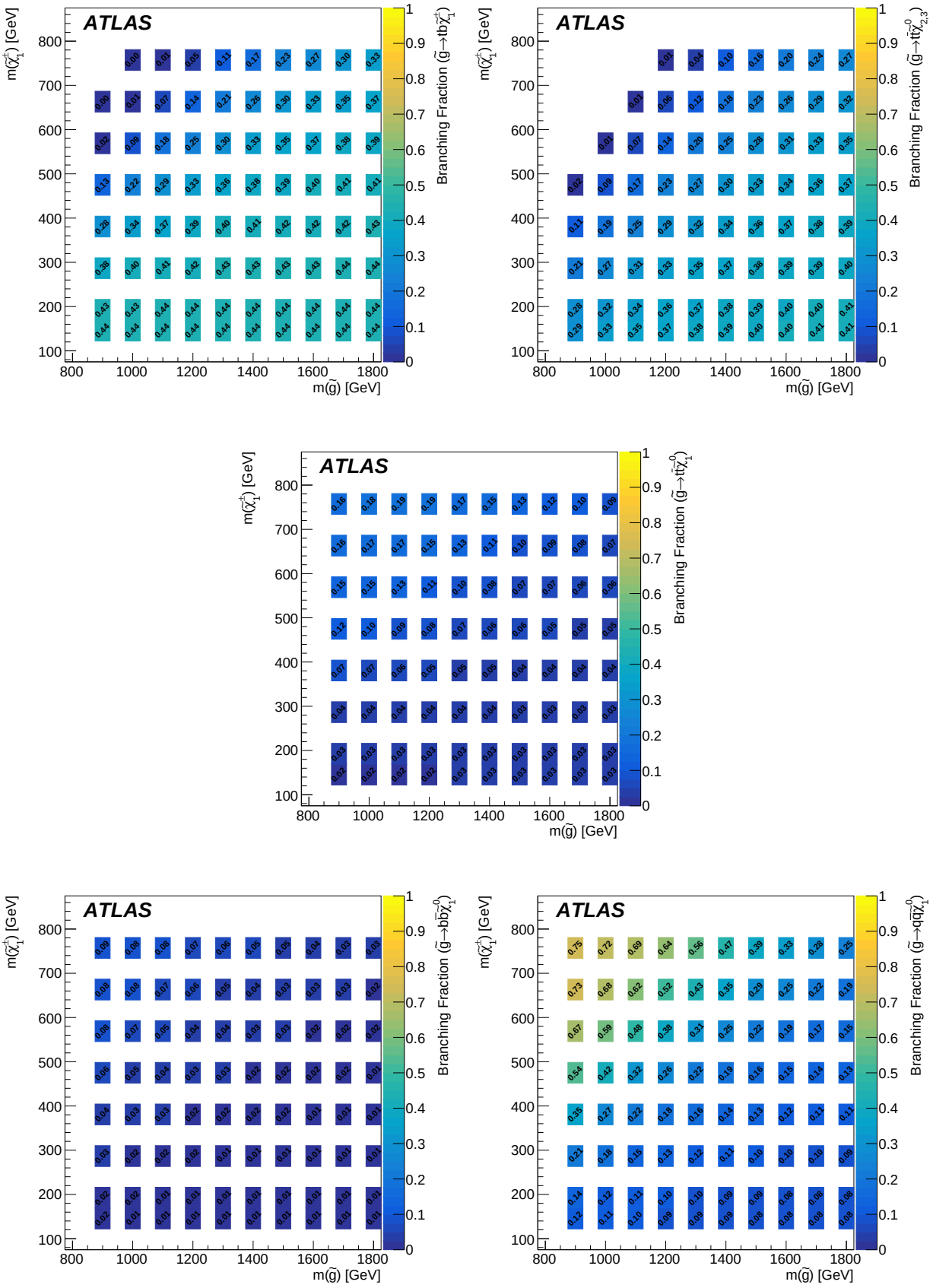


Figure B.1: Branching fractions of the various $\tilde{g}$ decay modes available in the pMSSM slice, from [2].

B.2 Alternative *b*-jet templates

A certain degree of disagreement between data and predictions was observed, seemingly originating from the multijet prediction in signal regions requiring b-jets. This could arise because the template for a `2b` region with N jets is formed from a control region with fewer jets, n, but the same number of b-jets. Thus the signal region has a b-jet fraction of $\sim \frac{2}{N}$ compared to $\sim \frac{2}{n}$ for the control region – i.e. 0.2 vs 0.33 for `10j50-2b` with its `6j50-2b` control region. This mismatch means there is relatively more $E_{\mathrm{T}}^{\mathrm{miss}}$ originating from B-hadron decays in the template region than the signal region, so the template will over-predict the number of high $E_{\mathrm{T}}^{\mathrm{miss}}/\sqrt{H_T}$ events.

The impact of this can be mitigated by forming templates with fractional numbers of b-jets, i.e. combining templates with particular weightings in order to match the b-jet fraction between signal and multijet control regions. For signal regions with one b-jet, this is obtained by combining `1b` and `0b` templates in the ratio $x : (1-x)$ such that

$$\frac{1}{N} = \frac{x \times 1}{n} + \frac{(1-x) \times 0}{n} \tag{B.1}$$

and so

$$x = \frac{n}{N} \tag{B.2}$$

For signal regions with two b-jets there is an ambiguity – a given b-jet fraction can be obtained through various combinations of `2b`, `1b` and `0b` templates. Here, equal weights $\frac{1}{2}(1-x)$ are given to each of `1b` and `0b`, satisfying

$$\frac{2}{N} = \frac{x \times 2}{n} + \frac{(1-x) \times 1}{2n} + \frac{(1-x) \times 0}{2n} \tag{B.3}$$

and so

$$x = \frac{1}{3}\left(\frac{4n}{N} - 1\right) \tag{B.4}$$

These calculations are approximate in four ways. Firstly the signal regions are inclusive in jet multiplicity, secondly the signal and control regions are inclusive in b-jet multiplicity, thirdly

N_j^{CR}	N_j^{SR}	0b	1b	2b
6	8	0.25	0.75	0
6	9	0.33	0.67	0
6	10	0.4	0.6	0
5	7	0.29	0.71	0
5	8	0.37	0.63	0

N_j^{CR}	N_j^{SR}	0b	1b	2b
6	8	0.17	0.17	0.66
6	9	0.22	0.22	0.56
6	10	0.27	0.27	0.46
5	7	0.19	0.19	0.62
5	8	0.25	0.25	0.5

Table B.1: Weightings applied to templates of each *b*-jet multiplicity, for 1b (left) and 2b (right) SRs, taken from eqs. (B.2) and (B.4) respectively.

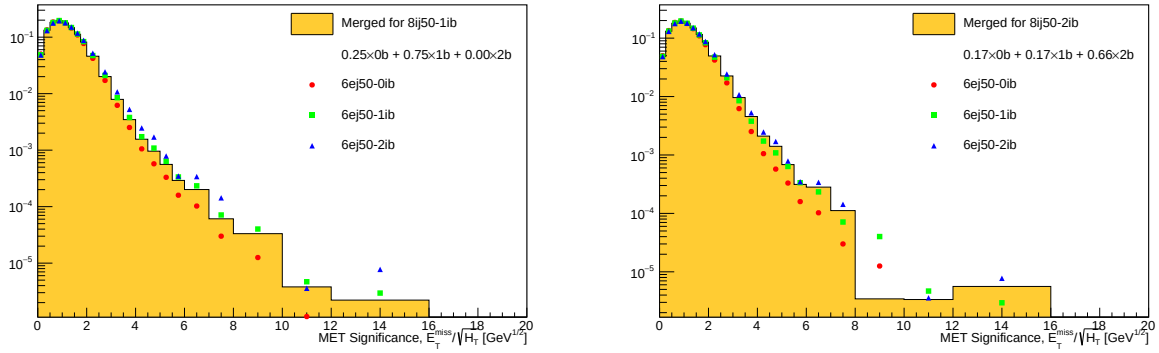


Figure B.2: Merged templates for 8j50-1b (left) and 8j50-2b (right). The templates formed from each *b*-jet multiplicity in turn are shown with the coloured markers.

a jet may be counted as a *b*-jet but not contribute to the region's jet count and fourthly it makes no consideration of *b*-tagging efficiencies. However, the resulting weightings, given in table B.1, may still be used as a test of the utility of the method.

Having obtained these weightings, they are applied to obtain mixed templates like those shown in figure B.2. These result, as expected, in narrower templates and correspondingly lower predictions of the multijet background. The overall impact of this is shown in figure B.3, with a general lowering of the template expectation for *b*-tagged regions observed. This change is by less than half of the total difference observed between prediction and data, and within the calculated uncertainties, so is not the full explanation for the slight mismatch. However, this approach may be of use for future versions of the analysis, with more data allowing better comparisons and finer segmentation of templates.

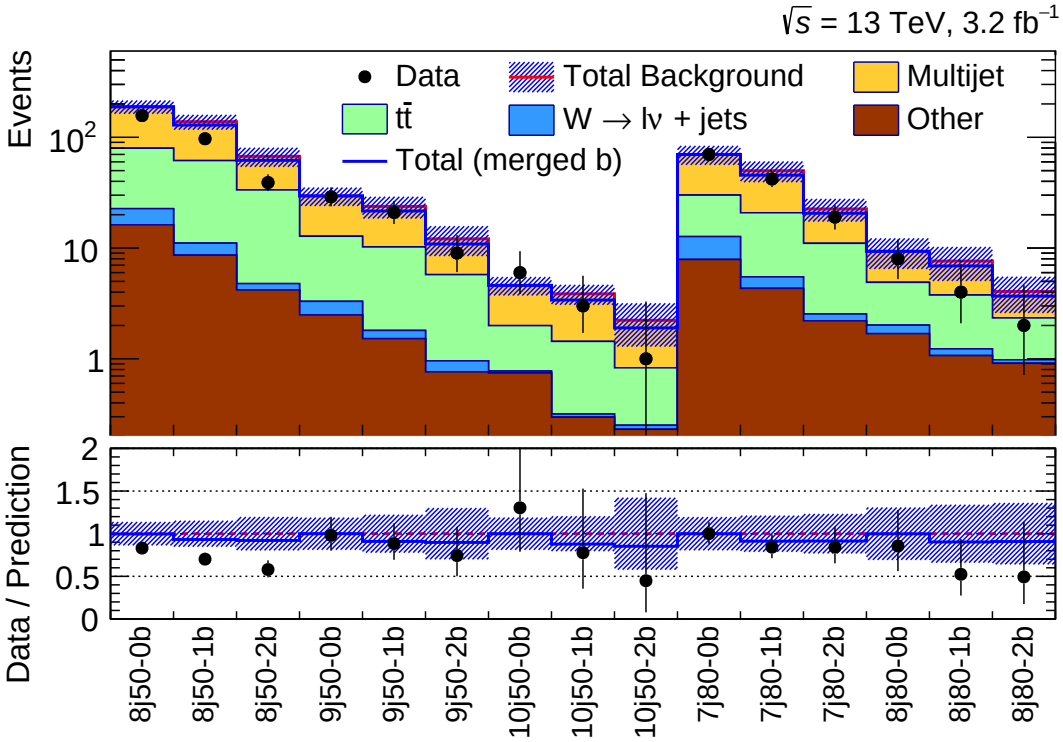


Figure B.3: Observed and expected yields for each signal region (see section 5.7.1), with the expectations resulting from the template merging procedure described here overlaid as blue horizontal lines. Systematic uncertainties, displayed as blue hatched bands, are not re-evaluated with these new templates.

B.3 Choice of H_T binning for multijet templates

As described in the description of the multijets search in chapter 5, the $E_{\mathrm{T}}^{\mathrm{miss}}/\sqrt{H_T}$ template is built in bins of H_T in order to factorise out the dependence of the template on H_T. These bins were chosen as: 0,600,800,1000,∞. In order to evaluate the uncertainty on the QCD background estimate as a result of this choice, an alternative H_T binning scheme of 0,500,700,900,1100,∞ (first two bins merged for `j80` regions, since as 6×80 GeV = 480 GeV there are almost no events in the lowest bin) is also considered, and the difference in predicted template yield taken as a (small) systematic uncertainty.

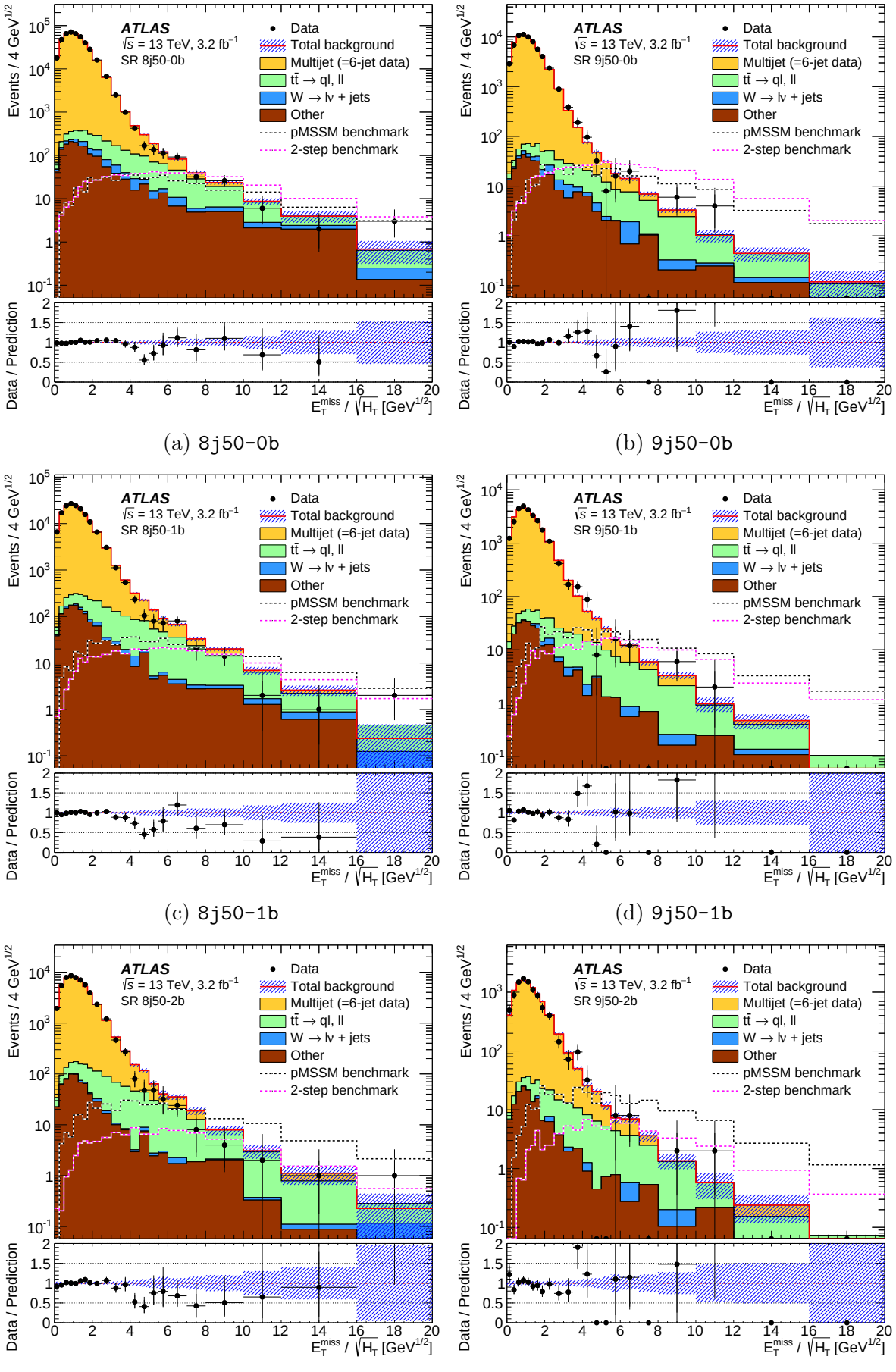
Table B.2 shows the difference between these binning choices, which result in predictions differing at the % level, peaking at 5.6%, far subdominant to the closure uncertainties described in the main text and in fact almost always less than the statistical uncertainty on the template prediction (arising principally from the finite number of events in the low $E_{\mathrm{T}}^{\mathrm{miss}}/\sqrt{H_T}$ but high jet multiplicity normalisation regions).

Region	Template Predictions		% Stat. Err.	% Difference
	$0-600-800-1000-\infty$	$0-(500)-700-900-1100-\infty$		
7j50-0b	663.90	659.59	2.12	-0.65
7j50-1b	372.31	373.28	3.23	0.26
7j50-2b	145.96	145.47	5.91	-0.33
8j50-0b	109.29	110.66	3.14	1.25
8j50-1b	76.73	77.67	4.50	1.22
8j50-2b	33.83	33.49	8.07	-0.99
9j50-0b	16.80	17.26	3.99	2.75
9j50-1b	13.53	13.79	5.54	1.94
9j50-2b	6.36	6.23	10.38	-2.07
10j50-0b	2.61	2.70	4.98	3.44
10j50-1b	2.42	2.48	6.61	2.48
10j50-2b	1.40	1.36	12.14	-2.68
6j80-0b	314.92	319.08	2.86	1.32
6j80-1b	198.77	202.57	3.97	1.91
6j80-2b	75.94	76.43	7.36	0.65
7j80-0b	39.96	41.38	3.78	3.57
7j80-1b	29.08	30.34	5.23	4.33
7j80-2b	11.53	11.41	10.32	-1.07
8j80-0b	4.45	4.69	4.49	5.31
8j80-1b	3.87	4.09	6.20	5.61
8j80-2b	1.72	1.65	11.63	-3.78

Table B.2: Comparison between two $H_{T,}$ binning schemes used to evaluate the binning systematic (the value in the right hand column) – the 80 GeV regions have a 'variation' set 0-700-900-1100 while the 50 GeV regions have 0-500-700-900-1100.

B.4 $E_{\mathrm{T}}^{\mathrm{miss}}/\sqrt{H_T}$ distributions in all signal regions

The following plots (figures B.4 to B.6) show the final $E_{\mathrm{T}}^{\mathrm{miss}}/\sqrt{H_T}$ distributions – i.e. following the fits to obtain the multijet, $t\bar{t}$ and W+jets backgrounds – in each signal region. These plots were also included as auxiliary material to [2]. It should be noted that their x-axes have variable bin widths, ranging from 0.25 $\mathrm{GeV}^{1/2}$ to 4 $\mathrm{GeV}^{1/2}$, and that their y-axes quote numbers of events per 4 $\mathrm{GeV}^{1/2}$. The signal 'benchmark' points referred to are the pMSSM point with $(m_{\tilde{g}},\ m_{\tilde{\chi}_1^{\pm}}) = (1300,\ 200)$ and the 2-step point with $(m_{\tilde{g}},\ m_{\tilde{\chi}_1^0}) = (1300,\ 200)$ – i.e. both just above the Run-1 observed limits.

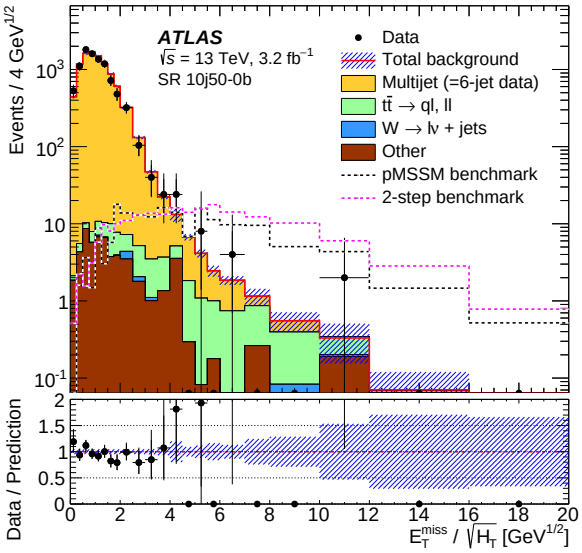


(a) `8j50-0b` (b) `9j50-0b`

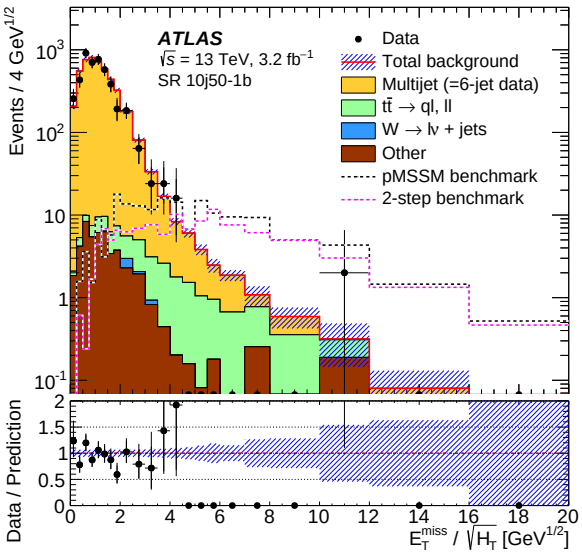
(c) `8j50-1b` (d) `9j50-1b`

(e) `8j50-2b` (f) `9j50-2b`

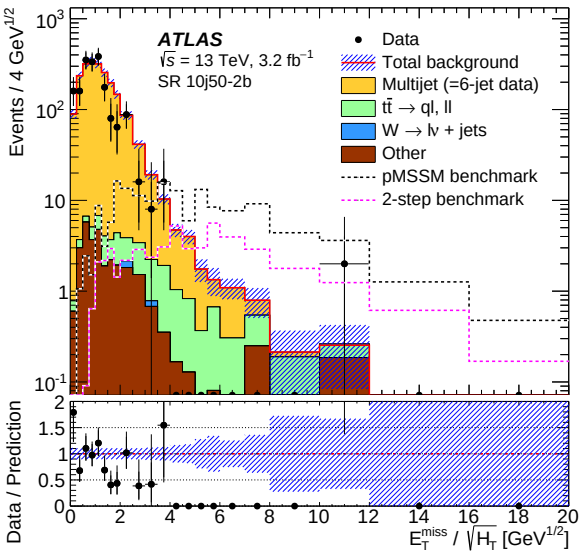
Figure B.4: $E_{\mathrm{T}}^{\mathrm{miss}}/\sqrt{H_T}$ distributions in the `8j50` and `9j50` signal regions, also shown in [2].



(a) `10j50-0b`

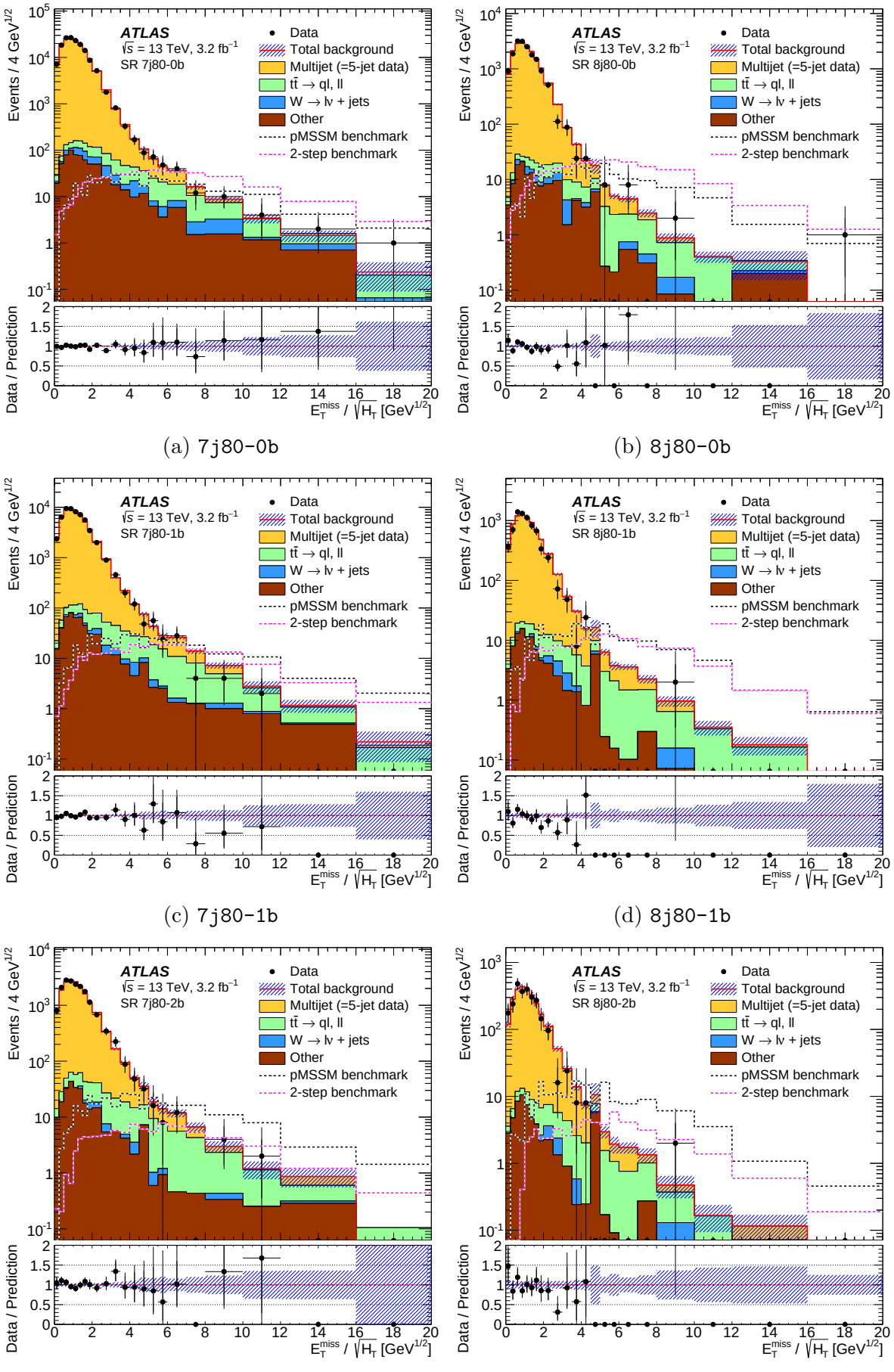


(b) `10j50-1b`



(c) `10j50-2b`

Figure B.5: $E_{\mathrm{T}}^{\mathrm{miss}}/\sqrt{H_T}$ distributions in the `10j50` signal regions, also shown in [2].



(a) `7j80-0b` (b) `8j80-0b`

(c) `7j80-1b` (d) `8j80-1b`

(e) `7j80-2b` (f) `8j80-2b`

Figure B.6: $E_{\mathrm{T}}^{\mathrm{miss}}/\sqrt{H_T}$ distributions in the `7j80` and `8j80` signal regions, also shown in [2].

Bibliography

[1] ATLAS Collaboration, *First validation plots in preparation for a search for new phenomena in final states with large jet multiplicities and missing transverse momentum at $\sqrt{s} = 13$ TeV proton–proton collisions using the ATLAS experiment*, ATL-PHYS-PUB-2015-030.

[2] ATLAS Collaboration, *Search for new phenomena in final states with large jet multiplicities and missing transverse momentum with ATLAS using $\sqrt{s} = 13$ TeV proton–proton collisions*, Phys. Lett. B **757** (2016) 334, arXiv:1602.06194 [hep-ex].

[3] ATLAS Collaboration, *Search for new phenomena in final states with large jet multiplicities and missing transverse momentum with ATLAS using $\sqrt{s} = 13$ TeV proton–proton collisions*, ATLAS-CONF-2015-077.

[4] ATLAS Collaboration, *Search for Scalar Charm Quark Pair Production in pp Collisions at $\sqrt{s} = 8$TeV with the ATLAS Detector*, Phys. Rev. Lett. **114** (2015) 161801, arXiv:1501.01325 [hep-ex].

[5] ATLAS Collaboration, *Performance and Calibration of the JetFitterCharm Algorithm for c-Jet Identification*, ATL-PHYS-PUB-2015-001.

[6] ATLAS Collaboration, *Search for direct third-generation squark pair production in final states with missing transverse momentum and two b-jets in $\sqrt{s} = 8$ TeV pp collisions with the ATLAS detector*, JHEP **10** (2013) 189, arXiv:1308.2631 [hep-ex].

[7] R. Munroe, *XKCD: fixion*,. http://xkcd.com/1621/.

[8] E. D. Bloom, D. H. Coward, H. DeStaebler, et al., *High-Energy Inelastic $e-p$ Scattering at 6° and 10°*, Phys. Rev. Lett. **23** (1969) 930.

[9] M. Breidenbach, J. I. Friedman, H. W. Kendall, et al., *Observed Behavior of Highly Inelastic Electron-Proton Scattering*, Phys. Rev. Lett. **23** (1969) 935.

[10] J. E. Augustin, A. M. Boyarski, M. Breidenbach, et al., *Discovery of a Narrow Resonance in e^+e^- Annihilation*, Phys. Rev. Lett. **33** (1974) 1406.

[11] J. J. Aubert, U. Becker, P. J. Biggs, et al., *Experimental Observation of a Heavy Particle J*, Phys. Rev. Lett. **33** (1974) 1404.

[12] S. W. Herb, D. C. Hom, L. M. Lederman, et al., *Observation of a Dimuon Resonance at 9.5 GeV in 400-GeV Proton-Nucleus Collisions*, Phys. Rev. Lett. **39** (1977) 252.

[13] CDF Collaboration, *Observation of Top Quark Production in $\overline{p}p$ Collisions with the Collider Detector at Fermilab*, Phys. Rev. Lett. **74** (1995) 2626.

[14] D0 Collaboration, *Search for High Mass Top Quark Production in $p\overline{p}$ Collisions at $\sqrt{s} = 1.8$ TeV*, Phys. Rev. Lett. **74** (1995) 2422.

[15] J. J. Thomson, *XL. Cathode Rays*, Philosophical Magazine Series 5 **44** (1897) 293.

[16] F. Reines and C. L. Cowan, *The Neutrino*, Nature **178** (1956) 446.

[17] C. D. Anderson and S. H. Neddermeyer, *Cloud Chamber Observations of Cosmic Rays at 4300 Meters Elevation and Near Sea-Level*, Phys. Rev. **50** (1936) 263.

[18] J. C. Street and E. C. Stevenson, *New Evidence for the Existence of a Particle of Mass Intermediate Between the Proton and Electron*, Phys. Rev. **52** (1937) 1003.

[19] G. Danby, J.-M. Gaillard, K. Goulianos, et al., *Observation of High-Energy Neutrino Reactions and the Existence of Two Kinds of Neutrinos*, Phys. Rev. Lett. **9** (1962) 036.

[20] M. L. Perl, G. S. Abrams, A. M. Boyarski, et al., *Evidence for Anomalous Lepton Production in $e^+ - e^-$ Annihilation*, Phys. Rev. Lett. **35** (1975) 1489.

[21] DONUT Collaboration, *Observation of tau neutrino interactions*, Phys. Lett. B **504** (2001) 218, arXiv:hep-ex/0012035.

[22] Particle Data Group Collaboration, K. A. Olive et al., *Review of Particle Physics*, Chin. Phys. C **38** (2014) 090001. and 2015 update.

[23] R. Davis, D. S. Harmer, and K. C. Hoffman, *Search for Neutrinos from the Sun*, Phys. Rev. Lett. **20** (1968) 1205.

[24] Super-Kamiokande Collaboration, Y. Fukuda et al., *Evidence for oscillation of atmospheric neutrinos*, Phys. Rev. Lett. **81** (1998) 1562, arXiv:hep-ex/9807003.

[25] SNO Collaboration, *Measurement of the rate of $\nu_e + d \rightarrow p + p + e^-$ interactions produced by ^8B solar neutrinos at the Sudbury Neutrino Observatory*, Phys. Rev. Lett. **87** (2001) 071301, arXiv:nucl-ex/0106015.

[26] SNO Collaboration, *Direct evidence for neutrino flavor transformation from neutral current interactions in the Sudbury Neutrino Observatory*, Phys. Rev. Lett. **89** (2002) 011301, arXiv:nucl-ex/0204008.

[27] T2K Collaboration, *Precise Measurement of the Neutrino Mixing Parameter θ_{23} from Muon Neutrino Disappearance in an Off-Axis Beam*, Phys. Rev. Lett. **112** (2014) 181801, arXiv:1403.1532 [hep-ex].

[28] A. H. Compton, *A Quantum Theory of the Scattering of X-rays by Light Elements*, Phys. Rev. **21** (1923) 483.

[29] UA1 Collaboration, *Experimental observation of isolated large transverse energy electrons with associated missing energy at s=540 GeV*, Phys. Lett. B **122** (1983) 103.

[30] UA2 Collaboration, *Observation of single isolated electrons of high transverse momentum in events with missing transverse energy at the CERN pp collider*, Phys. Lett. B **122** (1983) 476.

[31] UA1 Collaboration, *Experimental observation of lepton pairs of invariant mass around 95 GeV/c^2 at the CERN SPS collider*, Phys. Lett. B **126** (1983) 398.

[32] UA2 Collaboration, *Evidence for $Z^0 \to e^+e^-$ at the CERN $\bar{p}$ p Collider*, Phys. Lett. B **129** (1983) 130.

[33] P. Söding, *On the discovery of the gluon*, Eur. Phys. J. H **35** (2010) 003.

[34] ATLAS Collaboration, *Observation of a new particle in the search for the Standard Model Higgs boson with the ATLAS detector at the LHC*, Phys. Lett. B **716** (2012) 001, arXiv:1207.7214 [hep-ex].

[35] CMS Collaboration, *Observation of a new boson at a mass of 125 GeV with the CMS experiment at the LHC*, Phys. Lett. B **716** (2012) 030, arXiv:1207.7325 [hep-ex].

[36] M. McIrvin, *Renormalization in QED*,. https://commons.wikimedia.org/w/index.php?curid=1008752.

[37] http://www.nobelprize.org/nobel_prizes/physics/laureates/2004/phypub4highen.jpg.

[38] T. Sjöstrand, S. Mrenna, and P. Skands, *PYTHIA 6.4 physics and manual*, JHEP **05** (2006) 026, arXiv:hep-ph/0603175.

[39] M. Bähr et al., *Herwig++ Physics and Manual*, Eur. Phys. J. C **58** (2008) 639, arXiv:0803.0883 [hep-ph].

[40] S. Catani, F. Krauss, R. Kuhn, and B. Webber, *QCD matrix elements + parton showers*, JHEP **11** (2001) 063, arXiv:hep-ph/0109231.

[41] M. L. Mangano, M. Moretti, F. Piccinini, and M. Treccani, *Matching matrix elements and shower evolution for top-pair production in hadronic collisions*, JHEP **01** (2007) 013, arXiv:hep-ph/0611129.

[42] S. P. Martin, *A Supersymmetry primer*, arXiv:hep-ph/9709356.

[43] N. Ierushalmi, S. Iwamoto, G. Lee, V. Nepomnyashy, and Y. Shadmi, *LHC Benchmarks from Flavored Gauge Mediation*, arXiv:1603.02637 [hep-ph].

[44] B. C. Allanach et al., *The Snowmass points and slopes: Benchmarks for SUSY searches*, Eur. Phys. J. C **25** (2002) 113, arXiv:hep-ph/0202233.

[45] N. Ghodbane and H.-U. Martyn, *Compilation of SUSY particle spectra from Snowmass 2001 benchmark models*, in *Proceedings of APS / DPF / DPB Summer Study on the Future of Particle Physics (Snowmass 2001), Snowmass, Colorado, 30 Jun - 21 Jul 2001*. arXiv:hep-ph/0201233.

[46] C. Brenner Mariotto and M. C. Rodriguez, *Investigating gluino production at the LHC*, Braz. J. Phys. **38** (2008) 503, arXiv:0805.2395 [hep-ph].

[47] A. J. Barr and C. G. Lester, *A search for direct heffalon production using the ATLAS and CMS experiments at the Large Hadron Collider*, arXiv:1303.7367 [hep-ph].

[48] C. Lefèvre, *The CERN accelerator complex*,. https://cds.cern.ch/record/1260465.

[49] L. Evans and P. Bryant, *LHC Machine*, JINST **3** (2008) S08001.

[50] S. Myers, *The LEP collider, from design to approval and commissioning*, in *Proceedings of CERN Accelerator School, Nov. 26, 1990, CERN yellow report 91-08.* https://cas.web.cern.ch/cas/John%20Adams'%20Lectures/Myers.pdf.

[51] ATLAS Collaboration, *Luminosity Public Results*,. https://twiki.cern.ch/twiki/bin/view/AtlasPublic/LuminosityPublicResults.

[52] ATLAS Collaboration, *Luminosity Public Results in Run-2*,. https://twiki.cern.ch/twiki/bin/view/AtlasPublic/LuminosityPublicResultsRun2.

[53] ATLAS Collaboration, *The ATLAS Experiment at the CERN Large Hadron Collider*, JINST **3** (2008) S08003.

[54] J. Pequenao, *Computer generated image of the whole ATLAS detector*, CERN-GE-0803012 (2008).

[55] J. Pequenao, *Computer generated image of the ATLAS inner detector*, CERN-GE-0803014 (2008).

[56] ATLAS Collaboration, M. Kayl, *Tracking Performance of the ATLAS Inner Detector and Observation of Known Hadrons*, Proceedings, 22nd Hadron Collider Physics Conference (HCP 2010), arXiv:1010.1091 [physics.ins-det].

[57] ATLAS Pixel Collaboration, F. Hugging, *The ATLAS Pixel Detector*, IEEE Transactions on Nuclear Science **53** (2006) 1732, arXiv:physics/0412138 [physics.ins-det].

[58] ATLAS IBL Collaboration, A. La Rosa, *ATLAS IBL Pixel Upgrade*, Nucl. Phys. B Proceedings Supplements **215** (2011) 147, arXiv:1104.1980 [physics.ins-det].

[59] ATLAS Collaboration, *Operation and performance of the ATLAS semiconductor tracker*, JINST **9** (2014) P08009, arXiv:1404.7473 [hep-ex].

[60] ATLAS TRT Collaboration, J. M. Stahlman, *Commissioning and Performance of the ATLAS Transition Radiation Tracker with First High Energy pp and Pb-Pb collisions at LHC*, Physics Procedia **37** (2012) 506. Proceedings of the 2nd International Conference on Technology and Instrumentation in Particle Physics (TIPP 2011).

[61] J. Pequenao, *Computer generated image of the ATLAS calorimeter*, CERN-GE-0803015 (2008).

[62] ATLAS Collaboration, N. Nikiforou, *Performance of the ATLAS Liquid Argon Calorimeter after three years of LHC operation and plans for a future upgrade*, Proceedings, 3rd International Conference on Advancements in Nuclear Instrumentation Measurement Methods and their Applications (ANIMMA 2013), arXiv:1306.6756 [physics.ins-det].

[63] B. Sotto-Maior Peralva, *Calibration and Performance of the ATLAS Tile Calorimeter*, Proceedings, International School on High Energy Physics : Workshop on High Energy Physics in the near Future. (LISHEP 2013), arXiv:1305.0550 [physics.ins-det].

[64] J. Pequenao, *Computer generated image of the ATLAS Muons subsystem*, CERN-GE-0803017 (2008).

[65] W. Lampl, S. Laplace, D. Lelas, et al., *Calorimeter Clustering Algorithms: Description and Performance*, ATL-LARG-PUB-2008-002, ATL-COM-LARG-2008-003.

[66] ATLAS Collaboration, *Electron efficiency measurements with the ATLAS detector using the 2012 LHC proton-proton collision data*, ATLAS-CONF-2014-032.

[67] ATLAS Collaboration, *Electron identification measurements in ATLAS using $\sqrt{s}$ = 13 TeV data with 50 ns bunch spacing*, ATL-PHYS-PUB-2015-041.

[68] ATLAS Collaboration, *Measurement of the muon reconstruction performance of the ATLAS detector using 2011 and 2012 LHC protonproton collision data*, Eur. Phys. J. C **74** (2014) 3130, arXiv:1407.3935 [hep-ex].

[69] ATLAS Collaboration, *Muon reconstruction performance in early $\sqrt{s}$ = 13 TeV data*, ATL-PHYS-PUB-2015-037.

[70] G. P. Salam and G. Soyez, *A Practical Seedless Infrared-Safe Cone jet algorithm*, JHEP **05** (2007) 086, arXiv:0704.0292 [hep-ph].

[71] M. Cacciari, G. P. Salam, and G. Soyez, *The Anti-k_t jet clustering algorithm*, JHEP **04** (2008) 063, arXiv:0802.1189 [hep-ph].

[72] M. Cacciari and G. P. Salam, *Dispelling the N^3 myth for the k_t jet-finder*, Phys. Lett. B **641** (2006) 057, arXiv:hep-ph/0512210.

[73] ATLAS Collaboration, *Performance of pile-up mitigation techniques for jets in pp collisions at $\sqrt{s} = 8$ TeV using the ATLAS detector*, arXiv:1510.03823 [hep-ex].

[74] ATLAS Collaboration, *Jet Calibration and Systematic Uncertainties for Jets Reconstructed in the ATLAS Detector at $\sqrt{s} = 13$ TeV*, ATL-PHYS-PUB-2015-015.

[75] ATLAS Collaboration, *Jet global sequential corrections with the ATLAS detector in proton-proton collisions at $\sqrt{s}$ = 8 TeV*, ATLAS-CONF-2015-002.

[76] ATLAS Collaboration, *Expected performance of the ATLAS b-tagging algorithms in Run-2*, ATL-PHYS-PUB-2015-022.

[77] ATLAS Collaboration, *Commissioning of the ATLAS b-tagging algorithms using $t\bar{t}$ events in early Run-2 data*, ATL-PHYS-PUB-2015-039.

[78] ATLAS Collaboration, *Performance of Missing Transverse Momentum Reconstruction in ATLAS studied in Proton-Proton Collisions recorded in 2012 at 8 TeV*, ATLAS-CONF-2013-082.

[79] ATLAS Collaboration, *Expected performance of missing transverse momentum reconstruction for the ATLAS detector at $\sqrt{s} = 13$ TeV*, ATL-PHYS-PUB-2015-023.

[80] ATLAS Collaboration, *Selection of jets produced in 13 TeV proton-proton collisions with the ATLAS detector*, ATLAS-CONF-2015-029.

[81] GEANT4 Collaboration, Agostinelli et al., *GEANT4: A simulation toolkit*, Nucl. Instrum. Meth. A **506** (2003) 250.

[82] ATLAS Collaboration, *The ATLAS Simulation Infrastructure*, Eur. Phys. J. C **70** (2010) 823, arXiv:1005.4568 [physics.ins-det].

[83] ATLAS Collaboration, *Performance of the Fast ATLAS Tracking Simulation (FATRAS) and the ATLAS Fast Calorimeter Simulation (FastCaloSim) with single particles*, ATL-SOFT-PUB-2014-001.

[84] ATLAS Collaboration, *Search for squarks and gluinos with the ATLAS detector in final states with jets and missing transverse momentum using $\sqrt{s} = 8$ TeV proton–proton collision data*, JHEP **09** (2014) 176, arXiv:1405.7875 [hep-ex].

[85] ATLAS Collaboration, *Search for direct third-generation squark pair production in final states with missing transverse momentum and two b-jets in $\sqrt{s}$=8 TeV pp collisions with the ATLAS detector*, JHEP **10** (2013) 189, arXiv:hep-ex/1308.2631 [hep-ex].

[86] W. Beenakker, M. Krämer, T. Plehn, M. Spira, and P. Zerwas, *Stop production at hadron colliders*, Nucl. Phys. B **515** (1998) 003, arXiv:hep-ph/9710451.

[87] W. Beenakker, S. Brensing, M. Krämer, et al., *Supersymmetric top and bottom squark production at hadron colliders*, JHEP **08** (2010) 098, arXiv:1006.4771 [hep-ph].

[88] W. Beenakker, S. Brensing, M. Krämer, et al., *Squark and Gluino Hadroproduction*, Int. Jour. Mod. Phys. A **26** (2011) 2637, arXiv:1105.1110 [hep-ph].

[89] M. Krämer et al., *Supersymmetry production cross sections in pp collisions at $\sqrt{s}$ = 7 TeV*, CERN-PH-TH-2012-163 (2012), arXiv:1206.2892 [hep-ph].

[90] J. Alwall, M. Herquet, F. Maltoni, O. Mattelaer, and T. Stelzer, *MadGraph 5 : Going Beyond*, JHEP **06** (2011) 128, arXiv:1106.0522 [hep-ph].

[91] S. Frixione, P. Nason, and C. Oleari, *Matching NLO QCD computations with Parton Shower simulations: the POWHEG method*, JHEP **11** (2007) 070, arXiv:0709.2092 [hep-ph].

[92] B. P. Kersevan and E. Richter-Wąs, *The Monte Carlo event generator AcerMC version 2.0 with interfaces to PYTHIA 6.2 and HERWIG 6.5*, arXiv:hep-ph/0405247.

[93] T. Gleisberg et al., *Event generation with SHERPA 1.1*, JHEP **02** (2009) 007, arXiv:0811.4622 [hep-ph].

[94] R. Gavin, Y. Li, F. Petriello and S. Quackenbush, *FEWZ 2.0: A code for hadronic Z production at next-to- next-to-leading order*, Comput. Phys. Commun. **182** (2011) 2388, arXiv:1011.3540 [hep-ph].

[95] ATLAS Collaboration, *Calibration of b-tagging using dileptonic top pair events in a combinatorial likelihood appoach with the ATLAS experiment*, ATLAS-CONF-2014-004.

[96] ATLAS Collaboration, *Calibration of the performance of b-tagging for c and light-flavour jets in the 2012 ATLAS data*, ATLAS-CONF-2014-046.

[97] C. Lester and D. Summers, *Measuring masses of semiinvisibly decaying particles pair produced at hadron colliders*, Phys. Lett. B **463** (1999) 099, arXiv:hep-ph/9906349.

[98] A. Barr, C. Lester, and P. Stephens, *m_{T2}: The Truth behind the glamour*, J. Phys. G **29** (2003) 2343, arXiv:hep-ph/0304226.

[99] B. C. Allanach, A. J. Barr, A. Dafinca, and C. Gwenlan, *Discovery reach for generic supersymmetry at the LHC: MT2 versus missing transverse momentum selections for pMSSM searches*, JHEP **07** (2011) 104, arXiv:1105.1024 [hep-ph].

[100] M. Serna, *A Short comparison between m_{T2} and m_{CT}*, JHEP **06** (2008) 004, arXiv:0804.3344 [hep-ph].

[101] D. Tovey, *On measuring the masses of pair-produced semi-invisibly decaying particles at hadron colliders*, JHEP **04** (2008) 034, arXiv:0802.2879 [hep-ph].

[102] G. Polesello and D. Tovey, *Supersymmetric particle mass measurement with the boost-corrected contransverse mass*, JHEP **03** (2010) 030, arXiv:0910.0174 [hep-ph].

[103] S. Owen, *Data-driven estimation of the QCD multijet background to SUSY searches with jets and missing transverse momentum at ATLAS using jet smearing*, ATL-PHYS-INT-2012-008.

[104] ATLAS Collaboration, *Improved luminosity determination in pp collisions at $\sqrt{s}$ = 7 TeV using the ATLAS detector at the LHC*, Eur. Phys. J. C **73** (2013) 2518, arXiv:1302.4393 [hep-ex].

[105] P. Nason and B. Webber, *Next-to-Leading-Order Event Generators*, Ann. Rev. Nucl. Part. Sci. **62** (2012) 187, arXiv:1202.1251 [hep-ph].

[106] M. Blanke, B. Fuks, I. Galon, and G. Perez, *Gluino Meets Flavored Naturalness*, arXiv:1512.03813 [hep-ph].

[107] G. Perez, Y. Soreq, E. Stamou, and K. Tobioka, *Prospects for measuring the Higgs boson coupling to light quarks*, Phys. Rev. D **93** (2016) 013001, arXiv:1505.06689 [hep-ph].

[108] G. Perez, Y. Soreq, E. Stamou, and K. Tobioka, *Constraining the charm Yukawa and Higgs-quark coupling universality*, Phys. Rev. D **92** (2015) 033016, arXiv:1503.00290 [hep-ph].

[109] ATLAS Collaboration, *Search for new phenomena in final states with large jet multiplicities and missing transverse momentum at $\sqrt{s}$=8 TeV proton-proton collisions using the ATLAS experiment*, JHEP **10** (2013) 130, arXiv:1308.1841 [hep-ex]. [Erratum: JHEP **01** (2014) 109].

[110] C. Borschensky, Z. Gecse, M. Krämer, et al., *LHC SUSY Cross Section Working Group TWiki*,. https://twiki.cern.ch/twiki/bin/view/LHCPhysics/SUSYCrossSections.

[111] C. Borschensky, M. Krämer, A. Kulesza, et al., *Squark and gluino production cross sections in pp collisions at $\sqrt{s}$ = 13, 14, 33 and 100 TeV*, Eur. Phys. J. C **74** (2014) 3174, arXiv:1407.5066 [hep-ph].

[112] ATLAS Collaboration, *Summary plots from the ATLAS Supersymmetry physics group*,. https://atlas.web.cern.ch/Atlas/GROUPS/PHYSICS/CombinedSummaryPlots/SUSY/index.html.

[113] ATLAS Collaboration, *Summary of the ATLAS experiments sensitivity to supersymmetry after LHC Run 1 interpreted in the phenomenological MSSM*, JHEP **10** (2015) 134, arXiv:1508.06608 [hep-ex].

[114] ATLAS Collaboration, *Search for new phenomena in final states with large jet multiplicities and missing transverse momentum using $\sqrt{s} = 7$ TeV pp collisions with the ATLAS detector*, JHEP **11** (2011) 099, arXiv:1110.2299 [hep-ex].

[115] ATLAS Collaboration, *Hunt for new phenomena using large jet multiplicities and missing transverse momentum with ATLAS in $4.7 fb^{-1}$ of $\sqrt{s} = 7$ TeV proton-proton collisions*, JHEP **07** (2012) 167, arXiv:1206.1760 [hep-ex].

[116] ATLAS Collaboration, *Search for new phenomena using large jet multiplicities and missing transverse momentum with ATLAS in 5.8 fb^{-1} of $\sqrt{s} = 8$ TeV proton-proton collisions*, ATLAS-CONF-2012-103, ATLAS-COM-CONF-2012-142.

[117] ATLAS Collaboration, *Summary of the searches for squarks and gluinos using $\sqrt{s} = 8$ TeV pp collisions with the ATLAS experiment at the LHC*, JHEP **10** (2015) 054, arXiv:1507.05525 [hep-ex].

[118] ATLAS Collaboration, *Summary of the ATLAS experiments sensitivity to supersymmetry after LHC Run 1 interpreted in the phenomenological MSSM*, JHEP **10** (2015) 134, arXiv:1508.06608 [hep-ex].

[119] A. Buckley, *PySLHA: a Pythonic interface to SUSY Les Houches Accord data*, Eur. Phys. J. C **75** (2015) 467, arXiv:1305.4194 [hep-ph].

[120] ATLAS Collaboration, *Simulation of top quark production for the ATLAS experiment at $\sqrt{s}$ = 13 TeV*, ATL-PHYS-PUB-2016-004.

[121] S. Alioli, P. Nason, C. Oleari, and E. Re, *A general framework for implementing NLO calculations in shower Monte Carlo programs: the POWHEG BOX*, JHEP **06** (2010) 043, arXiv:1002.2581 [hep-ph].

[122] H.-L. Lai et al., *New parton distributions for collider physics*, Phys. Rev. D **82** (2010) 074024, arXiv:1007.2241 [hep-ph].

[123] P. Artoisenet, R. Frederix, O. Mattelaer, and R. Rietkerk, *Automatic spin-entangled decays of heavy resonances in Monte Carlo simulations*, JHEP **03** (2013) 015, arXiv:1212.3460 [hep-ph].

[124] T. Sjöstrand, S. Mrenna, and P. Z. Skands, *PYTHIA 6.4 physics and manual*, JHEP **05** (2006) 026, arXiv:hep-ph/0603175.

[125] J. Pumplin et al., *New generation of parton distributions with uncertainties from global QCD analysis*, JHEP **07** (2002) 012, arXiv:hep-ph/0201195.

[126] P. Z. Skands, *Tuning Monte Carlo Generators: The Perugia Tunes*, Phys. Rev. D **82** (2010) 074018, arXiv:1005.3457 [hep-ph].

[127] D. J. Lange, *The EvtGen particle decay simulation package*, Nucl. Instrum. Meth. A **462** (2001) 152.

[128] M. Czakon and A. Mitov, *Top++: a program for the calculation of the top-pair cross-section at hadron colliders*, Comput. Phys. Commun. **185** (2014) 2930, arXiv:1112.5675 [hep-ph].

[129] ATLAS Collaboration, *Modelling of the $t\bar{t}H$ and $t\bar{t}V$ ($V = W, Z$) processes for $\sqrt{s}$ = 13 TeV ATLAS analyses*, ATL-PHYS-PUB-2016-005.

[130] J. Alwall, R. Frederix, S. Frixione, et al., *The automated computation of tree-level and next-to-leading order differential cross sections, and their matching to parton shower simulations*, JHEP **07** (2014) 079, arXiv:1405.0301 [hep-ph].

[131] T. Sjöstrand, S. Mrenna, and P. Z. Skands, *A Brief Introduction to PYTHIA 8.1*, Comput. Phys. Commun. **178** (2008) 852, arXiv:0710.3820 [hep-ph].

[132] ATLAS Collaboration, *ATLAS Run 1 Pythia8 tunes*, ATL-PHYS-PUB-2014-021.

[133] NNPDF Collaboration, R. D. Ball et al., *Parton distributions with LHC data*, Nucl. Phys. B **867** (2013) 244, arXiv:1207.1303 [hep-ph].

[134] ATLAS Collaboration, *Monte Carlo Generators for the Production of a W or Z/γ^* Boson in Association with Jets at ATLAS in Run 2*, ATL-PHYS-PUB-2016-003.

[135] ATLAS Collaboration, *Multi-Boson Simulation for 13 TeV ATLAS Analyses*, ATL-PHYS-PUB-2016-002.

[136] T. Gleisberg and S. Höche, *Comix, a new matrix element generator*, JHEP **12** (2008) 039, arXiv:0808.3674 [hep-ph].

[137] F. Cascioli, P. Maierhöfer, and S. Pozzorini, *Scattering Amplitudes with Open Loops*, Phys. Rev. Lett. **108** (2012) 111601, arXiv:1111.5206 [hep-ph].

[138] S. Schumann and F. Krauss, *A Parton shower algorithm based on Catani-Seymour dipole factorisation*, JHEP **03** (2008) 038, arXiv:0709.1027 [hep-ph].

[139] S. Höche, F. Krauss, M. Schönherr, and F. Siegert, *QCD matrix elements + parton showers: The NLO case*, JHEP **04** (2013) 027, arXiv:1207.5030 [hep-ph].

[140] ATLAS Collaboration, *Comparison of Monte Carlo generator predictions from Powheg and Sherpa to ATLAS measurements of top pair production at 7 TeV*, ATL-PHYS-PUB-2015-011.

[141] M. Baak, G. Besjes, D. Côté, et al., *HistFitter software framework for statistical data analysis*, Eur. Phys. J. C **75** (2015) 153, arXiv:1410.1280 [hep-ex].

[142] ROOT Collaboration, K. Cranmer, G. Lewis, L. Moneta, A. Shibata, and W. Verkerke, *HistFactory: A tool for creating statistical models for use with RooFit and RooStats*, CERN-OPEN-2012-016 (2012).

[143] A. L. Read, *Presentation of search results: The CL(s) technique*, J. Phys. G **28** (2002) 2693.